



UNIVERSITY OF OSLO  
FACULTY OF MATHEMATICS AND NATURAL SCIENCES

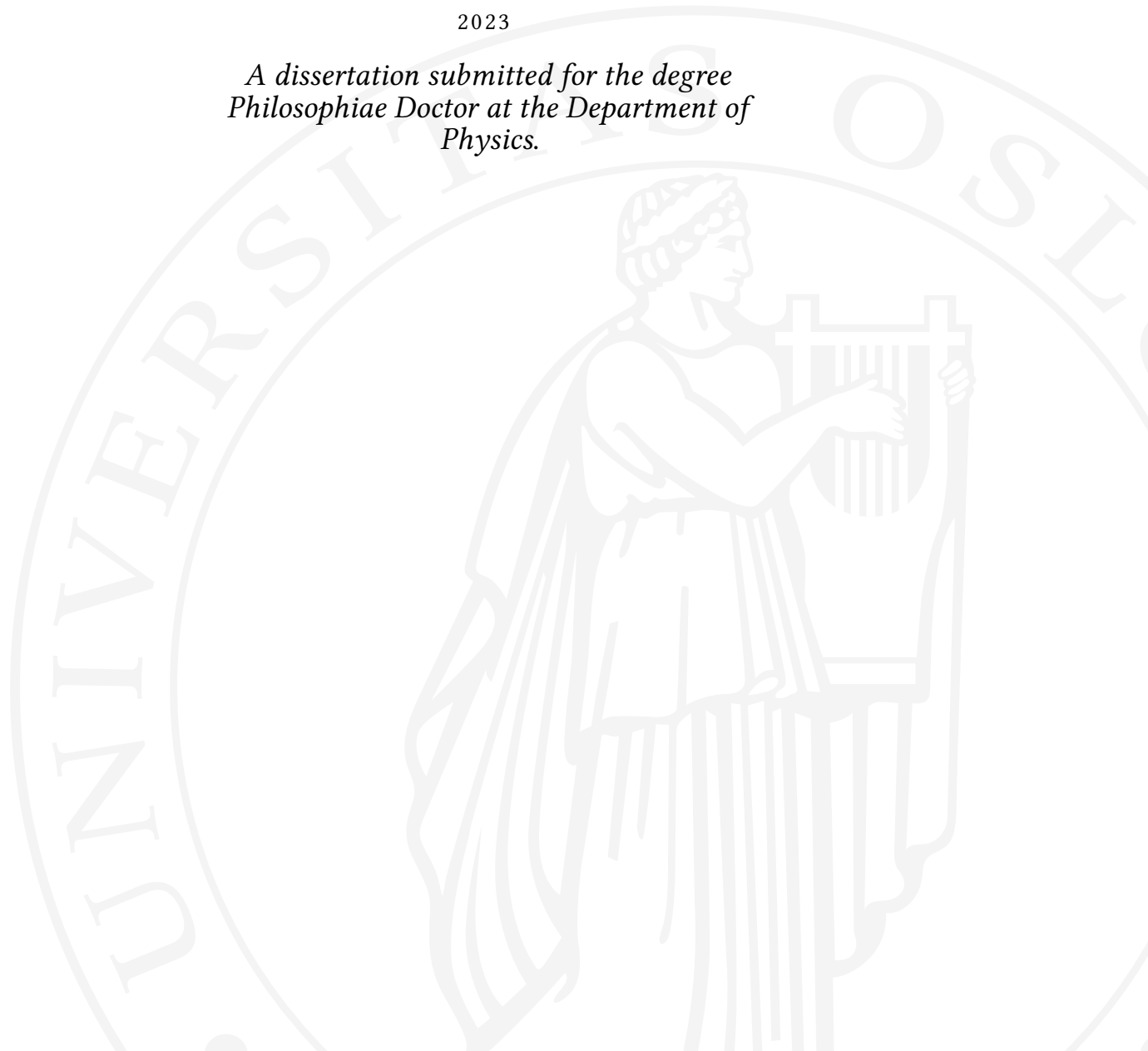
---

Symmetry, topology, and crystal deformations:  
a phase-field crystal approach

VIDAR SKOGVOLL

2023

*A dissertation submitted for the degree  
Philosophiae Doctor at the Department of  
Physics.*



© Vidar Skogvoll, 2023

*Series of dissertations submitted to the  
Faculty of Mathematics and Natural Sciences, University of Oslo  
No. 2622*

ISSN 1501-7710

All rights reserved. No part of this publication may be  
reproduced or transmitted, in any form or by any means, without permission.

Cover: UiO.  
Print production: Graphic Center, University of Oslo.



## ACKNOWLEDGMENT

This research was conducted at the University of Oslo in the Earthflows program under the Njord Center for Studies of the Physics of the Earth, in close collaboration with the Porelab Center of Excellence in the period of 2019-2023.

First and foremost, I would like to thank my supervisor, Prof. Luiza Angheluta. Your guidance and never-empty optimism has been invaluable through these muddy waters of topology and crystal symmetry. Thank you for letting me pursue my own interests, and always being excited about new ideas and results. It would not have been such an enjoyable experience otherwise. I owe Audun Skaugen a big thanks for inspiring me to pursue a Ph.D. in this field and, in general, for helping with the scientific work with extreme precision.

I also like to thank Jorge Viñals and Marco Salvalaglio for many exciting conversations, research collaborations, and last but not least, for welcoming me in your respective cities during my stays as covid travel restrictions were lifted.

The Njord center is a vibrant place of discussion and exchange of ideas, with lots of nice people who have made my stay enjoyable. It is led under the steady hand of François Renard, who I thank for greeting me with a smile as I arrived in the morning. Luca Menegon also deserves my gratitude for always being willing to discuss with enthusiasm the plasticity in geological materials and for bringing me along to look at rocks, lots of rocks, in the Wester Gneiss Regions of Norway. With me on this journey, I have always relied on the input and discussions with Jonas Rønning - whose thesis I look forward to rip apart as you have done to mine these last few weeks. Also, a special thanks to Franzi, Harish, and Richard - for going through this thesis with the finest of toothcombs.

There are, of course, a bunch of other physics colleagues to whom I owe gratitude, both in Oslo, Dresden, and Minnesota. There is one colleague in particular, however, not from physics, without whom I might not have finished my Ph.D. work: Ronja, my home office - and dance break partner during the pandemic. Thank you for listening to all the physics.

Finally, I would like to thank my friends and family for always being there and supporting me every step of the way.

April 2023 Vidar Skogvoll

The six images that adorn the first page of every chapter were generated using artificial intelligence. All other parts of this thesis, figures and text, were produced and improved upon using, exclusively, human intelligence.



## ABSTRACT

We adopt the phase-field crystal (PFC) approach to study nonequilibrium dynamics for systems with broken translational and rotational symmetry, i.e., crystalline materials. The focus is on understanding the fundamental defects of the crystalline lattice, i.e., dislocations, in relation to their topological and kinematic properties, and how dislocations are coupled with far-field elastic distortions. By restricting the diffusive PFC dynamics to mechanical equilibrium, we study and characterize the nucleation of dislocations induced by external stress. Extending this description to other crystal symmetries and higher dimensions, we formulate a description of the configurational stress, which is valid in any Ginzburg-Landau-type theory. This is further exploited in developing a hydrodynamic PFC theory for polycrystalline systems with elastic interactions. Then, we characterize dislocation lines in a 3D bcc crystal lattice, derive an explicit expression for the local dislocation velocity, and show that the dislocations are driven by overdamped motion in response to the Peach-Koehler force with an explicit expression for the mobility. Since the order parameter describing the crystal phase is continuous and well-defined at the crystal defects, we can define a non-singular theory of the defect density. This idea is generalized beyond the crystalline symmetry, and a unified framework is presented to describe both local non-linear excitations and topological defects, which is also applied to Bose-Einstein condensates, and active nematic liquid crystals.



## SAMMENDRAG

Vi anvender fase-feltkrystallen (PFC) for å studere ikke-likevektsdynamikk for systemer med brutt translasjons- og rotasjonssymmetri, dvs. krystallinske materialer. Fokuset er på å forstå de grunnleggende defektene i det krystallinske gitteret, dvs. dislokasjoner, i forhold til deres topologiske og kinematiske egenskaper, og hvordan dislokasjoner er koblet med elastiske fjernfelt. Ved å begrense den diffusive PFC-dynamikken til mekanisk likevekt, studerer og karakteriserer vi kjernedannelsen av dislokasjoner induisert av ytre stress. Ved å utvide denne beskrivelsen til andre krystallsymmetrier og høyere dimensjoner, formulerer vi en beskrivelse av konfigurasjonssstresset, som er gyldig i enhver Ginzburg-Landau-teori. Dette utnyttes videre for å utvikle en hydrodynamisk PFC-teori for polykrystallinske systemer med elastiske vekselvirkninger. Deretter karakteriserer vi dislokasjonslinjer i et 3D kroppssentrert krystallgitter, utleder et eksplisitt uttrykk for den lokale dislokasjonshastigheten, og viser at dislokasjonene er drevet av overdempet bevegelse respons til Peach-Koehler-kraften med et eksplisitt uttrykk for mobiliteten. Siden ordensparameteren som beskriver krystallfasen er kontinuerlig og veldefinert ved krystalldefektene, kan vi definere en ikke-singulær teori om defekttettheten. Denne idéen er generalisert utover den krystallinske symmetrien, og et enhetlig rammeverk presenteres for å beskrive både lokale ikke-lineære eksitasjoner og topologiske defekter, som også anvendes på Bose-Einstein-kondensater, og aktive nematiske flytende krystaller.



# CONTENTS

1	INTRODUCTION	<b>I</b>
2	CONDENSED MATTER PHYSICS APPROACH TO SOLID CRYSTALS	<b>7</b>
2.1	Statistical mechanics in out-of-equilibrium systems . . . . .	7
2.2	The structure of the crystalline solid . . . . .	11
2.3	Crystal diffraction . . . . .	12
2.4	Mean-field models . . . . .	15
3	SYMMETRY, GROUPS, AND TOPOLOGY	<b>19</b>
3.1	The order-disorder transition . . . . .	20
3.2	Symmetry and group theory . . . . .	21
3.3	Topological defects . . . . .	26
3.4	The Halperin-Mazenko method . . . . .	28
4	ELASTICITY AND PLASTICITY	<b>31</b>
4.1	Linear elasticity . . . . .	32
4.2	Plasticity and the dislocation . . . . .	36
4.3	The properties of dislocations . . . . .	38
4.4	Hydrodynamics of crystals . . . . .	44
4.5	Multiscale modeling of materials . . . . .	47
5	THE PHASE-FIELD CRYSTAL	<b>49</b>
5.1	Material properties and other symmetries . . . . .	51
5.2	The configurational stress . . . . .	53
5.3	The few-mode approximation . . . . .	53
5.4	The amplitude formulation of the PFC model . . . . .	57
5.5	Topological structures in the PFC model . . . . .	61
5.6	The time scale problem . . . . .	63
6	PAPERS SUMMARY AND OUTLOOK	<b>67</b>
6.1	Paper I: Dislocation nucleation in the phase-field crystal model . . . . .	67
6.2	Paper II: Stress in ordered systems: Ginzburg-Landau type density field theory . . . . .	69
6.3	Paper III: A phase field crystal theory of the kinematics of dislocation lines	73
6.4	Paper IV: Hydrodynamic phase field crystal approach to interfaces, dislocations and multi-grain networks . . . . .	76

6.5	Paper V: A unified field theory of topological defects and non-linear local excitations . . . . .	77
6.6	Outlook . . . . .	79
<b>APPENDIX A NUMERICAL METHODS</b>		<b>85</b>
A.1	Numerical simulation of loop annihilation in the PFC . . . . .	85
A.1.1	Preparation of the initial condition . . . . .	86
A.1.2	Coarse-graining . . . . .	87
A.1.3	Analysis of topological properties . . . . .	87
A.1.4	Time evolution schemes . . . . .	88
A.2	Solving partial differential equations with periodic boundary conditions	89
A.2.1	Finding the compatible displacement . . . . .	89
A.2.2	Finding the distortion from the dislocation density tensor . . .	90
<b>REFERENCES</b>		<b>92</b>
<b>PRINTED PAPERS</b>		<b>101</b>
	Paper I: Dislocation nucleation in the phase-field crystal model . . . . .	103
	Paper II: Stress in ordered systems: Ginzburg-Landau-type density field theory	113
	Paper III: A phase field crystal theory of the kinematics of dislocation lines . .	133
	Paper IV: Hydrodynamic phase field crystal approach to interfaces, dislocations and multi-grain networks . . . . .	155
	Paper V: A unified field theory of topological defects and non-linear local excitations	179



## LIST OF PUBLICATIONS

This thesis is based on these 5 publications, summarized in Chapter 6.

- Paper I *Dislocation nucleation in the phase-field crystal model*, Vidar Skogvoll, Audun Skaugen, Luiza Angheluta, and Jorge Viñals, *Physical Review B*, 103(1):014107, January 2021 [1].
- Paper II *Stress in ordered systems: Ginzburg-Landau-type density field theory*, Vidar Skogvoll, Audun Skaugen, and Luiza Angheluta., *Physical Review B*, 103(22):224107, June 2021 [2].
- Paper III *A phase field crystal theory of the kinematics of dislocation lines*, Vidar Skogvoll, Luiza Angheluta, Audun Skaugen, Marco Salvalaglio, and Jorge Viñals, *Journal of the Mechanics and Physics of Solids*, 166:104932, September 2022 [3].
- Paper IV *Hydrodynamic phase field crystal approach to interfaces, dislocations and multi-grain networks*, Vidar Skogvoll, Marco Salvalaglio, and Luiza Angheluta, *Modelling and Simulation in Materials Science and Engineering*, October 2022 [4].
- Paper V *Unified field theory of topological defects and non-linear local excitations*, Vidar Skogvoll, Jonas Rønning, Marco Salvalaglio, and Luiza Angheluta, Submitted to *npj Computational Materials*, arXiv: 2302.03035, 2023 [5].



## CHAPTER I

### *Introduction*



“ For the birth of something new, there has to be a happening. Newton saw an apple fall; James Watt watched a kettle boil; Röntgen fogged some photographic plates. And these people knew enough to translate ordinary happenings into something new.

- *Alexander Fleming* [6]

I wonder how long Wilhelm Conrad Röntgen looked at the glow on his platinobarium screen before, or if at all, he understood that he was about to catapult physics into its most productive century to date [7]. The year was 1895, the world was recovering from the Russian flu, and poor Röntgen was only trying to cover up his "Crookes tubes" with black cardboard when said screen started glowing with a blue-grayish glow. Something had passed through the cardboard! Excited by his discovery, he plunged into a seven-week-long study of the invisible, later to be named, *x-rays*. X-rays passed through some, but not all, tissue. Like skin but not bone, for instance, which he used to produce one of the first x-ray images — his wife's hand with a ring. The discovery awarded Röntgen the first-ever Nobel prize in physics, which he received in 1901. From there, it took only ten years before Max von Laue made another Nobel-prize-inducing discovery, namely that these were electromagnetic waves diffracting off certain solids. While the idea that crystals were made up of a periodic arrangement of atoms had been around for some time, this discovery was one of the final proofs needed to convince the scientific world [8]. This



Figure 1.1: *Hand mit Ringen*, the first x-ray image. Taken by Wilhelm Conrad Röntgen in 1895 of his wife's hand (public domain).

crucial knowledge could explain why solids have elastic properties and, combined with the contemporary development of quantum mechanics, why some solids are excellent conductors, and others are not.

The appearance of crystal structure in some solids is the emergence of order due to a lowering of temperature. Like how water in a bottle goes from a liquid state, in which molecules chaotically zoom about, to an orderly crystalline ice state, where the molecules line up like soldiers in a military tattoo. From one's first course in thermal physics, many are left with the misconception that everything in the universe evolves towards more disorder. While this is true globally, order may spontaneously arise in smaller subparts. How else would something as unique as the Eiffel Tower, the Solar System, or even Life itself, emerge in our corner of the universe? Or the water in the aforementioned bottle turn into ice? The fundamental driving force behind this process can be understood from the definition of a single, useful quantity, the so-called *free energy*  $\mathcal{F}$ . In the same way that energy, and the first law of thermodynamics, can explain how a roller coaster maintains its speed through a loop, the free energy, and the second law of thermodynamics, can explain this bottled water-ice transition. The exact form of  $\mathcal{F}$  varies but may, in some situations, be written as

$$\mathcal{F} = U - TS, \quad (\text{I.O.I})$$

where  $U$  is the internal energy,  $T$  the temperature and  $S$  the entropy — a measure of disorder. The second law of thermodynamics can be reformulated to state that  $\mathcal{F}$  monotonically decreases, i.e., the water molecules will organize themselves to minimize the free energy. At high temperatures, because of the second term  $-TS$ , the molecules seek to make the



Figure 1.2: One of the first diffraction patterns from x-ray scattering of ZnS, as reported in the publication by Max von Laues group in 1912 [9] (public domain).

entropy large, preferring a state of much disorder, i.e., they will organize themselves in the highly disordered *gas state*. As the temperature is reduced, the importance of  $-TS$  lessens, and the balance between the two terms in the free energy changes. At a critical temperature, the water will abruptly transition to a state where the molecules are much closer, creating bonds to reach a configuration of much lower internal energy. The water has condensed into a *liquid state*. The liquid still has a sizeable contribution to its entropy from the disorderly way the molecules glide past one another in all directions. As the temperature is further reduced, however, the contribution from  $-TS$  gets even smaller, and at a new critical temperature, the balance of terms in  $\mathcal{F}$  shifts again. The water molecules suddenly arrange themselves in an orderly, low entropy configuration, in which the internal energy is even lower. The water has frozen into a *solid state*.

The unification of liquids and solids under the common umbrella of *condensed matter*, began in the 1960s as solid-state scientists turned their attention to other, non-solid, states [10]. Condensed matter physics, therefore, is arguably the biggest branch of physics since it is the framework that unites specific physical theories across time and length scales. It has dominated the scene since the beginning of the 20th century with the discoveries by Röntgen and von Laue, and has since expanded to find strong cross-scale similarities and emergent properties in many exciting materials by uniting previously disconnected fields, such as metallurgy, elasticity, magnetism, and crystallography. The 1950s brought the full use of topology into its arsenal, deriving intriguing properties of metals from their Fermi surfaces' topological structure. In addition, it was discovered that many materials contained tiny defects which the topological constraints of the microscopic order could explain. Given the name topological defects, these were shown to control many vital features across

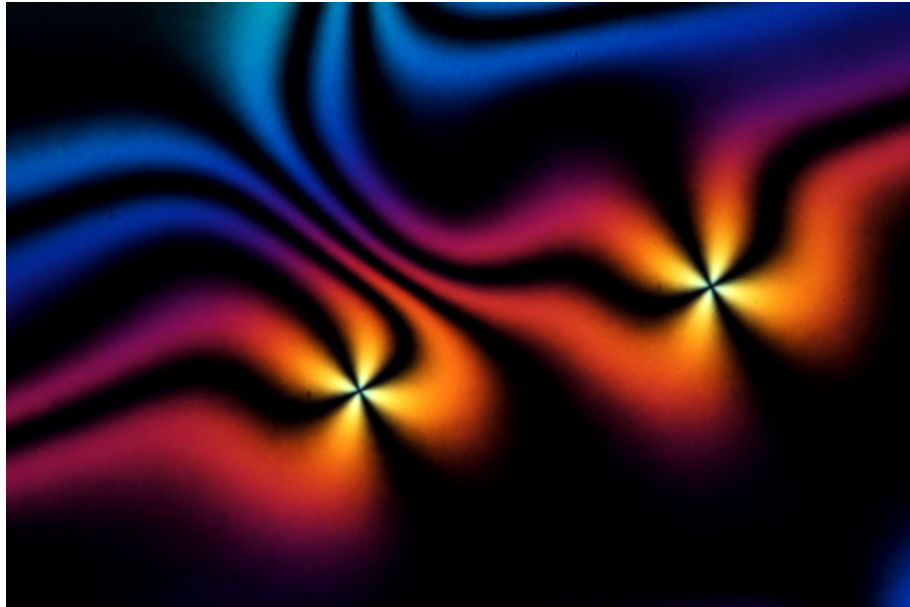


Figure 1.3: Polarizing microscope texture of a thin liquid crystalline film containing a pair of point topological defects. Reprinted from the National Science Foundation Multimedia gallery under a non-commercial license [11]. Copyright Oleg Lavrentovich, Liquid Crystal Institute, Kent State University.

systems of interest, such as the plastic properties in materials, turbulence in Bose-Einstein condensates, and optical properties of nematic liquid crystal films.

While quantum mechanics was used to determine the properties of small and idealized cases, physicists and engineers also started to simulate material behavior on longer scales with the enormous growth of computing power that evolved in the second half of the 20th century. The method of simulating every atom individually, i.e., molecular dynamics, was introduced in the 1950s, following the success of Monte Carlo simulations [12]. Although the continuum theory of elasticity could reasonably explain materials under moderate load, the exact nature of how materials yielded relied on the microscopic details of the interacting constituents. Thus, the dream of bridging these microscopic theories with the macroscopic theories of elasticity and phenomenological plasticity was born and later became known as Multiscale Modelling of Materials (MMM) [13]. Such a bridging of models is crucial to describe cross-scale phenomena, ranging from engineering materials with desirable electronic properties to technological progress in construction, and earthquake prediction through understanding the primary mechanism of sudden yields in the upper parts of the Earth's mantle. One of the new methods developed in the following decades was density functional theory (DFT), a theory building on the pioneering work of Llewellyn Thomas [14], and Enrico Fermi [15] in the late 1920s using functional theory on electron systems. In the novel context, however, DFT was applied to the atomic density, effectively coarse-graining out the thermal vibrations of the atoms, which, when coupled to a dynamical

equation of motion derived from microscopic considerations, allowed the theory to reach even longer time scales [16]. In the case of crystalline materials, however, DFT still needed to resolve the material length scale of the atomic lattice. To further extend the models to longer length scales, new theories were introduced that treated the crystalline defects, such as grain boundaries, cracks, and dislocations, as the interacting "particles". One example is the discrete dislocation dynamics (DDD) theory, introduced in the mid-1980s [17]. From this picture of interacting defects, statistical mechanics methods have been used to try and re-derive the effective theories of plasticity [18, 19]. It is in this hierarchical picture of modeling approaches that the phase-field crystal (PFC) fits. Introduced in 2004, it was a model resembling dynamical DFT but with some simplifying assumptions that allowed it to reach longer time scales while preserving the essential features of elasticity and defect interactions. As such, the model can be used to study the interactions of the defects from an emergent point of view, and, due to the simplicity of the method, derive analytical predictions for their motion. However, to achieve this goal, a good understanding of how to relate the topology of the PFC and its dynamical evolution with that of the dislocations, which are, in fact, *topological defects* of the crystal defect, is crucial. Some work in this regard had recently been done [20, 21], but was limited to a single 2D crystal symmetry with isotropic elasticity.

This thesis closes the gap between the PFC description of crystalline solids and continuum plasticity theory and shall serve as a travel guide through the fascinating world of symmetry, topology, and crystal deformations. To start, in Chapter 2, we give a brief introduction to non-equilibrium thermal physics and crystal structure. Therein, we will see that as the uniform and symmetric state of the liquid condenses into a crystalline solid, its symmetry is broken. Symmetry, topology, and topological defects will be expanded upon in Chapter 3 before we look at elasticity theory in Chapter 4. Finally, we will arrive at the concrete model for a crystalline lattice with the PFC, which is described in Chapter 5. The theoretical advances made by the papers on which this thesis is based will be given in Chapter 6.

## NOTATION

While the notation varies between papers, we will stick to a few standard conventions in this thesis. While index notation is precise, vector form notation is perceived as more readable. Therefore, we will switch between tensors written in index notation and vector form as appropriate (and sometimes give both).

$$\mathbf{u}_i \tag{1.0.2}$$

represents the  $i$ th Cartesian coordinate of the vector  $\mathbf{u}$ . Rank  $\geq 2$  tensors will not be denoted in bold font but are typically given greek letters, such as  $\alpha, \sigma, \epsilon$  or  $\omega$ . When ordinary letters denote rank  $\geq 2$  tensors, they will be given in blackboard bold, e.g.,  $\mathbb{U}$ . Repeated indices are summed over, e.g.,

$$\epsilon_{ij} a_i b_j = \epsilon_{11} a_1 b_1 + \epsilon_{12} a_1 b_2 + \epsilon_{21} a_2 b_1 + \epsilon_{22} a_2 b_2. \tag{1.0.3}$$

The dot-product is a contraction over the last index, e.g.,

$$\mathbf{a} \cdot \mathbf{b} = a_i b_i \quad (\nabla \cdot \sigma)_i = \partial_j \sigma_{ij}. \quad (\text{I.O.4})$$

Here, we also see the introduction of the gradient operator  $\nabla$ , whose component  $\partial_i$  is the partial derivative with respect to the  $i$ th Cartesian coordinate, i.e.,

$$\partial_i = \frac{\partial}{\partial r_i}. \quad (\text{I.O.5})$$

The double-dot symbol denotes a contraction over the last *two* indices, e.g.,

$$\alpha : \alpha = \alpha_{ij} \alpha_{ij} \quad (\mathcal{C} : \varepsilon)_{ij} = \mathcal{C}_{ijkl} \varepsilon_{kl}. \quad (\text{I.O.6})$$

The imaginary unit will be denoted  $\mathfrak{i}$  to avoid confusion with the index  $i$ . Index symmetrization  $(\ )$  and anti-symmetrization  $[\ ]$  will be used throughout. They are defined for an tensor  $A$  with two indices by

$$A_{(ij)} = \frac{1}{2}(A_{ij} + A_{ji}) \quad A_{[ij]} = \frac{1}{2}(A_{ij} - A_{ji}). \quad (\text{I.O.7})$$

The Fourier transform of a function  $f$  will be denoted  $f_{\mathfrak{f}}$  and is defined as

$$f_{\mathfrak{f}}(\mathbf{k}) = \int d^d r e^{-\mathfrak{i}\mathbf{k}\cdot\mathbf{r}} f(\mathbf{r}), \quad (\text{I.O.8})$$

and the inverse is given by

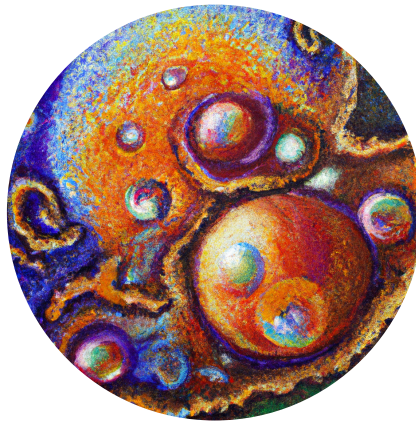
$$f(\mathbf{r}) = \frac{1}{(2\pi)^d} \int d^d k e^{\mathfrak{i}\mathbf{k}\cdot\mathbf{r}} f_{\mathfrak{f}}(\mathbf{k}), \quad (\text{I.O.9})$$

where  $d$  is the spatial dimension.



## CHAPTER 2

### *Condensed matter physics approach to solid crystals*



“ There are very few things that can be proved rigorously in condensed matter physics.

- *Anthony James Leggett* [22]

The phase-field crystal is known in condensed matter physics as a mean-field model. It describes the crystal phase through a one-body density function, which at equilibrium is a minimizer of a phenomenological free energy functional, which is well-defined for slightly out-of-equilibrium configurations. In this chapter, we will present some basic principles of density functional theory, which can be used to calculate the properties of such one-body densities. We will then see how the crystal structure is represented as periodic modulations in this density field and why this produces the diffraction pattern we referenced in the introduction. Finally, we will introduce a particular Ginzburg-Landau phenomenological mean-field theory for the liquid-solid phase transition, which resembles very closely the PFC model that will be presented in Chapter 5.

#### 2.1 Statistical mechanics in out-of-equilibrium systems

Statistical mechanics provides an extensive framework for discussing the equilibrium properties of liquids and solids. In equilibrium, one defines a suitable free energy (in an appropriate ensemble) that depends on the extensive and intensive variables that are controlled.

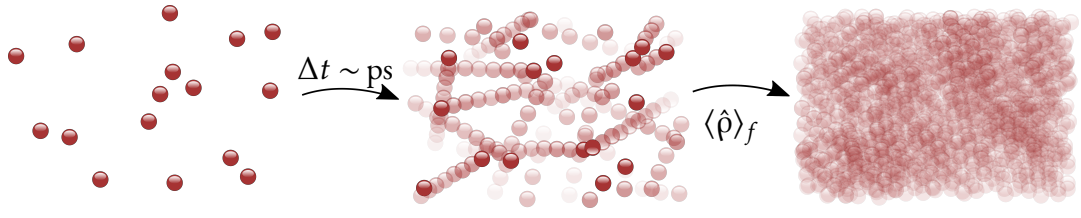


Figure 2.1: Averaging a density operator  $\hat{\rho}$  over a short time gives a picture of the liquid as a translational and rotationally invariant structure.

Other thermodynamic variables are defined as appropriate derivatives of this quantity. As mentioned, the phase-field crystal model, introduced in Chapter 5, builds upon the notion of a free energy defined both at, and away from, equilibrium. The principles of statistical mechanics must thus be extended to out-of-equilibrium situations, which must be done with care. In this section, we will follow Ref. [23] in deriving a consistent, classical framework for non-equilibrium statistical mechanics of out-of-equilibrium liquids, providing a theoretical basis for discussing the free energy in such configurations. The goal is to show how one can consistently express a free energy  $\mathcal{F}$  in terms of a one-body density function  $\rho$  of a single-component density, which can be thought of as a temporal average of the density operator

$$\hat{\rho}(\mathbf{r}) = \sum_{n=1}^N \delta^{(3)}(\mathbf{r} - \mathbf{r}_n), \quad (2.1.1)$$

summing over all the  $N$  particles in the system located at  $\{\mathbf{r}_n\}$ . The idea is shown in Fig. 2.1, where the density operator  $\hat{\rho}$  is shown in the left-most panel as a still image of the particle positions. Over a small time interval, the positions of the particles are "smeared out" (right-most panel), which can be mathematically described by a phase space probability function  $f$

$$\rho = \langle \hat{\rho} \rangle_f = \text{Tr}_{\text{cl}}(f \hat{\rho}), \quad (2.1.2)$$

The one-body density

where  $\text{Tr}_{\text{cl}}$  is the classical phase space trace, integrating over all positions  $\{\mathbf{r}_n\}$  and momenta  $\{\mathbf{p}_n\}$ , given by

$$\text{Tr}_{\text{cl}} = \sum_{N=1}^{\infty} \frac{1}{h^{3N} N!} \int d^d r_1 \dots d^d r_N \int d^d p_1 \dots d^d p_N, \quad (2.1.3)$$

where  $h$  is Planck's constant. Whether such a picture of time averaging can be expressed as a probability integral of canonical distributions in equilibrium is related to the ergodic hypothesis [24]. It is an exciting question with interesting philosophical implications, but not crucial for this thesis, so we shall assume such a picture and not discuss this point

further. We consider a system of interacting particles in the grand canonical ensemble, i.e., at a given temperature  $T$  and chemical potential  $\mu$ . Let  $f_0$  be the equilibrium probability density, given as a function of the thermodynamic beta  $\beta$ , by

$$f_0 = \Xi^{-1} \exp(-\beta(H_N - \mu N)), \quad (2.1.4)$$

where  $H_N$  is the  $N$ -particle Hamiltonian

$$H_N = K(\mathbf{p}_1, \dots, \mathbf{p}_N) + U(\mathbf{r}_1, \dots, \mathbf{r}_N) + \sum_{n=1}^N V_{\text{ext}}(\mathbf{r}_n), \quad (2.1.5)$$

where  $V_{\text{ext}}$  is an external potential and  $\Xi$  is the grand partition function

$$\Xi = \text{Tr}_{\text{cl}} \exp(-\beta(H_N - \mu N)), \quad (2.1.6)$$

from which we define  $\Omega_0 = -\beta^{-1} \ln \Xi$ , the grand potential. The kinetic and interaction contributions to the Hamiltonian are given by

$$K = \sum_{n=1}^N \frac{\mathbf{p}_n^2}{2m}, \quad (2.1.7)$$

with each particle having mass  $m$ , and

$$U = \sum_{n>m=1}^N V_{\text{int}}(\mathbf{r}_n - \mathbf{r}_m), \quad (2.1.8)$$

respectively, where  $V_{\text{int}}(\mathbf{r}_n - \mathbf{r}_m)$  is an interaction potential. The one-body density may be derived from  $\Xi$  by introducing a virtual shift in the chemical potential  $\mu N \rightarrow \int d^d r \mu(\mathbf{r}) \hat{\rho}(\mathbf{r})$  using the standard derivative technique in thermodynamics [25]

$$\rho(\mathbf{r}) = -\frac{\delta \Omega_0}{\delta \mu(\mathbf{r})}. \quad (2.1.9)$$

In addition, the Ursell function  $S_{\rho\rho}(\mathbf{r}, \mathbf{r}')$ , which expresses correlations in the deviation  $\Delta \hat{\rho} = \hat{\rho} - \rho$  from the equilibrium density  $\rho \equiv \langle \hat{\rho} \rangle_{f_0}$ , can be written as

$$S_{\rho\rho}(\mathbf{r}, \mathbf{r}') = \langle \Delta \hat{\rho}(\mathbf{r}) \Delta \hat{\rho}(\mathbf{r}') \rangle_{f_0} = -\beta^{-1} \frac{\delta^2 \Omega_0}{\delta \mu(\mathbf{r}) \delta \mu(\mathbf{r}')}. \quad (2.1.10)$$

The Ursell function

Now, we introduce the fundamental assumption in this approach to non-equilibrium statistical mechanics, namely that the following functional may serve as an extension of

the grand potential to out-of-equilibrium configurations, i.e., for an arbitrary phase space probability density  $f$ ,

$$\Omega[f] = \langle H_N \rangle_f - \mu \langle N \rangle_f - \beta^{-1} S_f = \text{Tr}_{\text{cl}}(f (H_N - \mu N + \beta^{-1} \ln f)), \quad (2.1.11)$$

where

$$S_f = -\text{Tr}_{\text{cl}}(f \ln f) \quad (2.1.12)$$

is the Shannon entropy of  $f$ . It can (easily) be shown that the equilibrium grand potential  $\Omega_0$  is found by inserting  $f_0$ , Eq. (2.1.4), into Eq. (2.1.11). It can also (less easily) be shown that for any other  $f$ ,  $\Omega[f] > \Omega[f_0]$  [23], which is crucial since the grand potential should be at a minimum in equilibrium. Furthermore, for a given one-body density  $\rho$ , there exists a unique (fictive) external potential  $V'_{\text{ext}}(\mathbf{r})$ , so that  $\rho = \text{Tr}_{\text{cl}} f' \hat{\rho}$ , where  $f'$  is the equilibrium phase space density corresponding to  $V'_{\text{ext}}(\mathbf{r})$ . In other words, given  $\rho$ , there exists a unique  $f'$  that we may use to define an *intrinsic* free energy  $\mathcal{F}[\rho]$ , given by

$$\mathcal{F}[\rho] = \langle K \rangle_{f'} + \langle U \rangle_{f'} - \beta^{-1} S_{f'} = \text{Tr}_{\text{cl}}(f' (K + U + \beta^{-1} \ln f')), \quad (2.1.13)$$

and the generalized grand potential can be written as

$$\Omega[\rho] = \mathcal{F}[\rho] + \int d^d r \rho V_{\text{ext}} - \mu \int d^d r \rho. \quad (2.1.14)$$

Note that while  $V'_{\text{ext}}$  is the fictive external potential used to construct  $\mathcal{F}$ ,  $V_{\text{ext}}$  is the actual external potential in consideration, and they coincide only in equilibrium. Since  $\Omega[\rho_0] = \Omega_0$ , we may take the functional derivative of Eq. (2.1.14) and find that, in equilibrium,

$$V_{\text{ext}} + \mu_{\text{in}} = \mu, \quad (2.1.15)$$

with the *intrinsic chemical potential*  $\mu_{\text{in}}$  defined as

$$\mu_{\text{in}} = \frac{\delta \mathcal{F}}{\delta \rho}. \quad (2.1.16)$$

Given an expression for  $\mathcal{F}$ , Eq. (2.1.15) can be used to find the equilibrium density. For instance, using the intrinsic free energy of the ideal gas,  $\mathcal{F}_{\text{id}}[\rho] = \beta^{-1} \int d^d r \rho (\ln(\lambda^3 \rho) - 1)$  with  $\lambda = (h^2 \beta / 2m\pi)^{1/2}$  and  $V_{\text{ext}} = 0$  results in

$$\rho(\mathbf{r}) = \rho_0 = \lambda^{-3} \exp(\beta\mu), \quad (2.1.17)$$

which is the uniform density field visualized in the right-most panel of Fig. 2.1. Given an expression for the intrinsic free energy  $\mathcal{F}$ , we may then calculate correlation functions, stresses, and other out-of-equilibrium quantities using the same equations, e.g., the Ursell function, Eq. (2.1.10), with  $\Omega_0$  replaced by  $\Omega$ . The resulting quantities, evaluated at equilibrium, coincide with those from regular statistical mechanics.

The assumption that a generalized probability distribution away from equilibrium, e.g., as in Eq. (2.1.11), may be used to calculate salient physical features is referred to as the *adiabatic approximation*. It is formally only correct in the infinitely slow time limit but, in practice, works well for many systems, even though exceptions exist [26, 27].

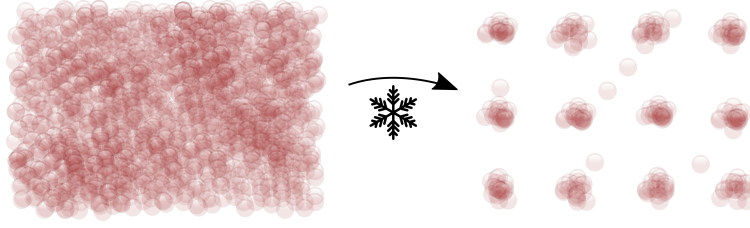


Figure 2.2: Lowering the temperature may cause the uniform liquid state to condense into a crystalline structure.

## 2.2 The structure of the crystalline solid

If we include interactions, the ground state is no longer guaranteed to be the uniform state shown in Fig. 2.1. As we shall see, for the intrinsic free energy that will be introduced for the PFC in chapter 5, the equilibrium state has a crystalline symmetry at low temperatures. Figure 2.2 shows a schematic representation of this process. To emphasize that the equilibrium density now contains spatial modulations on the microscopic (atomic) scale, we will denote it by  $\tilde{\rho}$ . The microscopically varying density  $\tilde{\rho}$  corresponds to a thermally blurred view of the particle positions, where a large spread corresponds to a high temperature with large thermal fluctuations. We will, in this section, lay out the essential features of such a periodic density field.

We limit our discussion to those systems where the resulting microscopic density  $\tilde{\rho}$  will have the symmetry of a *Bravais lattice*, a crystal structure that looks the same from any point. Panel (a) of Fig. 2.3 shows an example of the 2D square Bravais lattice, and panel (b) gives an example of a non-Bravais lattice. A Bravais lattice  $\mathcal{B}$  in 3 dimensions is generated by infinitely many translations of a point by a set of 3 linearly independent vectors  $\mathbf{a}^{(1)}, \mathbf{a}^{(2)}, \mathbf{a}^{(3)}$ , called *primitive lattice vectors*. These vectors are not unique since any three linearly independent lattice vectors will generate the lattice. The density  $\tilde{\rho}(\mathbf{r})$  must be invariant under any such translation. Thus, if  $\mathbf{a}$  is a lattice vector, then the density  $\tilde{\rho}$  must satisfy the following property

$$\tilde{\rho}(\mathbf{r}) = \tilde{\rho}(\mathbf{r} + \mathbf{a}). \quad (2.2.1)$$

By Fourier transforming both sides, we get

$$\begin{aligned} \tilde{\rho}_f(\mathbf{k}) &= \int d^d r e^{-i\mathbf{k}\cdot\mathbf{r}} \tilde{\rho}(\mathbf{r} + \mathbf{a}) \stackrel{(r'=r+a)}{=} \int d^d r' e^{-i\mathbf{k}\cdot(\mathbf{r}'-\mathbf{a})} \tilde{\rho}(\mathbf{r}') \\ &= \int d^d r' e^{-i\mathbf{k}\cdot\mathbf{r}'} e^{i\mathbf{k}\cdot\mathbf{a}} \tilde{\rho}(\mathbf{r}') = e^{i\mathbf{k}\cdot\mathbf{a}} \int d^d r' e^{-i\mathbf{k}\cdot\mathbf{r}'} \tilde{\rho}(\mathbf{r}') = e^{i\mathbf{k}\cdot\mathbf{a}} \tilde{\rho}_f(\mathbf{k}), \end{aligned} \quad (2.2.2)$$

which shows that if  $\tilde{\rho}_f(\mathbf{k}) \neq 0$ , then  $\mathbf{k} \cdot \mathbf{a} = 2\pi K$  for some integer  $K$ . Thus, we see that the Fourier transform of  $\tilde{\rho}$  can be non-zero only for a selected set of vectors  $\mathcal{R} = \{\mathbf{q}\}$  that satisfy

$$\mathbf{q} \cdot \mathbf{a} = 2\pi K \quad \forall \mathbf{a} \in \mathcal{B}. \quad (2.2.3)$$

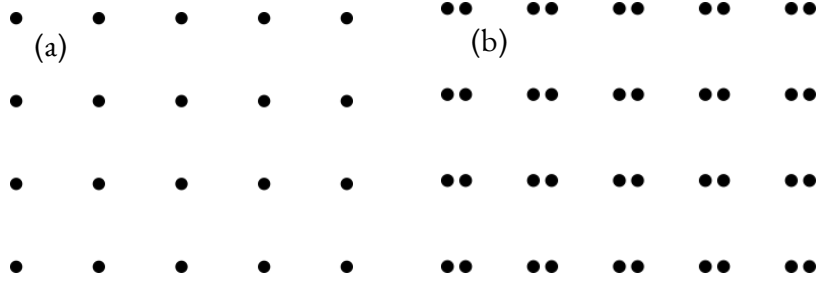


Figure 2.3: (a) A 2D square Bravais lattice, and (b) a non-Bravais lattice that is not invariant under the translation by arbitrary lattice vectors.

The set of vectors  $\mathcal{R}$  satisfying Eq. (2.2.3) is called the *reciprocal lattice* and can be generated from primitive reciprocal lattice vectors  $\{\mathbf{b}^{(m)}\}_{m=1}^3$  that satisfy  $\mathbf{a}^{(n)} \cdot \mathbf{b}^{(m)} = 2\pi\delta_{mn}$ . Figure 2.4 shows two examples of 2D Bravais lattices. In general, the crystalline state can be described in terms of a microscopic density of the form

$$\tilde{\rho} = \rho_0 + \sum_{q \in \mathcal{R}/\{\mathbf{0}\}} \eta_q e^{i\mathbf{q} \cdot \mathbf{r}}, \quad (2.2.4)$$

The crystal density

where  $\eta_q$  are amplitudes corresponding to Fourier modes with wave vector  $\mathbf{q}$ . The "zereth" amplitude  $\rho_0$  has been excluded from the sum as is customary. Note that since  $\tilde{\rho}$  is a real density, we also require that  $\eta_q = \eta_{-q}^*$ .

### 2.3 Crystal diffraction

It is instructive to see why the crystalline structure given by Eq. (2.2.4) produces the diffraction pattern alluded to in the introduction. Consider Fig. 2.5. The incoming particle is described by its (unnormalized) momentum eigenstate  $\langle \mathbf{r} | \mathbf{p}' \rangle = e^{i\mathbf{p}' \cdot \mathbf{r}}$  in position representation. By Fermi's golden rule, the transition rate between the incoming state  $|\mathbf{p}'\rangle$  and the outgoing state  $|\mathbf{p}\rangle$  is proportional to the matrix element of the interaction

$$\langle \mathbf{p} | \hat{U} | \mathbf{p}' \rangle = \int d^d r e^{-i\mathbf{p} \cdot \mathbf{r}} \left( \sum_{n=1}^N U(\mathbf{r} - \mathbf{r}_n) \right) e^{i\mathbf{p}' \cdot \mathbf{r}}, \quad (2.3.1)$$

where  $U(\mathbf{r} - \mathbf{r}_n)$  is the atomic potential of the particle located at  $\mathbf{r}_n$ . The differential cross-section  $\xi$ , which determines the intensity of diffracted radiation per solid angle, scales as

$$\xi \sim |\langle \mathbf{p} | \hat{U} | \mathbf{p}' \rangle|^2. \quad (2.3.2)$$

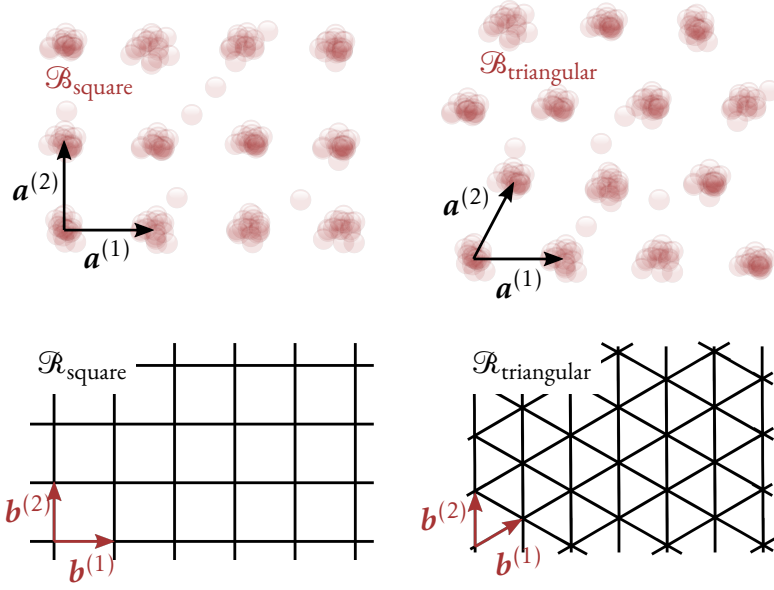


Figure 2.4: Bravais lattices  $\mathcal{B}$  and their reciprocal lattices  $\mathcal{R}$  for square and triangular symmetry. In each case,  $\{\mathbf{a}^{(n)}\}_{n=1}^2$  are primitive lattice vectors and  $\{\mathbf{b}^{(n)}\}_{n=1}^2$  primitive reciprocal lattice vectors that satisfy  $\mathbf{a}^{(n)} \cdot \mathbf{b}^{(m)} = 2\pi\delta_{nm}$ .

By introducing a change of coordinates for each term in the sum  $\mathbf{x} = \mathbf{r} - \mathbf{r}_n$ , we get

$$\langle \mathbf{p} | \hat{U} | \mathbf{p}' \rangle = \sum_{n=1}^N \int d^d x e^{-i\mathbf{p} \cdot (\mathbf{r}_n + \mathbf{x})} U_n(\mathbf{x}) e^{i\mathbf{p}' \cdot (\mathbf{r}_n + \mathbf{x})} = \sum_{n=1}^N U_{\mathbb{f}}(\mathbf{k}) e^{-i\mathbf{k} \cdot \mathbf{r}_n} \quad (2.3.3)$$

where  $\mathbf{k} = \mathbf{p} - \mathbf{p}'$  and

$$U_{\mathbb{f}}(\mathbf{k}) = \int d^d x U(\mathbf{x}) e^{-i\mathbf{k} \cdot \mathbf{x}} \quad (2.3.4)$$

is the *atomic form factor* of the atomic potential — its Fourier transform. This gives

$$\xi \sim |U_{\mathbb{f}}(\mathbf{k})|^2 \sum_{n,n'} e^{-i\mathbf{k} \cdot (\mathbf{r}_n - \mathbf{r}_{n'})}. \quad (2.3.5)$$

As discussed, the positions of the atoms in a solid, while centered at positions corresponding to a crystal Bravais lattice, vary in time due to thermal fluctuations. The measured quantity is the ensemble-averaged differential cross-section, i.e.,

$$\langle \xi \rangle_{f_0} \sim |U_{\mathbb{f}}(\mathbf{k})|^2 I_{\mathbb{f}}(\mathbf{k}), \quad (2.3.6)$$

where  $I_{\mathbb{f}}(\mathbf{k})$  is given by

$$\begin{aligned} I_{\mathbb{f}}(\mathbf{k}) &= \left\langle \sum_{n,n'} e^{-i\mathbf{k} \cdot (\mathbf{r}_n - \mathbf{r}_{n'})} \right\rangle_{f_0} = \left\langle \int d^d r d^d r' \sum_{n=1}^N \delta(\mathbf{r} - \mathbf{r}_n) \sum_{n'=1}^N \delta(\mathbf{r}' - \mathbf{r}_{n'}) e^{-i\mathbf{k} \cdot (\mathbf{r} - \mathbf{r}')} \right\rangle_{f_0} \\ &= \int d^d r d^d r' \langle \hat{\rho}(\mathbf{r}) \hat{\rho}(\mathbf{r}') \rangle_{f_0} e^{-i\mathbf{k} \cdot (\mathbf{r} - \mathbf{r}')}. \quad (2.3.7) \end{aligned}$$

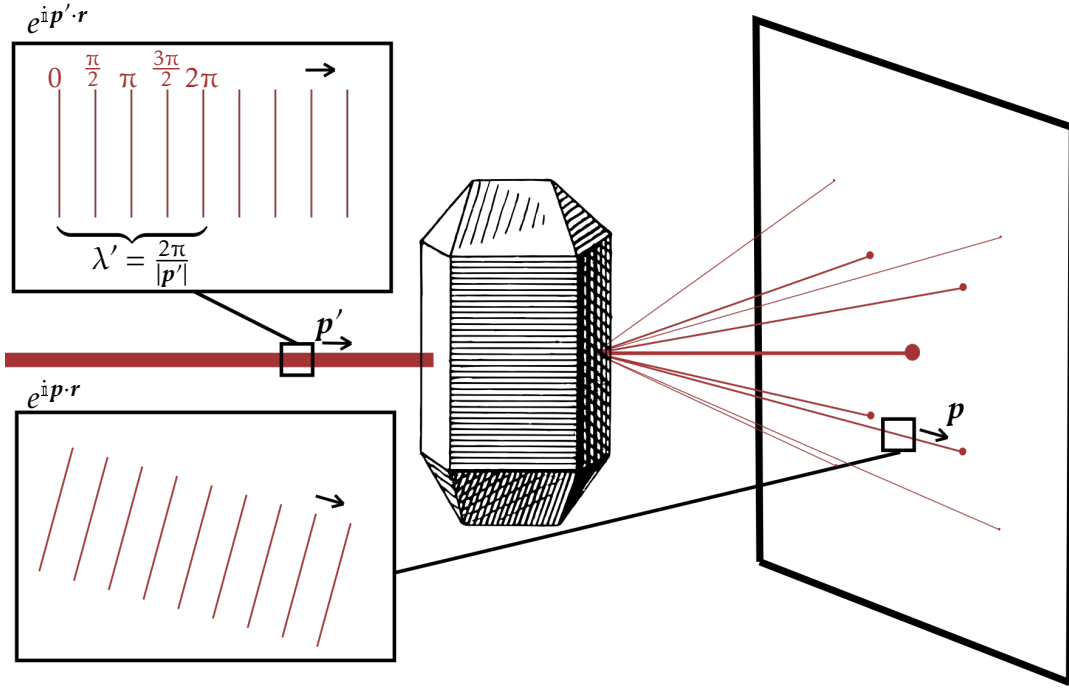


Figure 2.5: Schematic representation of crystal diffraction. An incoming wave with wave vector  $\mathbf{p}'$  and wavelength  $\lambda'$  interacts with the potential in the crystalline structure and produces a diffraction pattern. The insets show isosurfaces of the phase of the wave functions.

By writing  $\hat{\rho} = \bar{\rho} + \Delta\hat{\rho}$ , we see that this can be expressed as

$$I_{\mathbf{f}}(\mathbf{k}) = \int d^d r d^d r' (\bar{\rho}(\mathbf{r})\bar{\rho}(\mathbf{r}') + \langle \Delta\hat{\rho}(\mathbf{r})\Delta\hat{\rho}(\mathbf{r}') \rangle_{f_0}) e^{-i\mathbf{k}\cdot(\mathbf{r}-\mathbf{r}')} = |\bar{\rho}_{\mathbf{f}}(\mathbf{k})|^2 + V S_{\rho\rho_{\mathbf{f}}}(\mathbf{k}), \quad (2.3.8)$$

where we have used that  $\langle \bar{\rho}(\mathbf{r})\Delta\hat{\rho}(\mathbf{r}) \rangle_{f_0} = \bar{\rho}(\mathbf{r}) \langle \Delta\hat{\rho}(\mathbf{r}) \rangle_{f_0} = 0$ , and

$$S_{\rho\rho_{\mathbf{f}}}(\mathbf{k}) = \frac{1}{V} \int d^d r d^d r' \langle \Delta\hat{\rho}(\mathbf{r})\Delta\hat{\rho}(\mathbf{r}') \rangle_{f_0} e^{-i\mathbf{k}\cdot(\mathbf{r}-\mathbf{r}')}, \quad (2.3.9)$$

where  $V$  is the domain volume, is the analog of a Fourier transform of  $S_{\rho\rho}(\mathbf{r}, \mathbf{r}')$ . Experimental data from scattering experiments are typically presented in terms of the *structure factor*  $S_{\mathbf{f}}$ , given by

$$S_{\mathbf{f}}(\mathbf{k}) = \frac{1}{V} I_{\mathbf{f}}(\mathbf{k}) = \frac{1}{V} |\bar{\rho}_{\mathbf{f}}(\mathbf{k})|^2 + S_{\rho\rho_{\mathbf{f}}}(\mathbf{k}). \quad (2.3.10)$$

Determining the contribution to  $S_{\mathbf{f}}$  from  $S_{\rho\rho_{\mathbf{f}}}$  requires knowledge of the correlation of fluctuations in the system, which a suitable statistical mechanics model can obtain. However, if  $S_{\rho\rho}(\mathbf{r}, \mathbf{r}')$  is short range, then  $S_{\rho\rho_{\mathbf{f}}}(\mathbf{k})$  becomes an intensive quantity. A short-range Ursell function indicates a finite correlation length, whereas non-finite correlation lengths are present under critical conditions, e.g., at phase transitions, where a single fluctuation at a point may spread to the entire system. Experimentally, this corresponds



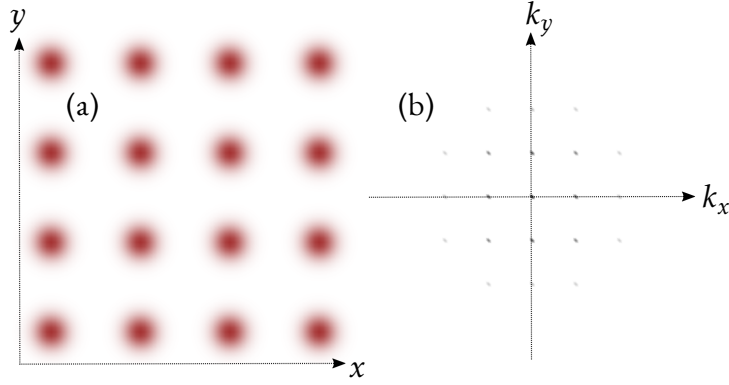


Figure 2.6: (a) A periodic density  $\tilde{\rho}(\mathbf{r})$  with 2D square symmetry and (b) its Fourier transform  $\tilde{\rho}_f(\mathbf{k})$ .

to the scattering amplitude of a beam going straight through the sample. However, for a crystal, the Fourier transform of a crystalline structure, such as Eq. (2.2.4), is

$$\tilde{\rho}_f(\mathbf{k}) = \int d^d r e^{-i\mathbf{k}\cdot\mathbf{r}} \left( \rho_0 + \sum_{\mathbf{q} \in \mathcal{R}} \eta_{\mathbf{q}} e^{i\mathbf{q}\cdot\mathbf{r}} \right) = N \delta_{\mathbf{k},0} + V \sum_{\mathbf{q} \in \mathcal{R}} \eta_{\mathbf{q}} \delta_{\mathbf{k},\mathbf{q}}, \quad (2.3.11)$$

and so

$$|\tilde{\rho}_f(\mathbf{k})|^2 = N^2 \delta_{\mathbf{k},0} + V^2 \sum_{\mathbf{q} \in \mathcal{R}} |\eta_{\mathbf{q}}|^2 \delta_{\mathbf{k},\mathbf{q}}, \quad (2.3.12)$$

which shows that the structure factor will receive extensive contributions, proportional to  $|\eta_{\mathbf{q}}|^2$ , for wave number vectors  $\mathbf{k}$  that lie on the reciprocal lattice of the crystal structure. For instance, Fig. 2.6 shows a microscopically varying density  $\tilde{\rho}$  with square symmetry and its Fourier transform. We see that the Fourier transform has a contribution for  $\mathbf{k} = 0$  while decaying for larger values of  $\mathbf{k}$  localized at the reciprocal lattice of the structure of  $\tilde{\rho}$ . Generally, the sharper the peaks in  $\tilde{\rho}$  are in real space, the more peaks are included in the Fourier spectrum  $\tilde{\rho}_f$ . Experimentally, the peaks in the Fourier spectrum of  $\tilde{\rho}$  appear as the diffraction pattern illustrated in Fig. 2.5.

## 2.4 Mean-field models

The amplitudes  $|\eta_{\mathbf{q}}|$  go from being 0 in the disordered (liquid) phase to being non-zero in the ordered (crystal) phase. Such parameters are called *order parameters* and are used ubiquitously in condensed matter physics to describe phase transitions. Other order parameters could be the magnetization  $m$  in a ferromagnet that goes from 0 in the disordered, non-magnetic phase, to  $\pm 1$  in the ordered, magnetic phase. Mean-field models are extremely valuable mathematical tools to get the qualitative and, in some cases, quantitative features of phase transitions. In its simplest form, a mean-field theory asserts that the order

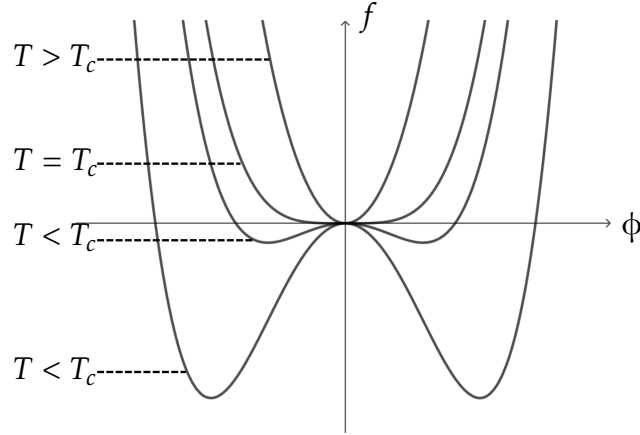


Figure 2.7: The mean-field free energy, Eq. (2.4.1) for different values of  $T_c$ .

parameter  $\phi$  is uniform in space. In such cases, since  $\phi$  is small near the phase transition, the free energy can be expanded in a (rescaled) power series

$$f = \frac{1}{2}r\phi^2 + \frac{1}{4}\phi^4. \quad (2.4.1)$$

The parameter  $r = a(T - T_c)$ , with  $T$  ( $T_c$ ) being the (critical) temperature and  $a$  a fitting parameter, is sometimes referred to as the quench depth, which controls the order-disorder transition. Plotting  $f(\phi)$  for different values of  $r$  gives Fig. 2.7. Differentiation yields the equilibrium value of  $\phi_0$ , which minimizes  $f$ , as

$$\phi_0 = \begin{cases} 0 & r > 0 \\ (-r)^{1/2} & r \leq 0, \end{cases} \quad (2.4.2)$$

suggesting that the order parameter scales with temperature as  $\phi_0 \sim (T_c - T)^{1/2}$ , i.e., with a critical exponent of  $1/2$ , near the phase transition. This simple argument shows how critical exponents may arise in systems at phase transitions. For real systems, however, complete uniformity of the order parameter is too strong an assumption, and observed critical exponents differ from the mean-field prediction of  $1/2$ .

It is possible to extend the idea of mean-field theory to the solid-liquid transition. For the ideal liquid, the only peak in its diffraction pattern given by the structure-factor  $S_f(\mathbf{k})$ , is for  $\mathbf{k} = \mathbf{0}$ . After the liquid has condensed into a solid at subcritical temperature, extensive contributions to  $S_f(\mathbf{k})$  appear at values of  $\mathbf{k}$  that lie on the reciprocal lattice. Experimentally, however, these peaks appear even before the solidification happens and serve as an indication that the fluid is approaching the critical temperature. Molecular dynamics simulations show that the ratio of  $S_{f\rho\rho}(q_0)$  to  $\rho_0$ , where  $q_0$  is the wavenumber corresponding to the crystal structure to form, at the phase transition is universally approximately 2.7. This is known as the *Hansen-Verlet* criterion, which has been confirmed by experiments [25]. Since the non-zero value of this ratio does not come from the structure of the system in the liquid state, it is clear that these are fluctuation contributions to  $S_f$ , i.e., the second term

$S_{\rho\rho_f}$  in Eq. (2.3.10). Following Ref. [28], a simple way to model the appearance of the peak in  $S_{\rho\rho_f}$  is to postulate a functional form of this peak as

$$S_{\rho\rho_f}(\mathbf{k}) = \frac{T}{r + c(k^2 - q_0^2)^2}, \quad (2.4.3)$$

where  $r$ , which is related to the temperature  $T$ , and  $c$  are fitting parameters. A free energy that predicts Eq. (2.4.3) is [25]

$$\mathcal{F}[\tilde{\rho}] = \int d^d r \delta\tilde{\rho} (r + c(\nabla^2 + q_0^2)^2) \delta\tilde{\rho} - w \int d^d r \delta\tilde{\rho}^3 + u \int d^d r \delta\tilde{\rho}^4, \quad (2.4.4)$$

where  $\delta\tilde{\rho} = \tilde{\rho} - \rho_0$ , which was used in Ref. [28] to study the liquid-solid transition. Given Eq. (2.4.4), it is possible to predict which crystalline structure will form at the phase transition since different lattices will give different values of the free energy. To determine the ground state of the system, one must evaluate Eq. (2.4.4) for every possible reciprocal lattice, minimize it with respect to the amplitudes  $\eta_q$ , compare the results against each other, and find coexistence regions using Maxwell construction. This makes calculating phase diagrams a challenging task, even though such efforts are routinely made in the PFC literature [29]. For  $c \gg 1$ , however, wave vectors of length not equal to  $q_0$  are penalized, and we can consider only the vectors in a given reciprocal lattice of size  $q_0$ . This approximation is called the one-mode approximation, and we will revisit it in the context of the PFC in Chapter 5. The third-order term in the free energy will then give a non-zero negative contribution to the free energy only if these vectors in reciprocal space arrange themselves to form equilateral triangles. This severely limits the possible lattice structures that can form. In fact, there are only three alternatives: the 2D hexagonal lattice, the 3D bcc lattice, and the 3D edges of an icosahedron. It can be shown that the state with the lowest free energy of these is that of the bcc lattice, where only the closest reciprocal lattice vectors are included, for which

$$f = \frac{1}{24} r \eta_0^2 - \frac{1}{36} w \eta_0^3 + \frac{1}{18} u \eta_0^4, \quad (2.4.5)$$

where  $\eta_0$  is the equilibrium amplitude of the non-zero mode, which undergoes a phase transition at

$$r_c = \frac{1}{4} \frac{w^2}{3u}. \quad (2.4.6)$$

The simple fact that the bcc lattice minimizes this free energy, arguably the most straightforward form one could postulate, prompted the authors of Ref. [28] to pose the question in the title of their paper, namely "Should All Crystals Be bcc?" Experiments have shown that a remarkable number of solids do, in fact, condense into bcc lattices. Eq. (2.4.4) resembles very closely the PFC free energy that will be introduced in Chapter 5.

During the liquid-solid transition shown in Fig. 2.2, the system went from a state which was symmetric under arbitrary rotations and translations to a less symmetric state, where only a discrete set of translations and rotations left the system unchanged. This is an example of spontaneous symmetry breaking. Symmetry, topology, and topological defects are the contents of the next chapter.



## CHAPTER 3

### *Symmetry, groups, and topology*



“ Nature seems to take advantage of the simple mathematical representations of the symmetry laws. When one pauses to consider the elegance and the beautiful perfection of the mathematical reasoning involved and contrast it with the complex and far-reaching physical consequences, a deep sense of respect for the power of the symmetry laws never fails to develop.

-Chen Ning Yang [30]

As we saw in the previous chapter, the symmetric properties of the liquid were changed as it condensed into a crystalline solid. It went from a highly symmetric and disordered state to a less symmetric, ordered state. While symmetry and order are both words with positive connotations, they are antonyms in the world of condensed matter physics. In this chapter, we will detail the mathematics of symmetry, topology, and how topological defects arise from the notion of broken continuous symmetries. We will present the mathematical structure of symmetry through group theory and topology. As motivation, we will first see how these tools are necessary through the example of an order-disorder transition in a model that exhibits rotational symmetry in the disordered phase.

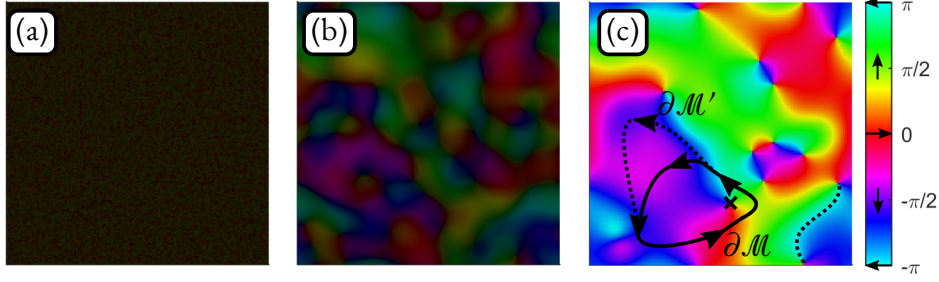


Figure 3.1: Continuous symmetry breaking in the  $O(2)$ -symmetric TDGL model. Panel (a) shows the initial isotropic state  $\Psi = 0$  containing small fluctuations, which then (b) evolves according to Eq. (3.1.2) with  $r < 0$  until (c)  $|\Psi|$  has reached the equilibrium value  $\Psi_0$ . The colorbar indicates the direction of  $\Psi$  while the brightness gives the magnitude  $|\Psi|$ , ranging from  $|\Psi| = 0$  (black) to  $|\Psi| = \Psi_0$  (colored). The paths  $\partial\mathcal{M}$  and  $\partial\mathcal{M}'$  define the charge of the topological defect ( $\times$ ).

### 3.1 The order-disorder transition

The  $O(2)$  symmetric time-dependent Ginzburg-Landau (TDGL) model is a mean-field model that can be used to model, e.g., superfluid helium. The order parameter is a 2D vector field  $\Psi$ , whose free energy is given by

$$\mathcal{F}[\Psi] = \int d^d r (\nabla\Psi)^2 + \frac{r}{2}|\Psi|^2 + \frac{1}{4}|\Psi|^4, \quad (3.1.1)$$

where  $(\nabla\Psi)^2 = \nabla\Psi : \nabla\Psi$ , and the kinematics are given by

$$\partial_t \Psi = -\frac{\delta\mathcal{F}}{\delta\Psi}, \quad (3.1.2)$$

which will lead to a minimization of the free energy. The exact form of Eq. (3.1.1) varies, but this unscaled version captures the essential features of the model. This model is called  $O(2)$  symmetric because a transformation of  $\Psi$  everywhere under an action of the *group*  $O(2)$ , which consists of rotations and mirror transformations, does not change the free energy. From Sec. 2.4, we know that the disordered state solution for  $r > 0$  is given by  $\Psi = \mathbf{0}$ , which also exhibits this symmetry. We will discuss symmetries and group theory in more detail in Sec. 3.2. Figure 3.1 shows an initial state of  $\Psi = 0$  containing small fluctuations and the subsequent evolution under Eq. (3.1.2) with  $r < 0$ , i.e., *quenching* the system. The equilibrium value of  $|\Psi|$  spontaneously increases from 0 to  $\Psi_0 = (-r)^{1/2}$  to minimize  $\mathcal{F}$ , as argued in Sec. 2.4. In panel (c) of Fig. 3.1, we have shown the angle of  $\Psi$  as a colorbar which wraps around at  $\theta = \pi$  and  $\theta = -\pi$ , the dotted line, emphasizing that these are the same physical configuration.

While the exact configuration of the field after the quenching results from the fluctuations in the initial conditions, at each point in space, the field is "forced" to take a directional

value to get a non-zero value of  $|\Psi|$ . The result is a physical state that, as opposed to the fully symmetric disordered state  $\Psi = 0$ , is not  $O(2)$ -symmetric. This is called *spontaneous symmetry breaking* and is a feature of many phase transitions, including the translational and rotational symmetry breaking during the liquid-solid transition.

After quenching, we also see the emergence of some point-like features, e.g., the  $\times$  marked in Fig. 3.1, around which the angle of  $\Psi$  changes by a circulation  $\pm 2\pi$ . These are called *topological defects* and are typical hallmarks under symmetry-breaking phase transitions — artifacts that a local continuous field perturbation cannot immediately undo. To understand why, consider a topological defect with circulation  $2\pi$  subjected to a local perturbation and path  $\partial\mathcal{M}$  drawn outside the latter so that on  $\partial\mathcal{M}$ ,  $\Psi$  is unchanged. Thus, the circulation on  $\partial\mathcal{M}$  is still  $2\pi$ , which means that the topological defect must still exist inside  $\partial\mathcal{M}$ . At most, the local perturbation has moved the defect around. In  $O(n)$  symmetry-breaking phase transitions, these defects are called *vortices*, a name borrowed from fluid dynamics in which vortices are axes around which a fluid revolves.

While the field configuration in Fig. 3.1 contains many vortices, the lowest energy state at  $r < 0$  is the uniform state with  $\Psi = \Psi_0 \mathbf{n}$  for some arbitrary direction  $\mathbf{n}$ . The *ground-state manifold* is the space of all such equivalent ground states, which in this case is given by all directions on a circle with radius  $\Psi_0$ . This can easily be rescaled to the unit circle, so the ground-state manifold  $R$  is homeomorphic to the unit circle  $R \simeq \mathcal{S}^1$ . Topological defects are defined with respect to this ground state manifold. Intuitively, the charge of the topological defect is given by whether the circulation around the defect amounts to a change of  $2\pi$  or  $-2\pi$ , which we call  $+1$  and  $-1$  defects, respectively. This definition is more rigorous with *homotopy theory*, which we will introduce in Sec. 3.3. Notice that at these topological defects, the angle of  $\Psi$  is undefined, meaning that  $|\Psi|$  must go to zero for the field to be well-defined. This motivates a method devised by Halperin and Mazenko to track and derive analytical properties of defects, which we will introduce in Sec. 3.4.

The interplay between the topological nature of the ground state manifold and the physical dimension determines the defect's structure. For instance, by quenching an initial condition in the  $O(2)$ -symmetric TDGL model in three dimensions, we arrive at a configuration that looks like Fig. 3.2. As can be seen, the vortices have become line defects. In Chapter 4, we will show how the fundamental defects of the crystal structure — dislocations — are line defects due to a similar interplay between the ground state manifold and the three physical dimensions.

## 3.2 Symmetry and group theory

A symmetry of a system is a transformation that leaves the system invariant and is best described in the language of group theory. A group  $\mathcal{G} = (\{a_n\}, \star)$  consists of elements  $a_n$  together with a binary operation  $\star$  that combines two of them, with the additional requirements that

- I.  $\star$  is associative, i.e.,  $a_1 \star (a_2 \star a_3) = (a_1 \star a_2) \star a_3$ ,

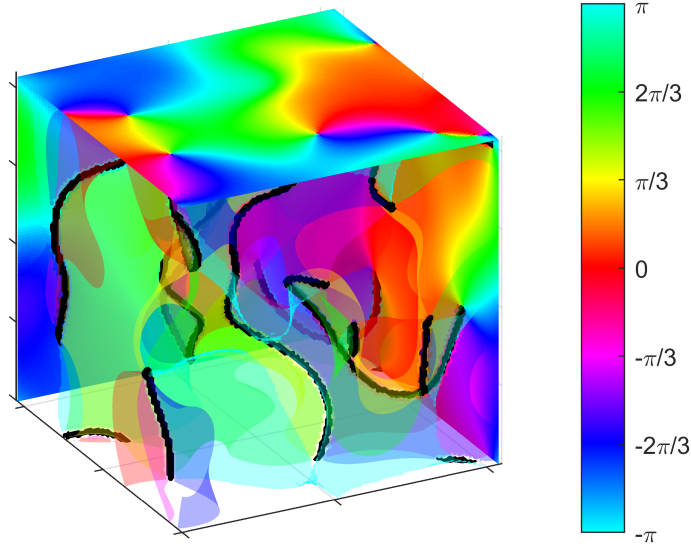


Figure 3.2: Snapshot of a quenched configuration in the  $O(2)$ -symmetric TDGL model in three dimensions (see text). Note that the angle shown in the colorbar is the angle in the topological space  $\mathcal{S}^1$  and does not correspond to a direction in physical space. The zeros of the field are shown as black lines.

2. there exists an identity element  $e \in \mathcal{G}$ , such that for all  $a_n \in \mathcal{G}$ ,  $e \star a_n = a_n \star e = a_n$ ,
3. for each  $a_n \in \mathcal{G}$ , there exists an inverse  $a_n^{-1}$ , such that  $a_n \star a_n^{-1} = e$ .

A simple example is  $(\mathbb{Z}, +)$ , i.e., the integers  $\{a_n\} \rightarrow \mathbb{Z}$  together with the binary operation of addition  $\star \rightarrow +$ , where the identity element is zero  $e \rightarrow 0$ . In this case, each integer  $n$  has its inverse  $(-n)$  since  $n + (-n) = 0$ . A system having symmetry means that certain actions taken upon it leave it unchanged, e.g., how a rotated sphere is indistinguishable from its unrotated counterpart. These actions are the group elements in the symmetry group of the system. The square, for instance, has four-fold rotational symmetry and four mirror symmetries. Figure 3.3 shows the symmetry actions of the square and the result of combining group elements in a table. This table represents the group in its totality, and many essential characteristics are read directly from it. For instance, the table is symmetric along the diagonal means the group operation is commutative, i.e., the group is Abelian.

Certain groups frequently reappear in physics and this thesis, so an explicit exposition is useful. These groups may often be represented as topological spaces [31], and some common examples are shown in Fig. 3.4.  $O(n)$  is the group of  $n \times n$  real matrices  $M$  that preserve the norm of  $n$ -dimensional real vectors  $\mathbf{v}$ , namely

$$\mathbf{v}^T M^T M \mathbf{v} = \mathbf{v}^T \mathbf{v}, \quad (3.2.1)$$

meaning

$$M^T M = \mathbb{1}. \quad (3.2.2)$$



★	<i>e</i>	<i>r</i> <sub>1</sub>	<i>r</i> <sub>2</sub>	<i>r</i> <sub>3</sub>	<i>m</i> <sub>1</sub>	<i>m</i> <sub>2</sub>	<i>m</i> <sub>3</sub>	<i>m</i> <sub>4</sub>
<i>e</i>	<i>e</i>	<i>r</i> <sub>1</sub>	<i>r</i> <sub>2</sub>	<i>r</i> <sub>3</sub>	<i>m</i> <sub>1</sub>	<i>m</i> <sub>2</sub>	<i>m</i> <sub>3</sub>	<i>m</i> <sub>4</sub>
<i>r</i> <sub>1</sub>	<i>r</i> <sub>1</sub>	<i>r</i> <sub>2</sub>	<i>r</i> <sub>3</sub>	<i>e</i>	<i>m</i> <sub>2</sub>	<i>m</i> <sub>3</sub>	<i>m</i> <sub>4</sub>	<i>m</i> <sub>1</sub>
<i>r</i> <sub>2</sub>	<i>r</i> <sub>2</sub>	<i>r</i> <sub>3</sub>	<i>e</i>	<i>r</i> <sub>1</sub>	<i>m</i> <sub>3</sub>	<i>m</i> <sub>4</sub>	<i>m</i> <sub>1</sub>	<i>m</i> <sub>2</sub>
<i>r</i> <sub>3</sub>	<i>r</i> <sub>3</sub>	<i>e</i>	<i>r</i> <sub>1</sub>	<i>r</i> <sub>2</sub>	<i>m</i> <sub>4</sub>	<i>m</i> <sub>1</sub>	<i>m</i> <sub>2</sub>	<i>m</i> <sub>3</sub>
<i>m</i> <sub>1</sub>	<i>m</i> <sub>1</sub>	<i>m</i> <sub>4</sub>	<i>m</i> <sub>3</sub>	<i>m</i> <sub>2</sub>	<i>e</i>	<i>r</i> <sub>3</sub>	<i>r</i> <sub>2</sub>	<i>r</i> <sub>1</sub>
<i>m</i> <sub>2</sub>	<i>m</i> <sub>2</sub>	<i>m</i> <sub>1</sub>	<i>m</i> <sub>4</sub>	<i>m</i> <sub>3</sub>	<i>r</i> <sub>1</sub>	<i>e</i>	<i>r</i> <sub>3</sub>	<i>r</i> <sub>2</sub>
<i>m</i> <sub>3</sub>	<i>m</i> <sub>3</sub>	<i>m</i> <sub>2</sub>	<i>m</i> <sub>1</sub>	<i>m</i> <sub>4</sub>	<i>r</i> <sub>2</sub>	<i>r</i> <sub>1</sub>	<i>e</i>	<i>r</i> <sub>3</sub>
<i>m</i> <sub>4</sub>	<i>m</i> <sub>4</sub>	<i>m</i> <sub>3</sub>	<i>m</i> <sub>2</sub>	<i>m</i> <sub>1</sub>	<i>r</i> <sub>3</sub>	<i>r</i> <sub>2</sub>	<i>r</i> <sub>1</sub>	<i>e</i>

Figure 3.3: The symmetry group of the square consisting of the identity "do-nothing" action  $e$ , three rotational symmetry actions  $r_1, r_2, r_3$ , and four mirror symmetries  $m_1, m_2, m_3, m_4$ . Combining two such actions amounts to a different action, as summarized in the table.

This implies  $\det(M)^2 = 1$ , which gives  $\det M = \pm 1$ .  $O(n)$  contains the actions of rotation and mirroring of vectors, whereas the *special* group obtained by restricting  $\det M = 1$  is called  $SO(n)$  and is the group of rotations. Visually,  $SO(2)$  is represented by the unit circle since a rotation in two dimensions is given by an angle, while  $SO(3)$  can be visualized as the ball of radius  $\pi$  where antipodal points are identified; this is because any rotation in three dimensions is given by the axis around which the rotation takes place and the magnitude of the rotation, and a rotation of  $\pi$  and  $-\pi$  being physically equivalent.  $U(n)$  is the group of  $n \times n$  complex matrices  $N$  that preserve the norm of  $n$ -dimensional complex vectors  $\psi$  in the sense

$$\psi^\dagger N^\dagger N \psi = \psi^\dagger \psi, \quad (3.2.3)$$

where  $\psi^\dagger$  is the conjugate transpose of  $\psi$ , meaning

$$N^\dagger N = \mathbb{1}, \quad (3.2.4)$$

implying that  $|\det N|^2 = 1$ , which gives  $\det N = e^{i\theta}$  for some angle  $\theta$ . The special group  $SU(n)$  is obtained by requiring  $\det N = 1$ .  $U(1)$  is the set of complex numbers with unit modulus, so  $U(1) \simeq SO(2)$ , i.e., it is isomorphic with  $SO(2)$ .

To showcase how the ground state manifold varies between systems, consider the nematic crystal mentioned in the introduction. A nematic crystal consists of elongated particles with head-tail symmetry, so the ground state manifold is a direction in space with

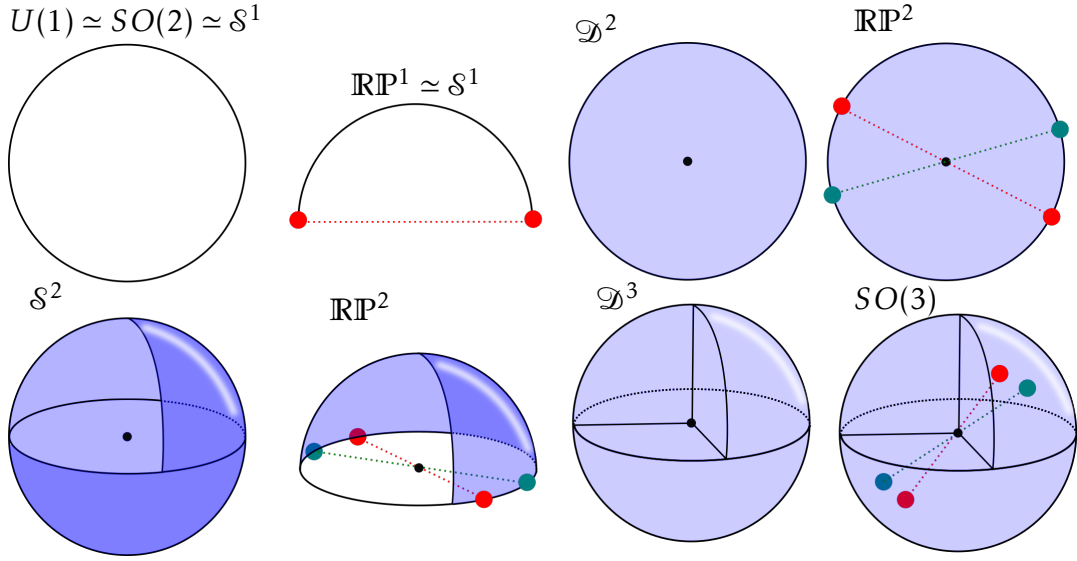


Figure 3.4: Some of the most common topological spaces.  $\mathcal{S}^1$  is the unit circle which is homeomorphic to  $\mathbb{R}\mathbb{P}^1$ , the half-circle with base points identified.  $\mathcal{S}^2$  is the (hollow) unit sphere, while  $\mathbb{R}\mathbb{P}^2$  is the half-sphere with antipodal points on the base circle identified.  $\mathcal{D}^2$  is the (filled) unit disk, which is homeomorphic to  $\mathbb{R}\mathbb{P}^2$  when antipodal points are identified.  $\mathcal{D}^3$  is the (filled) unit ball, which is homeomorphic to  $SO(3)$  when antipodal points are identified.

this specific symmetry, i.e., the space of lines going through the origin. In  $d$  dimensions, this is the group  $\mathbb{R}\mathbb{P}^n$ , the real projective plane, with  $n = d - 1$ , and in particular,  $\mathbb{R}\mathbb{P}^1$  may be visualized as a semi-circle in  $\mathbb{R}^2$  with  $(1, 0)$  and  $(-1, 0)$  identified as the same point. We may imagine gluing this point to itself, effectively rendering  $\mathbb{R}\mathbb{P}^1$  the same topological space as  $\mathcal{S}^1$ , which is a correct assertion. Thus, the topological nature of a 2D nematic crystal is topologically equivalent to that of a system with  $\mathcal{S}^1$  as a ground state manifold. However, in three dimensions, the ground state manifold of a nematic liquid crystal is  $\mathbb{R}\mathbb{P}^2$ , which may be visualized as a half-sphere where antipodal points on the base circle are identified. While  $\mathbb{R}\mathbb{P}^1 \simeq \mathcal{S}^1$ ,  $\mathbb{R}\mathbb{P}^2$  is fundamentally different from  $\mathcal{S}^2$ , since the base circle cannot be "shrunk down" to a single point, the same way the antipodal point of  $\mathbb{R}\mathbb{P}^1$  could.

On a particular topological space, we may construct what is called the homotopy group, which will prove helpful in categorizing the topological defects that will be introduced in the next section. Consider a topological space  $R$ , and a closed path  $\partial\mathcal{M}_R$  going through a specific point  $P$  in this space; see Fig. 3.5. The space  $R$  might have a particular structure, such as holes, which makes it impossible to continuously shrink  $\partial\mathcal{M}_R$  down to a point. Loops originating from the same point  $P$  can be combined by the binary operation  $\star$  by concatenating the end of one loop to the beginning of the other. We define two such loops, both going through  $P$ , as homotopic if one can be continuously deformed into another. This is an equivalency class, which we may denote by  $[\partial\mathcal{M}_R]$ . For the case shown in Fig. 3.5, we have  $[\partial\mathcal{M}_R^{(1)}] = [\partial\mathcal{M}_R^{(2)}]$ , and  $[\partial\mathcal{M}^{(3)}] = e$ , the identity element. The

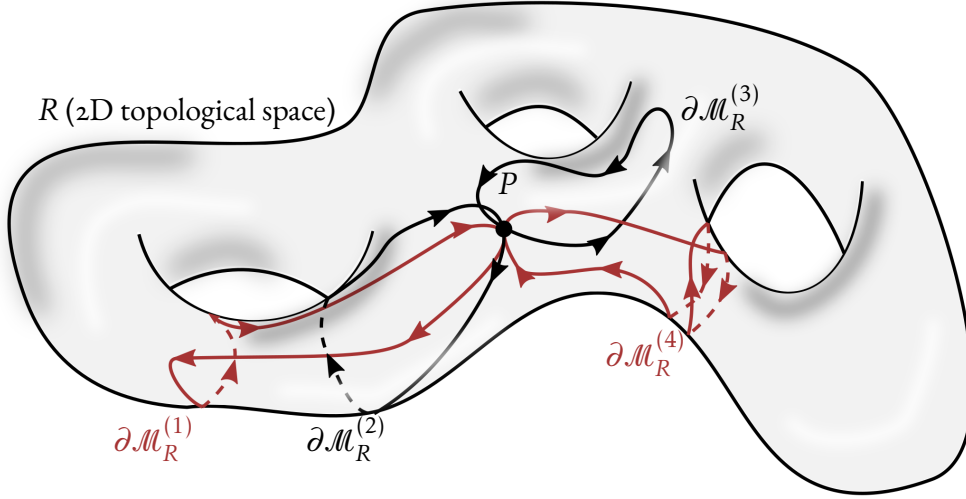


Figure 3.5: A topological space  $R$  and a selection of closed loops  $\partial \mathcal{M}^{(n)}$  originating from a common point  $P$ .  $\partial \mathcal{M}_R^{(1)}$  and  $\partial \mathcal{M}_R^{(2)}$  are homotopic because one can be continuously deformed the other, and both are represented by the group element  $[\partial \mathcal{M}^{(1)}] \in \pi_1(R)$ . In contrast,  $\partial \mathcal{M}_R^{(3)}$  can be shrunk down to the point  $P$ , so  $[\partial \mathcal{M}_R^{(3)}] = e$ , the identity element.

homotopy group of  $R$ , denoted  $\pi_1(R)$ , is defined by homotopically different loops. In the case of the space  $R$  in Fig. 3.5, this group will be infinitely big because loops can be wrapped around a hole arbitrarily many times. Of particular interest to this thesis is the fact that  $\pi_1(\mathcal{S}^1) = \mathbb{Z}$ , since the homotopic difference between two closed loops in  $\mathcal{S}^1$  is the number of times, positive or negative, they have looped around the circle. Other topological spaces that will be relevant when discussing crystal structure are the toruses  $\mathcal{T}^2$  and  $\mathcal{T}^3$  in two and three dimensions, respectively. These are shown in Fig. 3.6, together with loops from the homotopy group corresponding to different group elements. The two-torus  $\mathcal{T}^2$  can be visualized as a donut embedded in three dimensions. As a topological space, it can be described as the product space  $\mathcal{T}^2 = \mathcal{S}^1 \times \mathcal{S}^1$ , and the homotopy group is given by  $\pi_1(\mathcal{T}^2) = \mathbb{Z}^2$  [31]. The three-torus can be visualized as a cube with periodic boundary conditions, shown in the figure by closed paths that pass through the point  $P$ , exit one wall, and enter through the other. Like  $\mathcal{T}^2$ , it can be written as the product space  $\mathcal{T}^3 = \mathcal{S}^1 \times \mathcal{S}^1 \times \mathcal{S}^1$  and  $\pi_1(\mathcal{T}^3) = \mathbb{Z}^3$ .

The number 1 in " $\pi_1(R)$ " emphasizes that this is formally the *first* homotopy group of  $R$ , which is made up of equivalence classes of *loops*. It is possible to generalize this notion to higher order homotopy groups, consisting of closed *surfaces*, *volumes* etc.

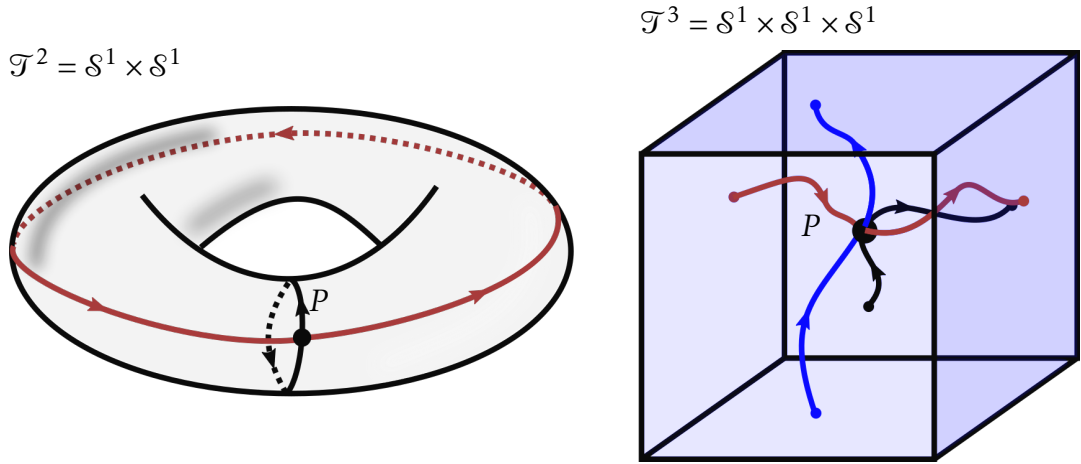


Figure 3.6: The two-torus  $\mathcal{T}^2$  and the three-torus  $\mathcal{T}^3$ . While  $\mathcal{T}^2$  can be visualized as a donut embedded in 3D space, the 3-torus is best shown as a cube with periodic boundary conditions. These topological spaces can be written as product spaces of  $\mathcal{S}^1$ , as visualized by the closed loops going through the point  $P$ .

### 3.3 Topological defects

In systems exhibiting spontaneous symmetry breaking, the ground state manifold  $R$  changes at the phase transition. In Sec. 3.1,  $R$  went from the single point  $\Psi = \mathbf{0}$  in the disordered phase to the unit circle in the ordered phase. We may construct a map from the real space coordinates to  $R$  by normalizing the vector field  $\Psi_n = \frac{1}{|\Psi|} \Psi \in \mathcal{S}^1$ . Consider then one of the topological defects in panel (c) of Fig. 3.1 and an oriented loop  $\partial\mathcal{M}$  around this defect, which is mapped to an oriented loop  $\partial\mathcal{M}_R$  in  $R$ . Only at defects, where  $\Psi = \mathbf{0}$ , does  $\Psi_n$  become undefined. Therefore, deforming  $\partial\mathcal{M} \rightarrow \partial\mathcal{M}'$  without crossing a different topological defect, corresponds to a continuous deformation of  $\partial\mathcal{M}_R$  in  $R$ , which by definition does not change the homotopy group element to which  $\partial\mathcal{M}_R$  belongs. Thus, with each topological defect, we may associate a specific group element  $[\partial\mathcal{M}_R]$  in  $\pi_1(\mathcal{S}^1)$  and a charge given by the isomorphism with  $\mathbb{Z}$ . The singled-out defect marked with  $\times$  in Fig. 3.1 is a +1-defect.

As we alluded to previously, the interplay between the structure of the ground state manifold and the physical dimensions determines the type of topological defects that arise. From Fig. 3.1, we see that for  $d = 2$  spatial dimensions and  $R = \mathcal{S}^1$ , the topological defects are points with integer charge. In the case of  $R = \mathcal{S}^1$  in three dimensions, the topological defects are lines as shown in Fig. 3.2. The reason for this can be seen by considering the map  $\Psi_n : \mathbb{R}^3 \rightarrow \mathcal{S}^1$ , which is shown in Fig. 3.7. We see that by enclosing the defect  $\ell$  with a path  $\partial\mathcal{M}$ , we get the same topological invariant corresponding to the winding number in  $\mathcal{S}^1$ , which means that there must be a point inside any 2D surface  $\mathcal{M}$  bounded by  $\partial\mathcal{M}$  where  $\Psi_n$  is undefined, i.e., where the topological defect is located. These points on different surfaces make up the defect line which has an integer charge. A 3D nematic liquid crystal does also have line defects, but since  $\pi_1(\mathbb{R}P^2) = \mathbb{Z}_2$ , these lines have no

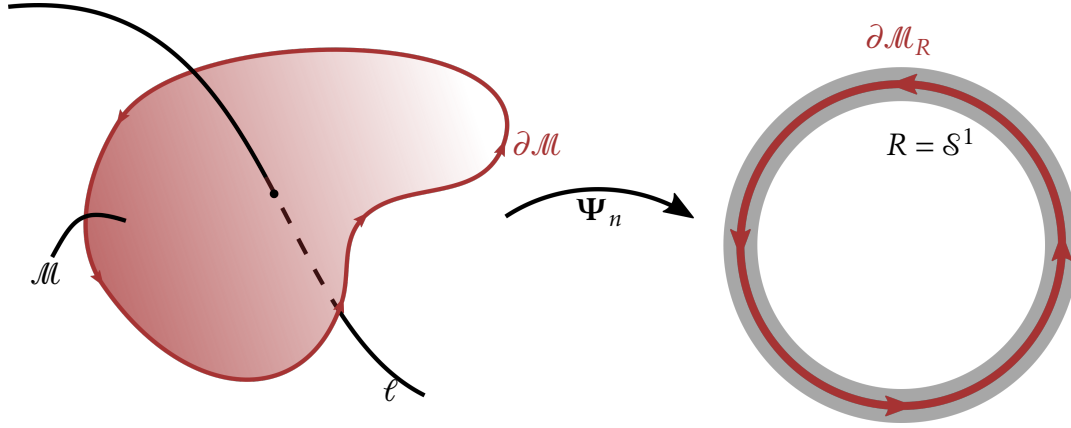


Figure 3.7: A topological line defect  $\ell$  for a map  $\Psi_n : \mathbb{R}^3 \rightarrow \mathcal{S}^1$ . Its charge is found by considering an enclosing loop  $\partial\mathcal{M}$  that bounds a surface  $\mathcal{M}$  which  $\ell$  pierces.  $\Psi_n$  maps  $\partial\mathcal{M}$  to  $\partial\mathcal{M}_R$  in  $R = \mathcal{S}^1$ . The charge of  $\ell$  is given by the homotopy group element to which  $\partial\mathcal{M}_R$  belongs, which in this case is given by the number of times  $\partial\mathcal{M}_R$  wraps around  $\mathcal{S}^1$ . Note that reversing the direction of  $\partial\mathcal{M}$  amounts to reversing the circulation in  $R$ . Therefore, the topological charge associated with the topological defect line  $\ell$  is defined with respect to a tangent vector  $\mathbf{t}$  that indicates the desired orientation of  $\partial\mathcal{M}$ .

direction and a charge of 1/2 or none at all [32].

The charge of the topological defects in  $\mathcal{S}^1$  fields in two dimensions can be determined by the integral

$$s = \frac{1}{2\pi} \oint_{\partial\mathcal{M}} d\theta = \frac{1}{2\pi} \oint_{\partial\mathcal{M}} (\nabla\theta) \cdot d\mathbf{l}, \quad (3.3.1)$$

where  $d\mathbf{l}$  is the line element along  $\partial\mathcal{M}$  and  $\theta$  is the angle of  $\Psi$ . It is important to remember that  $\theta$  should not be taken as the single-valued field, which we name  $\theta^T$ , plotted in Fig. 3.2. The gradient of  $\theta^T$  would contain arbitrary delta functions over the phase-slip  $-\pi \rightarrow \pi$ , which are not physical but result only from our choice of phase cut in extracting the angle from  $\Psi$ . Instead,  $\theta$  should be considered an element of  $\mathcal{S}^1$  so that  $\nabla\theta$  contains no singularities. We will find a similar distinction between quantities known as the *elastic distortion*  $\mathfrak{u}^E$  and *plastic distortion*  $\mathfrak{u}^P$  in the next chapter. Often, we are interested in a description of the topological defect density, a density function  $\rho_{\text{top}}$  such that

$$s = \int_{\mathcal{M}} d^2r \rho_{\text{top}}, \quad (3.3.2)$$

where  $\mathcal{M}$  is the area bounded by  $\partial\mathcal{M}$ . However, going from Eq. (3.3.1) to an expression for  $\rho_{\text{top}}$  is not trivial. In the next section, we shall look at the Halperin-Mazenko method, which uses the fact that the order parameter is zero at the topological defects to pinpoint their location and find an expression for  $\rho_{\text{top}}$ . In Paper V, we found a different method by slightly redefining the topological charge  $s$  which results in a non-singular defect density.

### 3.4 The Halperin-Mazenko method

In this section, we will present the method introduced by Halperin in Ref. [33] to track topological defects in mean-field theories such as the one in Sec. 3.1. Mazenko extended the method in Ref. [34] to include an explicit expression for the velocity of defects, which was subsequently used to derive analytical results for the statistics of vortex velocities.

Consider first the 2D theory. The fundamental insight is to recognize that the defects in the ordered phase are localized at positions  $\{\mathbf{r}_\alpha\}$  where the order parameter  $\Psi = \mathbf{0}$ . By the transformation of the delta function, one may therefore write

$$|D|\delta^{(2)}(\Psi) = \sum_{\alpha} \delta^{(2)}(\mathbf{r} - \mathbf{r}_\alpha), \quad (3.4.1)$$

where  $\delta^{(2)}(\Psi) = \delta(\Psi_1)\delta(\Psi_2)$  and  $D$  is the Jacobian determinant of the function  $\Psi$ , i.e.,

$$D = \frac{\partial(\Psi_1, \Psi_2)}{\partial(x, y)} = \partial_x \Psi_1 \partial_y \Psi_2 - \partial_x \Psi_2 \partial_y \Psi_1 = \frac{1}{2} \epsilon_{ij} \epsilon_{mn} (\partial_i \Psi_m) (\partial_j \Psi_n), \quad (3.4.2)$$

where  $\epsilon_{ij}$  is the Levi-Civita symbol. Furthermore, Halperin argued by considering an explicit ansatz for the point defect, that the absolute value of  $|D|$  can be lifted from the lhs. of Eq. (3.4.1), if the charge  $q_\alpha$  of the topological defect at  $\mathbf{r}_\alpha$  is included in the sum, yielding

$$\rho_{\text{top}} = \sum_{\alpha} q_{\alpha} \delta^{(2)}(\mathbf{r} - \mathbf{r}_{\alpha}) = D \delta^{(2)}(\Psi). \quad (3.4.3)$$

Defect density ( $R = S^1, d = 2$ )

Here, we have identified the lhs. as the topological defect density  $\rho_{\text{top}}$ , the quantity that satisfies Eq. (3.3.2). If the vector field  $\Psi$  evolves in time, the topological defects attain individual velocities  $\{\mathbf{v}_\alpha\}$ . By differentiating  $\rho_{\text{top}}$ , through the use of vector identities, Mazenko derived in Ref. [34] the following expression

$$\partial_t \rho_{\text{top}} + \nabla \cdot (\delta^{(2)}(\Psi) \mathbf{J}) = 0, \quad (3.4.4)$$

where

$$J_i = -\epsilon_{ij} \epsilon_{mn} (\partial_t \Psi_m) (\partial_j \Psi_n). \quad (3.4.5)$$

Since  $\rho_{\text{top}}$  is a conserved quantity, by comparison with the standard continuity equation

$$\partial_t \rho_{\text{top}} + \nabla \cdot \left( \sum_{\alpha} q_{\alpha} \mathbf{v}_{\alpha} \delta^{(2)}(\mathbf{r} - \mathbf{r}_{\alpha}) \right) = 0, \quad (3.4.6)$$

Mazenko identified the vortex velocity as

$$\mathbf{v}_{\alpha} = \left. \frac{\mathbf{J}}{D} \right|_{\mathbf{r}_{\alpha}}. \quad (3.4.7)$$

The method was extended to  $R = \mathcal{S}^1$  in three dimensions in Ref. [35]. In this case, the charge density becomes a vector field  $\boldsymbol{\rho}_{\text{top}}$  which satisfies

$$s = \int_{\mathcal{M}} \boldsymbol{\rho}_{\text{top}} \cdot d\mathbf{S}, \quad (3.4.8)$$

where  $d\mathbf{S}$  is a directed surface element of  $\mathcal{M}$ , a 2D surface pierced by the topological defect line. Using similar methods, Mazenko arrived at the following expression for the defect density

$$\boldsymbol{\rho}_{\text{top}} = \mathbf{D} \delta^{(2)}(\boldsymbol{\Psi}), \quad (3.4.9)$$

Defect density ( $R = \mathcal{S}^1$ ,  $d = 3$ )

where

$$D_i = \frac{1}{2} \epsilon_{ijk} \epsilon_{mn} (\partial_j \Psi_m) (\partial_k \Psi_n). \quad (3.4.10)$$

The velocities of the defects were found to have a similar form, namely

$$\mathbf{v} = \frac{\mathbb{J} \cdot \mathbf{D}}{|\mathbf{D}|^2} \Big|_{r \in \ell}, \quad (3.4.11)$$

evaluated on the defect line  $\ell$ , and  $\mathbb{J}$  is given by

$$\mathbb{J}_{ij} = -\epsilon_{ijk} \epsilon_{mn} (\partial_t \Psi_m) (\partial_k \Psi_n). \quad (3.4.12)$$

The framework has since been applied to a plethora of systems, including Bose-Einstein condensates [36, 37, 38], active nematics in two- and three dimensions [39, 40, 32], solid crystals in two dimensions [20] and in three dimensions in Paper III.





## CHAPTER 4

### *Elasticity and plasticity*



“ Plasticity [...] means the possession of a structure weak enough to yield to an influence, but strong enough not to yield all at once.

- *William James* [41]

The Egyptians and Romans were excellent builders, raising pyramids and theatres, showing that they possessed an advanced, intuitive understanding of the properties of material structures like beams, bricks, and columns. The first attempt at systematically categorizing the properties of materials and how exactly their carrying capacities scale with cross-sections and lengths may have been Leonardo Da Vinci's comprehensive research on the matter, even though this particular contribution of his to modern science is less known. The modern treatment of elasticity dates back to the 18th century when prominent physicists such as Bosevich, Poisson, Navier, and Cauchy in particular built on the theory of mechanics put forward by Newton [42]. In this chapter, we introduce linear elasticity, dislocations, and their contribution to the plastic response of single-crystals. We then extend this approach to formulate generic properties for a hydrodynamic theory of deformed crystals.

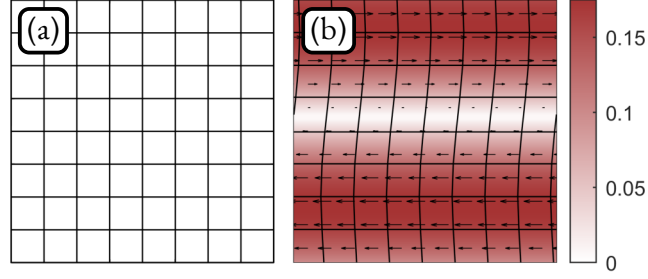


Figure 4.1: (a) An undistorted reference lattice that has been deformed by (b) a displacement field  $\mathbf{u}$ . The displacement field is given in units of the lattice constant  $a_0$ .

#### 4.1 Linear elasticity

An elastically distorted medium is described by a displacement field  $\mathbf{u}$ , exemplified in Fig. 4.1. A uniform lattice translation does not induce strain energy or cause forces to arise in the medium. Therefore, it is the gradient of the displacement field, the distortion

$$\mathbb{u}_{ij} = \partial_j u_i, \quad (4.1.1)$$

The distortion

that is of most interest. The equilibrium state of an undistorted medium is then given by  $\mathbb{u} = 0$  and letting  $\mathcal{F}_{\text{el}}$  represent the elastic energy, we obtain, to lowest order,

$$\mathcal{F}_{\text{el}} = \int d^d r \frac{1}{2} \mathcal{C}_{ijkl} \mathbb{u}_{ij} \mathbb{u}_{kl}, \quad (4.1.2)$$

where  $\mathcal{C}_{ijkl}$  is the rank four elastic constant tensor. The distortion may be decomposed into strains and rotations as described in the following; suppose that the displacement field is given by an infinitesimal rigid body rotation  $\delta\Omega$ , in which case  $\mathbf{u} = \delta\Omega \times \mathbf{r}$ , and  $\mathbb{u}_{ij} = \partial_j (\epsilon_{ikl} \delta\Omega_k r_l) = -\epsilon_{kij} \delta\Omega_k$ . Contracting  $\mathbb{u}_{ij}$  with  $\epsilon_{mij}$ , we get

$$\epsilon_{mij} \mathbb{u}_{ij} = -\delta\Omega_k \epsilon_{kij} \epsilon_{mij} = -2\delta\Omega_m. \quad (4.1.3)$$

Since  $\epsilon_{mij}$  is antisymmetric, only the antisymmetric part of  $\mathbb{u}$  contributed to this calculation. Thus, we define the antisymmetric part of the distortion as the rotation part

$$\omega_{ij} = \mathbb{u}_{[ij]}. \quad (4.1.4)$$

The rotation tensor

Being antisymmetric, it has only three independent components, making it helpful to express in a vector form, as suggested by Eq. (4.1.3),

$$\Omega_k = -\frac{1}{2}\epsilon_{kij}\omega_{ij}, \quad (4.1.5)$$

The rotation vector

which can also be inverted to

$$\omega_{ij} = -\epsilon_{ijk}\Omega_k. \quad (4.1.6)$$

Rigid body rotations will not increase the elastic energy  $\mathcal{F}_{el}$ , meaning  $\mathcal{F}_{el}$  is only a function of the symmetric part of the distortion, which, in linear elasticity, is called the strain tensor

$$\epsilon_{ij} = \mathbb{U}(ij). \quad (4.1.7)$$

The strain tensor

The strain tensor measures the changes in distances in the medium as it is deformed. This can be seen by considering an infinitesimal displacement  $d\mathbf{r}^2$ , which under the deformation  $\mathbf{u}$ , changes to

$$d\mathbf{r}'^2 = (d\mathbf{r} + d\mathbf{u})^2 = (dr_i + \partial_k u_i dr_k)^2 = d\mathbf{r}^2 + 2(\partial_k u_i)dr_k dr_i + \mathcal{O}(\mathbf{u}^2). \quad (4.1.8)$$

Only the symmetric part of the distortion  $\partial_k u_i$  is involved in this calculation since it is contracted with the symmetric  $dr_k dr_i$ . Having the elastic tensor be symmetric under the interchange of indices  $i \leftrightarrow j$  and  $k \leftrightarrow l$  ensures that the elastic energy only depends on the strain tensor. Furthermore, as Eq. (4.1.2) shows,  $\mathcal{C}$  should also satisfy the symmetry of interchanging both  $ij \rightarrow kl$ , and, on top of this,  $\mathcal{C}$  should respect the symmetries of the lattice. These symmetries severely restrict the number of independent components in  $\mathcal{C}$ , and for cubic symmetry, it can be written entirely in terms of three independent parameters

$$\mathcal{C}_{ijkl} = \lambda\delta_{ij}\delta_{kl} + 2\mu\delta_{k(i}\delta_{j)l} + \gamma\delta_{ijkl}, \quad (4.1.9)$$

The elastic constant tensor for cubic symmetry

where  $\lambda$  and  $\mu$  are called Lamé parameters, and  $\delta_{ijkl}$  is a generalization of the Kronecker-delta symbol, which is 1 if all indices are equal and zero otherwise.  $\gamma$  is a parameter associated with the anisotropy of the square lattice in two dimensions, and the cubic lattice in three, which is zero in the case of isotropic elasticity. An important point to note is that since  $\gamma\delta_{ijkl}$  represents an anisotropic contribution to the stress, its expression in this form is coordinate dependent. Thus, in Eq. (4.1.9), it is understood that the components  $\mathcal{C}_{ijkl}$  are expressed in a Cartesian coordinate system along the principal axes of the cubic symmetry. Being a well-defined tensor, it can be represented in a different coordinate system, in which case Eq. (4.1.9) will look slightly different. With these symmetries, the elastic energy can equally well be written in its more usual form

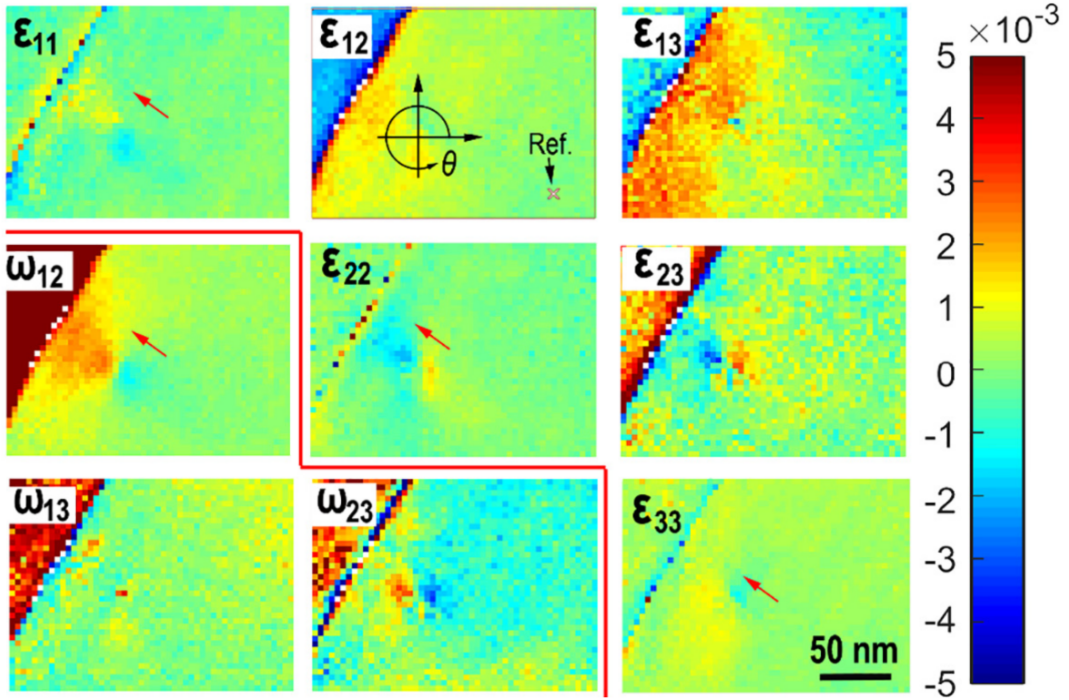


Figure 4.2: 2D slices of the strain  $\varepsilon_{ij}$  and rotation  $\omega_{ij}$  fields in a sample of tungsten measured by high-resolution transmission Kikuchi diffraction. The rotation field indicates a different orientation of the tungsten crystal in the upper left corner. Adapted and reprinted under Creative Commons Attribution License from Ref. [43]. Copyright 2019 by the authors.

$$\mathcal{F}_{\text{el}} = \int d^d r \frac{1}{2} \mathcal{C}_{ijkl} \varepsilon_{ij} \varepsilon_{kl}. \quad (4.1.10)$$

The elastic energy

Figure 4.2 shows the 9 independent components of the distortion tensor in a tungsten sample.

While the elastic energy gives the energy of the distorted medium, it is the stress tensor  $\sigma$  that describes the forces that arise inside the medium due to strains.  $\sigma_{ij}$  is the  $i$ th component of the force acting on a unit surface oriented along the  $j$ th direction. From the continuum theory of elasticity, it is also a key property of  $\sigma$  that it is a symmetric tensor [44]. In linear elasticity, the stress tensor scales linearly with the strain, which is a continuum elasticity version of Hooke's law

$$\sigma_{ij} = \mathcal{C}_{ijkl} \varepsilon_{kl}. \quad (4.1.11)$$

Hooke's law for the stress tensor

Due to their symmetry, the stress and strain only contain six independent components. Therefore, there is a standard convention of writing the relation between these six independent components, given by

$$\begin{pmatrix} \sigma_{xx} \\ \sigma_{yy} \\ \sigma_{zz} \\ \sigma_{yz} \\ \sigma_{xz} \\ \sigma_{xy} \end{pmatrix} = \begin{pmatrix} C_{11} & C_{12} & C_{13} & C_{14} & C_{15} & C_{16} \\ C_{12} & C_{22} & C_{23} & C_{24} & C_{25} & C_{26} \\ C_{13} & C_{23} & C_{33} & C_{34} & C_{35} & C_{36} \\ C_{14} & C_{24} & C_{34} & C_{44} & C_{45} & C_{46} \\ C_{15} & C_{25} & C_{35} & C_{45} & C_{55} & C_{56} \\ C_{16} & C_{26} & C_{36} & C_{46} & C_{56} & C_{66} \end{pmatrix} \begin{pmatrix} \varepsilon_{xx} \\ \varepsilon_{yy} \\ \varepsilon_{zz} \\ 2\varepsilon_{yz} \\ 2\varepsilon_{xz} \\ 2\varepsilon_{xy} \end{pmatrix} \quad (4.1.12)$$

Expressing the elastic constant tensor in this way is referred to as *Voigt Notation*, and the factor of 2 in front of the off-diagonal parts of the strain tensor is conventional. As mentioned, for a lattice with cubic, or 2D square, symmetry, there are only three independent elastic constants, which are  $C_{11}$ ,  $C_{12}$  and  $C_{44}$ . The other components are given by  $C_{mn} = 0$ , except for  $C_{23} = C_{13} = C_{12}$ ,  $C_{33} = C_{22} = C_{11}$  and  $C_{66} = C_{55} = C_{44}$ . The transformation between the Lamé parameters and the elastic constant tensor in Voigt notation is given by

$$C_{11} = \lambda + 2\mu + \gamma \quad C_{12} = \lambda \quad C_{44} = \mu. \quad (4.1.13)$$

Consider now a small volume element in an elastic body located in the region  $(x, x + \Delta x) \times (y, y + \Delta y) \times (z, z + \Delta z)$ . Given the definition of the stress tensor as the force per unit area, the  $x$ -component  $F_x \Delta V$  of the net force  $\mathbf{F} \Delta V$  acting on the element is to first order given by

$$\begin{aligned} F_x \Delta V &= (\sigma_{xx}(x + \Delta x, y, z) - \sigma_{xx}(x, y, z)) \Delta y \Delta z \\ &+ (\sigma_{xy}(x, y + \Delta y, z) - \sigma_{xy}(x, y, z)) \Delta x \Delta z + (\sigma_{xz}(x, y, z + \Delta z) - \sigma_{xz}(x, y, z)) \Delta x \Delta y. \end{aligned} \quad (4.1.14)$$

Here,  $\mathbf{F}$  is the force density, i.e., the force per unit volume in the elastic medium. Dividing by the volume  $\Delta V = \Delta x \Delta y \Delta z$ , taking the limit  $\Delta V \rightarrow 0$  and generalizing for  $F_y$  and  $F_z$ , we get the definition of the force density

$$\mathbf{F} = \nabla \cdot \boldsymbol{\sigma} \quad (F_i = \partial_j \sigma_{ij}). \quad (4.1.15)$$

The force density

If the elastic medium is at rest, the force density is zero, a condition commonly referred to as mechanical equilibrium

$$\nabla \cdot \sigma = 0. \quad (4.1.16)$$

Mechanical equilibrium

It is crucial to note that stresses are also present in the absence of a crystalline structure, e.g., in an isotropic liquid. In this case, if we ignore viscous contributions, the stress tensor is simply a diagonal matrix

$$\sigma_{ij} = p\delta_{ij}, \quad (4.1.17)$$

where  $p$  is the pressure of the liquid. It is, therefore, essential to be precise when relating the stress tensor to the strain and keep track of which independent variables are varied. We will make this effort in Sec. 4.4.

Linear elasticity is a theory valid near the equilibrium state of zero strain, in which the state of the crystal can be uniquely determined by the value of the deformation field, which is thought of as "detached" from the physical coordinates. In reality, a displacement field is properly defined as a deformation of a medium, in which case one must be careful in choosing the coordinate system. Using the undeformed medium as the reference lattice is called the Lagrangian representation, while using the deformed state as a reference is called the Eulerian representation. The strain tensor, Eq. (4.1.7), will then have non-linear contributions whose form depends on the chosen representation. In this thesis, we will limit ourselves to linear elasticity and not delve further into this distinction and the consequences of non-linearities.

## 4.2 Plasticity and the dislocation

Any real material only behaves as a perfectly elastic medium at low strains. At higher strains or stresses, the linear relationship between stress and strain, Eq. (4.1.11) breaks down as the material enters into a transient region of non-linear elasticity before transitioning into plastic yield. Figure 4.3 shows the measured stress-strain from wet quartz during a nanoindentation experiment. The dashed line in this figure depicts the linear stress relation, valid for this material up to a certain strain level, after which the material yields and starts to deform plastically. In the figure, the authors have not been able to identify a unique yield point signaling the transition from elastic to plastic behavior. This demonstrates the more general feature that plasticity is inherently an erratic and unpredictable process associated with large spatiotemporal fluctuations in sample composition and geometry. This feature is due to the stochastic nature of the mediators of plasticity, namely microstructures such as grain boundaries, cracks, and dislocations. Plasticity theories attempt to find effective models to predict the onset of yield and the mechanical properties of highly deformed media. Different mechanisms are important under different circumstances, and in this thesis, we are focusing on plastic deformation in single crystals, as described by the interaction of the topological defects of the crystal symmetry: dislocations.

A dislocation is a line defect, and exists because at the atomic level, crystalline solids are

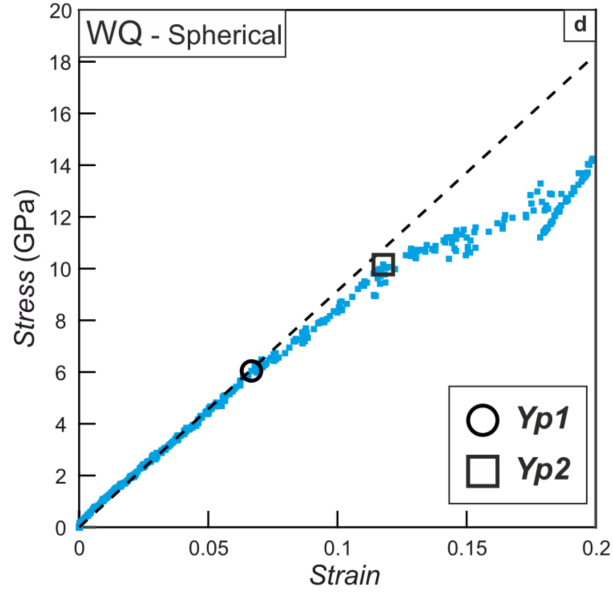


Figure 4.3: Measured stress-strain relationship during a spherical nanoindentation test on wet quartz (WQ).  $Yp_1$  and  $Yp_2$  refer to the two identified yield points. Reprinted under Creative Commons Attribution License from Ref. [45]. Copyright 2022 by the authors.

made up of unit cells with some minimal length: the lattice constant  $a_0$ . It is a connection error, characterized by the tangent vector  $\mathbf{t}$  to the line and its vector charge: the Burgers vector  $\mathbf{b}$ . This connection error becomes visible by tracing a path around the dislocation along the crystal unit cells in a right-hand manner with respect to the tangent vector. By "walking" a path consisting of equally many steps in each crystallographic direction in this way, one does not end up at the starting point; see Fig. 4.4. The connection error is then necessarily given by a lattice vector, the Burgers vector  $\mathbf{b}$ . If the Burgers vector is perpendicular to the tangent vector, it is called an edge dislocation which is shown in panel (b). In two dimensions, the direction of the tangent vector is always taken to point out of plane in the  $z$ -direction; therefore, all dislocations are edge dislocations, as shown in panel (a). If the Burgers vector is parallel to the tangent vector, it is called a screw dislocation, from how the medium screws around it in its direction. Note the physical nature of the dislocation is invariant under  $\mathbf{t} \rightarrow -\mathbf{t}$  and  $\mathbf{b} \rightarrow -\mathbf{b}$ .

Under applied stress, the dislocations will move; see Fig. 4.5. The motion of the dislocation results from effectively breaking and recombining adjacent atomic bonds, a process sometimes compared to the movement of a caterpillar. Under a plastic deformation, the solid dissipates energy due to the motion of dislocations, which may move by either glide or climb motion. The difference between these two modes of dissipation is that while glide motion happens in the slip plane, i.e., the plane spanned by  $\mathbf{b}$  and  $\mathbf{t}$ , and is not associated with any volumetric increase of the material, during climb motion, the dislocation moves out of this slip plane. Due to the high residual pressure in most materials at low



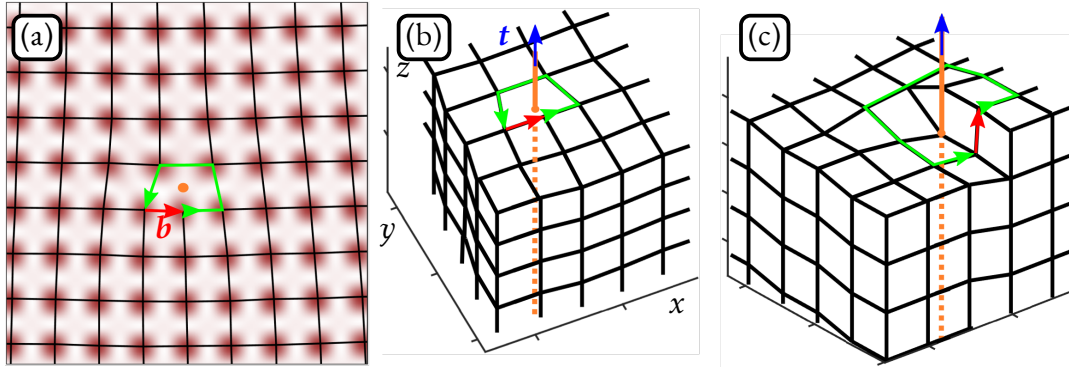


Figure 4.4: (a) The one-body density of a crystalline solid containing an edge dislocation in a 2D square lattice (superimposed), (b) a 3D simple cubic lattice with an edge dislocation ( $\mathbf{b} \perp \mathbf{t}$ ), and (c) a 3D simple cubic lattice with a screw dislocation ( $\mathbf{b} \parallel \mathbf{t}$ ). In all cases, a circulation (green) that is right-handed with respect to the tangent vector  $\mathbf{t}$ , i.e., following a path around the dislocation, gives rise to a connection error: the Burgers vector  $\mathbf{b}$ .

temperatures, the volumetric increase associated with climb motion makes it extremely disfavorable, in addition to it requiring matter transport through, e.g., vacancy diffusion, explaining why climb motion is often completely ignored in discrete models of dislocation dynamics. In fact, one often describes dislocation dynamics in terms of *slip systems*, which is a combination of a slip plane, with normal vector  $\mathbf{n}$ , and Burgers vector  $\mathbf{b}$ , and is often denoted  $(\mathbf{n})[\mathbf{b}]$ . For instance, in Fig. 4.4, the edge dislocation in panel (b) may slip in the  $x$ -direction, defining the slip system  $(0, 1, 0)[1, 0, 0]$ . Figure 4.6 shows the dislocation density in six different slip systems in a sample of olivine. In Paper I, we used the PFC model to calculate the resolved shear stress (RSS) along the three available slip systems in the triangular lattice and found that nucleation happened on the slip plane with the maximal value of the RSS.

### 4.3 The properties of dislocations

To generalize the theory of elasticity to include dislocations, a natural starting point is the displacement field. With the atomic resolution of the crystal lattice in mind, it is evident that displacing a perfect lattice with a lattice vector will lead to no observable change. Thus, the displacement field is only defined up to a lattice vector, and any attempt to show the displacement field in the vicinity of a dislocation will necessarily require a phase cut to get a single-valued field, over which the displacement field jumps a factor of  $\mathbf{b}$ . This is a situation identical to the challenge that arose trying to plot a single-valued version of the vortex in Fig. 3.1, requiring a phase-slip which we removed by clever choice of color scheme. To distinguish between this single-valued, plottable displacement field and the actual displacement field, we will denote the former by  $\mathbf{u}^T$ ; see Fig. 4.7. By naively taking the gradient  $\mathbf{u}^T$ , we obtain what is sometimes referred to as the *total distortion*  $u_{ij}^T = \partial_j u_i^T$



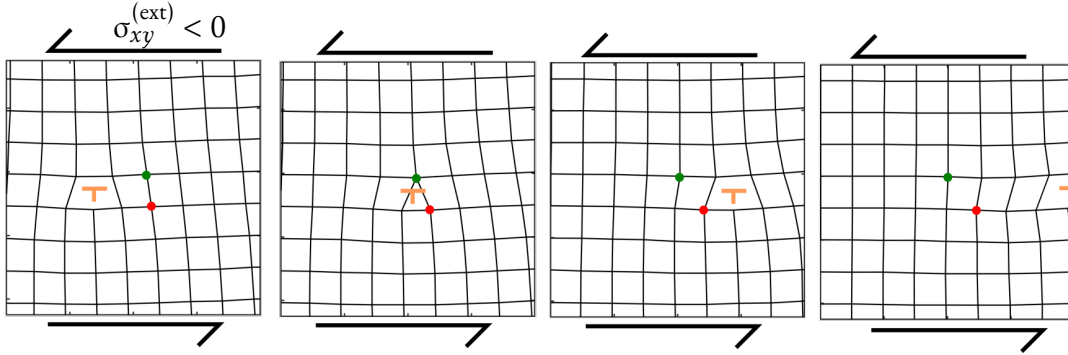


Figure 4.5: The motion of a dislocation along its slip plane, time going from left to right. The external force per area is given by  $\sigma_{xy}^{(\text{ext})} < 0$  on the volume element above the slip plane and  $-\sigma_{xy}^{(\text{ext})} > 0$  on the volume element under the slip plane, causing the motion of the dislocation.

[47]. The singularity that  $\mathfrak{u}^T$  contains along the slip surface is unphysical, as is shown by the added crystal structure superimposed on Fig. 4.7. Being the gradient of a single-valued field, integration of the total distortion yields

$$\oint_{\partial\mathcal{M}} \mathfrak{u}^T \cdot d\mathbf{l} = 0, \quad (4.3.1)$$

where  $\partial\mathcal{M}$  is a loop enclosing the dislocation line oriented in a right-handed manner with respect to  $\mathbf{t} = \mathbf{e}_z$ . A common practice in dislocation theory is to decompose  $\mathfrak{u}^T = \mathfrak{u}^P + \mathfrak{u}^E$  into a plastic distortion  $\mathfrak{u}^P$ , that represents the unphysical phase-slip and an elastic distortion  $\mathfrak{u}^E$ , which measures the physical state of the elastic medium. This leads to

$$\oint_{\partial\mathcal{M}} \mathfrak{u}^E \cdot d\mathbf{l} = -\oint_{\partial\mathcal{M}} \mathfrak{u}^P \cdot d\mathbf{l} = -b_j. \quad (4.3.2)$$

The minus sign in this equation reflects our choice of convention in defining the Burgers vector.

A more careful topological treatment admits that since the displacement field is only defined up to a lattice vector, its actual value is more accurately described as a point in the crystal unit cell with periodic boundary conditions, which is homeomorphic to the 3-torus  $\mathcal{T}^3$ , shown in Fig. 3.6. The distortion calculated from this field coincides with the definition of the elastic distortion, which gives

$$\oint_{\partial\mathcal{M}} d\mathbf{u} = -\mathbf{b}. \quad (4.3.3)$$

Burgers vector definition

From this point on, we will keep to the notion of the displacement field  $\mathbf{u} \in \mathcal{T}^3$  and call  $\mathfrak{u} \equiv \mathfrak{u}^E$  the *distortion*, which gives

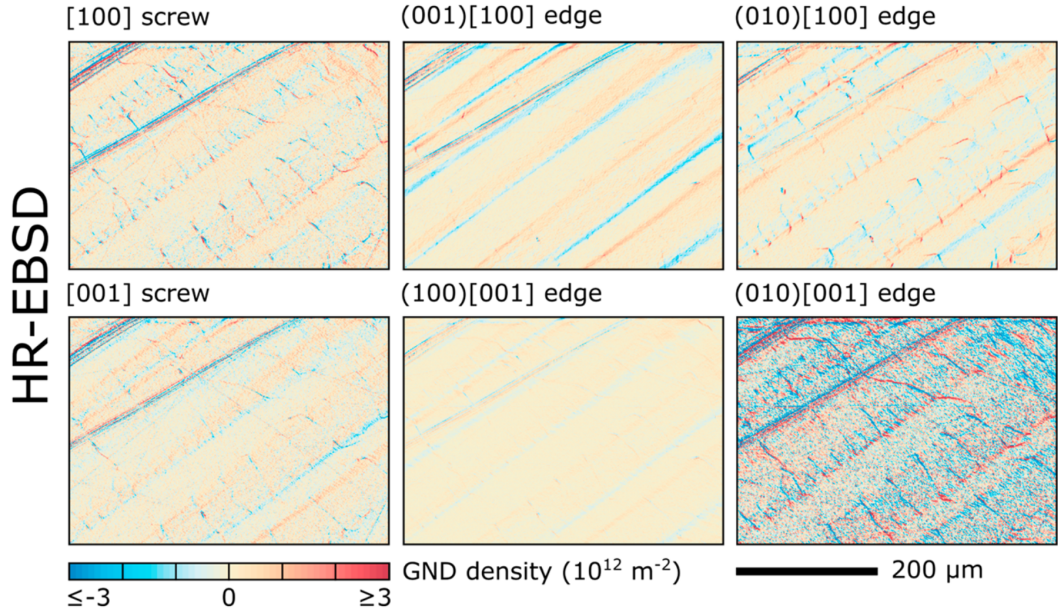


Figure 4.6: 2D slices of the geometrically necessary dislocations, Eq. (4.3.7), in different slip systems in a single crystal of olivine extracted by high-angular resolution electron backscatter diffraction. Reprinted under Creative Commons Attribution License from Ref. [46]. Copyright 2022 by the authors.

$$\oint_{\partial \mathcal{M}} \mathbb{u} \cdot d\mathbf{l} = -\mathbf{b}. \quad (4.3.4)$$

Burgers vector in terms of the distortion

Multiplying by  $-1$  and using Stokes' theorem, we can rewrite this as

$$\oint_{\mathcal{M}} (-\nabla \times \mathbb{u}) \cdot d\mathbf{S} = \mathbf{b}, \quad (4.3.5)$$

which defines the *dislocation density tensor*

$$\alpha = -\nabla \times \mathbb{u} \quad (\alpha_{ij} = -\epsilon_{ikl} \partial_k \mathbb{u}_{jl}). \quad (4.3.6)$$

The dislocation density tensor

This tensor resolves the dislocation density on the atomic level, given an atomic resolution of the distortion  $\mathbb{u}$ . In experiments, however, only a lower-resolution distortion  $\mathbb{u}_{\text{LR}}$  is available, as in Fig. 4.2, which typically is found by mapping the crystal orientation in different parts of the crystal. In this case, the dislocation density will only show those

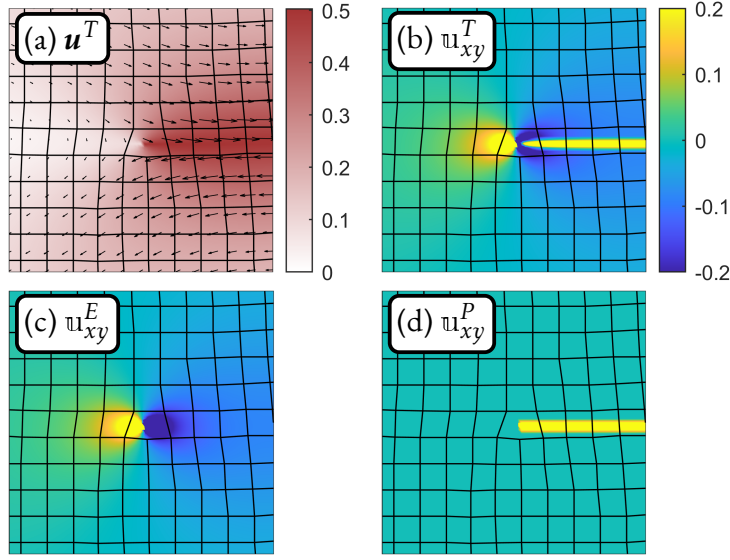


Figure 4.7: (a) (Single-valued) displacement field  $\mathbf{u}^T$  corresponding to a dislocation with Burgers vector  $\mathbf{b} = a_0 \mathbf{e}_x$  with the magnitude shown in units of  $a_0$ , and the  $xy$  component of (b) the total distortion  $\mathfrak{u}^T$ , (c) the elastic distortion  $\mathfrak{u}^E$ , and (d) the plastic distortion  $\mathfrak{u}^P$ . The fields diverge at the dislocation core and at the slip surface so the colorbars have been saturated. The tangent vector is pointing out-of-plane in the  $z$ -direction.

dislocations that are "necessary" for the sample geometry described by  $\mathfrak{u}_{\text{LR}}$ , yielding a quantity called the geometrically necessary dislocation (GND) density

$$\alpha_{\text{GND}} = -\nabla \times \mathfrak{u}_{\text{LR}}. \quad (4.3.7)$$

Even with the definition of  $\mathbf{u}$  as a field in  $\mathcal{T}^3$ , the distortion cannot be written as the gradient of  $\mathbf{u}$  everywhere. To see why, notice that if  $\mathfrak{u}_{ij} = \partial_j u_i$  at some point  $\mathbf{r}$ , then  $\alpha_{ij}(\mathbf{r}) = -\epsilon_{ikl} \partial_k \partial_l u_j = 0$ . Thus, the definition of  $\mathfrak{u}$  as the gradient of  $\mathbf{u}$  is only valid away from dislocations. In these dislocation-free regions, the distortion is fully determined by the three independent components of  $\mathbf{u}$ , which means that the components of  $\mathfrak{u}$  and, in particular,  $\epsilon$  are related. These relations are called "compatibility relations," and we say that the strain  $\epsilon$  is "compatible" if they hold. Incompatibility is related to the fact that the very notion of a displacement field breaks down at the dislocation core. However, it is possible to extract an average value of  $\mathfrak{u}_{\text{LR}}$  in a subregion of a crystal by, for instance, looking at the diffraction pattern of the subregion since this is related to the state of strain and rotation. This may subsequently be used to construct  $\alpha_{\text{GND}}$ . For instance, the plot of the dislocation density in Fig. 4.6 was found by measuring the state of rotation  $\mathbf{\Omega}$ , Eq. (4.1.5), in the olivine relative to a reference point, which was subsequently used to calculate the rotation tensor  $\omega_{\text{LR}}$ . Then,  $\alpha_{\text{GND}}$  was calculated directly from  $\omega_{\text{LR}}$ , neglecting the contribution to  $\alpha_{\text{GND}}$  from the undetermined strain  $\epsilon_{\text{LR}}$ . Neglecting the strain in this case was justified by estimating  $\epsilon_{\text{LR}}$  to be 1% of  $\omega_{\text{LR}}$  [46]. This shows that, in some sense, the distortion is a more fundamental quantity than the displacement field, and Eq. (4.3.4) holds even

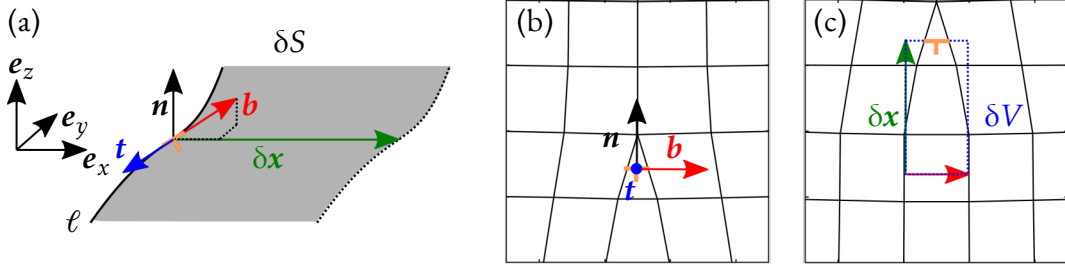


Figure 4.8: As (a) the dislocation line  $\ell$  moves a distance  $\delta\mathbf{x}$ , it spans a surface  $\delta S$  over which a slip  $-\mathbf{b}$  occurs, where  $\mathbf{b}$  is the Burgers vector. Note that  $\mathbf{b}$  is not necessarily aligned with the coordinates. In the case of (b)-(c) climb motion, where  $\mathbf{n} \cdot \mathbf{b} \neq 0$ , the motion is associated with a local increase in volume  $\delta V$ .

in places where there is a high density of dislocations, provided the rhs. be replaced by the sum of the Burgers vectors in the region. The field theory treating the distortion as a coarse-grained quantity directly is called field dislocation mechanics and will be presented in Sec. 4.5.

To understand the forces that act on dislocations, consider a dislocation line  $\ell$  with Burgers vector  $\mathbf{b}$  and tangent vector  $\mathbf{t}$  at the point  $\mathbf{r}' \in \ell$ , given by

$$\alpha_{ij} = b_j \int_{\ell} d\ell \delta^{(3)}(\mathbf{r} - \mathbf{r}') t_i, \quad (4.3.8)$$

The dislocation density for a dislocation line

that moves a distance  $\delta\mathbf{x}$ . Without loss of generality, we may align our coordinates so that  $\delta\mathbf{x}$  is along the x-axis and  $\mathbf{t}$  along the out-of-plane, negative y-axis; see Fig. 4.8. The motion of the dislocation spans a certain area  $\delta S$ , which has a unit vector  $\mathbf{n}$  perpendicular to  $\delta\mathbf{x}$  and  $\mathbf{t}$ , shown along the z-axis in Fig. 4.8.  $\delta S$  may be thought of as a 2D infinitesimal change in some 2D surface  $S$  bounded by the 1D line  $\ell$ . The motion of the dislocation is associated with the slip of  $-\mathbf{b}$  over the surface  $\delta S$ ; see Fig. 4.5. The displacement slip during the motion of the dislocation is thus extended over the area  $\delta S$  and if  $\sigma^{(\text{ext})}$  is the external stress acting on the dislocation, then the work done is given by

$$\begin{aligned} \delta W &= \int_{\ell} \sigma_{ij}^{(\text{ext})} n_j (-b_i) d(\delta S) = - \int_{\ell} d\ell \sigma_{ji}^{(\text{ext})} b_i \epsilon_{jkl} t_k \delta x_l = \int_{\ell} d\ell \epsilon_{lki} t_k (\sigma_{ij}^{(\text{ext})} b_j) \delta x_l \\ &= \int_{\ell} d\ell (\mathbf{t} \times (\sigma^{(\text{ext})} \cdot \mathbf{b})) \cdot \delta\mathbf{x}, \quad (4.3.9) \end{aligned}$$

where we have utilized the fact that the surface element  $\mathbf{n}d(\delta S)$  can be written as  $d\ell(\mathbf{t} \times \delta\mathbf{x})$ , and the symmetry of the stress tensor, in going from the second to third equality, and standard index manipulation in arriving at the final expression. This equation represents

all the work that is done by the external force at the slip surface over which the dislocation moves. This defines the Peach-Koehler force

$$\mathbf{F}_{PK} = \mathbf{t} \times (\boldsymbol{\sigma}^{(\text{ext})} \cdot \mathbf{b}), \quad (4.3.10)$$

The Peach-Koehler (PK) force

which is the dissipated energy associated with a motion  $\delta \mathbf{x}$  of the dislocation line. It takes its name from its inception in the seminal paper by Milton O. Peach and James S. Koehler [48]. Note that the stress in this derivation is the external stress acting *on* the dislocation, and not the stress induced by the dislocation itself. Some of the work associated with the PK force is due to the climb motion of the dislocation. In this case, where  $\mathbf{b} \cdot \mathbf{n} \neq 0$ , there is a volumetric change  $\delta V = (\mathbf{t} \times \mathbf{b}) \cdot \delta \mathbf{x} d\ell$  associated with the motion, as shown in Fig. 4.8(b-c). Since the external pressure is given by  $p = \frac{1}{d} \text{Tr}(\boldsymbol{\sigma}^{(\text{ext})})$ , we conclude that the work done by the external force due to volumetric changes is given by

$$\delta W^V = \int_{\ell} d\ell \frac{1}{d} \text{Tr}(\boldsymbol{\sigma}^{(\text{ext})}) (\mathbf{t} \times \mathbf{b}) \cdot \delta \mathbf{x} = \int_{\ell} d\ell (\mathbf{t} \times (\frac{1}{d} \text{Tr}(\boldsymbol{\sigma}^{(\text{ext})}) \mathbb{1} \cdot \mathbf{b})) \cdot \delta \mathbf{x}, \quad (4.3.11)$$

where  $\mathbb{1}_{ij} = \delta_{ij}$  is the identity tensor. It was argued in Ref. [49] that this contribution to the work done is more naturally thought of as the general work the external force does on the elastic field and should be excluded from the stress appearing in the PK force, in which case the deviatoric stress  $\boldsymbol{\sigma}^{(\text{ext})'} = \boldsymbol{\sigma}^{(\text{ext})} - \frac{1}{d} \text{Tr}(\boldsymbol{\sigma}^{(\text{ext})}) \mathbb{1}$  should replace  $\boldsymbol{\sigma}^{(\text{ext})}$  in Eq. (4.3.10).

There are two interesting things to note about the sign of the PK force. Firstly, given that the dislocation tangent vector and Burgers vector are defined only up to a common sign, the PK force should be invariant under simultaneously changing  $\mathbf{b} \rightarrow -\mathbf{b}$  and  $\mathbf{t} \rightarrow -\mathbf{t}$ , which is true. Secondly, and maybe more alarmingly, we stated that the Burgers vector is given as the connection error after a circulation, as in Fig. 4.4, i.e., the lattice vector difference between the ending point and the starting point. This, however, is only a convention, and some sources use the opposite definition, where the Burgers vector indicates the lattice displacement from the *starting* point of the circulation to the ending point. The same type of dislocation, *with the same* tangent vector, would then be given the opposite Burgers vector charge. Yet, this can not mean that the force on the dislocation changes direction. The resolution to this seeming paradox is that in calculating the dissipated energy, we accounted for a slip of  $-\mathbf{b}$  during the dislocation motion, informed by Fig. 4.5. Given a different convention for the Burgers vector sign, this slip would instead be  $\mathbf{b}$ . The calculation would yield the same expression of the PK force but with the opposite sign, which in much of the literature is expressed as the cross-product in the inverse order. As a sanity check, consider the dislocation in Fig. 4.5, which has  $\mathbf{b} = a_0 \mathbf{e}_x$ ,  $\mathbf{t} = \mathbf{e}_z$  and only  $\sigma_{xy}^{(\text{ext})} = \sigma_{yx}^{(\text{ext})}$  as components. Then  $\mathbf{F}_{PK} = a_0 \mathbf{e}_z \times (\boldsymbol{\sigma}^{(\text{ext})} \cdot \mathbf{e}_x) = a_0 \sigma_{yx}^{(\text{ext})} \mathbf{e}_z \times \mathbf{e}_y = -a_0 \sigma_{xy}^{(\text{ext})} \mathbf{e}_x$ , and since the applied stress  $\sigma_{xy}^{(\text{ext})} < 0$ , the PK force will move the dislocation to the right, as indicated in the figure.

By multiplying Eq. (4.3.3) with a reciprocal lattice vector  $-\mathbf{q}^{(n)}$  of the corresponding lattice, we find

$$\oint_{\partial\mathcal{M}} d(-\mathbf{u} \cdot \mathbf{q}^{(n)}) = \mathbf{q}^{(n)} \cdot \mathbf{b}. \quad (4.3.12)$$

Since  $\mathbf{b}$  is a lattice vector, we know from Sec. 2.2 that  $\mathbf{q}^{(n)} \cdot \mathbf{b} = 2\pi s_n$ , where  $s_n$  is an integer. This simple argument shows that the  $\theta_n \equiv -\mathbf{q}^{(n)} \cdot \mathbf{u}$  is a  $S^1$  field with corresponding vortex defects. Since there are three independent reciprocal lattice vectors, we get a sense of how defects in  $\mathcal{T}^3$  are described in terms of defects of its factor topologies  $S^1$ . In Paper IV, we made this connection exact.

#### 4.4 Hydrodynamics of crystals

The emergence of the displacement field degree of freedom when a liquid solidifies can be seen as a breaking of the translational symmetry that exists in the liquid state. In the following, we will present the hydrodynamic framework for a crystal, following Ref. [25]. We consider a small piece of the crystal with volume  $V$ , in which we can assume that local processes are happening so fast that the system is in local thermodynamic equilibrium. Hydrodynamics is a theory of long-wavelength disturbances, which are close to equilibrium. While the microscopic density  $\tilde{\rho}$  has modulations due to the arrangement of atoms, on a larger scale, these are not visible, other than from the overall displacement field  $\mathbf{u}$ . In this section, we will introduce the notion of coarse-graining, in which a field goes from being microscopically varying, which is often indicated with the overset symbol  $\sim$ , to slowly varying. In the case of the microscopic density  $\tilde{\rho} \rightarrow \rho$ , this operation is given by

$$\rho = \langle \tilde{\rho} \rangle \equiv \int d^d r' \mathcal{K}(\mathbf{r} - \mathbf{r}') \tilde{\rho}(\mathbf{r}'), \quad (4.4.1)$$

Coarse-graining

where  $\mathcal{K}(\mathbf{r}' - \mathbf{r})$  is a Gaussian kernel given by

$$\mathcal{K}(\mathbf{r}' - \mathbf{r}) = \frac{1}{(2\pi w^2)^{d/2}} \exp\left(-\frac{(\mathbf{r} - \mathbf{r}')^2}{2w^2}\right), \quad (4.4.2)$$

where  $w \sim V^{1/d}$  is the width over which this coarse-graining happens, and  $d$  is the spatial dimension. We will refer to  $\rho$  as the coarse density and  $\tilde{\rho}$  as the microscopic density.

Two very important properties of the coarse-graining operation is that it commutes with differentiation and integration in the following senses:

**Differentiation:** For any function  $\tilde{f}$ , we have

$$\begin{aligned}\langle \nabla \tilde{f} \rangle &= \int d^d r' \mathcal{K}(\mathbf{r}' - \mathbf{r}) \nabla' \tilde{f}(\mathbf{r}') = - \int d^d r' \nabla' (\mathcal{K}(\mathbf{r}' - \mathbf{r})) \tilde{f}(\mathbf{r}') \\ &= \int d^d r' \nabla (\mathcal{K}(\mathbf{r}' - \mathbf{r})) \tilde{f}(\mathbf{r}') = \nabla \int d^d r' \mathcal{K}(\mathbf{r}' - \mathbf{r}) \tilde{f}(\mathbf{r}') = \nabla \langle \tilde{f} \rangle,\end{aligned}\quad (4.4.3)$$

where we have used integration by parts in going from the second to third equality and that  $\nabla' \mathcal{K}(\mathbf{r} - \mathbf{r}') = -\nabla \mathcal{K}(\mathbf{r} - \mathbf{r}')$  in going from the third to the fourth. This means that a global derivative can be pulled out of the coarse-graining operation.

**Integration:** For any function  $\tilde{f}$ , we have

$$\begin{aligned}\int d^d r \langle \tilde{f} \rangle &= \int d^d r \int d^d r' \mathcal{K}(\mathbf{r} - \mathbf{r}') \tilde{f}(\mathbf{r}') = \int d^d r' \tilde{f}(\mathbf{r}') \int d^d r \mathcal{K}(\mathbf{r} - \mathbf{r}') \\ &= \int d^d r' \tilde{f}(\mathbf{r}') = \int d^d r \tilde{f},\end{aligned}\quad (4.4.4)$$

since  $\mathcal{K}(\mathbf{r} - \mathbf{r}')$  is normalized. Thus, the integrand can always be coarse-grained without changing the resulting integral. These properties are used throughout Papers II and IV.

Changes in the local entropy density  $s = S/V$  are brought on by changes in the energy density  $\epsilon$ , the coarse density  $\rho$ , the momentum density  $\mathbf{g}$  and the strain field  $\epsilon$  through

$$T ds = d\epsilon - \mu_c d\rho - \mathbf{v} \cdot d\mathbf{g} - \mathbb{h} : d\epsilon, \quad (4.4.5)$$

where  $\mu_c$  is the coarse chemical potential,  $\mathbf{v}$  is the velocity of the medium and

$$\mathbb{h}_{ij} = \left. \frac{\partial f}{\partial \epsilon_{ij}} \right)_{T, \rho, \mathbf{g}} \quad (4.4.6)$$

The strain conjugate (stress) at constant density

is the conjugate to the strain  $\epsilon_{ij}$  and  $f$  is the free energy density  $f = \epsilon - Ts$ . We can connect  $\mathbb{h}$  to the total stress tensor  $\sigma$  by performing a variational procedure, considering the work done by a virtual displacement  $\delta \mathbf{x}$ . The change in free energy within a volume  $\Omega$  is given by the work done

$$\delta \mathcal{F}_\Omega = \int_{\partial\Omega} dS_j \sigma_{ij} \delta x_i - \int_\Omega d^3 r \partial_j \sigma_{ij} \delta x_i. \quad (4.4.7)$$

Under such a deformation, the volume element, coarse density, and strain transform to first order in  $\delta \mathbf{x}$  as

$$d^3 r \rightarrow (1 + \partial_k \delta x_k) d^3 r, \quad (4.4.8)$$



$$\rho \rightarrow (1 - \partial_k \delta x_k) \rho, \quad (4.4.9)$$

$$\varepsilon_{ij} \rightarrow \varepsilon_{ij} + \partial_{(i} \delta x_{j)}. \quad (4.4.10)$$

As shown in Ref. [25], by varying the free energy  $\mathcal{F}_\Omega = \int_\Omega d^3 r f$  under these transformations, we recover Eq. (4.4.7) with the following expression for the stress tensor

$$\sigma_{ij} = \left( f - \rho \frac{\partial f}{\partial \rho} \Big|_\varepsilon \right) \delta_{ij} + \frac{\partial f}{\partial \varepsilon_{ij}} \Big|_\rho. \quad (4.4.11)$$

The stress tensor

We identify the latter part of this expression as lh.

Given the expression for the force density, Eq. (4.1.15), we can write the equations of motion for the displacement field in a perfectly elastic medium, namely Newton's second law

$$\rho \partial_t^2 u_i = \partial_j \sigma_{ij}. \quad (4.4.12)$$

For the isotropic case, we have

$$\sigma_{ij} = (\lambda \delta_{ij} \delta_{kl} + 2\mu \delta_{i(k} \delta_{l)j}) \partial_l u_k = \lambda \partial_k u_k \delta_{ij} + \mu \partial_j u_i + \mu \partial_i u_j, \quad (4.4.13)$$

so we get

$$\rho \partial_t^2 u_i = (\lambda + \mu) \partial_i \partial_k u_k + \mu \partial_k \partial_k u_i. \quad (4.4.14)$$

To analyze the motion, we Fourier transform in time and space

$$\mathbf{u}_\mathbb{f}(\mathbf{k}, \omega) = \int d^d r \int_{-\infty}^{\infty} dt e^{i(\omega t - \mathbf{k} \cdot \mathbf{r})} \mathbf{u}(\mathbf{r}, t), \quad (4.4.15)$$

which results in

$$-\rho \omega^2 u_{\mathbb{f}i} = -(\lambda + \mu) k_i k_k u_{\mathbb{f}k} - \mu \mathbf{k}^2 u_{\mathbb{f}i}. \quad (4.4.16)$$

We decompose this into independent components  $\mathbf{u}_\mathbb{f} = \mathbf{u}_\mathbb{f}^T + \mathbf{u}_\mathbb{f}^L$ , namely the transversal,  $\mathbf{u}_\mathbb{f}^T \perp \mathbf{k}$ , and longitudinal,  $\mathbf{u}_\mathbb{f}^L \parallel \mathbf{k}$ , component, which leads to

$$-\rho \omega^2 (u_{\mathbb{f}i}^T + u_{\mathbb{f}i}^L) = -(\lambda + \mu) k_i k_k u_{\mathbb{f}k}^L - \mu \mathbf{k}^2 (u_{\mathbb{f}i}^T + u_{\mathbb{f}i}^L). \quad (4.4.17)$$

This gives, for the transversal mode

$$\rho \omega_T^2 u_{\mathbb{f}i}^T = \mu \mathbf{k}^2 u_{\mathbb{f}i}^T, \quad (4.4.18)$$

with dispersion relation

$$\rho \omega_T^2 = \mu \mathbf{k}^2 \Rightarrow \omega_T = \pm \sqrt{\frac{\mu}{\rho}} |\mathbf{k}|, \quad (4.4.19)$$



and for the longitudinal mode

$$\rho\omega_L^2 u_{fi}^L = (\lambda + \mu)k_i k_k u_{fk}^L + \mu\mathbf{k}^2 u_{fi}^L, \quad (4.4.20)$$

with dispersion relation

$$\rho\omega_L^2 = (\lambda + 2\mu)\mathbf{k}^2 \Rightarrow \omega_L = \pm\sqrt{\frac{\lambda + 2\mu}{\rho}}|\mathbf{k}|. \quad (4.4.21)$$

The dispersion relations correspond to sound waves traveling without dissipation and velocities given by  $\sqrt{\mu/\rho}$  and  $\sqrt{(\lambda + 2\mu)/\rho}$  for transversal and longitudinal waves, respectively. Dissipation can be added by including a solid viscosity tensor on the rhs. of Eq. (4.4.12) [25]. These wave solutions correspond to peaks in the response function for  $\mathbf{u}$ . These peaks are called *modes* and describe how perturbations of the ground state spread in the system. Each component  $u_i$  has two modes, the positive and negative solution. Since there are one longitudinal and two transversal components of  $\mathbf{u}$  in three dimensions, we end up with 6 modes in total. There are as many modes as independent hydrodynamic variables in the system. From Eq. (4.4.5), we see that these are  $\epsilon$ ,  $\rho$ ,  $\{g_i\}_{i=1}^3$  and  $\{u_i\}_{i=1}^3$ . Thus we expect eight modes, consisting of the six aforementioned modes associated with sound waves, heat diffusion, and a vacancy diffusion mode, which is present since the coarse density  $\rho$  and displacement field can evolve independently of each other. Consistent use of coarse-graining to develop a hydrodynamic PFC theory was done in Paper IV.

## 4.5 Multiscale modeling of materials

While classical dislocation theory, as given in Ref. [47], is sufficient for small systems and single dislocations, a multiscale approach to plasticity requires several methods operating on different scales. If the spatiotemporal scale for the problem at hand is sufficiently small, such as crack propagation problems and fast indentation experiments, it becomes feasible to model each atom and its interactions explicitly, i.e., by molecular dynamics. At larger spatiotemporal scales, other methods are available, such as dynamical DFT [16] or Monte Carlo methods [50]. The PFC model, as will be introduced in Chapter 5, is an effective field theory meant to operate at time scales longer than those accessible to dynamical DFT.

Since dislocations are the primary drivers of plastic deformation in single crystals, an effort started in the 1980s to model dislocations as discrete identities interacting through their induced elastic fields, an approach come to be known as discrete dislocation dynamics (DDD) [17]. This approach uses continuum mechanics and dislocation theory to derive laws of motion, nucleation criteria, and recombination rules for dislocation lines. It has since become an essential tool for the simulation of plastic deformation on the mesoscale ( $\sim \mu\text{m}$ ) [13]. The lower length scale models serve as input to this effective theory, and in particular, in Paper III, we used the PFC model to derive that the dislocations move in an overdamped fashion subject to the PK force, Eq. (4.3.10), and found an explicit expression for the mobility.

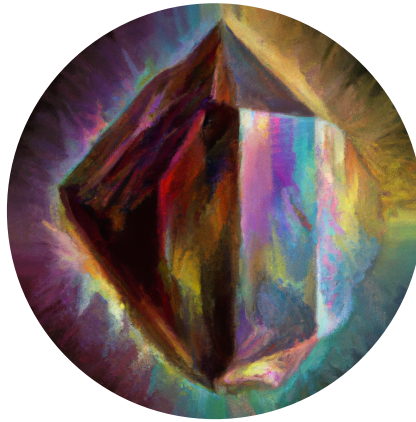
As an alternative approach to resolving the individual dislocations, field dislocation mechanics (FDM) aims to simulate the dislocation density  $\alpha$  as a smooth coarse-grained field [51]. In its complete form, the formalism allows the modeling of sizeable irreversible material deformations, including both inertial and dissipative effects. The primary variable of interest is thus not the "total" single-valued displacement field as in many of the traditional treatments of plasticity, but the smooth and single-valued distortion  $\mathfrak{u}$ . Of particular relevance to this thesis is the analysis of relating the dislocation density to the stress under periodic boundary conditions. If the dislocation density tensor  $\alpha$  is taken as in Eq. (4.3.6), i.e., a source for the distortion  $\mathfrak{u}$ , it only defines  $\mathfrak{u}$  up to a gradient of a vector field. Thus, another equation is required to fully determine  $\mathfrak{u}$ . In FDM, this additional information is provided by the condition of mechanical equilibrium

$$\nabla \cdot (\mathcal{C} : \mathfrak{u}) = \mathbf{0}. \quad (4.5.1)$$

The general method of solving Eqs. (4.3.6) and (4.5.1) for  $\mathfrak{u}$  on a periodic medium is given in Ref. [52] and numerical details are given in Appendix A.2.2. This method of finding the equilibrium elastic fields provided the dislocation density tensor as a source, was used in Paper III to verify the simulations in the PFC framework.

## CHAPTER 5

### *The phase-field crystal*



“ [T]he PFC model [...] incorporates most of the essential physics required to handle freezing: it is atomistic, anisotropies and elasticity are automatically there [...].

- Heike Emmerich et al. [53]

Having laid the framework for how crystalline symmetry, topology, and mean-field models work together to describe the structure of ordered matter, we turn to the specific model for crystal structure, which is the foundation of this thesis. The phase-field crystal was introduced by Elder and Grant in Ref. [54] by coupling a free energy description of the Rayleigh-Benard convection problem [55] with conserved dynamics. The phase-field  $\psi$  was introduced as the deviation from the average density. It was then argued that introducing a factor similar to  $(q_0^2 + \nabla^2)$  is the simplest way to include the peaks in the structure factor at  $q_0$  wavelengths associated with the emergence of periodic modulations. The proposed free energy was given in dimensionless units as

$$\mathcal{F}[\psi] = \int d^2r \frac{1}{2} (\mathcal{L}_1 \psi)^2 + \frac{r}{2} \psi^2 + \frac{1}{4} \psi^4, \quad (5.0.1)$$

The PFC free energy

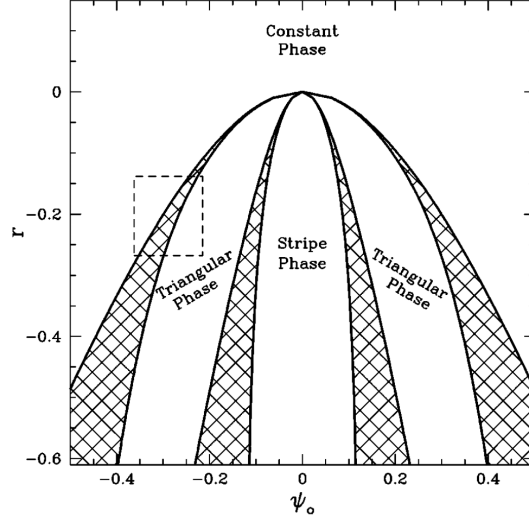


Figure 5.1: Reprinted figure with permission from Ref. [54]. Copyright 2004 by the American Physical Society.

where  $r$  is a parameter called the quenching depth, which controls the order-disorder transition, and  $\mathcal{L}_1 = 1 + \nabla^2$ . The conserved dynamics were given by

$$\partial_t \psi = \nabla^2 \frac{\delta \mathcal{F}}{\delta \psi}, \quad (5.0.2)$$

The PFC evolution equation

which is a simplified version of the central equation from dynamical density functional theory, with constant density-independent mobility approximation [16]. Given the conserved dynamics, the average density

$$\psi_0 = \frac{1}{V} \int d^2 r \psi, \quad (5.0.3)$$

The PFC average density

where  $V$  is the simulation volume, also becomes a parameter, and the free energy for different values of  $r$  and  $\psi_0$  are minimized by different lattice structures. The choice of conservative dynamics is related to the notion that the PFC represents a one-body density. By calculating the free energy associated with different symmetries near the critical point and using Maxwell construction to find the regions of coexistence, Elder and Grant mapped the phase diagram of the simplified model, which is shown in Fig. 5.1. It was shown that elastic properties depend solely on the periodic nature of the density field, thus motivating the introduction of such a simplified model. The model captured the essential features of

the density modulations with only two free parameters, an approach that, in many ways, echoes how the simple addition of two parameters to the ideal gas law, yielding the Van der Waals equation, could single-handedly explain the gas-liquid transition using methods from statistical mechanics [56]. While introduced on phenomenological grounds, it was later shown that the model could be derived from the Smoluchowski equation via dynamical DFT [57].

The computational advantage of the PFC model is two-fold. Firstly, by working directly with the one-body density, thermal vibrations are effectively averaged out, allowing us to reach diffusive time scales directly, a feature shared with dynamical DFT theory. Secondly, in contrast to DFT, the interaction part of the free energy is written in terms of a local gradient expansion, which allows for using powerful spectral methods to reach longer time scales. In the years following its introduction, the model was put to use to study a multitude of complex out-of-equilibrium processes for crystalline lattices in general (see Ref. [53] for review) and mesoscale plasticity in particular. Examples of the latter include elasticity theory [54, 58], dislocation dissociation [59], creep [60], boundary-driven grain migration [61, 62, 63], dislocation dynamics [64, 65, 20] and dislocation nucleation [66, 1]. In this chapter, we will discuss the interpretation of the PFC, how different symmetries arise, and look at the time-scale problem for the relaxation of elastic waves.

## 5.1 Material properties and other symmetries

Following its inception, numerous extensions of the PFC were derived to accommodate for other lattice symmetries and fit material properties. While the original unscaled version, Eq. (5.0.1), contained two independent parameters  $r$  and  $\psi_0$ , its scaled counterpart was fitted to iron in Ref. [67] by comparing the PFC model to the Ginzburg-Landau theory presented in Sec. 2.2 and comparing with molecular dynamics simulations. Several other works have made similar efforts [68, 69, 70, 71].

While material fitting is a worthwhile endeavor to make quantitative predictions, the primary focus of this thesis and the papers on which it is built is the symmetry of the ground state. In terms of symmetry, the model was quickly extended to 3D materials with bcc [67] and fcc structure [72] by adding more derivatives to the free energy, which favor second mode peaks in the reciprocal lattice matching that of the target lattice. Other approaches to creating different symmetries exist, such as adding exponential peaks in the reciprocal space of the correlation function [69]. The systematic exploration of adding higher order derivatives to the free energy, however, is called the multimode PFC model [73, 29] and is the approach followed in this thesis. To promote, for instance, a square lattice, we include the factor  $\mathcal{L}_2$  in the derivative operator, giving

$$\mathcal{F}_{\text{sq}}[\psi] = \int d^2r \frac{1}{2} (\mathcal{L}_1 \mathcal{L}_2 \psi)^2 + \frac{r}{2} \psi^2 + \frac{1}{4} \psi^4, \quad (5.1.1)$$

where  $\mathcal{L}_X = \mathbf{X} + \nabla^2$ . In Paper II, we exploited this point of view to construct and analyze the elastic properties of PFC with free energies that produce different phases. In addition

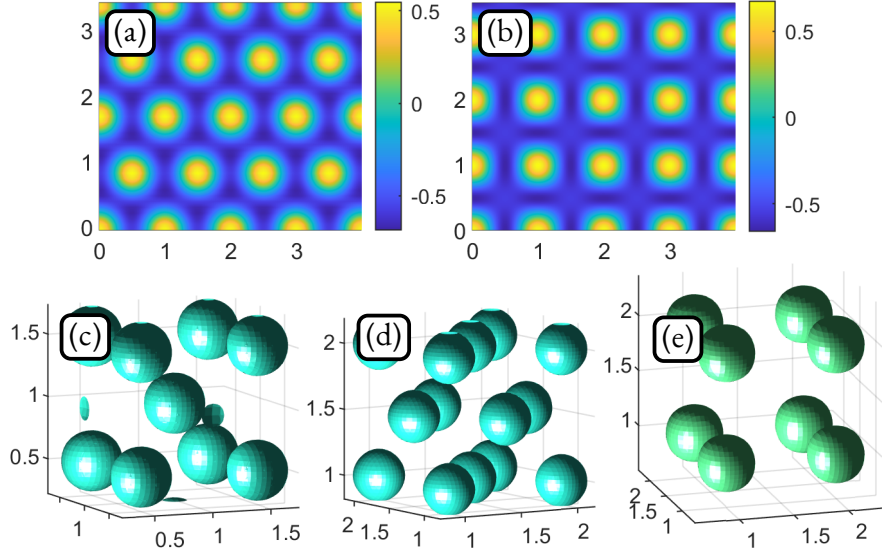


Figure 5.2: Equilibrium states  $\psi$  corresponding to different crystalline symmetries at parameters  $(r, \psi_0)$  producing a stable state. All fields are produced with  $r = -0.3$  and  $\psi_0 = -0.3$  ( $\psi_0 = -0.325$ ) for the 2D (3D) simulations. For the 3D fields, isosurfaces are drawn at  $\frac{\max[\psi] - \min[\psi]}{2}$ , where  $\min[\psi]$  ( $\max[\psi]$ ) is the minimum (maximum) value of  $\psi$  in the domain. Axes are in units of  $a_0$ , the lattice constant, and the panels show (a) triangular symmetry, (b) square symmetry, (c) bcc symmetry with  $(\min[\psi], \max[\psi]) = (-0.6309, 0.7445)$ , (d) fcc symmetry with  $(\min[\psi], \max[\psi]) = (-0.7055, 0.8025)$ , and (e) simple cubic symmetry with  $(\min[\psi], \max[\psi]) = (-0.5186, 0.9684)$ .

to the aforementioned triangular symmetry of Eq. (5.0.1) and  $\mathcal{F}_{\text{sq}}$ , we have

$$\mathcal{F}_{\text{bcc}}[\psi] = \int d^3r \frac{1}{2} (\mathcal{L}_1 \psi)^2 + \frac{r}{2} \psi^2 + \frac{1}{4} \psi^4, \quad (5.1.2)$$

$$\mathcal{F}_{\text{fcc}}[\psi] = \int d^3r \frac{1}{2} (\mathcal{L}_1 \mathcal{L}_{4/3} \psi)^2 + \frac{r}{2} \psi^2 + \frac{1}{4} \psi^4, \quad (5.1.3)$$

and

$$\mathcal{F}_{\text{sc}}[\psi] = \int d^3r \frac{1}{2} (\mathcal{L}_1 \mathcal{L}_2 \mathcal{L}_3 \psi)^2 + \frac{r}{2} \psi^2 + \frac{1}{4} \psi^4, \quad (5.1.4)$$

producing, for certain parameter ranges  $(r, \psi_0)$ , stable bcc, fcc and simple cubic phases, respectively. Whereas the first two were extensively studied in Refs. [67, 72], where phase diagrams and stability conditions were derived, the last example has seen little exploration. It was used in Paper II to study the elastic properties of the simple cubic phase. Fig. 5.2 shows the different symmetries considered in this thesis.

## 5.2 The configurational stress

In Ref. [54], Elder and Grant considered the ground state and applied certain transformations given by bulk, shear, and deviatoric displacement fields  $\mathbf{u}$ , expanding the free energy in the resulting distortion. By comparing the expression with Eq. (4.1.10), they found the elastic constants, matching those expected from the isotropic nature of triangular lattice symmetry. Later, in Ref. [20], an expression for the stress tensor was derived from varying the free energy with respect to coordinate distortions, finding elastic constants matching those of Ref. [54]. In both these approaches, the stress was derived for the particular example of the original PFC model, and the fact that a mass-conserving deformation must also change the *value* of the density, to keep the total mass  $\int d^d r \psi$  constant, was neglected.

These issues were addressed in Paper II, where we introduced a general variational procedure to determine the stress in any Ginzburg-Landau density field theory with an arbitrary number of gradients. The stress tensor of the PFC model of Eq. (5.0.1) is given by

$$\sigma_{ij} = \langle (\tilde{f} - \tilde{\mu}_c \psi) \rangle \delta_{ij} - 2 \langle (\mathcal{L}_1 \psi) \partial_{ij} \psi \rangle, \quad (5.2.1)$$

The stress tensor in the 2D triangular PFC

where  $\tilde{f}$  is the free energy density, the integrand of Eq. (5.0.1), and  $\tilde{\mu}_c = \frac{\delta \mathcal{F}}{\delta \psi}$ . A significant advantage compared to the stress derived in Ref. [54], is that the procedure is valid for any out-of-equilibrium state  $\psi$ , including defected states, polycrystalline materials and other symmetries, assuming that the adiabatic approximation mentioned in Sec. 2.1 holds. To illustrate this point, in Fig. 5.3, we show the  $\sigma_{xy}$  component of the stress tensor for three very different out-of-equilibrium configurations of the phase-field.

## 5.3 The few-mode approximation

As discussed, a perfectly symmetric lattice can be written in a Fourier series of the reciprocal lattice, Eq. (2.2.4). In the case of the PFC, near the critical point  $r = 0$ , the equilibrium states can be approximated by only a few reciprocal lattice vectors. The five different



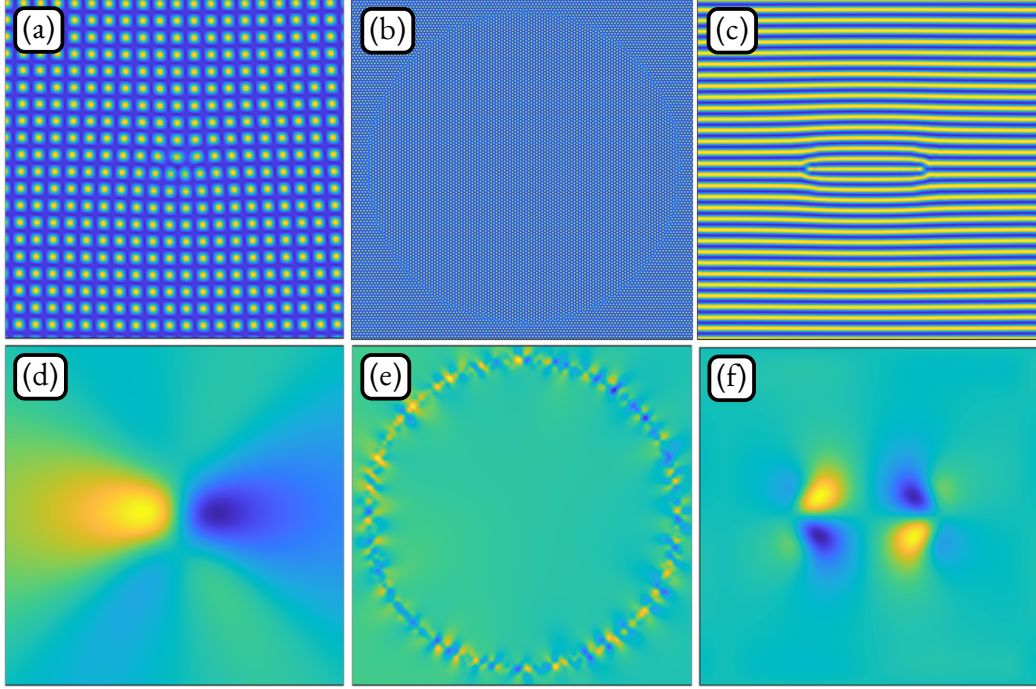


Figure 5.3: Different phase-field configurations and their corresponding stresses. (a) A dislocation in the square PFC model, Eq. (5.1.1), with  $(r, \psi_0) = (-0.3, -0.3)$ , (b) an inclusion in the triangular PFC model, Eq. (5.0.1), with  $(r, \psi_0) = (-0.3, -0.3)$  (c) a dislocation dipole in the stripe phase in the PFC model of Eq. (5.1.1) with  $(r, \psi_0) = (-0.3, 0)$ . (d-f) Stresses  $\sigma_{xy}$ , Eq. (6.2.6), for the configurations shown in (a-c), respectively.

symmetries shown in Fig. 5.2 have these sets of smallest reciprocal lattice vectors

$$\begin{aligned}
 \mathcal{R}_{\text{tri}}^{(1)} &= \left\{ \begin{array}{l} \mathbf{q}^{(1)} = (0, 1) \\ \mathbf{q}^{(2)} = (\sqrt{3}/2, -1/2) \\ \mathbf{q}^{(3)} = (-\sqrt{3}/2, -1/2) \\ \mathbf{q}^{(-1)}, \mathbf{q}^{(-2)}, \mathbf{q}^{(-3)} \end{array} \right\} & \mathcal{R}_{\text{sq}}^{(1)} &= \left\{ \begin{array}{l} \mathbf{q}^{(1)} = (1, 0) \\ \mathbf{q}^{(2)} = (0, 1) \\ \mathbf{q}^{(-1)}, \mathbf{q}^{(-2)} \end{array} \right\} \\
 \mathcal{R}_{\text{bcc}}^{(1)} &= \left\{ \begin{array}{l} \mathbf{q}^{(1)} = (0, 1, 1)/\sqrt{2} \\ \mathbf{q}^{(2)} = (1, 0, 1)/\sqrt{2} \\ \mathbf{q}^{(3)} = (1, 1, 0)/\sqrt{2} \\ \mathbf{q}^{(4)} = (0, -1, 1)/\sqrt{2} \\ \mathbf{q}^{(5)} = (-1, 0, 1)/\sqrt{2} \\ \mathbf{q}^{(6)} = (-1, 1, 0)/\sqrt{2} \\ \mathbf{q}^{(-1)}, \mathbf{q}^{(-2)}, \mathbf{q}^{(-3)}, \\ \mathbf{q}^{(-4)}, \mathbf{q}^{(-5)}, \mathbf{q}^{(-6)} \end{array} \right\} & \mathcal{R}_{\text{fcc}}^{(1)} &= \left\{ \begin{array}{l} \mathbf{q}^{(1)} = (-1, 1, 1)/\sqrt{3} \\ \mathbf{q}^{(2)} = (1, -1, 1)/\sqrt{3} \\ \mathbf{q}^{(3)} = (1, 1, -1)/\sqrt{3} \\ \mathbf{q}^{(4)} = (1, 1, 1)/\sqrt{3} \\ \mathbf{q}^{(-1)}, \mathbf{q}^{(-2)}, \\ \mathbf{q}^{(-3)}, \mathbf{q}^{(-4)} \end{array} \right\} & \mathcal{R}_{\text{sc}}^{(1)} &= \left\{ \begin{array}{l} \mathbf{q}^{(1)} = (1, 0, 0) \\ \mathbf{q}^{(2)} = (0, 1, 0) \\ \mathbf{q}^{(3)} = (0, 0, 1) \\ \mathbf{q}^{(-1)}, \mathbf{q}^{(-2)}, \mathbf{q}^{(-3)} \end{array} \right\}
 \end{aligned} \tag{5.3.1}$$

where  $\mathbf{q}^{(-n)} = -\mathbf{q}^{(n)}$ ; see Fig. 5.4. The one-mode approximation for the triangular PFC states that the equilibrium state can be written as



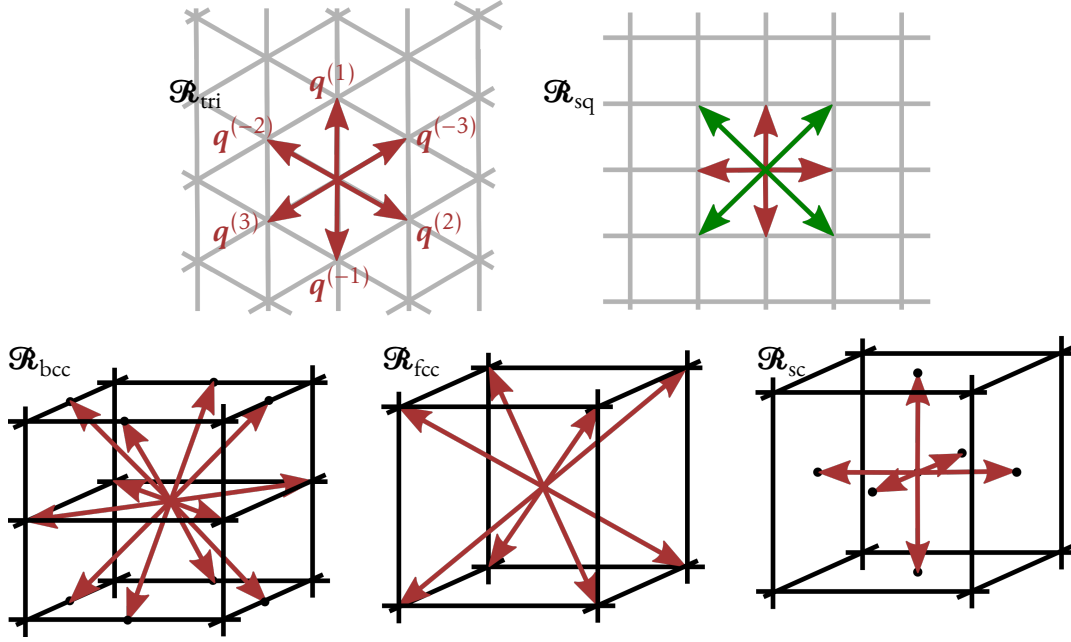


Figure 5.4: Reciprocal lattices  $\mathcal{R}$  of the Bravais lattices in Fig. 5.2, with the set of smallest reciprocal lattice vectors  $\mathcal{R}^{(1)}$ . The set  $\mathcal{R}_{\text{tri}}^{(1)} = \{q^{(n)}\}_{n=\pm 1}^{\pm 3}$ , Eq. (5.3.1), of the six smallest reciprocal lattice vectors of the triangular lattice has been indicated explicitly. For the 2D square reciprocal lattice, we have also drawn the second modes  $\mathcal{R}_{\text{sq}}^{(2)}$ , Eq. (5.3.8).

$$\psi^{\text{eq}} = \psi_0 + A_{\text{tri}} \sum_{n=\pm 1}^{\pm 3} e^{i q^{(n)} \cdot r}. \quad (5.3.2)$$

The one-mode approximation

As discussed,  $\psi_0$  is a simulation parameter, while  $A_{\text{tri}}$  must be determined by inserting the one-mode approximation into the free energy, Eq. (5.0.1), and minimizing with respect to  $A_{\text{tri}}$ . System states that are slightly distorted from equilibrium can be described by letting these amplitudes become slowly varying *fields*, i.e.,  $\psi_0 \rightarrow \bar{\psi}(\mathbf{r})$  and  $A_{\text{tri}} \rightarrow \eta_n(\mathbf{r})$ , so that

$$\psi = \bar{\psi} + \sum_{n=\pm 1}^{\pm 3} \eta_n e^{i q^{(n)} \cdot r}. \quad (5.3.3)$$

The amplitude approximation

While both Eqs. (5.3.2) and (5.3.3) are referred to as the one-mode approximation in the literature, we will refer to the second as the amplitude approximation.

Since  $\psi$  is real,  $\eta_{-n} = \eta_n^*$  and all amplitudes are thus not independent. In much of the literature, the amplitude approximation is written as

$$\psi = \bar{\psi} + \sum_{n=1}^3 \eta_n e^{i\mathbf{q}^{(n)} \cdot \mathbf{r}} + \text{c.c.} \quad (5.3.4)$$

For some calculations, however, it is useful to keep the sum over all reciprocal lattice vectors, which is why we have introduced the notation

$$\sum_{n=\pm 1}^{\pm 3} \eta_n e^{i\mathbf{q}^{(n)} \cdot \mathbf{r}} = \eta_1 e^{i\mathbf{q}^{(1)} \cdot \mathbf{r}} + \eta_{-1} e^{i\mathbf{q}^{(-1)} \cdot \mathbf{r}} + \eta_2 e^{i\mathbf{q}^{(2)} \cdot \mathbf{r}} + \eta_{-2} e^{i\mathbf{q}^{(-2)} \cdot \mathbf{r}} \\ + \eta_3 e^{i\mathbf{q}^{(3)} \cdot \mathbf{r}} + \eta_{-3} e^{i\mathbf{q}^{(-3)} \cdot \mathbf{r}}. \quad (5.3.5)$$

It is this notation that is used in Paper II when deriving the elastic constants for the five different symmetries therein considered, where the sum is expressed as a sum over elements in  $\mathcal{R}_{\text{tri}}^{(1)} = \{\mathbf{q}^{(n)}\}_{n=\pm 1}^{\pm 3}$ . Thus, in the context of summing over  $N$  reciprocal lattice vectors, these expressions are equivalent

$$\sum_{n=\pm 1}^{\pm N/2} f_n \equiv \sum_{\mathbf{q}^{(n)} \in \mathcal{R}^{(1)}} f_n, \quad (5.3.6)$$

where  $f_n$  is some function, which may depend on the reciprocal lattice vector  $\mathbf{q}^{(n)}$  or amplitude  $\eta_n$ .

For the triangular lattice, and the bcc lattice in three dimensions, with the free energy of Eq. (5.0.1), the one-mode approximation is excellent even at deeper quenches. For other symmetries, however, an accurate description requires the inclusion of bigger reciprocal lattice vectors. For example, the amplitude approximation of the square lattice reads

$$\psi = \bar{\psi} + \sum_{n=\pm 1}^{\pm 2} \eta_n e^{i\mathbf{q}^{(n)} \cdot \mathbf{r}} + \sum_{n=\pm 1}^{\pm 2} \eta_n e^{i\mathbf{p}^{(n)} \cdot \mathbf{r}}, \quad (5.3.7)$$

where  $\mathbf{q}^{(n)} \in \mathcal{R}_{\text{sq}}^{(1)}$  and  $\mathbf{p}^{(n)} \in \mathcal{R}_{\text{sq}}^{(2)}$ , where

$$\mathcal{R}_{\text{sq}}^{(2)} = \left\{ \begin{array}{l} \mathbf{p}^{(1)} = (1, -1)/\sqrt{2} \\ \mathbf{p}^{(2)} = (1, 1)/\sqrt{2} \\ \mathbf{p}^{(-1)}, \mathbf{p}^{(-2)}, \end{array} \right\} \quad (5.3.8)$$

with  $\mathbf{p}^{(-n)} = -\mathbf{p}^{(n)}$ , is shown in green in Fig. 5.4. In equilibrium, the amplitudes  $\eta_n$  will take equilibrium values  $A_{\text{sq}}$  and  $B_{\text{sq}}$  corresponding to the first and second modes,

respectively. Similar to the 2D square lattice, the 3D fcc lattice also requires a second mode in the amplitude approximation, whose lengths are  $\sqrt{4/3}$ , so this set is denoted  $\mathcal{R}_{\text{fcc}}^{(4/3)}$ . For the 3D simple cubic lattice produced by the free energy of Eq. (5.1.4), three modes,  $\mathcal{R}_{\text{sc}}^{(1)}$ ,  $\mathcal{R}_{\text{sc}}^{(2)}$  and  $\mathcal{R}_{\text{sc}}^{(3)}$  are necessary to express the ground state accurately. The mode approximations were used in Paper II to connect the stress tensor with the elastic constants derived in Refs. [54, 20], with the reciprocal lattice sets not given here found in the paper's appendix.

## 5.4 The amplitude formulation of the PFC model

The formulation of the phase-field in terms of slowly varying amplitudes allows for a shift of perspective between a microscopic view, the evolution of the phase-field itself, and a coarse-grained view where the evolution of the amplitudes is considered. This approach is called the amplitude formulation of the PFC (APFC), and due to the amplitudes' slowly varying nature, one may operate with a lower resolution in the bulk, especially when combined with methods like adaptive mesh refinement. This, in turn, allows to reach even longer time scales than those already accessible to the PFC model itself. Additionally, many of the analytical treatments of the PFC require closed expressions for the evolution of the amplitudes, which the APFC provides. While the evolution equations for the amplitudes can be derived in a formal and consistent way using a renormalization procedure [74, 75], in this section, we will see a "quick-and-dirty" way to obtain the same equations of motion from the phase-field evolution. For a more complete overview of the APFC framework, see Ref. [76].

The amplitudes may be extracted from the PFC by means of demodulation, which is the following operation

$$\langle \psi e^{-i\mathbf{q}^{(n)} \cdot \mathbf{r}} \rangle = \bar{\psi} \langle e^{-i\mathbf{q}^{(n)} \cdot \mathbf{r}} \rangle + \sum_{n'=\pm 1}^{\pm 3} \eta_{n'} \langle e^{i(\mathbf{q}^{(n')} - \mathbf{q}^{(n)}) \cdot \mathbf{r}} \rangle = \eta_n, \quad (5.4.1)$$

where  $\langle \cdot \rangle$  is the coarse-graining of Eq. (4.4.1) with  $w = a_0$ , the lattice constant. Here, we have made use of the central assumption in the APFC framework, namely that the amplitudes are slowly varying so that they may be taken out of the coarse-graining operation, leaving  $\langle e^{i(\mathbf{q}^{(n')} - \mathbf{q}^{(n)}) \cdot \mathbf{r}} \rangle \approx \delta_{n,n'}$ .

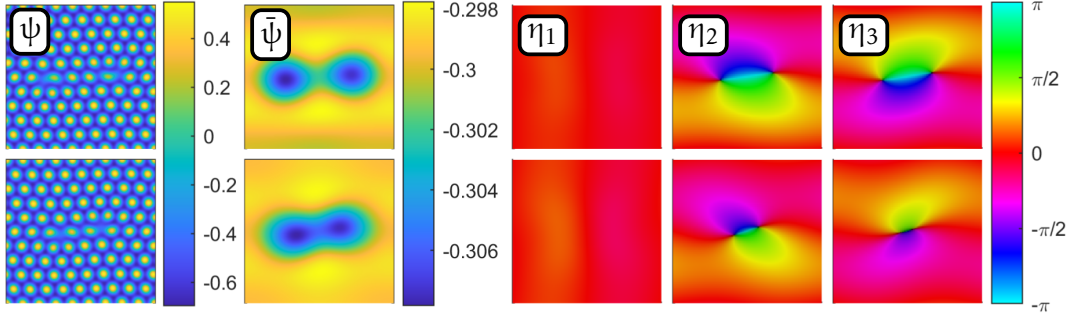


Figure 5.5: Snapshots of the annihilation of a dislocation dipole (left:  $\mathbf{b} = a_0 \mathbf{e}_x$ , right:  $\mathbf{b} = -a_0 \mathbf{e}_x$ ) in the 2D triangular PFC model at (top row)  $t = 0$  and (bottom row)  $t = 600$ . Parameters used were  $(r, \psi_0) = (-0.3, -0.3)$ . The columns show the demodulated fields  $\bar{\psi}$  and  $\{\eta_n\}_{n=1}^3$ , Eq. (5.4.1), where the complex fields are shown by their phase  $\theta_n$  and brightness corresponding to the magnitude  $|\eta_n|$ .

One of the main principles used in connecting the microscopic details of the PFC with slowly varying quantities such as the amplitudes or the macroscopic stress, is that of reciprocal lattice resonance. The main identity needed is that

$$\langle e^{i\mathbf{G}\cdot\mathbf{r}} \rangle \approx \delta_{\mathbf{G},\mathbf{0}}, \quad (5.4.2)$$

where  $\mathbf{G}$  is a vector on the reciprocal lattice. If integrated over a unit cell, the integral on the lhs. is zero unless  $\mathbf{G} = \mathbf{0}$ , due to the periodic nature of  $e^{i\mathbf{G}\cdot\mathbf{r}}$ . For numerical and some theoretical purposes, however, it is easier to work with the Gaussian kernel given in Eq. (4.4.1). In this case, we have  $\langle e^{i\mathbf{G}\cdot\mathbf{r}} \rangle = e^{-\frac{1}{2}a_0^2\mathbf{G}^2}$ . When  $\mathbf{G}$  is a non-zero reciprocal lattice vector, we have  $a_0|\mathbf{G}| \sim 2\pi$ , which gives  $\langle e^{i\mathbf{G}\cdot\mathbf{r}} \rangle \sim e^{-2\pi^2} = 2.67 \times 10^{-9}$ , which should be compared to  $\langle e^{i\mathbf{G}\cdot\mathbf{r}} \rangle = 1$  for  $\mathbf{G} = \mathbf{0}$ . Sticking to an indexing of reciprocal lattice vectors where  $\mathbf{q}^{(-n)} = -\mathbf{q}^{(n)}$ , this gives  $\langle e^{i(\mathbf{q}^{(n')} - \mathbf{q}^{(n)})\cdot\mathbf{r}} \rangle \approx \delta_{n,n'}$ , as used in this thesis and several of the papers.

Figure 5.5 shows the annihilation of a dislocation dipole in the 2D triangular PFC model together with the slowly varying average density  $\bar{\psi} = \langle \psi \rangle$  and the amplitudes  $\{\eta_n\}_{n=1}^3$ .

To derive an analytic expression for the evolution of the amplitudes, we may insert the amplitude approximation, Eq. (5.3.3), into the free energy, Eq. (5.0.1), and coarse-grain the integrand, using that coarse-graining commutes with integration. To emphasize that the result is now an approximation and depends on the  $\bar{\psi}$  and  $\eta_n$ , we write  $\mathcal{F}_\eta$  and get

$$\begin{aligned} \mathcal{F}_\eta[\bar{\psi}, \{\eta_n\}_{n=1}^3] = & \int d^2r \left( \frac{1}{2} (\mathcal{L}_1 \bar{\psi})^2 + \frac{r}{2} \bar{\psi}^2 + \frac{1}{4} \bar{\psi}^4 \right. \\ & \left. + \sum_{n=1}^3 |\mathcal{G}_n \eta_n|^2 + \left( \frac{r}{2} + 3\bar{\psi}^2 \right) \Phi + \bar{\psi} (\eta_1 \eta_2 \eta_3 + \eta_1^* \eta_2^* \eta_3^*) + \frac{3}{2} \Phi^2 - \frac{3}{2} \sum_{n=1}^3 |\eta_n|^4 \right), \end{aligned} \quad (5.4.3)$$

The amplitude free energy

where  $\mathcal{G}_n = \nabla^2 + 2i\mathbf{q}^{(n)} \cdot \nabla$ , and  $\Phi = 2 \sum_{n=1}^3 |\eta_n|^2$ . To derive an equation of motion for the amplitudes themselves, we may multiply the evolution equation, Eq. (5.0.2), with  $e^{-i\mathbf{q}^{(n)} \cdot \mathbf{r}}$  and coarse-grain to get

$$\begin{aligned} \partial_t \eta_n &= \partial_t \langle e^{-i\mathbf{q}^{(n)} \cdot \mathbf{r}} \psi \rangle = \int d^2r' \mathcal{K}(\mathbf{r} - \mathbf{r}') e^{-i\mathbf{q}^{(n)} \cdot \mathbf{r}'} \nabla'^2 \frac{\delta \mathcal{F}}{\delta \psi}(\mathbf{r}') \\ &= \int d^2r' \mathcal{K}(\mathbf{r} - \mathbf{r}') \nabla'_{\mathbf{q}^{(n)}} \cdot \left( e^{-i\mathbf{q}^{(n)} \cdot \mathbf{r}'} \nabla' \frac{\delta \mathcal{F}}{\delta \psi}(\mathbf{r}') \right) = \nabla_{\mathbf{q}^{(n)}}^2 \left\langle e^{-i\mathbf{q}^{(n)} \cdot \mathbf{r}} \frac{\delta \mathcal{F}}{\delta \psi} \right\rangle, \end{aligned} \quad (5.4.4)$$

where  $\nabla'$  is the gradient with respect to  $\mathbf{r}'$ ,  $\nabla_{\mathbf{q}^{(n)}} = \nabla + i\mathbf{q}^{(n)}$  and we have used that derivation commutes with coarse-graining. We now need an expression for the coarse-grained quantity  $\left\langle e^{-i\mathbf{q}^{(n)} \cdot \mathbf{r}} \frac{\delta \mathcal{F}}{\delta \psi} \right\rangle$ . Reading from Eq. (5.3.3), we have

$$\frac{\delta \psi(\mathbf{r}')}{\delta \eta_n(\mathbf{r})} = e^{i\mathbf{q}^{(n)} \cdot \mathbf{r}} \delta(\mathbf{r}' - \mathbf{r}), \quad (5.4.5)$$

and the inverse of this derivative is found by considering

$$\begin{aligned} & \int d^2r' \left( \delta(\mathbf{r}'' - \mathbf{r}') e^{-i\mathbf{q}^{(n)} \cdot \mathbf{r}'} \right) \frac{\delta \psi(\mathbf{r}')}{\delta \eta_n(\mathbf{r})} \\ &= \int d^2r' \left( \delta(\mathbf{r}'' - \mathbf{r}') e^{-i\mathbf{q}^{(n)} \cdot \mathbf{r}'} \right) e^{i\mathbf{q}^{(n)} \cdot \mathbf{r}} \delta(\mathbf{r}' - \mathbf{r}) = \delta(\mathbf{r} - \mathbf{r}''), \end{aligned} \quad (5.4.6)$$

which gives

$$\frac{\delta \eta_n(\mathbf{r}'')}{\delta \psi(\mathbf{r}')} = e^{-i\mathbf{q}^{(n)} \cdot \mathbf{r}'} \delta(\mathbf{r}'' - \mathbf{r}'). \quad (5.4.7)$$

$\psi$  can be decomposed into the slowly varying field  $\bar{\psi}$  and  $\{\eta_n\}$ , and  $\mathcal{F}$  expressed in these

variables is  $\mathcal{F}_\eta$ , so

$$\begin{aligned} \frac{\delta \mathcal{F}}{\delta \psi(\mathbf{r})} &= \int d^2 r' \left( \frac{\delta \mathcal{F}_\eta}{\delta \bar{\psi}(\mathbf{r}')} \frac{\delta \bar{\psi}(\mathbf{r}')}{\delta \psi(\mathbf{r})} + \sum_{n=\pm 1}^{\pm 3} \frac{\delta \mathcal{F}_\eta}{\delta \eta_n(\mathbf{r}')} \frac{\delta \eta_n(\mathbf{r}')}{\delta \psi(\mathbf{r})} \right) \\ &= \frac{\delta \mathcal{F}_\eta}{\delta \bar{\psi}(\mathbf{r})} + \sum_{n=\pm 1}^{\pm 3} \frac{\delta \mathcal{F}_\eta}{\delta \eta_n(\mathbf{r})} e^{-i\mathbf{q}^{(n)} \cdot \mathbf{r}} \end{aligned} \quad (5.4.8)$$

which results in

$$\left\langle e^{-i\mathbf{q}^{(n)} \cdot \mathbf{r}} \frac{\delta \mathcal{F}}{\delta \psi} \right\rangle = \frac{\delta \mathcal{F}_\eta}{\delta \eta_n^*}, \quad (5.4.9)$$

and thus

$$\partial_t \eta_n = \nabla_{\mathbf{q}^{(n)}}^2 \frac{\delta \mathcal{F}_\eta}{\delta \eta_n^*}. \quad (5.4.10)$$

A similar exercise with  $\bar{\psi}$  using  $\mathbf{q}^{(n)} = 0$  gives the following evolution equation for the slowly varying average density

$$\partial_t \bar{\psi} = \nabla^2 \frac{\delta \mathcal{F}_\eta}{\delta \bar{\psi}}. \quad (5.4.11)$$

With an initial condition of  $\eta_n = 0$ , and given Eq. (5.4.3), this is simply the dynamical equation of the PFC with  $\psi \rightarrow \bar{\psi}$ , leading to rapid variations in  $\bar{\psi}$  which is inconsistent with the assumptions used to derive  $F_\eta$  in the first place. The resolution to this inconsistency is to realize that if  $\eta_n$  is to be slowly varying, then the leading term on the rhs. of Eq. (5.4.10) should be given by only the last term in  $\nabla_{\mathbf{q}^{(n)}}^2 = \nabla^2 + 2i\mathbf{q}^{(n)} \cdot \nabla - \mathbf{q}^{(n)2}$ , thus yielding the governing equations for the evolution of the amplitudes

$$\partial_t \eta_n = -\mathbf{q}^{(n)2} \frac{\delta \mathcal{F}_\eta}{\delta \eta_n^*}. \quad (5.4.12)$$

The amplitude evolution equation

This, in turn, will lead to self-consistent equations of motion (no development of rapid spatial variations in  $\eta_n$ ) and has the added benefit of setting  $\partial_t \bar{\psi} = 0$  (since  $\mathbf{q}^{(0)} = \mathbf{0}$ ), which is a typical approximation for APFC models. Amplitude formulations that include variations in  $\bar{\psi}$  typically ignore the gradients in front of  $\bar{\psi}$  in  $F_\eta$ , and only then evolve it according to Eq. (5.4.11), perhaps earning the nomenclature of "quick-and-dirty." For more discussion on this point, see Ref. [77].

## 5.5 Topological structures in the PFC model

Consider the equilibrium state in the one-mode approximation, for any lattice structure, displaced by a displacement field  $\mathbf{u}$

$$\psi^{\text{eq}}(\mathbf{r} - \mathbf{u}) = \psi_0 + \eta_0 \sum_{\mathbf{q}^{(n)} \in \mathcal{R}^{(1)}} e^{i\mathbf{q}^{(n)} \cdot (\mathbf{r} - \mathbf{u})} = \psi_0 + \sum_{\mathbf{q}^{(n)} \in \mathcal{R}^{(1)}} (\eta_0 e^{-i\mathbf{q}^{(n)} \cdot \mathbf{u}}) e^{i\mathbf{q}^{(n)} \cdot \mathbf{r}}, \quad (5.5.1)$$

where  $\eta_0$  is the equilibrium amplitude of the first mode. This is a state described by the amplitude approximation, Eq. (5.3.3), with  $\eta_n = \eta_0 e^{-i\mathbf{q}^{(n)} \cdot \mathbf{u}}$ . Assuming that this holds in general, we see that the phase  $\arg(\eta_n) = -\mathbf{q}^{(n)} \cdot \mathbf{u}$  of the amplitude contains information about the displacement field of the PFC. Indeed,  $\arg(\eta_n)$  is the  $\mathcal{S}^1$  order parameter  $\Theta_n$  defined in Sec. 4.3, associated with the broken translational symmetry of the crystal

$$\Theta_n = \arg(\eta_n) = -\mathbf{q}^{(n)} \cdot \mathbf{u}. \quad (5.5.2)$$

The phase of the amplitudes

In Paper III, we showed that for the Bravais symmetries considered in this thesis, all of the sets of primary reciprocal lattice vectors  $\mathcal{R}^{(1)}$ , and the higher order modes, satisfy the following identity

$$\sum_{\mathbf{q}^{(n)} \in \mathcal{R}^{(1)}} q_i^{(n)} q_j^{(n)} = \frac{N}{d} \delta_{ij}, \quad (5.5.3)$$

Dyadic vector product identity for lattices with ( $\geq 4$ )-fold symmetry

where  $N$  is the number of reciprocal lattice vectors in  $\mathcal{R}^{(1)}$  and  $d$  is the dimension. While versions of Eq. (5.5.3) with specific crystalline symmetries have been used in other works, to our knowledge, the general form given above has not previously been utilized in the PFC literature. Note also that if the reciprocal lattice vectors in the sum have a length  $q_0 \neq 1$ , then the rhs. of Eq. (5.5.3) should have an additional factor of  $q_0^2$ . This identity can be used to solve Eq. (5.5.2) for  $\mathbf{u}$ , namely by dyadically multiplying with  $\mathbf{q}^{(n)}$  and summing over the primary reciprocal lattice vectors to get

$$\mathbf{u}^T = -\frac{d}{N} \sum_{\mathbf{q}^{(n)} \in \mathcal{R}^{(1)}} \Theta_n \mathbf{q}^{(n)}. \quad (5.5.4)$$

The (total) displacement field extracted from PFC amplitudes

This equation defines a single-valued displacement field, which in the presence of a dislocation requires a phase-slip across which the displacement field jumps the Burgers vector  $\mathbf{b}$ ,

which is why we have denoted it the *total* displacement field, as in Sec. 4.2. Given Eq. (5.5.4), this phase-slip coincides with the choice of phase-slip in extracting the phases  $\theta_n$  from  $\eta_n$ . However, the elastic distortion  $\mathfrak{u}$ , shown in Fig. 4.7 (c), does not contain such a phase-slip. Indeed, it is possible to derive an expression for  $\mathfrak{u}$ , by noting that

$$\frac{\nabla \eta_n}{\eta_n} = \frac{1}{|\eta_n| e^{-i \mathbf{q}^{(n)} \cdot \mathbf{u}}} \left( (\nabla |\eta_n|) e^{-i \mathbf{q}^{(n)} \cdot \mathbf{u}} - i |\eta_n| e^{-i \mathbf{q}^{(n)} \cdot \mathbf{u}} \nabla (\mathbf{q}^{(n)} \cdot \mathbf{u}) \right), \quad (5.5.5)$$

which we may multiply by  $i$  and take the imaginary part of to obtain

$$q_k^{(n)} \partial_j u_k = \text{Im} \left( i \frac{\partial_j \eta_n}{\eta_n} \right). \quad (5.5.6)$$

Now, multiplying with  $q_i^{(n)}$ , summing over  $\mathcal{R}^{(1)}$  and using Eq. (5.5.3), we get

$$\partial_j u_i = \mathfrak{u}_{ij} = \frac{d}{N} \sum_{\mathbf{q}^{(n)} \in \mathcal{R}^{(1)}} \text{Im} \left( i \frac{\partial_j \eta_n}{\eta_n} \right) q_i^{(n)}. \quad (5.5.7)$$

The distortion extracted from the PFC amplitudes

In the final expression, we are not required to extract a value for  $\theta_n$ , so it will contain no arbitrary phase-slips. In fact, Eqs. (5.5.4) and (5.5.7) were used to produce the plots in panels (a) and (c) of Fig. 4.7, respectively.

$\theta_n$  is the direction of the vector field  $\Psi = (\Re(\eta_n), \text{Im}(\eta_n))$ . Thus, the dislocations are located at the zeros of these amplitudes, as can be seen from the expression of the distortion in Eq. (5.5.7), which is well-defined everywhere  $\eta_n \neq 0$ . The method of Halperin and Mazenko, Sec. 3.4, can then be used with these amplitudes. In Paper III, we made this connection explicit and derived an expression for the dislocation density tensor and the velocity of dislocation lines. This allowed us to take an arbitrary phase-field configuration, calculate the dislocation density and reconstruct the Burgers vector and tangent vector, as illustrated in Fig. 5.6, and detailed in Appendix A.1.3.

The distortion given in Eq. (5.5.7) is defined everywhere as the gradient of a displacement field, except where it is undefined, i.e., at  $\eta_n = 0$ , and  $\mathfrak{u}$  diverges. As discussed in Paper III, the Halperin-Mazenko method employs precisely this fact to express the dislocation density in terms of a delta function of the amplitudes. As a result, this will be infinitely sharp. It is, however, questionable whether such a diverging distortion is reasonable since even the notion of a displacement field loses its meaning as one gets close to the core. From a physical point of view, the distortion diverging at the core leads to linear elasticity predicting infinite core energy, which is usually regularized by introducing a cutoff length. Additionally, the delta function is inconvenient from a numerical point of view, as it must be regularized by an arbitrary length scale, as we will see in Eq. (6.3.7). In Paper V, we proposed a generalization of the topological charge, Eq. (3.3.1), which allowed us to find a non-singular expression for the dislocation density. As we will outline in Sec. 6.6, this can also be used to derive a non-singular expression for the distortion.



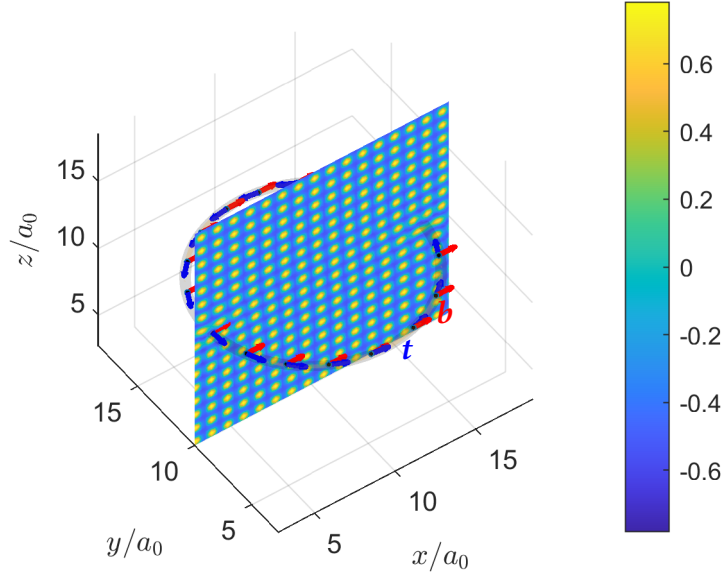


Figure 5.6: 2D slice of the simple cubic PFC, Eq. (5.1.4), with  $(r, \psi_0) = (-0.3, -0.325)$ , containing a dislocation loop in the  $xy$ -plane with Burgers vector  $\mathbf{b} = (1, 0, 0)$ . The dislocation content, i.e., the Burgers vector  $\mathbf{b}$  and tangent vector  $\mathbf{t}$ , was reproduced using Eq. (6.3.6). For details, see Appendix A.1.

## 5.6 The time scale problem

In Ref. [20], the motion of a dislocation in the PFC was considered. By using the APFC equations of motion, Skaugen et al. were able to derive a closed-form expression for the velocity of a dislocation under the influence of the Peach-Koehler force. Given two dislocations in a medium, we know that the elastic field set up by one will cause the other to move towards it and annihilate. The natural question, then, is which elastic field exactly does one dislocation *feel* from the other? In Ref. [20], the elastic fields predicted from continuum elasticity were used. However, when directly comparing the velocity predicted by this method with the numerically obtained velocity, the authors found a mismatch. While the topological nature of the defect puts some restrictions on the stress field produced by a dislocation, in continuum elasticity, there is the added condition of mechanical equilibrium. The PFC evolution, Eq. (5.0.2), is not guaranteed to ensure mechanical equilibrium, and this was singled out as the leading cause of the discrepancy.

Instead of elastic waves traveling through the PFC, relieving build-up stress as expected for a strained crystal, the phase-field slowly diffuses the elastic strains. The origin of this feature is that the PFC evolution equation only contains one independent variable, the phase-field; its time derivative is given as a first-order differential equation in terms of itself, which does not make it possible to have an independent momentum mode of transport. To quantify this behavior and understand how it is different from proper solid behavior, we look at the dispersion relation for elastic waves. As we saw in Sec. 4.4, the expected behavior

of crystals is a dispersion relation that scales with the wave number in the long wavelength limit. However, a linear stability analysis with the PFC dynamics reveals that the dispersion relation is far from wave-like. Consider a perturbation of the equilibrium state given by a displacement field  $\mathbf{u}$ . The distorted triangular PFC, in the one-mode approximation, is given by

$$\psi = \psi^{eq}(\mathbf{r} - \mathbf{u}) = \psi_0 + A_{\text{tri}} \sum_{n=\pm 1}^{\pm 3} e^{i\mathbf{q}^{(n)} \cdot (\mathbf{r} - \mathbf{u})}, \quad (5.6.1)$$

effectively setting the amplitudes  $\eta_n = A_{\text{tri}} e^{-i\mathbf{q}^{(n)} \cdot \mathbf{u}}$ . In the long wavelength limit, the approximations resulting in Eq. (5.4.12) are certainly valid, meaning that we can insert this amplitude ansatz and linearize in  $\mathbf{u}$ . The result is derived in Ref. [78] and gives

$$\partial_t \mathbf{u} = \nabla^2 \mathbf{u} + 2\nabla(\nabla \cdot \mathbf{u}). \quad (5.6.2)$$

Already here, we see how different this equation is from the supposed second-order differential equation assumed to govern elastic waves, Eq. (4.4.14). By finding the dispersion relations using the same procedure as in Sec. 4.4, we get

$$\omega_T = -i|\mathbf{k}|^2, \quad (5.6.3)$$

and

$$\omega_L = -3i|\mathbf{k}|^2, \quad (5.6.4)$$

for transversal and longitudinal waves, respectively. The purely imaginary nature of these dispersion relations means that the elastic distortions decay to equilibrium in an overdamped manner, clearly in contrast to the elastic behavior expected from solids given by sound modes, Eqs. (4.4.19) and (4.4.21).

In the literature, there have been two main ways of addressing this issue. One approach has been to explicitly set elastic excitations to zero. This was done for the APFC model in Ref. [79] and for the 2D triangular PFC model in Ref. [21]. In Ref. [79], the elastic excitations were set to zero by identifying the elastic excitations to be carried by the phase of the amplitudes, Eq. (5.5.2), and separating the equations of motion by letting this part equilibrate between each time step iteration of the APFC. For the 2D PFC model in Ref. [21], the elastic problem was examined by finding the equilibrium stress and then setting the PFC stress to this value by use of Airy stress functions. The Airy stress formalism is a useful method for solving the elastic problem in two dimensions. In Paper III, we proposed a different formalism, valid for any 3D cubic crystal structure.

The other way to address the problem of elastic waves in the PFC model has been to explicitly reintroduce the second time scale. The first attempt at this was to couple the PFC to second-order time derivatives as proposed in Ref. [80]. While this provided the propagation of some sound modes, it gives the wrong dispersion relation in the long wavelength limit [78]. In Ref. [81], the APFC framework, which naturally introduces a separation of length scales through the amplitudes, was used to add a hydrodynamic velocity field. Still, this approach is limited to single-crystal states in the amplitude approximation.

In Paper [IV](#), we introduced a complete hydrodynamic framework for the full PFC model to address this issue.



## CHAPTER 6

### *Papers summary and outlook*



“ We have the duty of formulating, of summarising, and of communicating our conclusions, in intelligible form, in recognition of the right of other free minds to utilize them in making their own decisions.

- *Ronald Fisher* [82]

In this chapter, we will look at the 5 papers on which this thesis is built, summarize the most important points and present an outlook for future research.

#### 6.1 Paper I: Dislocation nucleation in the phase-field crystal model

Vidar Skogvoll, Audun Skaugen, Luiza Angheluta, and Jorge Viñals.  
*Physical Review B*, 103(1):014107, January 2021.

The nucleation of defects in crystals is important to study many phenomena, including fragmentation, deformation processes, and crack propagation. One mechanism of nucleation is that dislocations form from a defect already present in the crystal, such as an inclusion or obstacle. A different source of nucleation is what is known as a Frank-Read source, in which the nucleation process happens from already existing dislocation lines.

However, under large stresses, the crystal may spontaneously nucleate defects in an otherwise perfect crystal, known as homogeneous nucleation. As mentioned, coarse-grained theories like DDD require rules for nucleation and recombination of dislocations. Thus, the search for reliable criteria of nucleation has been extensive in the literature [83, 84, 85, 86], which has later been compared with simulations from molecular dynamics under various conditions [87, 88, 89]. However, due to the complicated nature of this process, success has been limited. In this paper, we employed the model in Ref. [21] to study homogeneous nucleation of dislocations by coupling the PFC to an external stress, like an indentation, to shed light on the nucleation criteria that govern large plastic behavior.

In order to facilitate nucleation, we required a mechanism to impose external stress. To do so, we adapted the method introduced in Ref. [21] for evolving the PFC at mechanical equilibrium. This model was based on supplying the standard PFC evolution equation, Eq. (5.0.2), with an advection  $\psi \rightarrow \psi' = \psi(\mathbf{r} - \mathbf{u}^\delta)$  at every time step to ensure mechanical equilibrium. To find  $\mathbf{u}^\delta$ , it was exploited that the configurational stress  $\mathbb{h}^\psi$  could be calculated from the PFC itself [20]. Then,  $\mathbb{h}^\psi$  was compared to a target stress  $\mathbb{h}^{(\text{ME})}$  in mechanical equilibrium, and the necessary displacement  $\mathbf{u}^\delta$  needed to advect the PFC so that  $\mathbb{h}^{\psi'} = \mathbb{h}^{(\text{ME})}$  was found.  $\mathbb{h}^{(\text{ME})}$  can be found (in two dimensions) by  $\mathbb{h}_{ij}^{(\text{ME})} = \epsilon_{ik}\epsilon_{jl}\partial_k\partial_l\chi$ , where  $\chi$  is the Airy stress function, which satisfies

$$\frac{1-\kappa}{\mu}\nabla^4\chi = \eta_{33}, \quad (6.1.1)$$

where

$$\kappa = \frac{\lambda}{d\lambda + 2\mu}. \quad (6.1.2)$$

$d$  is the dimension, and  $\eta_{33}$  is the out-of-plane component of the *incompatibility tensor* [47], given by

$$\eta_{ij} = \epsilon_{ilm}\epsilon_{jpk}\partial_l\partial_p\epsilon_{mk}^\psi. \quad (6.1.3)$$

Note that this incompatibility field shares its symbol with the amplitudes in the phase-field expansion, but the incompatibility field is only discussed in this section of the thesis, so no confusion should arise. To find the source for the Airy stress function, Ref. [21] took advantage of the fact that the configurational stress  $\mathbb{h}_{ij}^\psi$  could be derived directly from the PFC, and assumed isotropic elasticity everywhere, so that

$$\mathbb{h}_{ij}^\psi = \lambda\epsilon_{kk}^\psi\delta_{ij} + 2\mu\epsilon_{ij}^\psi, \quad (6.1.4)$$

where  $\epsilon^\psi$  is the (out-of-equilibrium) strain state in the PFC, which could be inverted to get

$$\epsilon_{ij}^\psi = \frac{1}{2\mu}\left(\mathbb{h}_{ij}^\psi - \kappa\delta_{ij}\mathbb{h}_{kk}^\psi\right). \quad (6.1.5)$$

After solving Eq. (6.1.1) for  $\chi$ , the necessary compatible displacement  $\mathbf{u}^\delta$  to make  $\mathbb{h}^\psi = \mathbb{h}^{(\text{ME})}$  was calculated. To study the nucleation of defects, we accounted for external stresses

$\mathbb{h}^{(\text{ext})}$  by shifting the target stress by  $\mathbb{h}^{(\text{ME})} \rightarrow \mathbb{h}^{(\text{ME})} - \mathbb{h}^{(\text{ext})}$ . Then, by imposing a local indentation external stress profile, we observed the nucleation of a dislocation dipole above a critical value. We also discovered that by calculating the resolved shear stress in the crystal onto different slip planes, we were able to predict what type of dislocation would nucleate and further derived a theoretical prediction for how large this threshold should be, which was verified by simulations. The incompatibility field, Eq. (6.1.3), proved not only to be a well-suited order parameter for the process of nucleation but was also shown to identify the location and character of dislocations in three dimensions. This was illustrated in the paper by simulations of both edge and mixed-type dislocations in the 3D bcc PFC model.

## 6.2 Paper II: Stress in ordered systems: Ginzburg-Landau type density field theory

Vidar Skogvoll, Audun Skaugen, and Luiza Angheluta.  
*Physical Review B*, 103(22):224107, June 2021.

As was observed in both the time scale problem and also in the case of nucleation, the coarse-grained configurational stress in the PFC seemed to be the deciding factor. In Ref. [20], the stress tensor was derived by treating the phase-field  $\psi$  as a scalar field and performing a variation of the coordinate system. This, however, neglected the fact that the phase-field is meant to represent a one-body density. In this paper, we introduced the general variational procedure outlined below and derived a method to find the stress tensor for any Ginzburg-Landau theory. Note that in this paper, we worked with the divergence of the stress tensor in the other convention than that of this thesis, i.e.,  $(\nabla \cdot \sigma)_j = \partial_i \sigma_{ij}$ . In this section, we have therefore translated the pertinent results to match the convention used in this thesis. This is only crucial for the discussion about the symmetry of the microscopic stress tensor.

Writing the continuity equation in a discretized way, using that the velocity field  $\mathbf{v} = \frac{\delta \mathbf{x}}{\delta t}$  for some infinitesimal displacement  $\delta \mathbf{x}$  over an infinitesimal time  $\delta t$ , we have

$$\frac{\delta \psi}{\delta t} + \nabla \cdot \left( \psi \frac{\delta \mathbf{x}}{\delta t} \right) = 0. \quad (6.2.1)$$

Thus, we can consider a virtual displacement  $\delta \mathbf{x}$  to affect the phase-field to linear order by

$$\delta \psi = -\nabla \cdot (\psi \delta \mathbf{x}). \quad (6.2.2)$$

Defining the chemical potential as the driving force of phase-field dissipation, i.e.,  $\tilde{\mu}_c = \delta \mathcal{F} / \delta \psi$ , we may vary the free energy as

$$\delta \mathcal{F} = \int d^d r \frac{\delta \mathcal{F}}{\delta \psi} \delta \psi = - \int d^d r \tilde{\mu}_c \nabla \cdot (\psi \delta \mathbf{x}). \quad (6.2.3)$$

Using that  $\tilde{\mu}_c$  can be written in terms of partial derivatives of the free energy, and repeated integration by parts, we were able to rewrite this variational in the form

$$\delta\mathcal{F} = \int d^d r \tilde{\sigma} : (\nabla\delta\mathbf{x}), \quad (6.2.4)$$

which gave a closed form for the microscopic configurational stress tensor

$$\tilde{\sigma}_{ij} = \frac{\delta\mathcal{F}}{(\partial_j\delta x_i)} = (\tilde{f} - \tilde{\mu}_c\psi)\delta_{ij} + \tilde{\mathbb{h}}_{ij}, \quad (6.2.5)$$

The microscopic stress tensor

with an explicit (and complicated) expression for  $\tilde{\mathbb{h}}$ . The fact that the variation of  $\mathcal{F}$  could be expressed as a variation in  $\nabla\delta\mathbf{x}$  is a consequence of the translational invariance of the free energy. The reason for naming  $\tilde{\sigma}$  the *microscopic* stress tensor is that in the presence of microscopic variations in the density field  $\psi$ , it naturally features variations in the stress on this microscopic level too. To connect the microscopic stress tensor to the macroscopic stress used in continuum mechanics, we used the coarse-graining operation of Eq. (4.4.1) with  $w = a_0$ , defining the macroscopic stress as

$$\sigma = \langle \tilde{\sigma} \rangle. \quad (6.2.6)$$

The stress tensor

By this coarse-graining operation, we were also able to connect this expression of the macroscopic stress tensor to the one used in hydrodynamics, Eq. (4.4.11). This allowed us to find a closed-form expression for  $\mathbb{h}$ , the conjugate to the strain  $\varepsilon$  at constant density. The interpretation of the PFC becomes especially important in discussing its elastic properties. This is also of importance in the expression of the stress tensor, as can be seen from the following argument; in some of the PFC literature, the PFC is interpreted as the relative density deviation, i.e., the real one-body-density  $\tilde{\rho}$  is expressed in terms of  $\psi$  as

$$\tilde{\rho} = (1 + \psi)\rho_0. \quad (6.2.7)$$

Here, however, it should be  $\tilde{\rho}$  that varies under a displacement field according to Eq. (6.2.2), and not  $\psi$  itself, giving

$$\rho_0\delta\psi = -\rho_0\nabla\cdot((1 + \psi)\delta\mathbf{x}), \quad (6.2.8)$$

which gives

$$\delta\mathcal{F} = - \int d^d r \tilde{\mu}_c \nabla \cdot ((1 + \psi)\delta\mathbf{x}) = - \int d^d r \tilde{\mu}_c \nabla \cdot \delta\mathbf{x} - \int d^d r \tilde{\mu}_c \nabla \cdot (\psi\delta\mathbf{x}). \quad (6.2.9)$$

The second part of this variation will give the same stress tensor as in Eq. (6.2.5), but the first part will also give a contribution, resulting in the following expression for the microscopic



stress tensor

$$(\tilde{f} - \tilde{\mu}_c(1 + \psi))\delta_{ij} + \tilde{\mathbb{h}}_{ij}. \quad (6.2.10)$$

Thus, the nature of the isotropic part of the stress depends on the exact connection between the phase-field and the one-body density. The part  $\mathbb{h}$  of the stress, which is conjugate to the strain, however, seems to be independent of these details, which is why in much of our work, we have taken  $\mathbb{h}$  as the stress tensor and left the question of the isotropic contribution for future work.

Another problem we addressed in the paper was the symmetry of the stress tensor. In the variational procedure in Ref. [20], the result was a non-symmetric expression for the stress tensor, namely

$$\tilde{\mathbb{h}}_{ij} = -(\mathcal{L}_1 \psi)\partial_{ij}\psi + (\partial_i \psi)\partial_j \mathcal{L}_1 \psi, \quad (6.2.11)$$

which is also the expression one gets from Eq. (9) in Paper II without further modifications. The stress tensor of continuum mechanics, however, is related to the coarse-grained stress  $\sigma = \langle \tilde{\sigma} \rangle$ . In the paper, we showed that upon coarse-graining, the gradient terms are small compared to non-gradient terms, which allows us to effectively "move" derivatives under the coarse-graining operation, similar to integration by parts and ignoring boundary terms. This point was made explicitly in the paper, but we will give an intuitive explanation here; compare a function  $g$  with a function that can be written as a gradient  $\partial_i f$ . If none of the functions  $g$  or  $f$  tends towards infinity, in the limit of larger and larger coarse-graining,  $\langle g \rangle \rightarrow g_0$ , where  $g_0 = \frac{1}{V} \int d^d r g$ , the average value of  $g$ .  $\partial_i f$  on the other hand, tends towards  $\langle \partial_i f \rangle = \partial_i \langle f \rangle \rightarrow \partial_i \frac{1}{V} \int d^d r f = 0$ . This explains why, even though the derived stress was non-symmetric on the microscopic level it became symmetric upon coarse-graining. It turns out that the notion of a microscopic stress is hard to define uniquely. Indeed, the derivation in the paper only determines the stress tensor up to a divergence-free contribution. Under the divergence operator, we have the following identity,

$$\partial_j (A \partial_{ij} B) = \partial_j (\delta_{ij} \partial_m (A \partial_m B) - \partial_i A \partial_j B), \quad (6.2.12)$$

Identity for symmetrizing the microscopic stress tensor

which can be shown by expanding both sides, and effectively tells us that we may move the independent index  $i$  under the divergence if we compensate by adding a term that is symmetric in  $i \leftrightarrow j$ . Thus, an equivalent expression for the microscopic  $\mathbb{h}$  is

$$\tilde{\mathbb{h}}_{ij} = -\delta_{ij} \partial_m ((\mathcal{L}_1 \psi) \partial_m \psi) + 2(\partial_{(i} \psi) \partial_{j)} \mathcal{L}_1 \psi, \quad (6.2.13)$$

which is symmetric in the indices  $i \leftrightarrow j$ . The difficulty in defining a unique microscopic stress echoes the discussion of the uniqueness of the stress brought forth in Ref. [90]; in that work, the authors fought with the same problem of uniquely determining an expression for the microscopic stress tensor in a more general statistical mechanics context. They found six conditions for the uniqueness of the microscopic stress, one of which was the symmetry of the stress, which suggests that using the identity of Eq. (6.2.12) is necessary

for a well-defined microscopic stress tensor. A similar conclusion was reached in a paper using molecular dynamics simulations, which showed that the symmetry of the stress tensor is intimately linked with the continuum assumption[91].

To connect the descriptions derived for the PFC with continuum elasticity, we calculated the elastic constants predicted for the different lattices. For the triangular symmetry, we considered the PFC in its ground state deformed by a displacement field  $\mathbf{u}$ , Eq. (5.6.1). Focusing on the elastic constants corresponding to strains at constant average density, we inserted this expression into the expression for  $\mathbb{h}_{ij}$  and discarded non-linear terms in  $\mathbf{u}$  and higher-order gradients. In these calculations, we made repeated use of the approximation that the distortion  $\mathbf{u} = \nabla \mathbf{u}$  is slowly varying and can be pulled out of the coarse-graining operation. What is left are quantities of the type  $\langle e^{i\mathbf{G}\cdot\mathbf{r}} \rangle$ , where  $\mathbf{G}$  is a lattice vector on the reciprocal lattice. Using the principle of reciprocal lattice resonance, as discussed in Sec. 5.4, we arrived in the paper's appendix at the following expression for  $\mathbb{h}$

$$\mathbb{h}_{ij} = 4A_{\text{tri}}^2 \partial_k u_l \sum_{n=\pm 1}^{\pm 3} q_i^{(n)} q_j^{(n)} q_k^{(n)} q_l^{(n)}. \quad (6.2.14)$$

This tetratic product sum is a particular type of vector product sum made from the collection of reciprocal vectors  $\mathcal{R}_{\text{tri}}^{(1)} \equiv \{\mathbf{q}^{(n)}\}_{\pm 1}^{\pm 3}$  called a *4th order moment tensor*. Due to its limited number of components, this sum can be evaluated explicitly. However, it was shown in Ref. [92] that for a collection of vectors such as  $\mathcal{R}_{\text{tri}}^{(1)}$ , that has a 6-fold rotational symmetry, its 4th-order moment tensor is necessarily isotropic. This means that it can be written in terms of the only three rank four isotropic tensors  $\delta_{ij}\delta_{kl}$ ,  $\delta_{ik}\delta_{jl}$ , and  $\delta_{il}\delta_{jk}$ , and a comparison of terms reveals that

$$\sum_{n=\pm 1}^{\pm 3} q_i^{(n)} q_j^{(n)} q_k^{(n)} q_l^{(n)} = \frac{3}{4}(\delta_{ij}\delta_{kl} + 2\delta_{k(i}\delta_{j)l}), \quad (6.2.15)$$

which led directly to the expression of  $\mathbb{h}_{ij}$  as

$$\mathbb{h}_{ij} = \left( \lambda \delta_{ij}\delta_{kl} + 2\mu \delta_{k(i}\delta_{j)l} \right) \partial_k u_l, \quad (6.2.16)$$

with  $\lambda = \mu = 3A_{\text{tri}}^2$ . This is a curious mathematical relation displaying how the isotropic elastic property of the triangular lattice is related to the symmetries of the reciprocal crystal lattice. In the case of the square PFC, a similar calculation leads to tetratic product sums in terms of both the sets  $\mathcal{R}_{\text{sq}}^{(1)} = \{\mathbf{q}^{(n)}\}_{\pm 1}^{\pm 2}$  and  $\mathcal{R}_{\text{sq}}^{(2)} = \{\mathbf{p}^{(n)}\}_{\pm 1}^{\pm 2}$  with  $\mathbf{q}^{(n)}$  from Eq. (5.3.1) and  $\mathbf{p}^{(n)}$  from Eq. (5.3.8). In this case, however, the lattice vector sets only have a four-fold symmetry, which means that only 2nd order moment tensors are identically isotropic. This leaves an additional contribution to the elastic constant tensor, namely  $\delta_{ij}k_l$ , which is not an isotropic tensor and is responsible for the anisotropic properties of the square lattice. More details on these tetratic vector products are found in the paper's appendix.

### 6.3 Paper III: A phase field crystal theory of the kinematics of dislocation lines

Vidar Skogvoll, Luiza Angheluta, Audun Skaugen, Marco Salvalaglio, and Jorge Viñals.  
*Journal of the Mechanics and Physics of Solids*, 166:104932, September 2022.

In this paper, we generalized the procedure of characterizing the topological content of the PFC in three dimensions. We found a closed-form expression for the mobility of the dislocations as discussed in Sec. 5.5. Additionally, as discussed in Sec. 5.6, ensuring mechanical equilibrium in a 3D model is not straightforward, so we also introduced a different scheme for finding the necessary displacement  $\mathbf{u}^\delta$  needed to ensure mechanical equilibrium, effectively extending the model of Ref. [21] to three dimensions.

As discussed in Sec. 4.3,  $\Theta_n \equiv -\mathbf{q}^{(n)} \cdot \mathbf{u}$  is a  $\mathcal{S}^1$  field with corresponding vortex defects. In three dimensions, the defects in these fields are lines  $\ell$ , and to each corresponds then a topological charge density  $\rho_{\text{top}}^{(n)}$

$$\rho_{\text{top}}^{(n)} = s_n \int_{\ell} d\ell \delta^{(3)}(\mathbf{r} - \mathbf{r}') \mathbf{t}, \quad (6.3.1)$$

where  $\mathbf{t}$  is the tangent vector to the line. To relate these vector defect densities to the defect charge of the crystal, i.e., the dislocation density tensor, we multiply with  $\rho_{\text{top}}^{(n)}$  with  $\mathbf{q}^{(n)}$ , and used that  $2\pi s_n = \mathbf{b} \cdot \mathbf{q}^{(n)}$ , to get

$$\begin{aligned} \rho_{\text{top};i}^{(n)} q_j &= s_n q_j^{(n)} \int_{\ell} d\ell \delta^{(3)}(\mathbf{r} - \mathbf{r}') t_i = \frac{1}{2\pi} q_k^{(n)} q_j^{(n)} b_k \int_{\ell} d\ell \delta^{(3)}(\mathbf{r} - \mathbf{r}') t_i \\ &= \frac{1}{2\pi} q_k^{(n)} q_j^{(n)} \alpha_{ik}. \end{aligned} \quad (6.3.2)$$

Consider now the reciprocal lattice to which  $\mathbf{q}^{(n)}$  belongs. As discussed in Sec. 5.5, we derived in this paper the general expression of Eq. (5.5.3), which can be used to get

$$\sum_{\mathbf{q}^{(n)} \in \mathcal{R}^{(1)}} \rho_{\text{top};i}^{(n)} \mathbf{q}_j^{(n)} = \frac{1}{2\pi} \alpha_{ik} q_k^{(n)} q_j^{(n)} = \alpha_{ij} \frac{N}{2\pi d}, \quad (6.3.3)$$

which gives

$$\alpha_{ij} = \frac{2\pi d}{N} \sum_{\mathbf{q}^{(n)} \in \mathcal{R}^{(1)}} \rho_{\text{top};i}^{(n)} q_j^{(n)}. \quad (6.3.4)$$

The dislocation density in terms of  $\mathcal{S}^1$  defect densities

This equation relates the dislocation density tensor in terms of the defect densities for the  $\mathcal{S}^1$  fields  $\theta_n$ .

As mentioned in Sec. 5.5, by introducing the vector field  $\Psi = (\Re(\eta_n), \Im(\eta_n))$  we could use the Halperin-Mazenko method, Sec. 3.4, to find an expression for  $\rho_{\text{top}}^{(n)}$  in terms of  $\eta_n$  and thus, reconstruct the dislocation density from Eq. (6.3.4). We found

$$\rho_{\text{top}}^{(n)} = \mathbf{D}^{(n)} \delta^{(2)}(\eta_n), \quad (6.3.5)$$

where  $\delta^{(2)}(\eta_n) = \delta^{(2)}(\Psi) = \delta(\Re(\eta_n))\delta(\Im(\eta_n))$ , and  $\mathbf{D}^{(n)}$  as defined in Eq. (3.4.10). Using these, we derived the following expression for the dislocation density in the PFC model

$$\alpha_{ij} = \frac{2\pi d}{N} \sum_{n=\pm 1}^{N/2} \delta^{(2)}(\eta_n) D_i^{(n)} q_j^{(n)}, \quad (6.3.6)$$

The dislocation density in the PFC model

where the sum is over the  $N$  primary reciprocal lattice vectors in question. By using the  $N = 12$  primary reciprocal lattice vectors of the bcc lattice and  $d = 3$ , we get Eq. (12) of the paper. The factor  $q_0$ , which appears in the paper, is the length of the smallest reciprocal lattice, which has in this thesis been set to  $q_0 = 1$ . Notice that in this equation, we have the delta function acting on the amplitudes  $\eta_n$ . In the computations, this was done using a Gaussian approximation

$$\delta^{(2)}(\eta_n) \approx \frac{1}{2\pi w^2} e^{-|\eta_n|^2/(2w^2)}, \quad (6.3.7)$$

with  $w = \eta_0/10$  where  $\eta_0$  is the equilibrium value of the amplitudes.

Furthermore, by taking the time derivative of this quantity, we expressed the velocity of the dislocation lines directly in terms of the dynamics of the amplitudes, given by Eq. (5.4.12). This was used in the paper to express the line velocity as a function of the applied stress  $\mathbb{h}^{(\text{ext})}$  (denoted  $\tilde{\sigma}$  in the paper) and was found in Eq. (32) of the paper to be

$$\mathbf{v} = M \mathbf{t} \cdot (\mathbb{h}^{(\text{ext})} \cdot \mathbf{b}), \quad (6.3.8)$$

with an explicit expression for the mobility  $M$  given underneath Eq. (32) in the paper. Thus, the velocity was found to be proportional to the Peach-Koehler force, Eq. (4.3.10), with  $\mathbb{h}^{(\text{ext})}$  as the external stress.

There is an interesting side note to the derivation of the dislocation velocity, namely that it was only possible because the evolution equations of the amplitudes "decouple" at the dislocation core. We mean this in the following sense: the evolution of the amplitudes  $\eta_n$  derived from Eq. (5.4.12) is given in a generic form by

$$\partial_t \eta_n = -\mathbf{q}^{(n)2} \mathcal{G}_n^2 \eta_n + P_n(\{\eta_n\}_{\pm 1}^{\pm 6}) \quad (6.3.9)$$

where  $P_n(\{\eta_n\}_{\pm 1}^{\pm 6})$  is a polynomial in all the amplitudes  $\{\eta_n\}_{\pm 1}^{\pm 6}$ . At the dislocation core, the amplitude  $\eta_n$  itself goes to zero, so any term in  $P_n(\{\eta_n\}_{\pm 1}^{\pm 6})$  proportional to  $\eta_n$  will not contribute. Not only this but also some of the other amplitudes go to zero at the dislocation core, which means that also other terms in  $P_n(\{\eta_n\}_{\pm 1}^{\pm 6})$  will not contribute to the evolution of the amplitude at the dislocation core. It was observed in Ref. [20] that *for the subset of amplitudes that go zero*, i.e., those that contribute to the dislocation density tensor, for the triangular lattice, all terms in  $P_n(\{\eta_n\})$  vanish, leaving a decoupled set of equations for the amplitudes that contribute to the dislocation density tensor. In this paper, we learned that this is no coincidence and is due to the resonance conditions on the reciprocal lattice vectors that go into the polynomial terms in  $P_n(\{\eta_n\}_{\pm 1}^{\pm 6})$ . From the procedure in deriving the free energy, Eq. (5.4.3), using the resonance condition, it happens that every term in  $P_n(\{\eta_n\}_{\pm 1}^{\pm 6})$  results from selecting amplitude indices  $H \subset \{n'\}_{n'=\pm 1}^{\pm 6}$  corresponding to reciprocal lattice vectors  $\{\mathbf{q}^{(n')}\}_{n' \in H}$  that together with  $\mathbf{q}^{(n)}$  give 0, i.e.,

$$\mathbf{q}^{(n)} + \sum_{n' \in H} \mathbf{q}^{(n')} = 0. \quad (6.3.10)$$

Contracting this equation by  $\frac{1}{2\pi} \mathbf{b}$ , we get

$$s_n + \sum_{n' \in H} s_{n'} = 0. \quad (6.3.11)$$

If  $\eta_n$  is an amplitude that goes to zero at the dislocation core, then  $s_n \neq 0$ , and it follows that at least for one  $n' \in H$ ,  $s_{n'} \neq 0$  as well. This means that in every term in  $P_n(\{\eta_n\}_{\pm 1}^{\pm 6})$ , there is an amplitude that is zero at the dislocation core, and the amplitudes decouple, in the general case. It is enticing to imagine how this mechanism may be generalized to amplitude equations for any lattice symmetry. This indicates that there is a curious mathematical relation between the resonances of reciprocal lattice vectors and the evolution equations of the amplitudes near defects. It may thus be possible to generalize the equations of motion of dislocations in periodic lattices beyond the single-mode approximations typically used in PFC theories and make predictions on dislocation mobilities in the general case, which would be a powerful theoretical result.

The model introduced in Ref. [21] and used with Paper I to study nucleation was based on solving for the equilibrium stress tensor in two dimensions in isotropic elasticity. Going to three dimensions and anisotropic elasticity, we generalized the method and developed the following scheme to constrain the PFC to mechanical equilibrium. The goal, as in Ref. [21], was to find a displacement field  $\mathbf{u}^\delta$  that, when applied to the PFC, would make the stress  $\mathbb{h}^\psi$  as calculated by the PFC constrained to mechanical equilibrium. Supposing that this is possible, we have

$$\mathbb{h}^\psi + \mathcal{C} : \varepsilon^\delta = \mathbb{h}^{\text{eq}}, \quad (6.3.12)$$

where  $\varepsilon_{ij}^\delta = \partial_j u_i^\delta$ . Taking the divergence and using that  $\nabla \cdot \mathbb{h}^{\text{eq}} = 0$ , we get

$$\nabla \cdot (\mathcal{C} : \varepsilon^\delta) = -\nabla \cdot \mathbb{h}^\psi, \quad (6.3.13)$$

which is a system of three third-order partial differential equations for the three unknown components of  $\mathbf{u}^\delta$ . This can be solved using the Green's function in Fourier space for anisotropic elasticity, given in Ref. [93], as shown in Appendix A.2.1.

## 6.4 Paper IV: Hydrodynamic phase field crystal approach to interfaces, dislocations and multi-grain networks

Vidar Skogvoll, Marco Salvalaglio, and Luiza Angheluta.

*Modelling and Simulation in Materials Science and Engineering*, October 2022.

While the model introduced in Paper III was shown to produce stress fields that agreed with the continuum elasticity theory, it is still a theory that approximates the overdamped limit. In fast processes, however, such as crack propagation or dislocation nucleation, the time scale associated with dislocation motion and elastic waves approach each other. Thus, an explicit coupling of the mode of transport between the elastic degrees of freedom and dislocation motion is necessary, i.e., addressing the time scale problem by the second strategy outlined in Sec. 5.6. In this paper, we derived equations of motion by first proposing a free energy which included a kinetic energy term carried by a macroscopic velocity field, and deriving equations of motion that guaranteed a decrease in free energy, consistent with the second law of thermodynamics.

To understand the approach used in the paper, consider this very simple derivation of the equation of motion of the PFC, Eq. (5.0.2). Taking the time derivative of Eq. (5.0.1), we get

$$\partial_t \mathcal{F} = \int d^d r \frac{\delta \mathcal{F}}{\delta \psi} \partial_t \psi. \quad (6.4.1)$$

If  $\psi$  is a conserved field, it should evolve according to  $\partial_t \psi + \nabla \cdot \tilde{\mathbf{J}} = 0$  for some current  $\tilde{\mathbf{J}}$ , which after integration by parts give

$$\partial_t \mathcal{F} = - \int d^d r \nabla \cdot \left( \frac{\delta \mathcal{F}}{\delta \psi} \right) \cdot \tilde{\mathbf{J}}. \quad (6.4.2)$$

From this, we see that  $\tilde{\mathbf{J}} = \nabla \left( \frac{\delta \mathcal{F}}{\delta \psi} \right)$  gives a strictly decreasing free energy, which gives the following evolution equation for  $\psi$

$$\partial_t \psi = \nabla^2 \left( \frac{\delta \mathcal{F}}{\delta \psi} \right), \quad (6.4.3)$$

which is the PFC evolution equation, Eq. (5.0.2). This evolution equation, therefore, is arguably the simplest dynamical equation for a conserved field  $\psi$  that guarantees a decrease in the free energy. However, as outlined in Sec. 5.6, in the case of a crystalline state, there are modes of energy dissipation that are not characterized by this simple evolution equation,

which has caused the need for extensions. A similar exercise as the above, but with a free energy as a function of a density field  $\rho$  that is smoothly varying on the atomic scale, leads to the Navier-Stokes equations, shown in Sec. 2.1 in the paper, containing the modes associated to pressure waves in a liquid. The idea then, for this paper, was to show how to combine these two results consistently using the coarse-graining of Eq. (4.4.1). This effort led to the coupled set of Eqs. (22) in the paper, which reduced to the PFC evolution equation in one limit and the Navier-Stokes equations in the other. In particular, under some simplifying assumptions related to the average density of the PFC, we found an effective model which simulated the relaxation of elastic waves and benchmarked that against the model proposed in Paper III. We showed analytically that it recovered the same dispersion relation as that of Ref. [81] and that in some limits evolved the PFC in mechanical equilibrium  $\nabla \cdot \mathbb{h}\psi = 0$ . An additional benefit of the model is that it did not require a fixed lattice orientation reference, like the hydrodynamic APFC model in Ref. [81]. Thus, it could be used to study equilibrium systems such as polycrystalline materials, as we exemplified in the final section of the paper.

As discussed in section 4.4, due to the broken translational symmetry, one expects a diffusional mode of mass transport related to vacancy diffusion only in the presence of the crystal structure. In this paper, we found that a proper liquid limit could be found by using the *structure-function* of the PFC as a phenomenological spatially dependent mobility factor. This structure-function is given by

$$\mathcal{S} = \langle \nabla \psi \nabla \psi \rangle, \quad (6.4.4)$$

The structure-function of the PFC

and is zero in the liquid phase. The spatial dependency of  $\mathcal{S}$  made it hard to do large-scale simulations without further numerical development, but preliminary simulations were done. It was found that in the case of an anisotropic seed, the resulting microstructure using the spatially dependent mobility retained the anisotropy of the initial seed, as opposed to the constant mobility used in classical PFC modeling. The structure-function is an interesting object because it can also be shown to determine the strain in the PFC without the demodulation procedure of Eq. (5.4.1), which we only discovered after publishing the paper and is detailed in Sec. 6.6.

## 6.5 Paper V: A unified field theory of topological defects and non-linear local excitations

Vidar Skogvoll, Jonas Rønning, Marco Salvalaglio, and Luiza Angheluta.  
Submitted to *npj Computational Materials*, arXiv: 2302.03035, 2023.

In Papers I-IV and in many other works analyzing defects in Ginzburg Landau theories,



the defect density is expressed as a singular quantity at the zero of the order parameter. This procedure is necessary to connect the description to the homotopy group presented in Section 3.3, where the defect is defined in terms of the ground state manifold. It relates the definition of topological defect charge in Eq. (3.3.1) with the surface integral over the area contained in  $\partial\mathcal{M}$ . Thus, the method of Halperin and Mazenko presented in Sec. 3.4, relies on expressing the defect density in terms of the delta function, which for numerical purposes required arbitrary approximations, such as the one in Eq. (6.3.7). However, through much of the work on these kinds of systems, it has been seen that the  $D$ -field, which in the Halperin-Mazenko method is only an auxiliary Jacobian determinant in the transformation of the delta function, is itself an excellent indicator of topological defects. A theoretical understanding of why this is the case has been missing from the literature and was the topic of this paper. By redefining the topological charge in terms of the smooth order parameter  $\Psi$ , we were able to show that the  $D$  field is linked to a smooth defect density  $\rho$ , and that  $\rho$  also captures local non-linear perturbations of the field. Thus, besides being numerically more lenient than the Halperin Mazenko defect density,  $\rho$  could be used to study the physics leading *up to* nucleation.

The argument of the paper went as follows; we generalized the topological charge, Eq. (3.3.1), by considering the order parameter  $\Psi$  as an order parameter in  $R = \mathcal{D}^2$  and looked at the relative area of  $\mathcal{D}^2$  spanned by  $\Psi$  by a circuit  $\partial\mathcal{M}_R$

$$s = \frac{1}{\pi\Psi_0^2} \oint_{\partial\mathcal{M}_R} \frac{1}{2} \epsilon_{mn} \Psi_m d\Psi_n, \quad (6.5.1)$$

see Fig. 2 in the paper. If we are in the far field of a defect,  $|\Psi| = \Psi_0$ , and the topological charge  $s$  reduces to that of Eq. (3.3.1). From this expression of  $s$ , we applied Stokes' theorem and derived the defect density  $\rho$ , without the need to introduce delta functions or transformations thereof. Close to the core, the charge  $s$  goes to zero, which makes the topological defect appear as a blob-like feature in the density  $\rho$  derived from  $s$ . Since this approach was only based on Stokes theorem, and not a transformation of the delta function, it was more easily extended to higher dimensions, and we provided a full derivation for any order parameter dimension  $n$  and spatial dimension  $d$  in the paper's appendix.

As mentioned, we found that as opposed to  $\rho_{\text{top}}$ , the defect density  $\rho$  captured not only topological defects, but also a certain class of local excitations for which the magnitude of the field  $\Psi$  is reduced, such as shock waves in Bose-Einstein condensates and non-linear elastic distortions in the PFC. Via this, we were able to visualize the full process of nucleation, through the development of preliminary patterns in the defect density field. Further, we discovered relations between defects in different types of order, such as how the topological defects in the arches of a nematic liquid crystal become the nucleation sites for defects in the broken rotational order. In the case of the dislocation density of Eq. (6.3.4), inserting  $\rho_{\text{top}}^{(n)} = \frac{D^{(n)}}{\pi\eta_0^2}$  for the amplitude defect densities, we get



$$\alpha_{ij}^{\text{NS}} = \frac{2d}{N\eta_0^2} \sum_{\mathbf{q}^{(n)} \in \mathcal{R}^{(1)}} D_i^{(n)} q_j^{(n)}. \quad (6.5.2)$$

The non-singular dislocation density in the PFC model

This equation allowed for the extraction of a coarse-grained dislocation density, which showed the dislocation content as a smooth field localizing at the lattice incompatibility, as exemplified in Fig. 7 in the paper for a rotated inclusion in the PFC.

## 6.6 Outlook

This thesis puts forward a versatile theoretical framework that can be further extended and applied in several exciting research directions.

Firstly, it serves as an extensive guide on how to use topology and analysis of topological defects for field theories in which the topology of the ground state manifold is more complex than that of, e.g., a simple  $\mathcal{S}^1$  state. The expression of the dislocation density in terms of the PFC variables, Eq. (6.3.6), is useful in its own right, to anyone who wants to study dislocation dynamics using the PFC methodology. However, using the derived equations for the lattice reciprocal vectors, such as Eq. (5.5.3), Eq. (6.3.4) is a *generic* expression for the dislocation density in terms of the fundamental defect densities  $\rho_{\text{top}}^{(n)}$  corresponding to the  $\mathcal{S}^1$  fields. As we have seen, these fundamental defect densities may be extracted in different ways, so this expression may also be used for other computational problems where the defect densities  $\rho_{\text{top}}^{(n)}$  are available. Thus, the thesis represents a methodology for finding the defect density for topological fields where the topological space is decomposable into fundamental fields, e.g. how the 3-torus is decomposable into  $\mathcal{S}^1 \times \mathcal{S}^1 \times \mathcal{S}^1$ . A possible extension, then, is to analyze the defect structure of systems where the ground state manifold is more complicated. For instance, a fundamental analysis of the topological content in nematic liquid crystals in three dimensions, i.e., for the topological space  $\mathbb{R}P^2$ , was recently presented in Ref. [32], and the defect densities given in Paper V can be used for any  $\mathcal{S}^n$  theory. One might therefore speculate whether the methods presented here could be used to determine the structure of topological defect density of a system where the ground state manifold is even more complicated than the torus, e.g., given by  $\mathbb{R}P^2 \times \mathbb{R}P^2 \times \mathcal{S}^2$ . Another application of the methodology is the analysis of the topological content of quasi-crystals, which are crystal structures that a single Bravais lattice cannot describe.

Secondly, we have made explicit the coupling between the microscopic nature of the rapidly varying phase-field with the continuum theories of elasticity, using the formalism of spatial coarse-graining. Paper II represents essential work that can be used to derive stresses in any Ginzburg-Landau theory and also addresses fundamental questions regarding the relationship between the microscopic and continuum stress. The methodology can be extended to any theory in which a Ginzburg-Landau type free energy governs the order parameter. With the hydrodynamic framework applicable to the PFC in Paper IV, we have

derived a method that can be used to study non-equilibrium phenomena not limited to single-crystal configurations. Together with the analysis of topological defects provided in Paper III, this opens up the possibility for a systematic study of dislocation dynamics and grain boundary problems addressed using the PFC methodology. We have also seen how the symmetries of the reciprocal lattice vectors, captured by the lattice vector products described in Eq. (5.5.3) and the appendix of Paper II, upon coarse-graining are intimately linked with the elastic properties of the lattices. An extended investigation of these properties could shed new light on the link between the symmetry of lattices, and continuum elasticity. As an example of this, consider the following result for the structure-factor  $\mathcal{S}$ , which was derived in collaboration with M. Salvalaglio and J. Viñals after the publication of Paper IV: for a phase-field in the one-mode approximation distorted from equilibrium by a displacement field  $\mathbf{u}$ , Eq. (5.5.1), we get

$$\begin{aligned} \mathcal{S}_{ij} &= \eta_0^2 \sum_{\mathbf{q}^{(n)} \in \mathcal{R}^{(1)}} q_i^{(n)} q_j^{(n)} - \eta_0^2 \sum_{\mathbf{q}^{(n)} \in \mathcal{R}^{(1)}} \left( q_i^{(n)} \partial_j (q_k^{(n)} u_k) + q_j^{(n)} \partial_i (q_k^{(n)} u_k) \right) + \mathcal{O}(\mathbf{u}^2) \\ &= \eta_0^2 \frac{N}{d} \delta_{ij} - 2\eta_0^2 \frac{N}{d} \varepsilon_{ij} + \mathcal{O}(\mathbf{u}^2), \end{aligned} \quad (6.6.1)$$

after using Eq. (5.5.3). By ignoring higher orders in  $\mathbf{u}$  we get

$$\varepsilon_{ij} = \frac{1}{2} \delta_{ij} - \frac{d}{2N\eta_0^2} \mathcal{S}_{ij}. \quad (6.6.2)$$

This equation contains no singularities, and by assuming that it holds in general, one may suggest the following expression for a non-singular strain, extracted from a phase-field  $\psi$  directly

$$\varepsilon_{ij}^{\text{NS}} = \frac{1}{2} \delta_{ij} - \frac{d}{2N\eta_0^2} \mathcal{S}_{ij}. \quad (6.6.3)$$

Non-singular strain extracted from the PFC

Thus, the structure-function is closely linked with the elastic state of the PFC. In fact, we see that a non-zero value of  $\mathcal{S}$ , i.e., a non-zero  $\eta_0$ , is linked with the emergence of the crystalline state itself.

Through the formalism developed in Paper V, we saw that topological defects do really have a finite extension and that this extent determines the interaction with other non-linear perturbations. Thus, we may use it to study defects with extended cores in more detail and answer questions like: how does the interaction energy change as topological defects get close? In the case of crystalline solids, the dislocation density given by Eq. (6.5.2) is non-singular. A natural idea is to derive a non-singular distortion  $\mathbf{u}^{\text{NS}}$  to replace the unphysical divergences in  $\mathbf{u}$  shown in Fig. 4.7. As discussed in Sec. 4.5, the dislocation density  $\alpha^{\text{NS}}$  taken as a source of the curl of  $\mathbf{u}^{\text{NS}}$  is not enough to uniquely determine  $\mathbf{u}^{\text{NS}}$ . However, a

non-singular strain  $\varepsilon^{\text{NS}}$  can be derived from the PFC through Eq. (6.6.3). Together,  $\varepsilon^{\text{NS}}$  and  $\alpha^{\text{NS}}$  can be used to determine a non-singular distortion as seen by the following procedure: decomposing the distortion  $\mathfrak{u}$  into the strain  $\varepsilon$  and rotation  $\omega$ , Eq. (4.3.6) becomes

$$\nabla \times \omega = -\alpha - \nabla \times \varepsilon \equiv -\mathbb{S}, \quad (6.6.4)$$

where  $\mathbb{S} = \alpha + \nabla \times \varepsilon$  is treated as a rank 2 source tensor. Writing  $\omega_{ij} = -\epsilon_{ijk}\Omega_k$  as represented in its vector form  $\mathbf{\Omega}$ , Eq. (4.1.5), we get

$$-\epsilon_{ikm}\epsilon_{jml}\partial_k\Omega_l = -\mathbb{S}_{ij}. \quad (6.6.5)$$

The contraction over Levi-Civita symbols gives

$$\partial_j\Omega_i - \delta_{ij}\partial_k\Omega_k = \mathbb{S}_{ij}, \quad (6.6.6)$$

which we may trace to get

$$\partial_k\Omega_k = \frac{\mathbb{S}_{kk}}{1-d}, \quad (6.6.7)$$

so

$$\partial_j\Omega_i = \mathbb{S}_{ij} + \frac{\mathbb{S}_{kk}}{1-d}\delta_{ij}, \quad (6.6.8)$$

which defines  $\mathbf{\Omega}$  up to some reference point and may be solved using an appropriate partial differential equation solver. Together with Eq. (6.6.3), it is then sufficient to determine all the components of a non-singular distortion

$$\mathfrak{u}^{\text{NS}} = \varepsilon^{\text{NS}} + \omega^{\text{NS}}, \quad (6.6.9)$$

Non-singular distortion extracted from the PFC

where  $\varepsilon^{\text{NS}}$  is given by Eq. (6.6.3) and  $\omega^{\text{NS}}$  is determined by Eq. (6.6.8) with the source  $\mathbb{S}$  constructed from  $\varepsilon^{\text{NS}}$  and  $\alpha^{\text{NS}}$ , Eq. (6.5.2).

Finally, the work conducted in this thesis also paves the way for discoveries in applied research fields. Recent progress has made several new soft matter systems for probing, such as cells,  $k$ -atic colloids, and other organic materials. The order parameters in such systems are characterized by their topological space, but so far, the Halperin-Mazenko method has not yet been applied to all of these areas. For instance, the structure and topological defects in the organization of cells in biological materials have been shown to predict the nature of morphogenesis. These ordered states, and corresponding defects, arise because cells are trying to maximize area to circumference, forming a hexagonal structure, or aligning their elongation to minimize elastic distortion, forming nematic and polar order. The topological defects in the nematic order of actin fibers have been shown to be organizational centers for the growth of tentacles in hydra [94], and the polar order of cells has been shown to control the morphogenesis of heads or tails in Planarian flatworms [95]. In more exotic examples, cells have been shown to form square lattices in Crustacean *Parhyale hawaiiensis*,

and produce dislocations [96]. With the methods we have discussed in this thesis, one may explore the connection between the topological defects of these different systems and establish unified frameworks and analogies in which results and discoveries in the respective fields can be easily interpreted in the language of others. In the field of hard matter, artificial materials that exhibit exotic properties, metamaterial, e.g., displaying a negative refractive index, highly anisotropic heat conductivity, or extreme structural integrity, have recently gained scientific traction. The properties of these materials come from the microscopic structure, which is on a smaller length scale than the typical wavelength of the phenomena with which they interact. For instance, a negative refraction index, which has several potential fields of application, can be constructed by organizing microscopic wires in a structure, yielding effective permittivity and permeability when coarse-grained on the scale of the wavelength of the interacting electromagnetic waves [97]. Along the same lines, recent advances in detailed shape engineering have enabled the fine-tuning of the response of certain microscopic materials when exposed to external stimuli such as heat or light. Under these conditions, the arrangement of topological defects often controls the final structure, the control over which can be applied to advance several fields, with applications including tailored soft machines and deployable structures [98]. The idea of effective material properties due to the coarse-graining of microscopic structures has been a recurring theme in this thesis. With the knowledge of the nature of topological defect interactions, and the details on how to simulate them, the framework presented in this thesis can be applied to shed light on how topological defects affect the properties of such exotic materials. Maybe not catapulting, but hopefully gently nudging physics into a new century of great discoveries.

## APPENDICES



## APPENDIX A

### *Numerical methods*

#### A.1 Numerical simulation of loop annihilation in the PFC

In order to facilitate the verification of the results, and also to serve as a reference for groups that want to enter into the PFC research field, we provide in this section step-by-step instructions on how to initiate a full 3D bcc PFC model, with a loop and the subsequent evolution. See Table A.1 for the parameters necessary to initiate loops in other crystalline symmetries. A 3D computational grid is set up with a predefined number of atomic lattice units ( $m_x, m_y, m_z$ ) in each direction and the spatial resolution set  $\Delta x = \Delta y = \Delta z = a_0/7$ , where  $a_0 = 2\pi\sqrt{2}$  is the lattice constant. From the  $N_x = 7m_x$  grid points in  $x$  defined by  $x = (0, \Delta x, \dots, m_x a_0 - \Delta x)$ , we construct the grid points in Fourier space

$$k_x = \frac{2\pi}{m_x a_0} \left( 0, 1, \dots, \left\lfloor \frac{N_x}{2} \right\rfloor, -\left\lfloor \frac{N_x - 1}{2} \right\rfloor, \dots, -1 \right), \quad (\text{A.I.1})$$

where  $\lfloor \frac{N_x}{2} \rfloor$  is  $\frac{N_x}{2}$  rounded down to the closest integer.  $y, k_y, z$  and  $k_z$  are defined similarly and  $\mathbf{k}^2$  is a 3D matrix defined by

$$\mathbf{k}^2 = k_x^2 + k_y^2 + k_z^2. \quad (\text{A.I.2})$$

For a field  $\psi$  encoded in a  $N_x \times N_y \times N_z$  matrix,  $k_x$  is used to calculate derivatives of the field  $\psi$  by

$$\partial_x \psi = \text{ifftn}(\text{i}k_x \cdot \text{fftn}(\psi)), \quad (\text{A.I.3})$$

where  $\text{fftn}$  ( $\text{ifftn}$ ) is the (inverse) fast Fourier transform algorithm, and  $\cdot$  is the element-wise multiplication of each slice  $\psi(i, :, :)$  by  $k_x(i)$ ,  $i = 1, \dots, N_x$ , where  $(:)$  denotes all the elements in that dimension. This operation is done automatically in `MATLAB` if the dimensions are defined appropriately. Similar expressions hold for  $y$  and  $z$ .

Note: If the resolution is not an odd number, the numerical procedure of Fourier transforming back and forth will produce spurious imaginary contributions to nominally real quantities such as  $\partial_x \psi$ .

### A.I.I. Preparation of the initial condition

Given the parameters  $\psi_0$  and  $r$ , the equilibrium value  $A$  of the amplitude is calculated by  $A = -\frac{2}{15}\psi_0 + \frac{1}{15}\sqrt{-5r - 11\psi_0}$  [67]. For the symmetries where several modes are needed, the equilibrium values of the first, second, and third modes,  $A, B$ , and  $C$ , respectively, are found by solving the set of equations given in Tab. A.I. The initial amplitudes  $\{\eta_n\}_{n=1}^6$  are then constructed as constant  $N_x \times N_y \times N_z$  matrices with the value  $A$ . Note that we are only calculating 6 of the 12 modes of the first modes in the reciprocal lattice since the remaining 6 are only complex conjugates of these. In order to insert a dislocation into the system, these fields are then multiplied with the matrix  $e^{i\theta_n}$

$$\eta_n \rightarrow \eta_n e^{i\theta_n}, \quad (\text{A.I.4})$$

Adding dislocations to amplitudes

where  $\theta_n$  is the phase circulation needed to produce the desired dislocation.

Details are given in Ref. [3], but here we state the result. To produce a circular dislocation with Burgers vector  $\mathbf{b}$ , centered at  $\mathbf{r}_0 = (x_0, y_0, z_0)$ , with radius  $R$ , in the plane normal to the unit vector  $\mathbf{n} = (n_x, n_y, n_z)$ , we must calculate

$$m_2 = n_x(x - x_0) + n_y(y - y_0) + n_z(z - z_0), \quad (\text{A.I.5})$$

and

$$m_1 = \sqrt{(x - x_0 - m_2 n_x)^2 + (y - y_0 - m_2 n_y)^2 + (z - z_0 - m_2 n_z)^2}, \quad (\text{A.I.6})$$

from which we get

$$\theta_1 = \text{atan2}(m_2, m_1 + R), \quad (\text{A.I.7})$$

and

$$\theta_2 = \text{atan2}(m_2, m_1 - R). \quad (\text{A.I.8})$$

We then get

$$\theta_n = s_n(\theta_1 - \theta_2), \quad (\text{A.I.9})$$

The phase corresponding to a dislocation ring

where

$$s_n = \frac{1}{2\pi} \mathbf{q}^{(n)} \cdot \mathbf{b}, \quad (\text{A.I.10})$$

where  $\mathbf{q}^{(n)}$  is the reciprocal lattice vector associated to  $\eta_n$ . Once  $\{\eta_n\}$  are calculated, the field  $\psi$  is reconstructed through

$$\psi = \psi_0 + \sum_{n=1}^6 \eta_n e^{i\mathbf{q}^{(n)} \cdot \mathbf{r}} + \text{c.c.} \quad (\text{A.I.11})$$



Near the core,  $\psi$  will contain sharp gradients since the amplitudes were only given the correct value of the phase. Thus, the state is evolved according to standard dissipative dynamics, Sec. A.1.4, for 100 time steps, which is sufficient to regularize the core.

### A.1.2. Coarse-graining

Coarse-graining is done using the convolution theorem, which states that

$$\begin{aligned} \text{fftn}(\langle \tilde{A} \rangle(\mathbf{r})) &= \text{fftn} \left( \int d^d r' \tilde{\sigma}(\mathbf{r}') \frac{1}{(2\pi w^2)^{d/2}} \exp \left( -\frac{(\mathbf{r} - \mathbf{r}')^2}{2w^2} \right) \right) \\ &= \text{fftn}(\tilde{A}) \text{fftn} \left( \frac{1}{(2\pi w^2)^{d/2}} \exp \left( -\frac{\mathbf{r}^2}{2w^2} \right) \right) = \text{fftn}(\tilde{A}) e^{-w^2 \mathbf{k}^2/2}. \end{aligned} \quad (\text{A.1.12})$$

Thus, the coarse-graining in Eq. (4.4.1), with width  $w$ , is given by

$$\langle \tilde{A} \rangle(\mathbf{r}) = \text{ifftn} \left( \text{fftn}(\tilde{A}) \exp \left( -\frac{w^2}{2} \mathbf{k}^2 \right) \right). \quad (\text{A.1.13})$$

Numerical coarse-graining

### A.1.3. Analysis of topological properties

Given a phase-field configuration by the 3D matrix  $\psi$ , we first find the amplitudes by demodulation, Eq. (5.4.1). Numerically, this is done by

$$\eta_n = \text{ifftn} \left( \text{fftn} \left( \exp \left( -i \left( q_x^{(n)} x + q_y^{(n)} y + q_z^{(n)} z \right) \right) \psi \right) \exp \left( -\frac{w^2}{2} \mathbf{k}^2 \right) \right). \quad (\text{A.1.14})$$

Numerical demodulation

Then, the 9 components of the dislocation density tensor  $\alpha$  are computed using Eq. (6.3.6), with the approximation of the delta function given in Eq. (6.3.7).  $\alpha$  will be a mostly zero matrix with large values on the dislocation line. If calculated correctly,  $\alpha$  will be roughly given by the outer product  $t_i B_j$ , where  $B_j$  is a Burgers vector density in the plane  $\mathcal{M}$  perpendicular to  $\mathbf{t}$ . To identify dislocation nodes and their character, we construct the auxiliary quantity

$$B = \sqrt{\alpha_{ij} \alpha_{ij}} \quad \left( = \sqrt{t_i B_j t_i B_j} = \sqrt{\mathbf{B}^2} = |\mathbf{B}| \right). \quad (\text{A.1.15})$$

Given a point  $\mathbf{r}_0 = (x_0, y_0, z_0)$  with a large value of  $B$ , we calculate

$$b_0 = \frac{1}{R} \text{sum}_{|\mathbf{r} - \mathbf{r}_0| < R} (B), \quad (\text{A.1.16})$$

for  $R = \frac{1}{2}a_0$ , which is an approximation of

$$\int_{\mathcal{M}} d^2r \sqrt{\alpha_{ij}\alpha_{ij}} = \int_{\mathcal{M}} d^2r |\mathbf{B}|. \quad (\text{A.1.17})$$

If

$$b_0 > \text{tol} \cdot a_0, \quad (\text{A.1.18})$$

where  $\text{tol} \sim 0.5$ , we accept the point  $r_0$  as belonging to the dislocation line and determine the character by considering the matrix  $\alpha_0$  of  $\alpha$  at  $r_0$ . This matrix is decomposed by singular value decomposition

$$\alpha_0 = U \Sigma V^T, \quad (\text{A.1.19})$$

where  $\Sigma$  is a diagonal matrix containing the singular values of  $\alpha_0$  and  $U$  and  $V$  are unitary matrices.  $\Sigma$  will only contain one nonzero singular value and the corresponding columns of  $U$  and  $V$  will be  $\mathbf{t}$  and  $\mathbf{b}/|\mathbf{b}|$ , respectively.  $\mathbf{b}$  is then found by comparing  $\mathbf{b}/|\mathbf{b}|$  to the principal lattice vectors in the lattice.

The velocity is calculated either by the Halperin-Mazenko method or by numerical differentiation of tracked points on the loop. In the former case, the time derivative of the amplitudes is required to calculate the amplitude currents (Eq. 14 in Ref. [3]). We have found that the most robust method is by demodulation of the numerical time derivative of  $\psi$ , i.e.,

$$\partial_t \eta_n = \langle e^{-i\mathbf{q}^{(n)} \cdot \mathbf{r}} \partial_t \psi \rangle, \quad (\text{A.1.20})$$

where this demodulation is done as in Eq. (A.1.14) and

$$\partial_t \psi \approx \frac{\psi(t) - \psi(t - \Delta t)}{\Delta t}. \quad (\text{A.1.21})$$

After identifying the node and dislocation character, the region of radius  $2R$  around  $r_0$  in  $B$  was set to zero, and the algorithm repeated until no new identified point passed the tolerance test, Eq. (A.1.18).

#### A.1.4. Time evolution schemes

The phase-field evolution, Eq. (5.0.2), was done using a semi-explicit integration scheme, as outlined in Sec. 5.1 in Ref. [99]. The advection of the PFC to mechanical equilibrium was done using a simple Taylor expansion to third order, and the velocity field used in the hydrodynamic model of Ref. [4] was implemented using a midpoint method. In all simulations, we used a time step of  $\Delta t = 0.1$ . However, for some of the simulations in the hydrodynamic framework, where a velocity field was included, we found that a time step of  $\Delta t = 0.05$  was necessary to reach convergence for the models that needed also other higher modes in the expansion, e.g., the 2D square model.

## A.2 Solving partial differential equations with periodic boundary conditions

In this thesis, we have extensively solved partial differential equations in Fourier space. The main idea behind this approach is to change the problem of partial differential equations into a problem of linear algebra. To see how this is done, consider the simple problem of solving for the function  $\xi$  given some source field  $f$

$$\nabla^2 \xi = f. \quad (\text{A.2.1})$$

By Fourier transforming this equation, we get

$$-\mathbf{k}^2 \xi_{\mathbf{f}} = f_{\mathbf{f}}, \quad (\text{A.2.2})$$

and we can divide by  $\mathbf{k}^2$  to get

$$\xi_{\mathbf{f}} = -\frac{1}{\mathbf{k}^2} f_{\mathbf{f}}. \quad (\text{A.2.3})$$

This defines  $\xi_{\mathbf{f}}$  for all wave vectors except  $\mathbf{k} = 0$ , which corresponds to an overall average density, which is indetermined from the original equation. We typically set this to zero. The field  $\xi$  can then be found numerically simply by Fourier transforming the field  $\xi_{\mathbf{f}}$ .

### A.2.1. Finding the compatible displacement

In Paper II, we needed to find the field  $\mathbf{u}^{\delta}$  that solves the equation

$$\partial_j \mathcal{C}_{ijkl} \partial_l u_k = -g_i^{\psi}, \quad (\text{A.2.4})$$

where  $g_i^{\psi} = -\partial_j \mathbb{h}_{ij}^{\psi}$ , and  $\mathcal{C}$  is as given in Eq. (4.1.9). This equation is solved in Fourier space by

$$u_{\mathbf{f}i}^{\delta} = G_{\mathbf{f}ij} g_j^{\psi}, \quad (\text{A.2.5})$$

where the Greens function  $G_{\mathbf{f}ij}$  is given in Ref. [93] as

$$G_{\mathbf{f}ij}(\mathbf{k}) = \frac{1}{\mathbf{k}^2} \left( \frac{\delta_{ij}}{\mu + \gamma \kappa_{(i)}^2} - \frac{\kappa_i \kappa_j}{(\mu + \gamma \kappa_{(i)}^2)(\mu + \gamma \kappa_{(j)}^2)} \frac{\mu + \lambda}{1 + \sum_{l=1}^3 \frac{\mu + \lambda}{\mu + \gamma \kappa_l^2} \kappa_l^2} \right), \quad (\text{A.2.6})$$

where  $\kappa = \mathbf{k}/|\mathbf{k}|$ , and there is no implicit summation over indices  $(i), (j)$ . By defining  $k_3 = 0$ , this equation is also valid for the triangular and square symmetry in two dimensions.

### A.2.2. Finding the distortion from the dislocation density tensor

In this thesis, we have seen two ways of obtaining the dislocation density tensor  $\alpha$  from the PFC. Either a singular version using the Halperin-Mazenko method, Eq. (6.3.6), or a non-singular expression using Eq. (6.5.2). As discussed in Sec. 4.5, the problem of finding the distortion  $\mathfrak{u}$  from the dislocation density tensor  $\alpha$ , is a problem treated by field dislocation dynamics. In this thesis, we employed the same procedure of spectral methods, which was outlined in Sec. A.6. of Paper III.

Crystal structure	$a_0$	Resolution	Suggested $(r, \psi_0)$	Equilibrim Eqs. for $(A, B, C)$
2D triangular	$\frac{4\pi}{\sqrt{3}}$	$[7, 12]^{-1} a_0$	$(-0.3, -0.3)$	$A = -\frac{1}{5}\psi_0 + \frac{1}{15}\sqrt{-15r - 36\psi_0^2} \quad [54]$ $\left. \begin{aligned} 12\psi_0^2 A + 48\psi_0 AB + 36A^3 \\ + 72AB^2 + 4Ar = 0 \\ 12\psi_0^2 B + 24\psi_0 A^2 + 36B^3 \\ + 72A^2 B + 4Br = 0 \end{aligned} \right\} [29]$
2D square	$2\pi$	$[7, 7]^{-1} a_0$	$(-0.3, -0.3)$	
3D bcc	$2\pi\sqrt{2}$	$[7, 7, 7]^{-1} a_0$	$(-0.3, -0.325)$	$A = -\frac{2}{15}\psi_0 + \frac{1}{15}\sqrt{-5r - 11\psi_0} \quad [62]$ $\left. \begin{aligned} 27A^2 + 36B^2 + 18B\psi_0 \\ + 3\psi_0^2 + r = 0 \\ 72A^2(4B + \psi_0) + 90B^3 \\ + 12B\psi_0^2 + 6B = 0 \end{aligned} \right\} [72]$
3D fcc	$2\pi\sqrt{3}$	$[11, 11, 11]^{-1} a_0$	$(-0.3, -0.325)$	
3D simple cubic	$2\pi$	$[5, 5, 5]^{-1} a_0$	$(-0.3, -0.325)$	$\left. \begin{aligned} 15A^3 + 24A^2 C + 24BC(3B + \psi_0) \\ + 96AB^2 + 36AC^2 + 24AB\psi_0 \\ + 3A\psi_0^2 + Ar = 0 \\ 12AC(6B + \psi_0) + 6A^2(8B + \psi_0) \\ + 45B^3 + 54BC^2 + 12B^2\psi_0 \\ + 3B\psi_0^2 + Br = 0 \\ 6A^3 + 27A^2 C + 18AB(3B + \psi_0) \\ + 81B^2 C + 27C^3 \\ + 3C\psi_0^2 + Cr = 0 \end{aligned} \right\} [2]$

Table A.1: The different PFC simulation parameters used to simulate the crystal structures studied in this thesis.



## REFERENCES

- [1] V. Skogvoll, A. Skaugen, L. Angheluta, and J. Viñals. Dislocation nucleation in the phase-field crystal model. *Physical Review B*, 103(1):014107, January 2021.
- [2] V. Skogvoll, A. Skaugen, and L. Angheluta. Stress in ordered systems: Ginzburg-Landau-type density field theory. *Physical Review B*, 103(22):224107, June 2021.
- [3] V. Skogvoll, L. Angheluta, A. Skaugen, M. Salvalaglio, and J. Viñals. A phase field crystal theory of the kinematics of dislocation lines. *Journal of the Mechanics and Physics of Solids*, 166:104932, September 2022.
- [4] Vidar Skogvoll, Marco Salvalaglio, and Luiza Angheluta. Hydrodynamic phase field crystal approach to interfaces, dislocations and multi-grain networks. *Modelling and Simulation in Materials Science and Engineering*, October 2022.
- [5] V. Skogvoll, J. Rønning, M. Salvalaglio, and L. Angheluta. A unified field theory of topological defects and non-linear local excitations. February 2023. Submitted to npj Computational Materials, arXiv: 2302.03035.
- [6] Quoted by André Maurois, *The Life of Sir Alexander Fleming*, trans. by Gerard Hopkins (1959), 167.
- [7] The American Physical Society. APS NEWS. November 2001.
- [8] W. Kohn. An essay on condensed matter physics in the twentieth century. *Reviews of Modern Physics*, 71(2):S59–S77, March 1999.
- [9] W. Friedrich, P. Knipping, and M. von Laue. Interferenz-Erscheinungen bei Röntgenstrahlen. *Sitzungsberichte der Math. Phys. Klasse (Kgl.)*, Bayerische Akademie der Wissenschaften:303–322, 1912.
- [10] J. D. Martin. When condensed-matter physics became king. *Physics Today*, 72(1):30–37, January 2019.
- [11] National Science Foundation. Multimedia Gallery - Pair of point defects called "Boojums" in thin hybrid-aligned nematic film. [https://www.nsf.gov/news/mmg/mmg\\_disp.jsp?med\\_id=68656](https://www.nsf.gov/news/mmg/mmg_disp.jsp?med_id=68656), 2012-07-19. Accessed: 2023-03-19.

- [12] E. J. Maginn and J. R. Elliott. Historical Perspective and Current Outlook for Molecular Dynamics As a Chemical Engineering Tool. *Industrial & Engineering Chemistry Research*, 49(7):3059–3078, April 2010.
- [13] N. M. Ghoniem, E. P. Busso, N. Kioussis, and H. Huang. Multiscale modelling of nanomechanics and micromechanics: An overview. *Philosophical Magazine*, 83(31-34):3475–3528, October 2003.
- [14] L. H. Thomas. The calculation of atomic fields. *Mathematical Proceedings of the Cambridge Philosophical Society*, 23(5):542–548, January 1927.
- [15] E. Fermi. Eine statistische Methode zur Bestimmung einiger Eigenschaften des Atoms und ihre Anwendung auf die Theorie des periodischen Systems der Elemente. *Zeitschrift für Physik*, 48(1):73–79, January 1928.
- [16] M. te Vrugt, H. Löwen, and R. Wittkowski. Classical dynamical density functional theory: From fundamentals to applications. *Advances in Physics*, 69(2):121–247, April 2020.
- [17] H. M. Zbib. Introduction to discrete dislocation dynamics. In Carlo Sansour and Sebastian Skatulla, editors, *Generalized Continua and Dislocation Theory: Theoretical Concepts, Computational Methods and Experimental Verification*, pages 289–317. Springer Vienna, Vienna, 2012.
- [18] J.S. Langer, E. Bouchbinder, and T. Lookman. Thermodynamic theory of dislocation-mediated plasticity. *Acta Materialia*, 58(10):3718–3732, 2010.
- [19] J. S. Langer. Thermodynamic theory of dislocation-enabled plasticity. *Phys. Rev. E*, 96(5):053005, November 2017.
- [20] A. Skaugen, L. Angheluta, and J. Viñals. Dislocation dynamics and crystal plasticity in the phase-field crystal model. *Phys. Rev. B*, 97(5):054113, February 2018.
- [21] A. Skaugen, L. Angheluta, and J. Viñals. Separation of elastic and plastic timescales in a phase field crystal model. *Phys. Rev. Lett.*, 121(25):255501, December 2018.
- [22] Anthony James Leggett, Nobel Lecture (2003).
- [23] R. Evans. The nature of the liquid-vapour interface and other topics in the statistical mechanics of non-uniform, classical fluids. *Advances in Physics*, 28(2):143–200, April 1979.
- [24] C. C. Moore. Ergodic theorem, ergodic theory, and statistical mechanics. *Proceedings of the National Academy of Sciences*, 112(7):1907–1911, February 2015.
- [25] P. M. Chaikin and T. C. Lubensky. *Principles of Condensed Matter Physics*. Cambridge University Press, 1995.



- [26] J. M. Brader and M. Schmidt. Dynamic correlations in Brownian many-body systems. *The Journal of Chemical Physics*, 140(3):034104, January 2014.
- [27] T. Schindler and M. Schmidt. Dynamic pair correlations and superadiabatic forces in a dense Brownian liquid. *The Journal of Chemical Physics*, 145(6):064506, August 2016.
- [28] S. Alexander and J. McTague. Should All Crystals Be bcc? Landau Theory of Solidification and Crystal Nucleation. *Physical Review Letters*, 41(10):702–705, September 1978.
- [29] A. Emdadi, Mohsen Asle Z., and E. Asadi. Revisiting phase diagrams of two-mode phase-field crystal models. *Computational Materials Science*, 123:139–147, October 2016.
- [30] Chen Ning Yang, Nobel Lecture (1957).
- [31] J.R. Munkres. *Topology*. Topology. Prentice-Hall, 2000.
- [32] C. D. Schimming and J. Viñals. Singularity identification for the characterization of topology, geometry, and motion of nematic disclination lines. *Soft Matter*, 18(11):2234–2244, March 2022.
- [33] B. I. Halperin. Statistical Mechanics of Topological Defects. In R. Balian, M. Kléman, and J. P. Poirier, editors, *Physique Des Défauts/ Physics of Defects*, pages 812–857. North-Holland, Amsterdam, 1981.
- [34] G. F. Mazenko. Vortex velocities in the O(n) symmetric time-dependent ginzburg-landau model. *Phys. Rev. Lett.*, 78(3):401–404, January 1997.
- [35] G. F. Mazenko. Velocity distribution for strings in phase-ordering kinetics. *Physical Review E*, 59(2):1574–1584, February 1999.
- [36] L. Angheluta, P. Jeraldo, and N. Goldenfeld. Anisotropic velocity statistics of topological defects under shear flow. *Phys. Rev. E*, 85(1):011153, January 2012.
- [37] A. Skaugen and L. Angheluta. Vortex clustering and universal scaling laws in two-dimensional quantum turbulence. *Physical Review E*, 93(3):032106, March 2016.
- [38] A. Skaugen and L. Angheluta. Velocity statistics for nonuniform configurations of point vortices. *Physical Review E*, 93(4):042137, April 2016.
- [39] L. Angheluta, Z. Chen, M. C. Marchetti, and M. J. Bowick. The role of fluid flow in the dynamics of active nematic defects. *New Journal of Physics*, 23(3):033009, March 2021.

- [40] J. Rønning, C. M. Marchetti, M. J. Bowick, and L. Angheluta. Flow around topological defects in active nematic films. *Proceedings of the Royal Society A: Mathematical, Physical and Engineering Sciences*, 478(2257):20210879, January 2022.
- [41] W. James. *The Principles of Psychology*. H. Holt and company, New York, 1890.
- [42] S. Timoshenko. *History of Strength of Materials: With a Brief Account of the History of Theory of Elasticity and Theory of Structures*. Courier Corporation, January 1983.
- [43] H. Yu, J. Liu, P. Karamched, A. J. Wilkinson, and F. Hofmann. Mapping the full lattice strain tensor of a single dislocation by high angular resolution transmission Kikuchi diffraction (HR-TKD). *Scripta Materialia*, 164:36–41, April 2019.
- [44] L. D. Landau and E. M. Lifshitz. *Theory of Elasticity*, volume 7 of *Course of Theoretical Physics*. Pergamon Press, London, 1959.
- [45] A. Ceccato, L. Menegon, and L. N. Hansen. Strength of Dry and Wet Quartz in the Low-Temperature Plasticity Regime: Insights From Nanoindentation. *Geophysical Research Letters*, 49(2):e2021GL094633, 2022.
- [46] D. Wallis, A. J. Parsons, and L. N. Hansen. Quantifying geometrically necessary dislocations in quartz using HR-EBSD: Application to chessboard subgrain boundaries. *Journal of Structural Geology*, 125:235–247, 2019.
- [47] A. M. Kosevich. Crystal dislocations and the theory of elasticity. In F. R. N. Nabarro, editor, *Dislocations in Solids, Vol. 1*, pages 33–141. North-Holland, Amsterdam, 1979.
- [48] M. Peach and J. S. Koehler. The forces exerted on dislocations and the stress fields produced by them. *Phys. Rev.*, 80(3):436–439, November 1950.
- [49] J. Weertman. The Peach–Koehler equation for the force on a dislocation modified for hydrostatic pressure. *The Philosophical Magazine: A Journal of Theoretical Experimental and Applied Physics*, 11(114):1217–1223, June 1965.
- [50] J. Hammersley. *Monte Carlo Methods*. Springer Science & Business Media, March 2013.
- [51] A. Acharya, R. J. Knops, and J. Sivaloganathan. On the structure of linear dislocation field theory. *Journal of the Mechanics and Physics of Solids*, 130:216–244, September 2019.
- [52] R. Brenner, A.J. Beaudoin, P. Suquet, and A. Acharya. Numerical implementation of static Field Dislocation Mechanics theory for periodic media. *Philosophical Magazine*, 94(16):1764–1787, June 2014.

- [53] H. Emmerich, H. Löwen, R. Wittkowski, T. Gruhn, G. I. Tóth, G. Tegze, and L. Gránásy. Phase-field-crystal models for condensed matter dynamics on atomic length and diffusive time scales: An overview. *Advances in Physics*, 61(6):665–743, 2012.
- [54] K. R. Elder and M. Grant. Modeling elastic and plastic deformations in nonequilibrium processing using phase field crystals. *Phys. Rev. E*, 70(5):051605, November 2004.
- [55] J. Swift and P. C. Hohenberg. Hydrodynamic fluctuations at the convective instability. *Physical Review A*, 15(1):319–328, January 1977.
- [56] J. G. Dash. History of the search for continuous melting. *Reviews of Modern Physics*, 71(5):1737–1743, October 1999.
- [57] S. van Teeffelen, R. Backofen, A. Voigt, and H. Löwen. Derivation of the phase-field-crystal model for colloidal solidification. *Physical review. E, Statistical, nonlinear, and soft matter physics*, 79:051404, June 2009.
- [58] Z. F. Huang and K. R. Elder. Mesoscopic and Microscopic Modeling of Island Formation in Strained Film Epitaxy. *Physical Review Letters*, 101(15):158701, October 2008.
- [59] J. R. Mianroodi and B. Svendsen. Atomistically determined phase-field modeling of dislocation dissociation, stacking fault formation, dislocation slip, and reactions in fcc systems. *Journal of the Mechanics and Physics of Solids*, 77:109–122, April 2015.
- [60] J. Berry, J. Rottler, C. W. Sinclair, and N. Provatas. Atomistic study of diffusion-mediated plasticity and creep using phase field crystal methods. *Phys. Rev. B*, 92(13):134103, October 2015.
- [61] N. Provatas, J. A. Dantzig, B. Athreya, P. Chan, P. Stefanovic, N. Goldenfeld, and K. R. Elder. Using the phase-field crystal method in the multi-scale modeling of microstructure evolution. *JOM*, 59(7):83–90, July 2007.
- [62] K. A. Wu and P. W. Voorhees. Phase field crystal simulations of nanocrystalline grain growth in two dimensions. *Acta Materialia*, 60(1):407–419, January 2012.
- [63] M. Salvalaglio, R. Backofen, K. R. Elder, and A. Voigt. Defects at grain boundaries: A coarse-grained, three-dimensional description by the amplitude expansion of the phase-field crystal model. *Physical Review Materials*, 2(5):053804, May 2018.
- [64] J. Berry, M. Grant, and K. R. Elder. Diffusive atomistic dynamics of edge dislocations in two dimensions. *Physical Review E*, 73(3):031609, March 2006.

- [65] P. Y. Chan, G. Tsekenis, J. Dantzig, K. A. Dahmen, and N. Goldenfeld. Plasticity and Dislocation Dynamics in a Phase Field Crystal Model. *Physical Review Letters*, 105(1):015502, June 2010.
- [66] J. Berry, N. Provatas, J. Rottler, and C. W. Sinclair. Phase field crystal modeling as a unified atomistic approach to defect dynamics. *Phys. Rev. B*, 89(21):214117, June 2014.
- [67] K. A. Wu and A. Karma. Phase-field crystal modeling of equilibrium bcc-liquid interfaces. *Phys. Rev. B*, 76(18):184107, November 2007.
- [68] K. R. Elder, N. Provatas, J. Berry, P. Stefanovic, and M. Grant. Phase-field crystal modeling and classical density functional theory of freezing. *Physical Review B*, 75(6):064107, February 2007.
- [69] M. Greenwood, N. Provatas, and J. Rottler. Free energy functionals for efficient phase field crystal modeling of structural phase transformations. *Phys. Rev. Lett.*, 105(4):045702, July 2010.
- [70] M. Seymour, F. Sanches, K. Elder, and N. Provatas. Phase-field crystal approach for modeling the role of microstructure in multiferroic composite materials. *Physical Review B*, 92(18):184109, November 2015.
- [71] P. Hirvonen, M. M. Ervasti, Z. Fan, M. Jalalvand, M. Seymour, S. M. Vaez Allaei, N. Provatas, A. Harju, K. R. Elder, and T. Ala-Nissila. Multiscale modeling of polycrystalline graphene: A comparison of structure and defect energies of realistic samples from phase field crystal models. *Physical Review B*, 94(3):035414, July 2016.
- [72] K. A. Wu, A. Adland, and A. Karma. Phase-field-crystal model for fcc ordering. *Phys. Rev. E*, 81(6):061601, June 2010.
- [73] S. K. Mkhonta, K. R. Elder, and Z. F. Huang. Exploring the Complex World of Two-Dimensional Ordering with Three Modes. *Physical Review Letters*, 111(3):035501, July 2013.
- [74] N. Goldenfeld, B. P. Athreya, and J. A. Dantzig. Renormalization group approach to multiscale simulation of polycrystalline materials using the phase field crystal model. *Phys. Rev. E*, 72(2):020601, August 2005.
- [75] B. P. Athreya, N. Goldenfeld, and J. A. Dantzig. Renormalization-group theory for the phase-field crystal equation. *Physical Review E*, 74(1):011601, July 2006.
- [76] M. Salvalaglio and K. R. Elder. Coarse-grained modeling of crystals by the amplitude expansion of the phase-field crystal model: An overview. *Modelling and Simulation in Materials Science and Engineering*, 30(5):053001, May 2022.

- [77] D. H. Yeon, Z. F. Huang, K.R. Elder, and K. Thornton. Density-amplitude formulation of the phase-field crystal model for two-phase coexistence in two and three dimensions. *Philosophical Magazine*, 90(1-4):237–263, 2010.
- [78] V. Heinonen, C. V. Achim, and T. Ala-Nissila. Long-wavelength properties of phase-field-crystal models with second-order dynamics. *Physical Review E*, 93(5):053003, May 2016.
- [79] V. Heinonen, C. V. Achim, K. R. Elder, S. Buyukdagli, and T. Ala-Nissila. Phase-field-crystal models and mechanical equilibrium. *Phys. Rev. E*, 89(3):032411, March 2014.
- [80] P. Stefanovic, M. Haataja, and N. Provatas. Phase-field crystals with elastic interactions. *Phys. Rev. Lett.*, 96(22):225504, June 2006.
- [81] V. Heinonen, C. V. Achim, J. M. Kosterlitz, S. Ying, J. Lowengrub, and T. Ala-Nissila. Consistent Hydrodynamics for Phase Field Crystals. *Physical Review Letters*, 116(2):024303, January 2016.
- [82] R. Fisher. Statistical Methods and Scientific Induction. *Journal of the Royal Statistical Society. Series B (Methodological)*, 17(1):69–78, 1955.
- [83] R. Phillips. *Crystals, Defects and Microstructures: Modeling Across Scales*. Cambridge University Press, February 2001.
- [84] J. Li, K. J. Van Vliet, T. Zhu, S. Yip, and S. Suresh. Atomistic mechanisms governing elastic limit and incipient plasticity in crystals. *Nature*, 418(6895):307–310, July 2002.
- [85] R. E. Miller and A. Acharya. A stress-gradient based criterion for dislocation nucleation in crystals. *Journal of the Mechanics and Physics of Solids*, 52(7):1507–1525, 2004.
- [86] A. Garg, A. Acharya, and C. E. Maloney. A study of conditions for dislocation nucleation in coarser-than-atomistic scale models. *Journal of the Mechanics and Physics of Solids*, 75:76–92, February 2015.
- [87] C. L. Kelchner, S. J. Plimpton, and J. C. Hamilton. Dislocation nucleation and defect structure during surface indentation. *Physical Review B*, 58(17):11085–11088, November 1998.
- [88] T. Zhu, J. Li, A. Samanta, A. Leach, and K. Gall. Temperature and Strain-Rate Dependence of Surface Dislocation Nucleation. *Physical Review Letters*, 100(2):025502, January 2008.
- [89] X. Li, Y. Wei, L. Lu, K. Lu, and H. Gao. Dislocation nucleation governed softening and maximum strength in nano-twinned metals. *Nature*, 464(7290):877–880, April 2010.

- [90] E. Wajnryb, A. R. Altenberger, and J. S. Dahler. Uniqueness of the microscopic stress tensor. *The Journal of Chemical Physics*, 103(22):9782–9787, 1995.
- [91] J. Rigelesaiyin, A. Diaz, W. Li, L. Xiong, and Y. Chen. Asymmetry of the atomic-level stress tensor in homogeneous and inhomogeneous materials. *Proceedings. Mathematical, physical, and engineering sciences*, 474(2217):20180155–20180155, September 2018.
- [92] H. Chen and S. Orszag. Moment isotropy and discrete rotational symmetry of two-dimensional lattice vectors. *Philosophical Transactions of the Royal Society A: Mathematical, Physical and Engineering Sciences*, 369(1944):2176–2183, June 2011.
- [93] P. H. Dederichs and G. Leibfried. Elastic Green’s Function for Anisotropic Cubic Crystals. *Physical Review*, 188(3):1175–1183, December 1969.
- [94] Y. Maroudas-Sacks, L. Garion, L. Shani-Zerbib, A. Livshits, E. Braun, and K. Keren. Topological defects in the nematic order of actin fibres as organization centres of Hydra morphogenesis. *Nature Physics*, 17(2):251–259, February 2021.
- [95] H. T. K. Vu, S. Mansour, M. Kücken, C. Blasse, C. Basquin, J. Azimzadeh, E. W. Myers, L. Brusch, and J. C. Rink. Dynamic Polarization of the Multiciliated Planarian Epidermis between Body Plan Landmarks. *Developmental Cell*, 51(4):526–542.e6, November 2019.
- [96] D. Cislo, H. Qin, F. Yang, M. J. Bowick, and S. J. Streichan. Active Cell Divisions G.rate Exotic Fourfold Orientationally Ordered Phase in Living Tissue, July 2021.
- [97] Y. Liu and X. Zhang. Metamaterials: A new frontier of science and technology. *Chemical Society Reviews*, 40(5):2494–2507, 2011.
- [98] D. Duffy and J. S. Biggins. Defective nematogenesis: Gauss curvature in programmable shape-responsive sheets with topological defects. *Soft Matter*, 16(48):10935–10945, 2020.
- [99] A. Skaugen. *A Unified Perspective on Two-Dimensional Quantum Turbulence and Plasticity*. PhD thesis, The University of Oslo, 2018.

## PRINTED PAPERS





# PAPER I



**Dislocation nucleation in the phase-field crystal model**Vidar Skogvoll <sup>1</sup>, Audun Skaugen <sup>2</sup>, Luiza Angheluta <sup>1</sup> and Jorge Viñals<sup>3</sup><sup>1</sup>*PoreLab, The Njord Centre, Department of Physics, University of Oslo, P.O. Box 1048, 0316 Oslo, Norway*<sup>2</sup>*Computational Physics Laboratory, Tampere University, P.O. Box 692, 33014 Tampere, Finland*<sup>3</sup>*School of Physics and Astronomy, University of Minnesota, Twin Cities, Minneapolis, Minnesota 55455, USA*

(Received 16 September 2020; revised 17 November 2020; accepted 17 December 2020; published 12 January 2021)

We use the phase-field crystal model to study nucleation of edge dislocations in two dimensions under an applied stress field. A dislocation dipole nucleates under the applied stress, consistent with Burgers vector conservation. The phase field correctly accounts for elastic energy storage prior to nucleation and for dissipative relaxation during the nucleation event. We show that a lattice incompatibility field is a sensitive diagnostic of the location of the nucleation event and of the Burgers vector and slip direction of the dislocations that will be nucleated above threshold. A direct calculation of the phase-field energy accurately correlates with the nucleation event, as signaled by the lattice incompatibility field. We show that a Schmid-like criterion concerning the resolved stress at the nucleation site correctly predicts the critical nucleation stress. Finally, we present preliminary results for a three-dimensional, bcc lattice. The phase field allows direct computation of the lattice incompatibility tensor for both dislocation lines and loops.

DOI: [10.1103/PhysRevB.103.014107](https://doi.org/10.1103/PhysRevB.103.014107)**I. INTRODUCTION**

Unlike the spontaneous homogeneous nucleation of topological defects in a symmetry-breaking phase transition [1–3], the formation of dislocation lines in a material is typically studied as an athermal process largely driven by local stresses [4]. Since the existence and mobility of such defects are essential contributors to the strength and ductility of crystalline materials, understanding the mechanisms behind their creation and motion is a fundamental goal of material science in general and of plasticity theory in particular. Along parallel developments in the continuum theory of crystal plasticity, a number of empirical criteria have been introduced to predict dislocation nucleation thresholds, the resulting Burgers vector distribution, and line direction [5–8]. These macroscopic criteria have been extensively compared with microscopic results from molecular dynamics (MD) simulations of model crystalline solids in a variety of configurations and imposed stresses [8–11]. However, the details of the mechanical conditions that lead to dislocation nucleation still remain poorly understood, with criteria from continuum mechanics approaches and numerical simulations often yielding conflicting phenomenology. The two main reasons why a precise comparison between the two is difficult include the disparity in length scales between crystal plasticity theory and molecular simulation and the necessity in the latter to thermally average phase space trajectories that take place over characteristic energy scales which are much higher than thermal scales. Fundamental questions such as whether the nucleation event is local or nonlocal remain unresolved [8]. We bridge here microscopic and continuum scales by introducing a phase-field crystal model [12,13] of dislocation nucleation and show that the nucleation event is well captured at the mesoscale by a

continuum lattice incompatibility field. Our numerical results for the nucleation of edge dislocations in a two-dimensional (2D), hexagonal lattice indicate that the nucleation event is governed by a local balance between the resolved stresses along lattice slip planes and the force acting between the nucleating dislocation pair and that a lattice incompatibility field derived from the phase field predicts the Burgers vector of the nucleating defect pair. The simplest dislocation nucleation criterion is based on the Schmid stress decomposition [5,7,14–17]. When an appropriate projection of an atomic level shear stress exceeds a material-dependent threshold, a dislocation loop is predicted to be nucleated. On the one hand, while fcc lattices generally obey the Schmid criterion, there exist entire classes of “non-Schmid” lattices, including bcc crystals [18]. Furthermore, a recent, careful MD study of nucleation in a nanoindentation configuration for a model Lennard-Jones solid shows that the Schmid criterion not only fails to account for the site of the nucleation event but nucleation, in fact, occurs in regions in which the resolved shear stress is relatively small [8]. A second class of criteria associates the nucleation event to a buckling or phonon instability of the lattice (the Hill or  $\Lambda$  criteria based on mechanical stability arguments [7,16]). Molecular dynamics simulations and experiments in different crystal indentation configurations, however, have revealed very complex nucleation processes in which the lattice is locally quite distorted and therefore far from the conditions of applicability of such a phonon stability analysis. Large regions of partial dislocations and extended stacking faults have been argued to be present at nucleation [9], as well as extended and complex networks involving surfaces and grain boundaries [11]. More recently, the stability of the perfect lattice against homogeneous nucleation was formulated in terms of the kinematic equation that governs the temporal evolution

of the dislocation density tensor. This approach is sensitive to the creation of nontrivial local topology [8] and yields predictions that are qualitatively different than the Schmid criterion. To contribute to the elucidation of the criteria for nucleation, we examine here a simple, prototypical configuration: a 2D hexagonal lattice in which nucleation occurs through the formation of a dislocation dipole of zero net Burgers vector. In this idealized configuration, we show that the incompatibility field directly computed from the phase field identifies the nucleation event and that it can be used to predict the Burgers vector at nucleation. The critical stress for nucleation is seen to be in quantitative agreement with that of the Schmid criterion in this 2D lattice.

## II. THE PHASE-FIELD CRYSTAL

The phase-field crystal (PFC) model is a mesoscale description of a crystalline solid in which vibrational degrees of freedom have been averaged out, in the same spirit as density functional theory [13,19]. The crystalline phase is described by a scalar order parameter field  $\psi(\mathbf{r})$ , which obeys a phenomenological free energy given, in dimensionless form, by

$$\mathcal{F}[\psi] = \int d\mathbf{r} \left[ \frac{1}{2} [\mathcal{L}\psi]^2 + \frac{r}{2} \psi^2 + \frac{1}{4} \psi^4 \right], \quad (1)$$

where  $\mathcal{L} = 1 + \nabla^2$  and  $r$  is a dimensionless parameter representing the deviation from the liquid-solid phase boundary.

We further assume that  $\psi$  is a conserved variable, with its spatial average  $\bar{\psi}$  being constant [19]. The two constants  $r$  and  $\bar{\psi}$  completely define the model. In two dimensions, for a range of values of  $\bar{\psi}$  and  $r < 0$ , a triangular Bravais lattice  $\psi^{\text{eq}}(\mathbf{r})$  is the equilibrium phase, which we consider here.

Upon deformation of the equilibrium state  $\psi^{\text{eq}}$  by a displacement field  $\mathbf{u}(\mathbf{x})$ , it is possible to define the equilibrium stress tensor as the variation of the free energy with respect to the displacement gradient [20],

$$\tilde{\sigma}_{ij}^{\psi} = -\partial_m [\psi \partial_m \mathcal{L}\psi] \delta_{ij} + 2[\partial_i \mathcal{L}\psi][\partial_j \psi], \quad (2)$$

where  $X_{(i}Y_{j)}$  refers to symmetrization of indices  $i, j$  [21]. This quantity still shows spatial variations within a unit cell due to the variation of  $\psi$ . We therefore further define an averaged stress field as  $\sigma_{ij}^{\psi} = \langle \tilde{\sigma}_{ij}^{\psi} \rangle$ , where  $\langle \cdot \rangle$  refers to averaging over an area approximately equal to a unit lattice cell.

For small distortions, the hexagonal lattice is elastically isotropic. We define a symmetric strain as

$$e_{ij}^{\psi} = \frac{1}{2\mu} (\sigma_{ij}^{\psi} - \kappa \delta_{ij} \sigma_{kk}^{\psi}), \quad (3)$$

where  $\mu$  is the shear modulus and  $\kappa = \lambda/[2(\lambda + \mu)]$ , where  $\lambda$  is the standard Lamé coefficient. In our dimensionless variables, we have  $\lambda = \mu = 3A_0^2$ , where  $A_0$  is the amplitude of  $\psi^{\text{eq}}$  [20].

Dislocations lead to lattice incompatibility [4,22]. In two dimensions and given a Burgers vector density  $\mathbf{B}(\mathbf{r})$ , the incompatibility field is  $\eta = \epsilon_{ik}\epsilon_{jl}\partial_{ij}e_{kl} = \epsilon_{ij}\partial_i B_j$ . A key assumption of our analysis is that the configuration of  $\psi$  contains the complete strain incompatibility [23,24]. Thus,

from Eq. (3) we find

$$\eta^{\psi} = \frac{1}{2\mu} (\epsilon_{ik}\epsilon_{jl}\partial_{ij}\sigma_{kl}^{\psi} - \kappa \nabla^2 \sigma_{kk}^{\psi}). \quad (4)$$

The dissipative evolution of  $\psi$  is diffusive,

$$\partial_t \psi = \nabla^2 \frac{\delta \mathcal{F}}{\delta \psi}, \quad (5)$$

with a constant kinetic mobility coefficient, which we set to 1 in our study and which sets the unit of time. As discussed in Refs. [23,25], lattice distortion needs to be treated separately from diffusive relaxation of  $\psi$  in order to incorporate elastic response into the phase field and to maintain elastic equilibrium at all times. In addition, in order to induce nucleation, we consider an externally imposed bulk stress  $\sigma_{ij}^{\text{ext}}(\mathbf{r})$ . In elastic equilibrium  $\partial_i \sigma_{ij}^{\psi} = \partial_i \sigma_{ij}^{\text{ext}}$ . Following Ref. [23], for a nonequilibrium configuration of  $\psi$ , we solve  $\partial_i (\sigma_{ij}^{\psi} - \sigma_{ij}^{\text{ext}} + \sigma_{ij}^{\delta}) = 0$ , where  $\sigma_{ij}^{\delta} = \lambda e_{kk}^{\delta} + 2\mu e_{ij}^{\delta}$  and  $e_{ij}^{\delta}$  is a compatible strain,  $e_{ij}^{\delta} = (\partial_i u_j^{\delta} + \partial_j u_i^{\delta})/2$ . Diffusion of  $\psi$  is supplemented at each time by distortion  $\psi(\mathbf{r}) \rightarrow \psi(\mathbf{r} - \mathbf{u}^{\delta})$ .

In two dimensions, the condition for elastic equilibrium means that the stress tensor difference can be written in terms of an Airy potential  $\chi$ ,  $\sigma_{ij}^{\psi} - \sigma_{ij}^{\text{ext}} + \sigma_{ij}^{\delta} = \epsilon_{ik}\epsilon_{jl}\partial_{kl}\chi$ . For each instantaneous configuration of  $\psi$  we solve [23]

$$\frac{1 - \kappa}{2\mu} \nabla^4 \chi = \eta^{\psi} - \eta^{\text{ext}}, \quad (6)$$

where  $\eta^{\text{ext}}$  accounts for the fact that the imposed stress does not necessarily derive from a compatible displacement. The solution allows the computation of  $e_{ij}^{\delta}$  and, from it, of the displacement  $u_i^{\delta}$ .

## III. NUMERICAL METHOD

A square computational domain is considered with periodic boundary conditions, with  $100 \times 100$  hexagonal unit cells of length  $a_0 = \frac{4\pi}{\sqrt{3}}$  and grid spacings  $\Delta x = a_0/7$  and  $\Delta y = a_0\sqrt{3}/12$ . The model parameters used are  $r = -1$  and  $\bar{\psi} = -0.45$ . The initial condition of  $\psi$  is a periodic, undistorted hexagonal lattice. For our choice of model parameters, the corresponding Lamé coefficients are  $\mu = \lambda = 0.227$ .

Calibrating the parameter values to experiments is a difficult task due to a lack of high-resolution data and corresponding measurable quantities. Since the PFC free energy is an effective coarse graining of the intermolecular potential related to high-order density gradients, a substantial amount of fitting is required, beginning with energy scales, but also relaxation timescales [13]). Hence, the strength of the PFC model is not in modeling with specific dimensional units, but rather in modeling generic behavior described by rescaled units. To this end, the shear modulus  $\mu$  sets the unit for measuring stress, while strain and incompatibility fields are dimensionless. For instance, the critical stress of 0.081 in Fig. 2 would correspond in physical units to  $\sigma_c^* = 0.081/0.227\mu \approx 0.36\mu$ .

We impose a shear stress  $\sigma_{xx}^{\text{ext}} = \sigma_{yy}^{\text{ext}} = 0$  and  $\sigma_{xy}^{\text{ext}} = \sigma_0 e^{-\frac{|\mathbf{r}-\mathbf{r}_0|^2}{2w^2}}$ , with  $\mathbf{r}_0$  being an arbitrary center. Nucleation is induced by a sequence of steps of increasing value of  $\sigma_0$ .

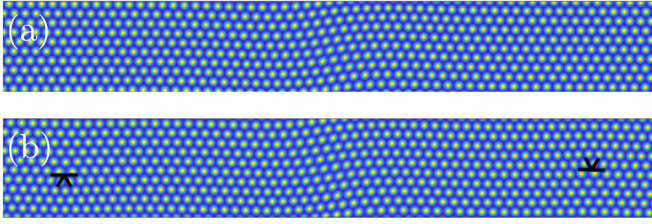


FIG. 1. Central region of the computational domain with (a) the PFC configuration in equilibrium at  $\sigma_0 = 0.080$  prior to nucleation and (b) the equilibrium configuration at  $\sigma_0 = 0.081$  after nucleation.

A given configuration is allowed to relax to equilibrium for constant  $\sigma_0$ . After equilibration has been achieved, the configuration is used as the initial condition for another relaxation step in which the value of  $\sigma_0$  is increased. The details are as follows: Diffusive relaxation of  $\psi$  is allowed for 100 steps by using an exponential time differencing method, with a time step of  $\Delta t = 0.1$  [26]. After these 100 steps,  $\psi$  is brought to mechanical equilibrium by a compatible displacement as described above and in Refs. [23,27]. Diffusive relaxation and elastic distortion cycles are continued until the largest change in  $\psi$  between two such cycles is less than 0.01. We then increase  $\sigma_0$  by an increment  $\Delta\sigma_0 = 0.001$  and repeat the relaxation procedure. The external stress amplitude considered ranges from zero to  $\sigma_0 = 0.086$ . Figure 1 shows the equilibrated field  $\psi$  for some amplitude of  $\sigma_0$  prior to ( $\sigma_0 = 0.080$ ) and after a nucleation event ( $\sigma_0 = 0.081$ ) for  $w = 4a_0$ . The nucleation event gives rise to two edge dislocations with opposite Burgers vectors  $a_0\mathbf{e}_x$  and  $-a_0\mathbf{e}_x$ . When the configuration comprising two defects is allowed to evolve, the defects move away from each other along the  $x$  direction. Note that since a dislocation in a hexagonal lattice has two extra half planes, we represent the location of the dislocation by the symbol  $\sphericalangle$ . This is in contrast to the conventional symbol representing an edge dislocation ( $\perp$ ), which indicates the directions of the slip and extra inserted half plane. A video animation of the nucleation event sequence can be found in the Supplemental Material [28].

#### IV. TWO-DIMENSIONAL DISLOCATION NUCLEATION

The incompatibility field  $\eta^\psi$  from Eq. (4) accurately indicates where dislocations form. Figures 2(a) and 2(b) show the  $\eta^\psi$  field corresponding to the  $\psi$  density field in Fig. 1, before and after the nucleation event. The extremes in the value of  $\eta^\psi$  identify the location of the defect cores. Also, the quadrupolar structure of Fig. 2(a) prior to nucleation reflects the Burgers vectors of the dislocation pair to be nucleated. More quantitatively, Fig. 2(c) shows the evolution of the maximal value of  $\eta^\psi$  in time and upon increasing  $\sigma_0$  quasistatically (shown by the left y axis). The point at which  $\sigma_0$  attains the critical value for nucleation is marked by the vertical dashed line at  $t = 2050$ , and the dislocations become distinct at  $t \approx 2300$ . We observe that  $\max(\eta^\psi)$  rises before the dislocations become distinct. Prior to nucleation, the crystal lattice is elastically loaded with a quasistatic increase of  $\sigma_0$ . After nucleation, the external stress  $\sigma_0$  remains constant (corresponding to a plateau

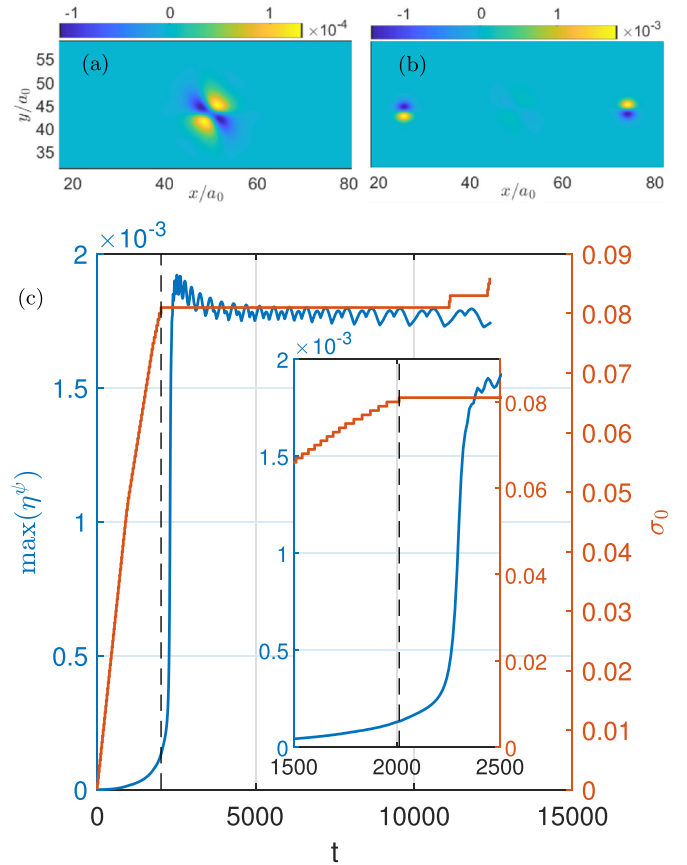


FIG. 2. Incompatibility field  $\eta^\psi$  (a) at  $t = 2050$  ( $\sigma_0 = 0.080$ ), before the nucleation event, and (b) at  $t = 12170$  ( $\sigma_0 = 0.081$ ), after nucleation. (c) Maximum of  $\eta^\psi$  as a function of time  $t$ . The dashed line at  $t = 2050$  marks where  $\sigma_0$  has attained the critical value for nucleation. The dislocations become distinct at  $t \approx 2300$ . The right axis shows the value of  $\sigma_0$  for the corresponding times. The plateaus in time indicate nonequilibrium relaxation at constant external stress.

in the  $\sigma_0$  curve), while the crystal lattice evolves diffusively in time.

Figure 3 further shows the corresponding change in the PFC free energy  $\mathcal{F}$  upon increasing  $\sigma_0$ , together with the elastic energy defined as  $E_{el} = \frac{1}{2} \int d\mathbf{r} \sigma_{ij}^\psi e_{ij}^\psi$ . Note that despite the purely diffusive dynamics obeyed by  $\psi$ , the lattice is capable of storing (reversible) elastic energy upon increasing the value of  $\sigma_0$ , as seen previously in Fig. 2(c). This reversible evolution is enabled through the compatible distortion added to the field  $\psi$  to preserve elastic equilibrium. As the nucleation event is reached, the phase-field energy exhibits a large discontinuity at the value of  $\sigma_0$  that corresponds to the dashed line in Fig. 2(c).

For this simple 2D setup, it is possible to predict the critical stress for nucleation from the value of the resolved shear stress along each slip plane, in analogy with the classical Schmid criterion. For a given stress  $\sigma_{ij}$ , the resolved shear stress  $\tau_{\mathbf{a},\mathbf{n}}$  on a slip plane defined by the normal unit vector  $\mathbf{n}$  along a direction in the slip plane given by the unit vector  $\mathbf{a}$  is  $\tau_{\mathbf{a},\mathbf{n}} = a_i \sigma_{ij} n_j$ . In two dimensions,  $\mathbf{n}$  is determined up to a sign by  $n_i = \epsilon_{ij} a_j$ , and for the hexagonal symmetry, there are three slip planes defined by lattice vectors

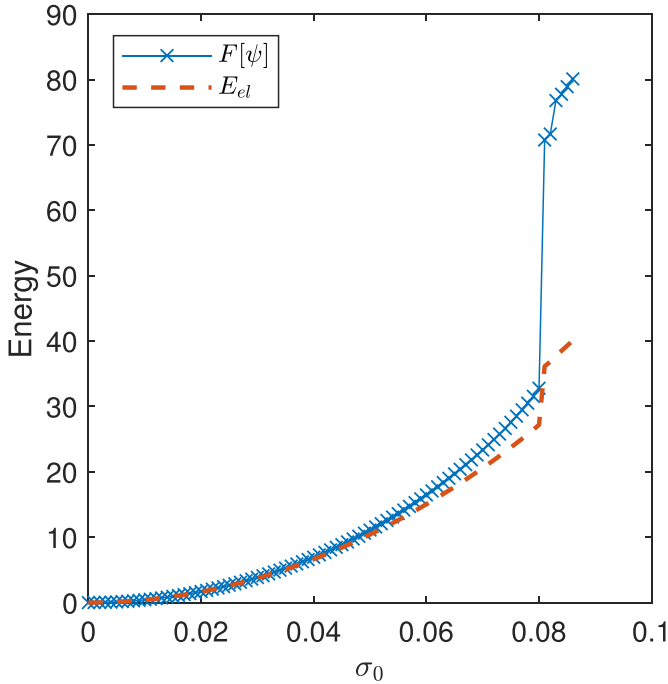


FIG. 3. Total free energy  $\mathcal{F}$  and elastic energy  $E_{el}$  as a function of  $\sigma_0$ .

$\mathbf{a}_1 = [1, 0]$ ,  $\mathbf{a}_2 = [1/2, \sqrt{3}/2]$ , and  $\mathbf{a}_3 = [-1/2, \sqrt{3}/2]$ . One thus considers three different scalar fields  $\tau_1$ ,  $\tau_2$ , and  $\tau_3$ , which are the resolved shear stresses along the slip directions corresponding to  $\mathbf{a}_1$ ,  $\mathbf{a}_2$ , and  $\mathbf{a}_3$ , respectively. Figures 4(a)–4(f) show the fields  $\tau_1$ ,  $\tau_2$ ,  $\tau_3$  right before and after nucleation. The resolved shear stress is largest along the  $\mathbf{a}_1$  direction, the slip plane along which the dislocation pair nucleates, and is centered at the origin, the nucleation site. The other two resolved stresses remain small during nucleation. The change in the largest resolved stress  $\tau_1$  is shown in Fig. 4(g), using the same coordinates as in Fig. 2(c). Nucleation initiates (vertical dashed line) when the resolved shear stress approaches the critical value of  $|\tau_c| = 0.046$ , followed by a small drop and then a slow rise as the newly nucleated dislocation dipole moves away from the center region. Notice that this value of  $\tau_c$  at the moment of nucleation is smaller than the external shear stress  $\sigma_{xy}^{\text{ext}} = 0.080$ . This is because at mechanical equilibrium, the two stresses are equal only up to a divergence-free term. The critical value of the resolved stress  $\tau_c$  can be estimated as follows: Consider an otherwise perfect lattice with a bound dislocation pair of opposite Burgers vectors. The force acting on the dislocations (in opposite directions) because of the external stress is the Peach-Koehler force projected on the slip plane defined by  $\mathbf{a}_k$  and is  $F_k^{\text{PK}} = b\tau_k = \pm a_0\tau_k$  for dislocations with Burgers vectors  $\mathbf{b} = \pm a_0\mathbf{a}_k$ . As the two dislocations in the dipole separate at nucleation to become distinct, their mutual elastic interaction results in an attractive force. If both dislocations are on the  $x$  axis, this force is [29,30]  $|f_x| = Y_2 b^2 / (4\pi d)$ , where  $Y_2 = 4\mu(\lambda + \mu) / (\lambda + 2\mu)$  is the 2D Young's modulus and  $d$  is the dislocation separation. We estimate  $\tau_c$  as the applied stress for which the resulting Peach-Koehler force on one dislocation equals the force

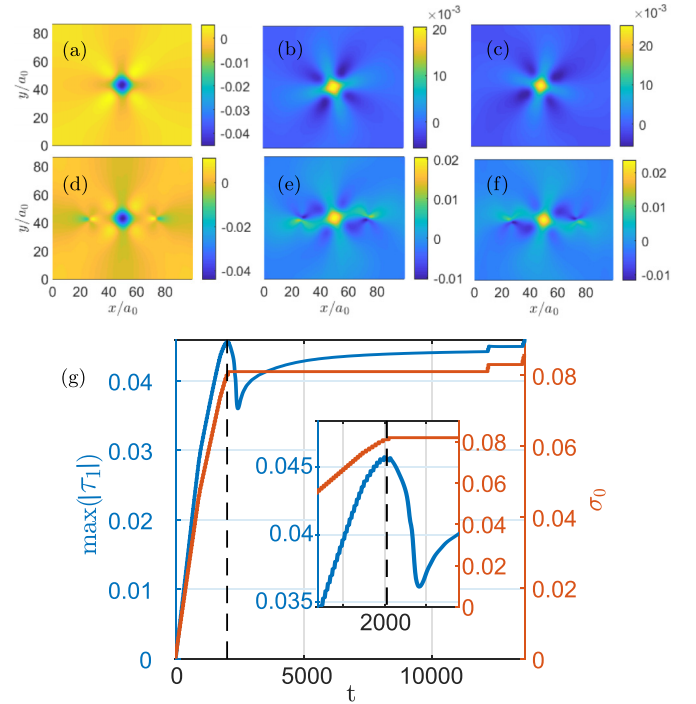


FIG. 4. The resolved shear stresses just prior to and after the nucleation event. (a)–(c)  $\tau_1$ ,  $\tau_2$ , and  $\tau_3$  at  $t = 2050$  ( $\sigma_0 = 0.080$ ), respectively, and (d)–(f)  $\tau_1$ ,  $\tau_2$ , and  $\tau_3$  at  $t = 12170$  ( $\sigma_0 = 0.081$ ), respectively. (g)  $\max(|\tau_1|)$  as a function of time  $t$  during the nucleation event.

from the other dislocation when the separation is one lattice constant. We find that  $\tau_c = Y_2 / (4\pi)$ . Using the numerical values of  $\mu = \lambda = 0.2271$ ,  $Y_2 / (4\pi) = 0.048$ , which is in close agreement with the observed value of  $|\tau_c| = 0.046$ .

In order to further test the nucleation criterion, we have performed additional calculations in which the imposed stress  $\sigma_{ij}^{\text{ext}}$  is rotated relative to the lattice,  $\sigma_{ij}^{\text{ext}}(\theta) = R_{ki}^{(\theta)} \sigma_{kl}^{\text{ext}} R_{lj}^{(\theta)}$ , where  $R_{ij}^{(\theta)}$  is the standard rotation matrix in two dimensions and  $\theta$  is the rotation angle. Figure 5 shows the maximal resolved stress at nucleation along the three lattice directions as a function of  $\theta$ . Since  $\sigma_{ij}^{\text{ext}}$  is invariant under a rotation of  $\pi$ ,  $\sigma_{ij}^{\text{ext}}(x) = \sigma_{ij}^{\text{ext}}(\pi + x)$ , we show only values ranging from  $\theta = 0$  to  $\pi$ . Figure 5 shows that the resolved stress consistently predicts the type of dislocation dipole to nucleate, but the value of the critical resolved stress depends on  $\theta$  and is, in general, lower than  $Y_2 / (4\pi)$ . The discrepancy is likely due to anisotropic contributions to lattice distortions at the length scale of the core which are not described by isotropic linear elasticity.

### V. THREE-DIMENSIONAL INCOMPATIBILITY FIELD

The simplest example of a 2D hexagonal lattice has only point edge dislocations and is described by isotropic elasticity. However, more realistic crystal lattices have more complex loop defects and lattice anisotropy, where the Schmid-like criterion might not readily apply. Therefore, it is important to understand how the incompatibility field applies to three



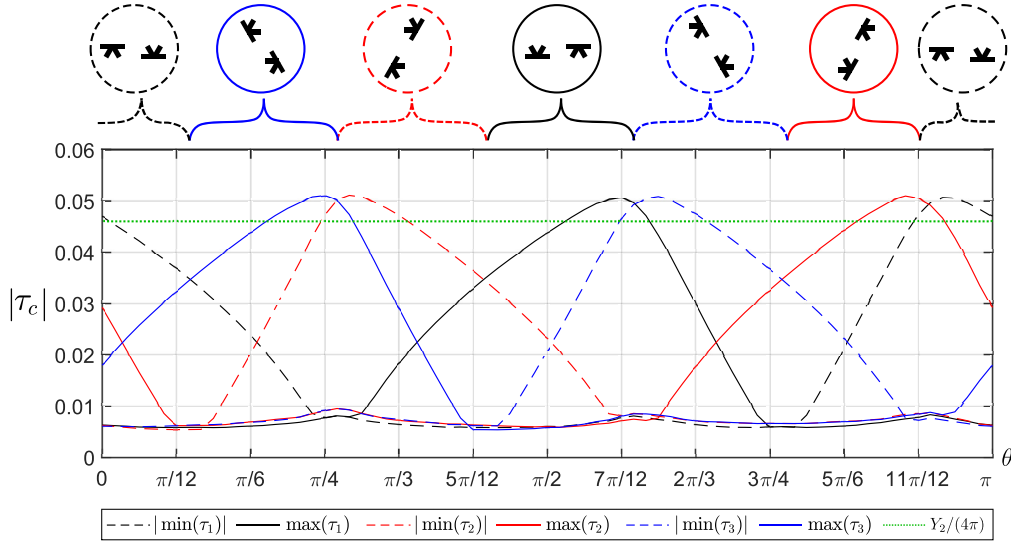


FIG. 5. The value of  $|\tau_c|$  at nucleation as a function of the rotation angle  $\theta$  of the externally imposed stress  $\sigma_{ij}^{\text{ext}}(\theta)$ . The top row shows the type of dislocation dipole that nucleates. The resolved stress along the slip plane with the largest value determines the type of dislocation dipole to nucleate.

dimensions and behaves near a nucleation event. Here we derive the incompatibility field from the  $\psi$  density field corresponding to a bcc lattice in three dimensions and visualize it for a dislocation that is seeded into an otherwise perfect crystal. Since the incompatibility field is determined by the topology of the system, it accurately locates the dislocation strings and provides a powerful tool to visualize mixed edge/screw dislocation loops.

For a suitable range of parameters  $\bar{\psi}$  and  $r$ , the equilibrium state that minimizes the free energy functional in Eq. (1) is given by a bcc lattice in three dimensions. The corresponding reciprocal lattice vectors lie on a fcc lattice with a lattice constant of unity. We choose as parameter values  $\bar{\psi} = -0.371$ ,  $r = -0.4$  for the results presented below. The amplitude of the reciprocal modes in equilibrium is  $A_0 = -\frac{2}{15}\bar{\psi} + \frac{1}{15}\sqrt{-5r - 11\bar{\psi}} = 0.2139$  [31]. The orientation of the lattice is chosen by defining the following set of reciprocal lattice vectors of unit length:  $\mathbf{q}_1 = [1, 1, 0]/\sqrt{2}$ ,  $\mathbf{q}_2 = [1, 0, 1]/\sqrt{2}$ ,  $\mathbf{q}_3 = [0, 1, 1]/\sqrt{2}$ ,  $\mathbf{q}_4 = \mathbf{q}_1 - \mathbf{q}_3$ ,  $\mathbf{q}_5 = \mathbf{q}_2 - \mathbf{q}_3$ ,  $\mathbf{q}_6 = \mathbf{q}_1 - \mathbf{q}_2$ . A cubic computational domain is considered with  $30 \times 30 \times 30$  bcc unit cells of length  $a_0 = 2\pi$  with grid spacings  $\Delta x = \Delta y = \Delta z = a_0/4$ .

We first examine a configuration with two dislocation lines added to the phase field by multiplying the initially constant amplitudes  $A_{\mathbf{q}_n}$  of the PFC by phase factors  $e^{s_n i\theta}$  corresponding to (i) a pure edge dislocation with Burgers vector  $\mathbf{b}_1 = \mathbf{e}_x$  and constant tangent line  $\mathbf{l}_1 = \mathbf{e}_z$  at  $[x_1, y_1] = [20a_0, 15a_0]$  and (ii) a pure edge dislocation with Burgers vector  $\mathbf{b}_2 = -\mathbf{e}_x$  and constant tangent line  $\mathbf{l}_1 = \mathbf{e}_z$  at  $[x_1, y_1] = [10a_0, 15a_0]$ . Here  $\theta$  is the angle in the  $xy$  plane relative to the  $x$  plane, and  $s_n$  is the charge of the dislocation, calculated as in Ref. [20]. The PFC is subsequently prepared, in the one-mode approximation, as  $\psi = \psi_0 + \sum_{n=1}^6 [A_{\mathbf{q}_n}(\mathbf{r})e^{i\mathbf{q}_n \cdot \mathbf{r}} + \text{c.c.}]$  and is allowed to evolve diffusively for few time steps to regularize the dislocation core. The stress tensor is calculated according to Eq. (2), and the strain  $e_{ij}^{\psi}$  is found by inverting the stress

tensor according to linear elasticity, using the (anisotropic) elastic constants of the bcc lattice given in Ref. [31].

The incompatibility is now a rank-2 tensor with components given by  $\eta_{ab}^{\psi} = \epsilon_{aci}\epsilon_{bdj}\partial_{cd}e_{ij}^{\psi}$  [22]. Figure 6(a) shows 2D slices of the PFC after relaxation, with the complex amplitude  $A_{\mathbf{q}_1}$  determined by amplitude demodulation of the phase field [23] in Fig. 6(b) and the largest component  $\eta_{zz}^{\psi}$  of the incompatibility tensor in Fig. 6(c). Figure 6 demonstrates how the core of the dislocation lines becomes zeros of the complex amplitudes, with a phase discontinuity of  $2\pi$  going around a dislocation line. The incompatibility tensor in terms of the dislocation density tensor  $\alpha_{ij}$  is given by  $\eta_{ik} = (\epsilon_{ipl}\partial_p\alpha_{kl} + \epsilon_{kpl}\partial_p\alpha_{il})$  [32]. For a straight dislocation line with Burgers vector  $\mathbf{b} = a_0\mathbf{e}_x$  and tangential vector  $\mathbf{l} = \mathbf{e}_z$  [as illustrated in Fig. 6(b) by black lines], the dislocation density tensor is given by its only nonzero component  $\alpha_{zx}$ , which gives  $\eta_{xx} = \eta_{yy} = \eta_{xy} = \eta_{xz} = \eta_{yz} = 0$  and  $\eta_{zz} = -\partial_y\alpha_{zx}$ , which is shown in Fig. 6(c). Thus, in this case,  $-\eta_{zz}$  is the  $y$  component of the gradient of the dislocation density, which explains its dipole structure. The spatial extent of  $\eta_{zz}$  around the dislocation line gives a measure of the spatial smoothing of the dislocation core [27]. This configuration is the straightforward extension of the 2D edge dislocations of Fig. 1(b) to three dimensions. This explains the similarity between the 2D slice of Fig. 6(c) to Fig. 2(b).

In order to demonstrate the intrinsic capability of the phase field and its associated incompatibility field to identify dislocations of mixed edge/screw character, we prepare an initial configuration with a dislocation loop. The Burgers vector of the dislocation line is constant and equal to  $a_0\mathbf{e}_x$ , while the tangent vector  $\mathbf{l}$  rotates in the  $xy$  plane. Since  $\mathbf{l}$  switches between being parallel to  $\mathbf{b}$  and perpendicular, this leads to a mixed edge/screw dislocation. Figure 7(a) shows 2D slices of the PFC, including the defect after relaxation, and the amplitude  $A_{\mathbf{q}_1}$  of the first reciprocal lattice vector is shown in Fig. 7(b). For an ideal dislocation loop with Burgers vector  $\mathbf{b} = a_0\mathbf{e}_x$

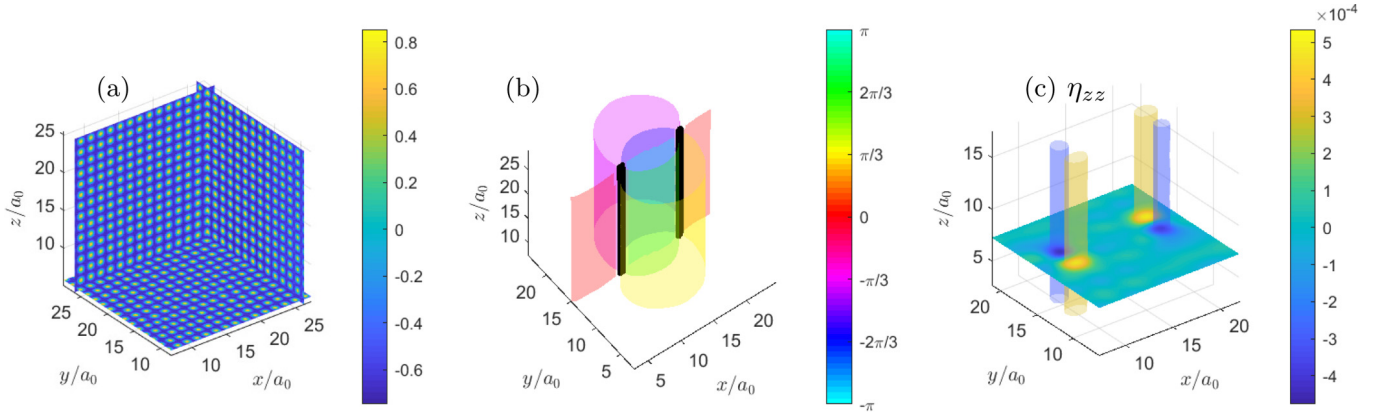


FIG. 6. (a) Two-dimensional slices of the field  $\psi$  showing edge dislocations at  $[x, y] = [10a_0, 15a_0]$  and  $[x, y] = [20a_0, 15a_0]$ . (b) The amplitude  $A_1$  of the two dislocation lines in the PFC model. The black subvolume indicates the zeros of the amplitudes and thus the position of the dislocation lines, while the color map gives the complex argument. (c) The  $\eta_{zz}^\psi$  component of the incompatibility of dislocation lines in the PFC model. The other components of the incompatibility tensor are small relative to this component (see text).

along the dislocation loop purely in the  $xy$  plane, we obtain only a contribution to the dislocation density tensor from  $\alpha_{ix}$  with  $i \neq z$ . To see how the incompatibility field calculated

from  $\psi$  captures the nature of the defects, consider the portion of the dislocation loop at  $\mathbf{r} = [5, 15, 15]$  [red dot in Fig. 7(c)]. Here we have  $\mathbf{l} = -\mathbf{e}_y$ , which gives  $\alpha_{yx}$  as the nonzero com-

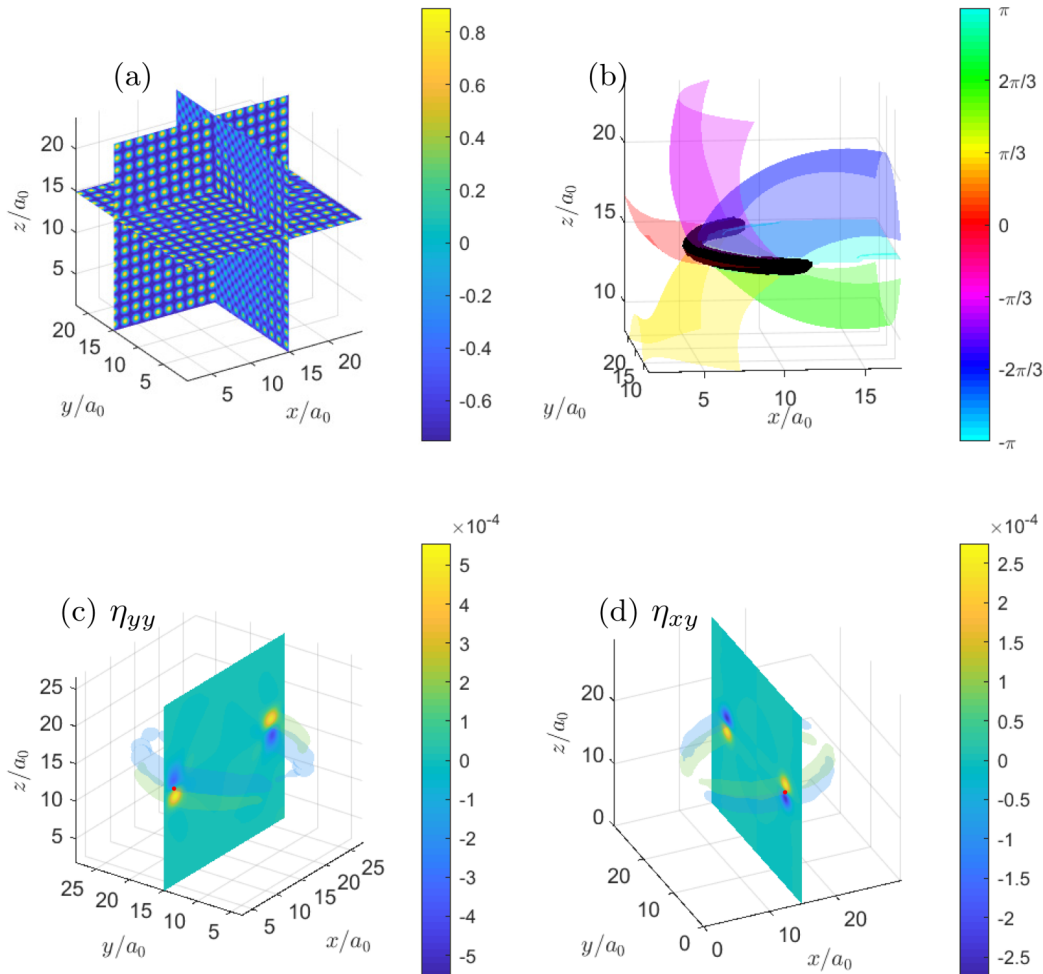


FIG. 7. (a) Two-dimensional slices of the field  $\psi$  showing the mixed types of dislocations that appear for a dislocation loop. (b) The amplitude  $A_1$  of the dislocation loop in the PFC model. The black subvolume indicates the zeros of the amplitudes and thus the position of the dislocation lines, while the color map gives the argument. (c) and (d) Two components of the incompatibility tensor  $\eta_{ij}^\psi$ . The red dots indicate positions at which the incompatibility field assumes a dipole structure similar to that of Fig. 6(c) as explained in the text.



ponent of the dislocation density tensor. We get  $\eta_{yy} = \partial_z \alpha_{yx}$ , the  $z$  component of the gradient of the dislocation density, and an identical dipole structure as in Fig. 6(c) appears, this time in the  $z$  direction. Similarly, at  $\mathbf{r} = [15, 5, 15]$  [red dot in Fig. 7(d)], the nonzero component of the dislocation density tensor is  $\alpha_{xx}$ , with which  $\eta_{xy} = \partial_z \alpha_{xx}/2$ , and we recover the dipole structure of Figs. 6(c) and 7(c), its magnitude halved due to the factor of  $1/2$  in  $\eta_{xy}$ .

We have exemplified here how the phase field  $\psi$  and its associated incompatibility tensor can correctly describe any dislocation string or loop in a given bcc lattice. In further studies, this formalism can be further generalized to other lattice symmetries and also coupled with the evolution of the  $\psi$  field to study the dynamics and nucleation of dislocation strings.

## VI. CONCLUSION

We have shown for the case of a 2D hexagonal lattice that the incompatibility field  $\eta^\psi$  derived from the phase field is a very sensitive diagnostic of the nucleation of a dislocation dipole and that it signals the nucleation event prior to the formation of a stable topological dipole. The symmetry of the field  $\eta^\psi$  prior to nucleation also gives the direction of the Burgers vectors of the defect pair about to nucleate. By examining the distribution of the resolved stress for a hexagonal lattice, we have also found it to be a good indicator of nucleation. Furthermore, a balance between the Peach-Koehler force on either one of the defects of the dipole and their mutual elastic interaction force allows a prediction of the resolved critical stress at nucleation that agrees well with the numerical results.

While our results serve to extend those of macroscopic plasticity by allowing the direct observation of the incompatibility field and its evolution under an applied stress, the conclusion that a Schmid-like criterion identifies the nucleation event is in contrast to several existing molecular

dynamics simulations. Some of these simulations show that the resolved stress does not predict the location or type of dislocations to nucleate. Instead, it is generally observed that the nominal extent of the nucleation region is very large, with a complex network of stacking faults, partial dislocations, and other significant sources of lattice distortion. These results would imply that the nucleation path in three-dimensional (3D) configuration space can be much more complex than in our 2D configuration, with possibly multiple competing trajectories that depend on details such as boundaries or applied stress protocols.

Our results indicate that the phase-field crystal model provides adequate control over configurations and applied stresses around the nucleation threshold and hence is a suitable platform for testing nucleation criteria. The model offers the necessary separation between length scales, eliminates fluctuations of thermal origin, and allows the computation of internally generated stress that contributes to lattice incompatibility and, ultimately, to nucleation. This bypasses the need for extensive averaging of molecular dynamics trajectories along paths in configuration space in which fluctuations are very small.

Finally, we presented results for a 3D bcc lattice to show that the phase field can be used to describe dislocations in this lattice and that it offers the possibility of computing the incompatibility tensor directly from the phase field for arbitrary, nonequilibrium configurations.

## ACKNOWLEDGMENTS




We thank A. Acharya, K. Olsen, and J. Rønning for many stimulating discussions. The research of J.V. was supported by the National Science Foundation, Grant No. DMR-1838977. L.A. acknowledges support from the Kavli Institute for Theoretical Physics through the National Science Foundation under Grant No. NSF PHY-1748958.

- 
- [1] J. S. Langer, *Ann. Phys. (NY)* **54**, 258 (1969).
  - [2] J. Gunton, M. San Miguel, and P. Sahni, in *Kinetics of First Order Phase Transitions*, edited by C. Domb and J. Lebowitz, Phase Transitions and Critical Phenomena Vol. 8 (Academic, London, 1983).
  - [3] A.-C. Davis and R. H. Brandenberger, *Formation and Interactions of Topological Defects*, NATO Advanced Studies Institute, Series B: Physics (Plenum, New York, 1995), Vol. 349.
  - [4] J. Friedel, in *Dislocations in Solids*, edited by F. R. N. Nabarro (North-Holland, Amsterdam, 1979), Vol. 1, pp. 1–32.
  - [5] R. Phillips, *Crystals, Defects and Microstructures: Modeling Across Scales* (Cambridge University Press, 2001).
  - [6] J. Li, K. J. Van Vliet, T. Zhu, S. Yip, and S. Suresh, *Nature (London)* **418**, 307 (2002).
  - [7] R. E. Miller and A. Acharya, *J. Mech. Phys. Solids* **52**, 1507 (2004).
  - [8] A. Garg, A. Acharya, and C. E. Maloney, *J. Mech. Phys. Solids* **75**, 76 (2015).
  - [9] C. L. Kelchner, S. J. Plimpton, and J. C. Hamilton, *Phys. Rev. B* **58**, 11085 (1998).
  - [10] T. Zhu, J. Li, A. Samanta, A. Leach, and K. Gall, *Phys. Rev. Lett.* **100**, 025502 (2008).
  - [11] X. Li, Y. Wei, L. Lu, K. Lu, and H. Gao, *Nature (London)* **464**, 877 (2010).
  - [12] K. R. Elder, M. Katakowski, M. Haataja, and M. Grant, *Phys. Rev. Lett.* **88**, 245701 (2002).
  - [13] H. Emmerich, H. Löwen, R. Wittkowski, T. Gruhn, G. Tóth, G. Tegze, and L. Gránásy, *Adv. Phys.* **61**, 665 (2012).
  - [14] J. R. Rice, *J. Mech. Phys. Solids* **40**, 239 (1992).
  - [15] J. Li, T. Zhu, S. Yip, K. J. Van Vliet, and S. Suresh, *Mater. Sci. Eng., A* **365**, 25 (2004).
  - [16] R. E. Miller and D. Rodney, *J. Mech. Phys. Solids* **56**, 1203 (2008).
  - [17] A. Garg and C. E. Maloney, *J. Appl. Mech.* **83**, 121006 (2016).
  - [18] M. Duesbery and V. Vitek, *Acta Mater.* **46**, 1481 (1998).

- [19] K. R. Elder, N. Provatas, J. Berry, P. Stefanovic, and M. Grant, *Phys. Rev. B* **75**, 064107 (2007).
- [20] A. Skaugen, L. Angheluta, and J. Viñals, *Phys. Rev. B* **97**, 054113 (2018).
- [21] This version of the microscopic stress tensor is slightly different than that in [20], but it has the same divergence. Therefore, they are physically equivalent.
- [22] E. Kröner, in *Physics of Defects*, edited by R. Balian, M. Kléman, and J.-P. Poirier, Les Houches, Session 35 (North-Holland, Amsterdam, 1981), pp. 215–315.
- [23] A. Skaugen, L. Angheluta, and J. Viñals, *Phys. Rev. Lett.* **121**, 255501 (2018).
- [24] A. Acharya and J. Viñals, *Phys. Rev. B* **102**, 064109 (2020).
- [25] V. Heinonen, Ph.D. thesis, Aalto University, 2016.
- [26] S. M. Cox and P. C. Matthews, *J. Comput. Phys.* **176**, 430 (2002).
- [27] M. Salvalaglio, L. Angheluta, Z.-F. Huang, A. Voigt, K. R. Elder, and J. Viñals, *J. Mech. Phys. Solids* **137**, 103856 (2020).
- [28] See Supplemental Material at <http://link.aps.org/supplemental/10.1103/PhysRevB.103.014107> for a video animation of the nucleation event sequence.
- [29] P. M. Chaikin and T. C. Lubensky, *Principles of Condensed Matter Physics* (Cambridge University Press, Cambridge, 1995).
- [30] B. Perreault, J. Viñals, and J. M. Rickman, *Phys. Rev. B* **93**, 014107 (2016).
- [31] K.-A. Wu and A. Karma, *Phys. Rev. B* **76**, 184107 (2007).
- [32] A. M. Kosevich, in *Dislocations in Solids*, edited by F. R. N. Nabarro (North-Holland, Amsterdam, 1979), Vol. 1, pp. 33–141.

## PAPER II



**Stress in ordered systems: Ginzburg-Landau-type density field theory**Vidar Skogvoll <sup>1</sup>, Audun Skaugen <sup>2</sup>, and Luiza Angheluta <sup>1</sup><sup>1</sup>*PoreLab, The Njord Centre, Department of Physics, University of Oslo, P.O. Box 1048, 0316 Oslo, Norway*<sup>2</sup>*Computational Physics Laboratory, Tampere University, P.O. Box 692, FI-33014 Tampere, Finland*

(Received 13 March 2021; revised 11 June 2021; accepted 14 June 2021; published 28 June 2021)

We present a theoretical method for deriving the stress tensor and elastic response of ordered systems within a Ginzburg-Landau-type density field theory in the linear regime. This is based on spatially coarse graining the microscopic stress which is determined by the variation of a free energy with respect to mass displacements. We find simple expressions for the stress tensor for phase field crystal models for different crystal symmetries in two and three dimensions. Using tetradic product sums of reciprocal lattice vectors, we calculate elastic constants and show that they are directly related to the symmetries of the reciprocal lattices. We also show that except for bcc lattices there are regions of model parameters for which the elastic response is isotropic. The predicted elastic stress-strain curves are verified by numerical strain-controlled bulk and shear deformations. Since the method is independent of a reference state, it extends also to defected crystals. We exemplify this by considering an edge and screw dislocation in the simple cubic lattice.

DOI: [10.1103/PhysRevB.103.224107](https://doi.org/10.1103/PhysRevB.103.224107)**I. INTRODUCTION**

Classical deformation theories are formulated on the assumption that a solid is a deformable continuum medium on length scales much larger than the size of any microscopic structures. This macroscopic deformation field is independent of the system size such that scale invariance becomes a symmetry of the solid [1]. However, this property is lost for solids that are micron and submicron in size, which deform erratically while exhibiting an overall strain hardening with decreasing system size [2–4]. Small crystals are still sufficiently big in size compared to the atomic scale of their crystal lattice, such that the continuum approximation remains valid, and in fact desirable, for a theory that aims to describe macroscopic properties. While the elastic degrees of freedom can still be coarse grained to elastic fields, dislocations, which are the main carriers of low-temperature plastic slips, cannot be readily coarse grained due to their topological nature which induces long-range interactions and persistent correlations. Conventional plasticity theories assume that the representative volume element is sufficiently large to contain a statistically significant number of dislocations such that the plastic deformation can be described in terms of a single average quantity, e.g., the dislocation density tensor, while ignoring fluctuations around it. This coarse graining procedure breaks down at the micron and submicron scales because there are not sufficiently many dislocations to substantiate a continuum approximation for the dislocation density, and the correlation length becomes comparable to the crystal size. We are thus left to imagine that on these scales dislocations remain discrete entities interacting through their internally generated stress fields. Discrete dislocation dynamics models are formulated precisely on these premises and consider dislocations as mobile singularities in a linearly elastic medium (see, e.g., Ref. [5]). This modeling approach has been successful at reproducing qualitatively the scale-free statistical properties

of plastic slip avalanches [6–8] and the size dependence of plastic yield [9,10]. The model is nonetheless empirical in the way reaction rates and dislocation mobilities are introduced as *ad hoc* tuning parameters.

There are several field formulations which attempt to link atomic with continuum scales through hybrid continuum/discrete models [11–13], or by introducing free-tuning intrinsic length parameters as in strain-gradient plasticity theories [14–16]. We are still lacking a theoretical model with no *ad hoc* parameters that captures quantitatively the rich plastic behavior of small crystals while also being able to shed light on the microscopic mechanisms behind the macroscopic plastic instabilities and fluctuations. A promising contender is the phase field crystal (PFC) model [17,18] which accommodates more naturally the linkage between atomic and continuum scales. It models the crystal lattice as a continuous density field and encodes both the state of elastic deformation and the plastic slip. For this reason, it has been used to model various crystal-related phenomena [19]. A caveat with the standard PFC model is that it lacks the separation of timescales between the overdamped dislocation motion and the very fast relaxation to equilibrium of elastic modes [20,21]. Recently, we have proposed a way to remedy this by constraining the diffusive relaxation to accommodate instantaneous mechanical equilibrium on continuum scales [22,23], which makes it possible to study how dislocations nucleate under stress [24].

Our method of linking between the continuum scale of elasticity and the discrete nature of dislocations is based on computing the macroscopic stress tensor directly from the PFC free energy functional, hence the order parameter. We have done this derivation for a specific free energy in two dimensions in Ref. [25]. A generalization is needed to compute the stress field from an arbitrary free energy in any dimensions, and this we address in this paper. Density functional

theories provide a similar conceptual technique for computing the microscopic stress from more *ab initio* free energies and based on Irving-Kirkwood transport theory [26–30]. However, this stress is not coarse grained or maintained at mechanical equilibrium. In molecular dynamics models, the microscopic stress is also computed through the Irving-Kirkwood formula, a generalization of the virial expression of the equation of state to nonequilibrium systems [31,32], but the system is confined to both atomic length scales and fast timescales. By contrast to these approaches, the PFC model with mechanical equilibrium handles multiple scales both in space and time. Another advantage of the PFC modeling formalism is that dislocations are emergent features, determined by the topological defects in the complex amplitudes obtained by the mode expansion of the crystal order parameter [25]. We have shown that the profile of the macroscopic stress around a dislocation matches the analytical solutions from linear elasticity in the far field and is regular at the dislocation core due to the smooth properties of the order parameter [22,23]. Thus, the formalism presented in this paper can be extended to plastic deformation and flow due to the presence of dislocations.

In this paper, we propose a systematic method that links the macroscopic stress field which describes the deformation state of a continuum elastic medium with the microscopic stress field, which, in turn, is directly determined by the order parameter of the broken crystal symmetries (a crystal density field). The generic procedure is based on finding the microscopic stress through a variational calculus of an appropriate free energy with respect to mass displacements followed by a coarse graining procedure to upscale the microscopic stress to continuum scales. This method is valid for a Ginzburg-Landau-type theory in which the free energy is given in terms of an order parameter and any order of its gradients. We provide several examples of free energies for crystals in two and three dimensions. Expanding the crystal order parameter in its reciprocal modes, we find that the elastic constants of the macroscopic stress are directly linked to tetradic product sums (fourth order moment tensors) of the reciprocal lattices of the microscopic structure. In particular, this shows how the isotropic elastic response of the two-dimensional (2D) hexagonal PFC arises directly from the sixfold symmetry of its reciprocal lattice, since only isotropic tetradic product sums can be formed from such vector sets [33].

The rest of the paper is structured as follows: In Sec. II, we present the variational procedure for a microscopic one-body density and formally connect its expression with the chemical potential. In Sec. III, we coarse grain the microscopic stress tensor over a representative volume element and show how it relates to the macroscopic stress in the linear regime. We then consider specific forms of the free energy in Sec. IV, for which we derive explicit expressions for the stress tensor and compute the elastic constants. Finally, a brief summary and concluding remarks are given in Sec. V.

## II. MICROSCOPIC STRESS FIELDS

The microscopic Cauchy stress  $\tilde{\sigma}_{ij}$  can be determined by variational changes of a free energy  $F$  with respect to adia-

batic mass displacement variations  $\delta\mathbf{x}$  through

$$\delta F = - \int_{\partial\Omega} d^D r \partial_i \tilde{\sigma}_{ij} \delta x_j + \int_{\partial\Omega} dS_j \tilde{\sigma}_{ij} \delta x_j, \quad (1)$$

where  $\partial\Omega$  is the surface of the volume element  $\Omega$  of dimension  $D$ . In continuum mechanics, the stress is determined through a variation of the free energy with respect to an underlying displacement field  $\mathbf{u}$ , which determines how a medium has been deformed from some reference state. The stress definition of Eq. (1), however, is independent of such a reference state and we will show in Sec. III how we relate this definition to the continuum stress in the linear regime. In conventional density functional theory,  $F$  is the sum of the ideal gas free energy  $F_{id}[\tilde{\rho}]$ , an external potential energy  $F_{ext}[\tilde{\rho}]$ , and an excess free energy  $F_{exc}$  which accounts for particle mutual interactions. The former two are expressed as functionals of the microscopic one-body density  $\tilde{\rho}$  which is the ensemble average of the density operator for  $N$  particles

$$\tilde{\rho}(\mathbf{r}) = \left\langle \sum_{i=1}^N \delta(\mathbf{r} - \mathbf{r}_i) \right\rangle_{\text{Ens}}, \quad (2)$$

while  $F_{exc}$  must be approximated for practical purposes [34]. In this paper, we are interested in Ginzburg-Landau-type field theories, in which  $F_{exc}$  is expressed in terms of gradients, and its exact expression is typically determined by the symmetries of the ordered phase. Thus,  $F$  is given as a functional of  $\tilde{\rho}$  and its gradients,  $F[\tilde{\rho}] = \int d^D r \tilde{f}(\tilde{\rho}, \{\partial_i \tilde{\rho}\}, \{\partial_{ij} \tilde{\rho}\}, \dots)$ , where  $\tilde{f}$  is the free energy density. Therefore, variational changes in  $F$  relate directly to variational changes in the microscopic density, and the corresponding conjugate variable defines the chemical potential:

$$\tilde{\mu}_c(\tilde{\rho}) = \frac{\delta F}{\delta \tilde{\rho}} = \frac{\partial \tilde{f}}{\partial \tilde{\rho}} - \partial_i \frac{\partial \tilde{f}}{\partial (\partial_i \tilde{\rho})} + N(\{i, j\}) \partial_{ij} \frac{\partial \tilde{f}}{\partial (\partial_{ij} \tilde{\rho})} \dots, \quad (3)$$

where  $N(\{i, j\}) = (1 + \delta_{ij})/2$  is a necessary prefactor to not overcount contributions from the off-diagonal variables (see Appendix A 1).

To derive Eq. (1) for variational changes of  $F$  in terms of  $\delta\mathbf{x}$ , we use that mass density is a locally conserved quantity, so that its variations  $\delta\tilde{\rho}$  are determined by the mass displacement variations through the conservation law, written as

$$\delta\tilde{\rho} = -\partial_j(\tilde{\rho}\delta x_j). \quad (4)$$

This implies that the variational of  $F$  relates to  $\delta\mathbf{x}$  as

$$\begin{aligned} \delta F &= \int_{\Omega} d^D r \tilde{\mu}_c \delta\tilde{\rho} \\ &= \int_{\Omega} d^D r (\tilde{\rho} \partial_j \tilde{\mu}_c) \delta x_j - \int_{\partial\Omega} dS_j (\tilde{\mu}_c \tilde{\rho}) \delta x_j. \end{aligned} \quad (5)$$

Identifying this with the expression in Eq. (1), we obtain that a net mechanical force leads to mass transport along the chemical potential gradient, namely,

$$\partial_i \tilde{\sigma}_{ij} = -\tilde{\rho} \partial_j \tilde{\mu}_c. \quad (6)$$

This expression tells us equivalently that when the system is in chemical equilibrium (steady-state microscopic density) then the associated microscopic stress is in mechanical equilibrium and vice versa. To obtain an explicit expression for  $\tilde{\sigma}_{ij}$ , we



consider a free energy density  $\tilde{f}(\tilde{\rho}, \{\partial_i \tilde{\rho}\}, \{\partial_{ij} \tilde{\rho}\})$  that only depends on  $\tilde{\rho}$  and its first and second order gradients, so that the free energy changes by

$$\delta F = \int_{\Omega} d^D r \left( \frac{\partial \tilde{f}}{\partial \tilde{\rho}} \delta \tilde{\rho} + \frac{\partial \tilde{f}}{\partial (\partial_i \tilde{\rho})} \delta (\partial_i \tilde{\rho}) + N(\{i, j\}) \frac{\partial \tilde{f}}{\partial (\partial_{ij} \tilde{\rho})} \delta (\partial_{ij} \tilde{\rho}) \right). \quad (7)$$

Using Eq. (4), and repeated integration by parts and renaming of indices, we obtain that (up to some surface terms)

$$\begin{aligned} \delta F &= \int_{\Omega} d^D r \delta x_j \partial_i \left[ (\tilde{f} - \tilde{\mu}_c \tilde{\rho}) \delta_{ij} - \frac{\partial \tilde{f}}{\partial (\partial_i \tilde{\rho})} \partial_j \tilde{\rho} \right. \\ &\quad \left. + N(\{i, m\}) \left( \partial_m \frac{\partial \tilde{f}}{\partial (\partial_{im} \tilde{\rho})} \right) \partial_j \tilde{\rho} \right. \\ &\quad \left. - N(\{i, m\}) \frac{\partial \tilde{f}}{\partial (\partial_{im} \tilde{\rho})} \partial_{mj} \tilde{\rho} \right] \\ &\equiv \int_{\Omega} d^D r \delta x_j \partial_i \tilde{\sigma}_{ij}, \end{aligned} \quad (8)$$

with the microscopic stress tensor defined as

$$\tilde{\sigma}_{ij} = (\tilde{f} - \tilde{\mu}_c \tilde{\rho}) \delta_{ij} + \tilde{h}_{ij}, \quad (9)$$

where  $\tilde{h}_{ij}$  arises from the gradient expansion of the nonlocal interaction and is given by

$$\tilde{h}_{ij} = -\tilde{f}'_i \partial_j \tilde{\rho} - \tilde{f}'_{im} \partial_{jm} \tilde{\rho} + (\partial_m \tilde{f}'_{im}) \partial_j \tilde{\rho}. \quad (10)$$

Here, we have introduced the notation  $\tilde{f}'_i = \partial \tilde{f} / \partial (\partial_i \tilde{\rho})$  and  $\tilde{f}'_{im} = N(\{i, m\}) \partial \tilde{f} / \partial (\partial_{im} \tilde{\rho})$ . Taking the divergence of Eq. (9), a lengthy but straightforward calculation shows that it satisfies the force balance Eq. (6) (see the general derivation in Appendix A).

Closer inspection of the method outlined here reveals a gauge freedom in the determination of the microscopic stress. Both the force balance Eq. (6) and the variation calculus of Eq. (8) only define the stress tensor up to a divergence free contribution. Additionally, since the dynamics is independent of any constant surface contribution to the free energy, local free energies are undetermined up to a divergence in  $\tilde{f}$ . The ambiguity is of no physical importance since it does not change the force density and is fundamentally associated with the difficulty in attributing a local (pointwise) energy contribution to a system in which there are nonlocal interactions [29,35,36]. Indeed, for structures with an intrinsic length scale, such as crystals, coarse graining over a representative volume will in part remove this ambiguity, as we will demonstrate shortly.

Equation (9) suggests a generalization which is valid for a free energy density  $\tilde{f}(\tilde{\rho}, \{\partial_i \tilde{\rho}\}, \{\partial_{ij} \tilde{\rho}\}, \dots)$  that is a function of arbitrary density gradients, where  $\tilde{h}_{ij}$  is replaced by

$$\tilde{h}_{ij} = \sum_{\alpha=1}^{\infty} \tilde{M}_{ij}^{(\alpha)}, \quad (11)$$

where

$$\tilde{M}_{ij}^{(\alpha)} = \sum_{\beta=1}^{\alpha} (-1)^{\beta} (\partial_{m_1 \dots m_{\beta-1}} \tilde{f}'_{m_1 \dots m_{\alpha-1} i}) \partial_{j m_{\beta} \dots m_{\alpha-1}} \tilde{\rho}, \quad (12)$$

and the short-form notation has been generalized to

$$\tilde{f}'_{m_1 \dots m_{\alpha}} = N(\{m_i\}) \frac{\partial \tilde{f}}{\partial (\partial_{m_1 \dots m_{\alpha}} \tilde{\rho})}. \quad (13)$$

The combinatorial factor is the inverse of the multinomial coefficient

$$N(\{m_i\}_{i=1}^{\alpha}) = \frac{N_x! N_y! N_z!}{\alpha!} \quad (14)$$

where  $N_x, N_y$ , and  $N_z$  are the numbers of elements in  $\{m_i\}_{i=1}^{\alpha} = \{m_1, \dots, m_{\alpha}\}$  that equal  $x, y$ , and  $z$ , respectively. While it is possible to redo the variational calculus for an arbitrary number of gradients, the easiest method is to confirm that the generalization satisfies the force balance Eq. (6). In Appendix A 1, we show that  $\partial_i \tilde{h}_{ij} = \tilde{\mu}_c \partial_j \tilde{\rho} - \partial_j \tilde{f}$  from which Eq. (6) follows.

As an example of this general expression of the microscopic stress, we take the Ginzburg-Landau free energy  $\tilde{f}(\tilde{\rho}, \{\partial_i \tilde{\rho}\})$ , for which Eq. (9) reduces to

$$\tilde{\sigma}_{ij} = (\tilde{f} - \tilde{\mu}_c \tilde{\rho}) \delta_{ij} - \frac{\partial \tilde{f}}{\partial (\partial_i \tilde{\rho})} \partial_j \tilde{\rho} \quad (15)$$

which is the expression derived in Ref. [30]. For a free energy density  $\tilde{f}(\tilde{\rho}, \{\partial_i \tilde{\rho}\}, \{\partial_{ij} \tilde{\rho}\})$  dependent on second order gradients, such as the basic Swift-Hohenberg free energy functional used in the PFC model, we get an expression of Eq. (9) which is the general form of the stress tensor used in Ref. [25]. It should be noted that the stress tensor in Ref. [25] omits the combinatorial factor  $N(\{i, j\})$  since this included only terms diagonal in  $ij$ , for which  $N(\{i, j\}) = 1$ . It also lacks the second term  $-\tilde{\mu}_c \tilde{\rho}$  in the isotropic part of the stress tensor as this arises from considering mass-conserving deformations, which were not considered in Ref. [25]. For more general free energy expressions, e.g., those given in Refs. [37–40], the general expression must be employed and we present in this paper some of these expressions.

### III. COARSE GRAINED DESCRIPTION: CONTINUUM LIMIT

The notion of the stress tensor defined in the previous section is valid for any density field  $\tilde{\rho}$ . A crystal as a continuum elastic medium, by contrast, has far fewer degrees of freedom and is typically characterized by a *macroscopic* density field  $\rho(\mathbf{r}) = \langle \tilde{\rho} \rangle(\mathbf{r})$ , defined as a spatial average of  $\tilde{\rho}$  over a unit representative volume, which for a crystal is given by the lattice unit  $a_0$ . For the remainder of this paper, we consider the Gaussian convolution

$$\langle \tilde{\rho} \rangle(\mathbf{r}) = \int d^D r' \frac{\tilde{\rho}(\mathbf{r}')}{(2\pi a_0^2)^{D/2}} \exp\left(-\frac{(\mathbf{r} - \mathbf{r}')^2}{2a_0^2}\right) \quad (16)$$

as the definition of a coarse graining procedure. The evolution of this density is dictated by minimizing the coarse grained free energy density  $f = \langle \tilde{f} \rangle$ . The deformation varies on scales much larger than the crystal lattice, so it is described by a macroscopic (slowly varying) displacement field  $\mathbf{u}$ . This appears as changes in the phases of the complex amplitudes of the demodulated density field. In linear elasticity, the strain field  $e_{ij}$  is the symmetric part of the displacement gradient,  $e_{ij} = \partial_i u_j$ , where  $[\dots]_{(ij)} = ([\dots]_{ij} + [\dots]_{ji})/2$

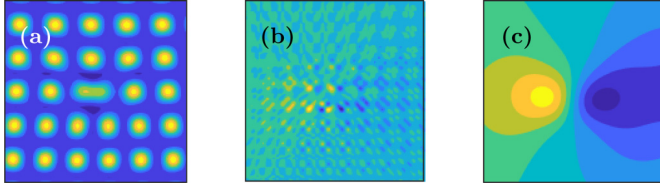


FIG. 1. (a) Microscopic density field  $\tilde{\rho}$  in a 2D PFC system with square lattice symmetry and an edge dislocation, (b) its microscopic stress field  $\tilde{\sigma}_{xy}$ , and (c) the macroscopic stress field  $\sigma_{xy} = \langle \tilde{\sigma}_{xy} \rangle$ , the object of continuum deformation theories.

is the symmetrization over indices  $ij$ . The constitutive law connecting this strain with the stress emerges on continuum scale, after coarse graining the atomic-scale interactions. The Eulerian picture [41] provides the natural framework to define mass displacement variations  $\delta \mathbf{x}$  and how they induce changes in  $\mathbf{u}$  and  $\rho$ . Namely, the volume element and macroscopic density change according to  $d^D r' \rightarrow (1 + \partial_k \delta x_k) d^D r'$  and  $\rho \rightarrow (1 - \partial_k \delta x_k) \rho$ . Additionally, the distance between planes of constant phase changes by  $\delta \mathbf{x}$ , so that the linear strain tensor transforms as  $e_{ij} \rightarrow e_{ij} + \partial_i \delta x_j$ . Thus the variation in free energy becomes

$$\begin{aligned} \delta F &= \int_{\Omega} d^D r \left( f \partial_k \delta x_k - \rho \left. \frac{\partial f}{\partial \rho} \right|_{e_{ij}} \partial_k \delta x_k + \left. \frac{\partial f}{\partial e_{ij}} \right|_{\rho} \partial_i \delta x_j \right) \\ &= \int_{\partial \Omega} dS_i \sigma_{ij} \delta x_j - \int_{\Omega} \partial_i \sigma_{ij} \delta x_j \end{aligned} \quad (17)$$

where the macroscopic stress tensor  $\sigma_{ij}$  is given by

$$\sigma_{ij} = \left( f - \rho \left. \frac{\partial f}{\partial \rho} \right|_{e_{ij}} \right) \delta_{ij} + \left. \frac{\partial f}{\partial e_{ij}} \right|_{\rho}. \quad (18)$$

Limiting our attention to crystals, we are interested in a macroscopic stress tensor in the form given by Eq. (18). Assuming that the microscopic density field  $\tilde{\rho}$  that minimizes the free energy is given by a Bravais lattice with lattice constant  $a_0$ , we can coarse grain Eq. (9) with respect to this length scale. In equilibrium,  $\tilde{\mu}_c$  is spatially constant, so for a small deviation from equilibrium, such as given by a macroscopically varying density field  $\delta \rho(\mathbf{r})$  or a macroscopic displacement field  $\mathbf{u}$ ,  $\tilde{\mu}_c$  is slowly varying and invariant under coarse graining,  $\mu_c = \langle \tilde{\mu}_c \rangle = \tilde{\mu}_c$ . Thus,  $\langle \tilde{\mu}_c \tilde{\rho} \rangle = \tilde{\mu}_c \langle \tilde{\rho} \rangle = \mu_c \rho$  and by coarse graining Eq. (9) we find

$$\langle \tilde{\sigma}_{ij} \rangle = (f - \mu_c \rho) \delta_{ij} + h_{ij}, \quad (19)$$

where  $h_{ij} = \langle \tilde{h}_{ij} \rangle$ . One can show that  $\tilde{\mu}_c = \delta F / \delta \tilde{\rho} = \delta F / \delta \rho$  which allows us to identify  $\sigma_{ij} = \langle \tilde{\sigma}_{ij} \rangle$  if

$$\left. \frac{\partial f}{\partial e_{ij}} \right|_{\rho} = h_{ij}, \quad (20)$$

which shows that  $h_{ij}$  is the thermodynamic conjugate of the strain at constant macroscopic density in the linear regime. Figure 1 shows an example of a microscopic density field, its associated microscopic stress, and the macroscopic stress field after coarse graining. While the microscopic stress tensor describes internal stresses across all length scales, the macroscopic stress tensor  $\sigma_{ij}$  describes stresses between representative volume elements bigger than that of the unit

cell. Thus, while  $\partial_i \tilde{\sigma}_{ij} = 0$  [complete chemical equilibrium, Eq. (6)] implies  $\partial_i \sigma_{ij} = 0$  the converse is not true in general. In fact, it is known that for dislocation dynamics the evolution of long wavelength distortions (macroscopic disturbances) is much faster than the diffusive dynamics of local distortions, such as the motion of dislocation lines. The typical dissipative evolution of dynamical density functional theory and phase field modeling makes no explicit distinction between the evolution of disturbances at short and long wavelengths, which has led to the development of several theories that treat this separation of timescales explicitly [21,22,42].

Since the gauge invariance of the stress tensor is related to the difficulty of having a well-defined local free energy under interactions, the act of coarse graining with respect to a length scale defined by the density field periodicity partly removes this ambiguity. As an example, consider the product  $\langle (\nabla A) B \rangle$  under coarse graining of two fields  $A, B$  that vary on the microscopic scale respective of the underlying lattice, but are slowly varying under coarse graining. Such fields can be expanded in terms of slowly varying amplitudes  $A_n(\mathbf{r}), B_n(\mathbf{r})$  as  $A = \sum_{\mathbf{K} \in \mathcal{R}} A_n(\mathbf{r}) e^{i\mathbf{K} \cdot \mathbf{r}}$ ,  $B = \sum_{\mathbf{K} \in \mathcal{R}} B_n(\mathbf{r}) e^{i\mathbf{K} \cdot \mathbf{r}}$ , where  $\mathcal{R}$  is the reciprocal lattice of the microscopic structure. We find

$$\begin{aligned} \langle (\nabla A) B \rangle &= \sum_{\mathbf{K}_n \in \mathcal{R}} \sum_{\mathbf{K}_{n'} \in \mathcal{R}} \langle \nabla (A_n(\mathbf{r}) e^{i\mathbf{K}_n \cdot \mathbf{r}}) B_n(\mathbf{r}) e^{i\mathbf{K}_{n'} \cdot \mathbf{r}} \rangle \\ &\approx \sum_{\mathbf{K}_n \in \mathcal{R}} \sum_{\mathbf{K}_{n'} \in \mathcal{R}} [(\nabla A_n(\mathbf{r}) + i\mathbf{K}_n A_n) B_n(\mathbf{r}) \\ &\quad \times \langle e^{i(\mathbf{K}_n + \mathbf{K}_{n'}) \cdot \mathbf{r}} \rangle], \end{aligned} \quad (21)$$

where we have used that the fields  $A_n(\mathbf{r}), B_n(\mathbf{r})$  vary slowly on the periodicity of the lattice to take the coarse graining through. The coarse grained value of  $e^{i(\mathbf{K}_n + \mathbf{K}_{n'}) \cdot \mathbf{r}}$  will only be nonzero at resonance, given by  $\mathbf{K}_{n'} = -\mathbf{K}_n$ , i.e.,  $\langle e^{i(\mathbf{K}_n + \mathbf{K}_{n'}) \cdot \mathbf{r}} \rangle \equiv \delta_{n', -n}$  [43], and using that for slowly varying amplitudes  $|\nabla A_n(\mathbf{r})| \ll |\mathbf{K} A_n(\mathbf{r})|$  we find

$$\begin{aligned} \langle (\nabla A) B \rangle &\approx \sum_{\mathbf{K}_n \in \mathcal{R}} i\mathbf{K}_n A_n(\mathbf{r}) B_{-n}(\mathbf{r}) \\ &= \sum_{\mathbf{K}_n \in \mathcal{R}} i(-\mathbf{K}_{-n}) B_{-n}(\mathbf{r}) A_n(\mathbf{r}) \approx -\langle A(\nabla B) \rangle, \end{aligned} \quad (22)$$

as can be shown by expanding the right-hand side under similar assumptions. The exact difference between the left- and right-hand side of this equation is given by

$$\langle (\nabla A) B \rangle - (-\langle A(\nabla B) \rangle) = \langle \nabla(A B) \rangle = \nabla \langle A B \rangle, \quad (23)$$

since the gradient operator commutes with the coarse graining operation as can be seen by

$$\begin{aligned} \partial_i \langle \tilde{X} \rangle &= \int d^D r' \frac{\tilde{X}(\mathbf{r}')}{(2\pi a_0)^{D/2}} \partial_i \exp\left(-\frac{(\mathbf{r} - \mathbf{r}')^2}{2a_0^2}\right) \\ &= - \int d^D r' \frac{\tilde{X}(\mathbf{r}')}{(2\pi a_0)^{D/2}} \partial_{r'} \exp\left(-\frac{(\mathbf{r} - \mathbf{r}')^2}{2a_0^2}\right) \\ &= \int d^D r' \frac{\partial_{r'} \tilde{X}(\mathbf{r}')}{(2\pi a_0)^{D/2}} \exp\left(-\frac{(\mathbf{r} - \mathbf{r}')^2}{2a_0^2}\right) = \langle \partial_i \tilde{X} \rangle. \end{aligned} \quad (24)$$



TABLE I.  $h_{ij}$  and its associated elastic constants in terms of amplitudes ( $A, B, C$ ) of the mode expansion for different PFC models. The free energy functionals for the different PFC models are given by Eqs. (27), (43), (54), (60), and (70), respectively, where  $\mathcal{L}_X = X + \nabla^2$ . The elastic constants can be expressed in Voigt notation by  $C_{11} = \lambda + 2\mu + \gamma$ ,  $C_{12} = \lambda$ ,  $C_{44} = \mu$ . The last column gives the relationship between PFC model parameters  $r, \bar{\psi}$  for which the elastic response is isotropic.

PFC model	$h_{ij}$	Elastic constants	Isotropic elastic domain
2D hex	$-2\langle(\mathcal{L}_1\psi)\partial_{ij}\psi\rangle$	$\lambda = 3A^2$ $\mu = 3A^2$ $\gamma = 0$	Always
2D sq	$-2\langle(\mathcal{L}_1\mathcal{L}_2\psi)(\mathcal{L}_1 + \mathcal{L}_2)\partial_{ij}\psi\rangle$	$\gamma = 16B^2$ $\mu = 16B^2$ $\gamma = 8A^2 - 32B^2$	$r = -\frac{25}{3}\bar{\psi}^2$
3D bcc	$-2\langle(\mathcal{L}_1\psi)\partial_{ij}\psi\rangle$	$\lambda = 4A^2$ $\mu = 4A^2$ $\gamma = -4A^2$	Never
3D fcc	$-2\langle(\mathcal{L}_1\mathcal{L}_3\psi)(\mathcal{L}_1 + \mathcal{L}_3)\partial_{ij}\psi\rangle$	$\lambda = \frac{32}{81}A^2$ $\mu = \frac{32}{81}A^2$ $\gamma = \frac{32}{81}(2B^2 - A^2)$	$r = -\frac{255}{49}\bar{\psi}^2$
3D sc	$-2\langle(\mathcal{L}_1\mathcal{L}_2\mathcal{L}_3\psi)(\mathcal{L}_2\mathcal{L}_3 + \mathcal{L}_1\mathcal{L}_3 + \mathcal{L}_1\mathcal{L}_2)\partial_{ij}\psi\rangle$	$\lambda = 16B^2 + 128C^2$ $\mu = 16B^2 + 128C^2$ $\gamma = 32A^2 - 16B^2 - 256C^2$	$r \approx -2.10144\bar{\psi}^2$

Thus, by employing Eq. (22) to rewrite expressions, we are ignoring the variations in the coarse grained boundary terms. In the case of a crystalline lattice, we have seen computationally that this identity holds far beyond the regime of linear elasticity. Equation (22) shows how gradient terms of the microscopic stress tensor can be rewritten under coarse graining, indicating that different descriptions of the stress on the microscopic scale are equivalent upon coarse graining. In particular, it allows rewriting Eq. (12) in a coarse grained form as

$$\langle\tilde{M}_{ij}^{(\alpha)}\rangle \approx -\alpha\langle\tilde{f}_{m_1\dots m_{\alpha-1}i}^i\partial_{jm_1\dots m_{\alpha-1}}\tilde{\rho}\rangle. \quad (25)$$

As will be shown for the PFC models introduced in the next section, this expression will be symmetric in the indices,  $i \leftrightarrow j$ , indicating that coarse graining will make the stress tensor explicitly symmetric. This is consistent with results of recent work which used molecular dynamics simulations to show that the symmetric nature of the stress tensor is intimately linked with the continuum assumption and may break down on a microscopic resolution [44].

#### IV. APPLICATION TO PHASE FIELD CRYSTAL MODELS

In this section, we consider forms of the free energy  $F$  specific to systems with different crystal symmetries. An already well-established minimal model for this is the PFC which was introduced as a phenomenological field theory to model crystallization and related phenomena [17]. We investigate five PFC models—2D hexagonal (2D hex), 2D square (2D sq), three-dimensional (3D) bcc, 3D fcc, and 3D simple cubic (3D sc)—using established free energy functionals for the first four and an adapted PFC model for the sc phase. As customary for phase field modeling, we employ the notation  $\psi$  for the microscopically varying density field under consideration. The stress tensor  $\tilde{\sigma}_{ij}$  is defined in terms of a microscopic density field  $\tilde{\rho}$ , so its expression in terms of  $\psi$  depends on the exact connection between these two quantities. Here, we

define  $\psi \equiv \tilde{\rho}$ , and consider the elastic response of  $\psi$  during an adiabatic deformation at constant macroscopic density  $\langle\psi\rangle$ , which is achieved by the following transformation of the field:

$$\psi'(\mathbf{r}) = \psi^{\text{eq}}(\mathbf{r} - \mathbf{u}), \quad (26)$$

where  $\psi^{\text{eq}}(\mathbf{r})$  is the unstrained equilibrium crystal configuration and  $\mathbf{u}$  is an arbitrary macroscopic displacement field. We employ the method developed in the previous sections to find explicit forms of the stress tensors in terms of  $\psi$ . Then, for each PFC model, we expand the ground state in an appropriate number of reciprocal lattice modes to obtain expressions for the elastic constants in terms of the reciprocal mode amplitudes by use of tetradic product sums. For the established free energy functionals, we find the elastic constants in agreement with previous works. From the expressions of the elastic constants, we find that there are particular model parameters for which all the PFC models exhibit isotropic elasticity except for the 3D bcc model which always exhibits anisotropic elastic behavior. The results are summarized in Table I. We then prepare a  $60 \times 60 (\times 5)$  unit cells periodic lattice for the 2D (3D) PFC models and numerically subject them to two types of distortions and calculate the elastic response and stress given by  $h_{ij}$ . The results are shown in Fig. 2 and demonstrate that  $h_{ij}$  measures the energetic response for a deformation at constant macroscopic density, as suggested by Eq. (20).

The field transformation of Eq. (26) is a strain-controlled adiabatic deformation at constant macroscopic density  $\bar{\psi}$ , with no diffusive relaxation. We will thus recover the elastic constant tensor  $C_{ijkl}$  at constant macroscopic density. These are not the same elastic constants as will be obtained if  $\rho$  and  $\mathbf{u}$  are not varied independently, and differ, for instance, from the elastic constants at constant chemical potential or at constant vacancy concentration [41]. Denoting the free energy under strain  $e_{ij}$  as  $F_{e_{ij}}$ , we are thus focusing on strains in which only the planes of constant phase are displaced, using the equilibrium amplitudes  $\{A_{\mathbf{k}}^{(0)}\}$  of the reciprocal modes

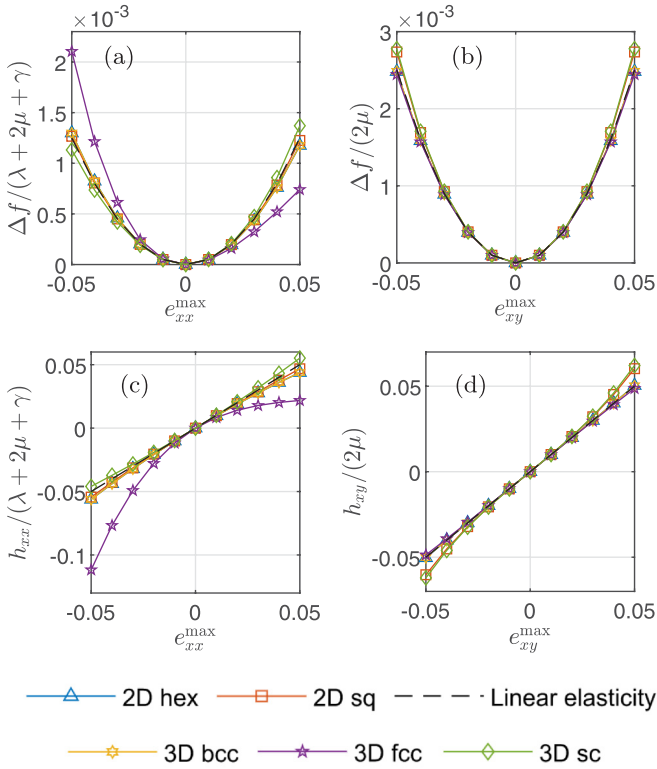


FIG. 2. (a), (b) Difference in the free energy density  $\Delta f = \langle \tilde{f}(\psi') \rangle - \langle \tilde{f}(\psi^{\text{eq}}) \rangle$  in the center region [red dots in Figs. 4(c) and 4(d)] for  $\psi'(\mathbf{r})$ , Eq. (26), strained by (a) the bulk displacement field  $\mathbf{u}^{(B)}$ , Eq. (38), and (b) the shear displacement field  $\mathbf{u}^{(S)}$ , Eq. (39). (c), (d) The nonzero stress components for the PFC strained by the (c) bulk and (d) shear displacement fields. In all plots, the dashed lines indicate the prediction from linear elasticity, Eqs. (41) and (42).

$\{\mathbf{K}\}$ . This is equivalent to straining the reciprocal lattice vectors  $\mathbf{K} \rightarrow \mathbf{K}_{e_{ij}}$ , so that  $F_{e_{ij}} = F[A_{\mathbf{K}}^{(0)}, \{\mathbf{K}_{e_{ij}}\}, \bar{\psi}, V]$ . If the order parameter is interpreted as a one-body density, the physical process of straining at constant macroscopic density requires counteracting vacancy diffusion, unless the applied strain is traceless. The deformation is adiabatic in the sense that no minimization of the free energy at the given strain is performed. Reference [45] considered isothermal strain-controlled deformation at constant macroscopic density by also minimizing the free energy under strain, given by  $F_{e_{ij}} = \min_{A_{\mathbf{K}}} F[\{A_{\mathbf{K}}\}, \{\mathbf{K}_{e_{ij}}\}, \bar{\psi}, V]$ . Since the equilibrium values of the amplitudes are minima in configuration space by definition, this deformation will lead to nonlinear effects, and does not influence the elastic constants. References [46,47] considered strain-controlled isothermal deformation including the resulting volumetric deformation of the macroscopic density  $\bar{\psi} \rightarrow \bar{\psi}_{e_{ij}}$  as well as induced changes in the region volume  $V \rightarrow V_{e_{ij}}$ , i.e.,  $F_{e_{ij}} = \min_{A_{\mathbf{K}}} F[\{A_{\mathbf{K}}\}, \{\mathbf{K}_{e_{ij}}\}, \bar{\psi}_{e_{ij}}, V_{e_{ij}}]$ . They showed that the elastic constants associated to such a deformation differ from those obtained here or in previous works, and are also dependent on the exact connection between the order parameter  $\psi$  and the physical one-body density. This type of deformation corresponds to a mass displacement at constant vacancy concentration and hence these elastic constants could be derived from the stress tensor of Eq. (19). However, in

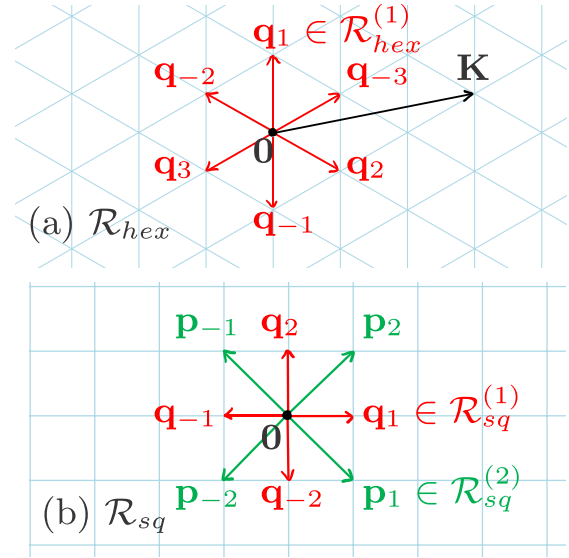


FIG. 3. Reciprocal lattices of the 2D crystal structures. (a) Modes  $\mathcal{R}_{\text{hex}}$  of the hexagonal reciprocal lattice where  $\mathbf{K}$  denotes a general mode:  $\mathcal{R}_{\text{hex}}^{(1)} = \{\mathbf{q}_n\}$  are the closest reciprocal lattice modes ( $\mathbf{q}_n^2 = 1$ ). (b) Modes  $\mathcal{R}_{\text{sq}}$  of the square reciprocal lattice:  $\mathcal{R}_{\text{sq}}^{(1)} = \{\mathbf{q}_n\}$  are the closest reciprocal lattice modes ( $\mathbf{q}_n^2 = 1$ ) and  $\mathcal{R}_{\text{sq}}^{(2)} = \{\mathbf{p}_n\}$  are the next-to-closest modes ( $\mathbf{p}_n^2 = 2$ ).

this case, the variational procedure must also be reevaluated under the specific connection between the order parameter and the physical one-body density. In Ref. [24], we performed stress-controlled isothermal and quasistatic deformation of the PFC for which we found the nucleation of crystal defects occurring at strains  $|e_{ij}| \approx 0.1$ .

### A. 2D hexagonal lattice

In its simplest form, the PFC free energy is based on the Swift-Hohenberg free energy given by  $F = \int d^2r \tilde{f}^{(\text{hex})}$ , with the free energy density

$$\tilde{f}^{(\text{hex})} = \frac{1}{2}(\mathcal{L}_1\psi)^2 + \frac{r}{2}\psi^2 + \frac{1}{4}\psi^4, \quad (27)$$

where  $\mathcal{L}_1 = 1 + \nabla^2$  and  $r$  is a parameter which is proportional to the deviation from the critical temperature. For the free energy density given in Eq. (27), we find

$$\tilde{f}'_{m_1} = 0, \quad \tilde{f}'_{m_1 m_2} = \mathcal{L}_1\psi \delta_{m_1 m_2}, \quad (28)$$

which gives

$$\tilde{h}_{ij} = -(\mathcal{L}_1\psi)\partial_{ij}\psi + (\partial_i\mathcal{L}_1\psi)\partial_j\psi. \quad (29)$$

For  $r < 0$  and a range of parameters  $\bar{\psi}$ , the free energy  $F$  is minimized in two dimensions by a hexagonal lattice with lattice constant  $a_0 = 4\pi/\sqrt{3}$ . Thus, for a perfect lattice, the density field  $\psi$  can be expressed as a superposition of periodic modes in the reciprocal space associated to that lattice:

$$\psi_{\text{hex}}^{\text{eq}}(\mathbf{r}) = \bar{\psi} + \sum_{\mathbf{K} \in \mathcal{R}_{\text{hex}} \setminus \{0\}} A_{\mathbf{K}} e^{i\mathbf{K} \cdot \mathbf{r}}, \quad (30)$$

where  $\mathbf{K}$  is a nonzero mode of the hexagonal reciprocal lattice  $\mathcal{R}_{\text{hex}}$  [see Fig. 3(a)] and  $A_{\mathbf{K}}$  is the corresponding amplitude. When  $|r| < 1$ , the equilibrium state  $\psi_{\text{hex}}^{\text{eq}}(\mathbf{r})$  is well approximated in the one-mode expansion in terms of the principal

reciprocal lattice vectors:

$$\psi_{\text{hex}}^{\text{eq}}(\mathbf{r}) \approx \bar{\psi} + A_{\text{hex}} \sum_{\mathbf{q}_n \in \mathcal{R}_{\text{hex}}^{(1)}} e^{i\mathbf{q}_n \cdot \mathbf{r}}, \quad (31)$$

where  $\mathcal{R}_{\text{hex}}^{(1)} = \{\mathbf{q}_{-3}, \mathbf{q}_{-2}, \mathbf{q}_{-1}, \mathbf{q}_1, \mathbf{q}_2, \mathbf{q}_3\}$  are the closest nonzero modes on the hexagonal reciprocal lattice, which can be chosen as

$$\begin{aligned} \mathbf{q}_1 &= (0, 1), \\ \mathbf{q}_2 &= (\sqrt{3}/2, -1/2), \\ \mathbf{q}_3 &= (-\sqrt{3}/2, -1/2), \end{aligned} \quad (32)$$

$\mathbf{q}_{-n} = -\mathbf{q}_n$ , and  $A_{\text{hex}}$  is the equilibrium amplitude.  $A_{\text{hex}}$  is determined by inserting  $\psi_{\text{eq}}^{\text{hex}}$  into the free energy density of Eq. (27), averaging over a unit cell and minimizing with respect to  $A_{\text{hex}}$  [17]. Given the length scale of the lattice constant, we can define the stress tensor (associated to a continuum elastic medium) in terms of  $\psi$  by coarse graining:

$$\sigma_{ij}^{(2D \text{ hex})} = \delta_{ij}(f - \mu_c \langle \psi \rangle) + h_{ij}^{(2D \text{ hex})}, \quad (33)$$

where  $f = \langle \tilde{f}^{\text{hex}} \rangle$ ,  $\mu_c = \delta F / \delta \psi$ , and we have used Eq. (25) to write

$$h_{ij}^{(2D \text{ hex})} = -2 \langle (\mathcal{L}_1 \psi) \partial_{ij} \psi \rangle. \quad (34)$$

The elastic coefficients  $C_{ijkl}$  of the corresponding hexagonal lattice can be computed by deforming the one-mode approximation by a macroscopic displacement field  $\mathbf{u}$  according to the field transformation of Eq. (26), which gives to first order in the distortion  $\partial_k u_l$  (see Appendix B 1)

$$h_{ij}^{(2D \text{ hex})} = 4A_{\text{hex}}^2 \partial_k u_l \sum_{\mathbf{q}_n \in \mathcal{R}_{\text{hex}}^{(1)}} q_{ni} q_{nj} q_{nk} q_{nl}, \quad (35)$$

where  $q_{ni}$  is the  $i$ th Cartesian coordinate of the reciprocal lattice vector  $\mathbf{q}_n$ . This shows that the elastic constants are directly determined by the tetradic product sum of  $\mathcal{R}_{\text{hex}}^{(1)}$ . This is a general feature of all the PFC models which we consider in this paper. It is given by

$$\sum_{\mathbf{q}_n \in \mathcal{R}_{\text{hex}}^{(1)}} q_{ni} q_{nj} q_{nk} q_{nl} = \frac{3}{4} (\delta_{ij} \delta_{kl} + 2\delta_{k(i} \delta_{j)l}), \quad (36)$$

as can be shown by checking all components. Thus, we find

$$C_{ijkl} = \lambda \delta_{ij} \delta_{kl} + 2\mu \delta_{k(i} \delta_{j)l} + \gamma \delta_{ijkl} \quad (37)$$

where  $\lambda = \mu = 3A_{\text{hex}}^2$ , which are the standard Lamé parameters of an isotropic elastic medium,  $\gamma = 0$ , which is an elastic coefficient quantifying any elastic anisotropy, and  $\delta_{ijkl}$  is a generalization of the Kronecker-delta symbol which is 1 if all indices are equal and zero otherwise. These are the same elastic constants as those found in Refs. [17,25]. For the 2D hexagonal lattice,  $\gamma = 0$ , since the tetradic product sum of  $\mathcal{R}_{\text{hex}}^{(1)}$  is isotropic. This isotropy, and hence the isotropic elastic properties of the hexagonal lattice, is a direct result of the sixfold rotational symmetry of  $\mathcal{R}_{\text{hex}}^{(1)}$  [33].

We prepare a  $60 \times 60$  2D hexagonal PFC lattice in the one-mode approximation with periodic boundary conditions and lattice vectors reciprocal to  $\mathcal{R}_{\text{hex}}^{(1)}$ , which gives a lattice constant of  $a_0 = 4\pi/\sqrt{3}$ . We choose grid spacing  $\Delta x = a_0/7$  and  $\Delta y = a_0\sqrt{3}/12$  and parameters  $r = -0.3$  and  $\bar{\psi} = -0.25$ .

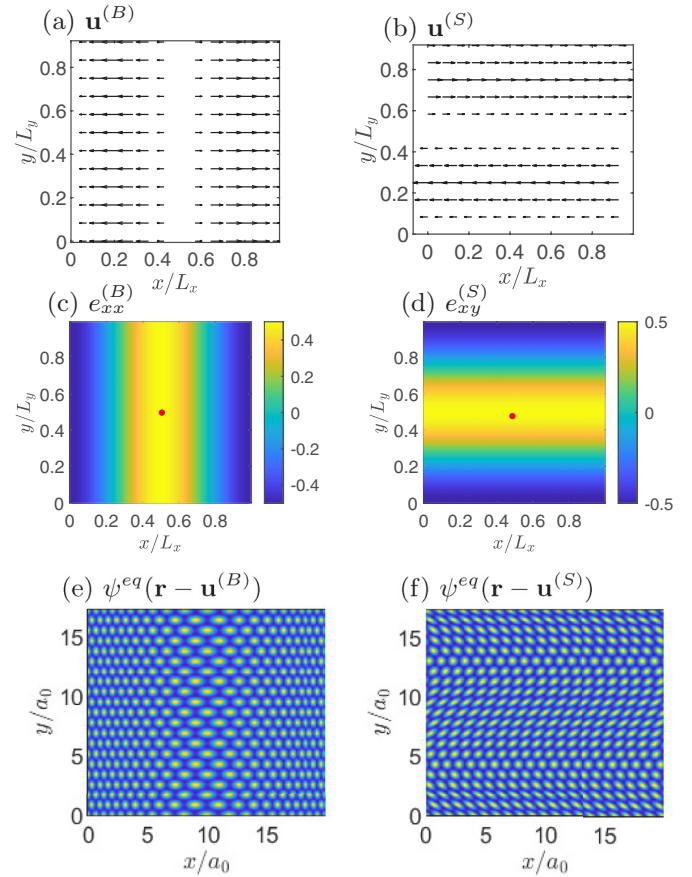


FIG. 4. (a) Bulk displacement field  $\mathbf{u}^{(B)}$  with  $e_{xx}^{\text{max}} = 0.5$ , (b) shear displacement field  $\mathbf{u}^{(S)}$  with  $e_{xy}^{\text{max}} = 0.5$ , (c)  $e_{xx}^{(B)}$ , and (d)  $e_{xy}^{(S)} = u_{xy}^{(S)}/2$ . The bottom row shows a  $20 \times 20$  2D hexagonal PFC distorted by (e)  $\mathbf{u}^{(B)}$  and (f)  $\mathbf{u}^{(S)}$ . Such highly strained configurations would be prone to melting and nucleation of dislocations if allowed to evolve diffusively, and are included only to illustrate the effects of the applied strains. The dot in (c) and (d) marks the central region of the computational domain at which both displacement fields are at their maximal strains.

The PFC was deformed by two different displacement fields: (1) a bulk displacement field,

$$u_x^{(B)} = -e_{xx}^{\text{max}} \frac{L_x}{2\pi} \sin\left(2\pi \frac{x}{L_x}\right), \quad u_y^{(B)} = 0, \quad (38)$$

which corresponds to uniaxial compression/extension in the  $(1,0)$  direction; and (2) a shear displacement field,

$$u_x^{(S)} = -e_{xy}^{\text{max}} \frac{L_y}{\pi} \sin\left(2\pi \frac{y}{L_y}\right), \quad u_y^{(S)} = 0, \quad (39)$$

which corresponds to pure shear in the  $(0,1)$  direction. Here,  $L_x$  and  $L_y$  are the lengths of the simulation domain in the  $x$  and  $y$  direction, respectively.  $e_{xx}^{\text{max}}$  and  $e_{xy}^{\text{max}}$  are parameters used to tune the magnitude of the displacement fields. Figure 4 shows the displacement fields and the nonzero components of the strains. The displacement fields are constructed in such a way that for  $\mathbf{u}^{(B)}$  ( $\mathbf{u}^{(S)}$ ) the only nonzero component of the strain is  $e_{xx}$  ( $e_{xy}$ ), the maximal value of which is  $e_{xx}^{\text{max}}$  ( $e_{xy}^{\text{max}}$ ) along the line  $x = L_x/2$  ( $y = L_y/2$ ). For illustrative purposes, we have included the distortion of a  $20 \times 20$  hexagonal lattice

by the bulk and shear displacement fields in Figs. 4(e) and 4(f), respectively. For the given distortion, the linear elastic energy density is given by

$$\Delta f_{\text{el}} = \frac{1}{2} C_{ijkl} e_{ij} e_{kl}, \quad (40)$$

which for the bulk deformation in the central region, where  $e_{xx} = e_{xx}^{\text{max}}$ , gives

$$\Delta f_{\text{el}}^{(B)} = \frac{1}{2} (\lambda + 2\mu + \gamma) (e_{xx}^{\text{max}})^2. \quad (41)$$

The free energy density under the bulk deformation, calculated by directly coarse graining Eq. (27), is shown in Fig. 2(a), where the dashed line indicates the elastic energy of Eq. (41). For the shear deformation, the elastic energy density is given by

$$\Delta f_{\text{el}}^{(S)} = (2\mu) (e_{xy}^{\text{max}})^2. \quad (42)$$

The free energy under the shear deformation is shown in Fig. 2(b), where the dashed line indicates the linear elastic energy of Eq. (42). We see that the energy stored in the PFC under deformation is correctly accounted for by linear elasticity for small strains. Figures 2(c) and 2(d) show the values of  $h_{xx}^{(2D \text{ hex})}$  and  $h_{xy}^{(2D \text{ hex})}$  in the central region [red dot in Figs. 4(c) and 4(d)] as functions of the applied strains  $e_{xx}^{\text{max}}$  and  $e_{xy}^{\text{max}}$ , respectively, where the dashed line indicates the linear stresses  $h_{ij} = C_{ijkl} e_{kl}$ . We see that the stress in the 2D hexagonal PFC is accounted for by linear elasticity for small strains.

## B. 2D square lattice

One of the challenges of the PFC formalism is finding suitable free energy functionals that favor a particular lattice symmetry. In order to ensure phase stability in the presence of disturbances, such as dislocations or external stresses, the phase diagram of a proposed free energy must be calculated and parameters chosen so that the desired lattice symmetry minimizes the free energy. The postulation of free energy functionals and subsequent calculation of phase diagrams has thus been the subject of much research [17,38–40,48–51]. However, a straightforward generalization of the free energy in Eq. (27) to obtain a square lattice is obtained by noting that the  $\mathcal{L}_1$  term was introduced to favor spatial modulations corresponding to the closest modes  $\mathbf{q}_n^2 = 1$  on the reciprocal lattice. For the reciprocal lattice of the square lattice, shown in Fig. (3), the next-to-closest modes  $\mathcal{R}_{\text{sq}}^{(2)} = \{\mathbf{p}_n\}$  with length  $\mathbf{p}_n^2 = 2$  will give sizable contributions to the average free energy of Eq. (27). Thus, by modifying the free energy to also favor these second modes, one can postulate the free energy functional  $F = \int d^2r \tilde{f}^{(\text{sq})}$  with

$$\tilde{f}^{(\text{sq})} = \frac{1}{2} (\mathcal{L}_1 \mathcal{L}_2 \psi)^2 + \frac{r}{2} \psi^2 + \frac{1}{4} \psi^4, \quad (43)$$

where

$$\mathcal{L}_X = X + \nabla^2 \quad (44)$$

is a factor introduced to energetically favor modes of length  $\sqrt{X}$ . This free energy was shown to produce a 2D square phase in Ref. [37]. The phase diagram for this free energy shows that it has a stable region for the square lattice for a range of values of  $r$  [50]. Similar to the hexagonal lattice, we

get nonzero contributions to  $h_{ij}$  from

$$\begin{aligned} \tilde{f}'_{m_1 m_2} &= 3 \mathcal{L}_1 \mathcal{L}_2 \psi \delta_{m_1 m_2}, \\ \tilde{f}'_{m_1 m_2 m_3 m_4} &= \mathcal{L}_1 \mathcal{L}_2 \psi \delta_{(m_1 m_2) \delta_{m_3 m_4)}. \end{aligned} \quad (45)$$

Here we are using the general notation for symmetrizing over multiple indices:

$$[\dots]_{(m_1 \dots m_\alpha)} = \frac{1}{\alpha!} \sum_{\sigma \in S_\alpha} [\dots]_{\sigma(m_1) \dots \sigma(m_\alpha)}, \quad (46)$$

where  $S_\alpha$  is the symmetric group of  $\alpha$  elements. This gives

$$\begin{aligned} h_{ij}^{(2D \text{ sq})} &= \langle M_{ij}^{(2)} \rangle + \langle M_{ij}^{(4)} \rangle \\ &= -6 \langle (\mathcal{L}_1 \mathcal{L}_2 \psi) \partial_{ij} \psi \rangle - 4 \langle (\mathcal{L}_1 \mathcal{L}_2 \psi) \partial_{ij} \psi \rangle \\ &= -2 \langle (\mathcal{L}_1 \mathcal{L}_2 \psi) (\mathcal{L}_1 + \mathcal{L}_2) \partial_{ij} \psi \rangle. \end{aligned} \quad (47)$$

Since the square lattice will give sizable contributions also to the second closest modes on the reciprocal lattice, we expand the ground state of the PFC density  $\psi$  in the two-mode approximation:

$$\psi^{\text{eq}} = \bar{\psi} + A_{\text{sq}} \sum_{\mathbf{q}_n \in \mathcal{R}_{\text{sq}}^{(1)}} e^{i\mathbf{q}_n \cdot \mathbf{r}} + B_{\text{sq}} \sum_{\mathbf{p}_n \in \mathcal{R}_{\text{sq}}^{(2)}} e^{i\mathbf{p}_n \cdot \mathbf{r}}, \quad (48)$$

where  $A_{\text{sq}}$  and  $B_{\text{sq}}$  are the equilibrium amplitudes of the modes on the 2D square reciprocal lattice  $\mathcal{R}_{\text{sq}}^{(1)} = \{\mathbf{q}_{-2}, \mathbf{q}_{-1}, \mathbf{q}_1, \mathbf{q}_2\}$  and  $\mathcal{R}_{\text{sq}}^{(2)} = \{\mathbf{p}_{-2}\mathbf{p}_{-1}, \mathbf{p}_1, \mathbf{p}_2\}$ , respectively, where

$$\begin{aligned} \mathbf{q}_1 &= (1, 0), & \mathbf{p}_1 &= (1, -1), \\ \mathbf{q}_2 &= (0, 1), & \mathbf{p}_2 &= (1, 1), \end{aligned} \quad (49)$$

$\mathbf{q}_{-n} = -\mathbf{q}_n$ , and  $\mathbf{p}_{-n} = -\mathbf{p}_n$  [see Fig. 3(b)].  $A_{\text{sq}}, B_{\text{sq}}$  are determined by minimization of the free energy. By deforming the two-mode approximation by a displacement field  $\mathbf{u}$ , we find (Appendix B 2)

$$\begin{aligned} h_{ij}^{(2D \text{ sq})} &= 4A_{\text{sq}}^2 \partial_k u_l \sum_{\mathbf{q}_n \in \mathcal{R}_{\text{sq}}^{(1)}} q_{ni} q_{nj} q_{nl} q_{nk} \\ &\quad + 4B_{\text{sq}}^2 \partial_k u_l \sum_{\mathbf{p}_n \in \mathcal{R}_{\text{sq}}^{(2)}} p_{ni} p_{nj} p_{nk} p_{nl}. \end{aligned} \quad (50)$$

The tetradic product sums are given by

$$\sum_{\mathbf{q}_n \in \mathcal{R}_{\text{sq}}^{(1)}} q_{ni} q_{nj} q_{nl} q_{nk} = 2\delta_{ijkl}, \quad (51)$$

$$\sum_{\mathbf{p}_n \in \mathcal{R}_{\text{sq}}^{(2)}} p_{ni} p_{nj} p_{nk} p_{nl} = 4(\delta_{ij} \delta_{kl} + 2\delta_{k(i} \delta_{j)l} - 2\delta_{ijkl}). \quad (52)$$

This gives elastic constants  $\lambda = \mu = 16B_{\text{sq}}^2$  and  $\gamma = 8A_{\text{sq}}^2 - 32B_{\text{sq}}^2$ , which match those found in previous work for the 2D square PFC lattice [38]. Reference [33] showed that for a collection of vectors that have a fourfold symmetry, such as  $\mathcal{R}_{\text{sq}}^{(1)}$ , only rank 2 moment tensors are identically isotropic, which explains the anisotropic nature of the 2D square PFC model. However, the model exhibits isotropic elasticity ( $\gamma = 0$ ) in the case of  $B_{\text{sq}} = A_{\text{sq}}/2$ , which can be solved with the equilibrium conditions on the amplitudes to give

$$r = -\frac{25}{3} \bar{\psi}^2, \quad (53)$$



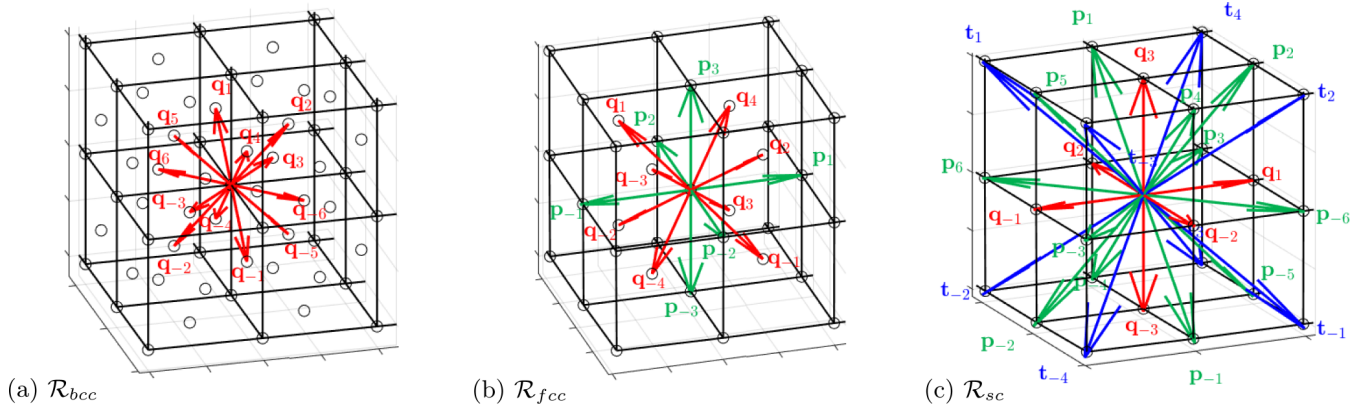


FIG. 5. Reciprocal lattices of the 3D crystal structures. (a) Modes  $\mathcal{R}_{\text{bcc}}$  of the bcc reciprocal lattice:  $\mathcal{R}_{\text{bcc}}^{(1)} = \{\mathbf{q}_n\}$  are the closest reciprocal lattice modes ( $\mathbf{q}_n^2 = 1$ ). (b) Modes  $\mathcal{R}_{\text{fcc}}$  of the fcc reciprocal lattice:  $\mathcal{R}_{\text{fcc}}^{(1)} = \{\mathbf{q}_n\}$  are the closest reciprocal lattice modes ( $\mathbf{q}_n^2 = 1$ ) and  $\mathcal{R}_{\text{fcc}}^{(4/3)} = \{\mathbf{p}_n\}$  are the next-to-closest modes ( $\mathbf{p}_n^2 = 4/3$ ). (c) Modes  $\mathcal{R}_{\text{sc}}$  of the sc reciprocal lattice:  $\mathcal{R}_{\text{sc}}^{(1)} = \{\mathbf{q}_n\}$  are the closest reciprocal lattice modes ( $\mathbf{q}_n^2 = 1$ ),  $\mathcal{R}_{\text{sc}}^{(2)} = \{\mathbf{p}_n\}$  are the next-to-closest modes ( $\mathbf{p}_n^2 = 2$ ), and  $\mathcal{R}_{\text{sc}}^{(3)} = \{\mathbf{t}_n\}$  are the third closest modes ( $\mathbf{t}_n^2 = 3$ ).

which falls within the region of a stable square lattice phase, indicating that a stable configuration for the isotropic square crystal does exist [50].

We prepare a  $60 \times 60$  2D square PFC lattice in the two-mode approximation on periodic boundaries with lattice vectors reciprocal to  $\mathcal{R}_{\text{sq}}^{(1)}$ , which gives a lattice constant of  $2\pi$ . We choose grid spacings  $\Delta x = \Delta y = a_0/7$  and parameters  $r = -0.3$  with  $\bar{\psi} = -0.25$ . The PFC is deformed according to the displacement fields of Eqs. (38) and (39), for which the elastic energy density again scales with the square of the strain as in Eqs. (41) and (42) and is shown in Fig. 2.

### C. 3D bcc lattice

In three dimensions, for a suitable range of parameters, the equilibrium configuration of the original PFC model with the free energy given in Eq. (27) is that of a bcc lattice [48]. The associated free energy is  $F = \int d^3r \tilde{f}^{(\text{bcc})}$  with

$$\tilde{f}^{(\text{bcc})} = \frac{1}{2}(\mathcal{L}_1\psi)^2 + \frac{r}{2}\psi^2 + \frac{1}{4}\psi^4. \quad (54)$$

The nonzero free energy derivatives are the same as for the 2D hexagonal lattice, so

$$h_{ij}^{(3\text{D bcc})} = -2\langle(\mathcal{L}_1\psi)\partial_{ij}\psi\rangle. \quad (55)$$

The elastic constants are calculated by expanding the ground state in the one-mode expansion

$$\psi^{\text{eq}} = \bar{\psi} + A_{\text{bcc}} \sum_{\mathbf{q}_n \in \mathcal{R}_{\text{bcc}}^{(1)}} e^{i\mathbf{q}_n \cdot \mathbf{r}}, \quad (56)$$

where  $A_{\text{bcc}}$  is the equilibrium amplitude of the closest modes on the reciprocal lattice for the bcc lattice. The latter can be chosen as  $\mathcal{R}_{\text{bcc}}^{(1)} = \{\mathbf{q}_{-6}, \dots, \mathbf{q}_{-1}, \mathbf{q}_1, \dots, \mathbf{q}_6\}$ , where

$$\begin{aligned} \mathbf{q}_1 &= (0, 1, 1)/\sqrt{2}, & \mathbf{q}_4 &= (0, -1, 1)/\sqrt{2}, \\ \mathbf{q}_2 &= (1, 0, 1)/\sqrt{2}, & \mathbf{q}_5 &= (-1, 0, 1)/\sqrt{2}, \\ \mathbf{q}_3 &= (1, 1, 0)/\sqrt{2}, & \mathbf{q}_6 &= (-1, 1, 0)/\sqrt{2}, \end{aligned} \quad (57)$$

and  $\mathbf{q}_{-n} = -\mathbf{q}_n$  [see Fig. 5(a)].  $A_{\text{bcc}}$  is found by minimization of the free energy. By straining the equilibrium state in the

one-mode approximation, we find (Appendix B 3)

$$h_{ij}^{(3\text{D bcc})} = 4A_{\text{bcc}}^2 \partial_k u_l \sum_{\mathbf{q}_n \in \mathcal{R}_{\text{bcc}}^{(1)}} q_{ni} q_{nj} q_{nk} q_{nl}. \quad (58)$$

Now, using the tetradic product sum of  $\mathcal{R}_{\text{bcc}}^{(1)}$ ,

$$\sum_{\mathbf{q}_n \in \mathcal{R}_{\text{bcc}}^{(1)}} q_{ni} q_{nj} q_{nk} q_{nl} = (\delta_{ij} \delta_{kl} + 2\delta_{k(i} \delta_{j)l} - \delta_{ijkl}), \quad (59)$$

we find the elastic constants  $\lambda = \mu = 4A_{\text{bcc}}^2$  and  $\gamma = -4A_{\text{bcc}}^2$ , as found for the fcc PFC in Ref. [38]. Since  $\gamma \neq 0$ , this PFC model will not exhibit isotropic elasticity.

We prepare a  $60 \times 60 \times 5$  bcc PFC lattice in the one-mode approximation on periodic boundaries with lattice vectors reciprocal to  $\mathcal{R}_{\text{bcc}}^{(1)}$ , which gives a lattice constant of  $2\pi\sqrt{2}$ . We choose a grid spacing of  $\Delta x = \Delta y = \Delta z = a_0/7$  and parameters  $r = -0.3$  with  $\bar{\psi} = -0.325$ . The PFC is deformed according to the displacement fields of Eqs. (38) and (39), extended to three dimensions with  $u_z^{(B)} = u_z^{(S)} = 0$ , for which the elastic energy density scales with the square of the strain as in Eqs. (41) and (42). The results are shown in Fig. 2.

### D. 3D fcc lattice

The introduction of  $\mathcal{L}_2$  in the free energy functional for the 2D square PFC was motivated by contributions from the next-to-closest reciprocal modes. Similarly, the inclusion of a differential operator that favors density waves at reciprocal modes of length  $\sqrt{4/3}$  might produce a stable fcc lattice. This motivates the following form of the PFC fcc model:  $F = \int d^3r \tilde{f}^{(\text{fcc})}$  with

$$\tilde{f}^{(\text{fcc})} = \frac{1}{2}(\mathcal{L}_1 \mathcal{L}_{\frac{4}{3}} \psi)^2 + \frac{r}{2}\psi^2 + \frac{1}{4}\psi^4, \quad (60)$$

which has been shown to produce a stable fcc phase [38]. The nonzero derivatives of the free energy density are

$$\begin{aligned} \tilde{f}'_{m_1 m_2} &= \frac{7}{3} \mathcal{L}_1 \mathcal{L}_{\frac{4}{3}} \psi \delta_{m_1 m_2}, \\ \tilde{f}'_{m_1 m_2 m_3 m_4} &= \mathcal{L}_1 \mathcal{L}_{\frac{4}{3}} \psi \delta_{(m_1 m_2} \delta_{m_3 m_4)}, \end{aligned} \quad (61)$$

SO

$$h_{ij}^{(3D\text{ fcc})} = \langle M_{ij}^{(2)} \rangle + \langle M_{ij}^{(4)} \rangle \\ = -2\langle (\mathcal{L}_1 \mathcal{L}_{\frac{4}{3}} \psi) (\mathcal{L}_1 + \mathcal{L}_{\frac{4}{3}}) \partial_{ij} \psi \rangle. \quad (62)$$

The elastic constants are calculated by expanding the ground state in the two-mode expansion

$$\psi^{\text{eq}} = \bar{\psi} + A_{\text{fcc}} \sum_{\mathbf{q}_n \in \mathcal{R}_{\text{fcc}}^{(1)}} e^{i\mathbf{q}_n \cdot \mathbf{r}} + B_{\text{fcc}} \sum_{\mathbf{p}_n \in \mathcal{R}_{\text{fcc}}^{(4/3)}} e^{i\mathbf{p}_n \cdot \mathbf{r}}, \quad (63)$$

where  $A_{\text{fcc}}$  and  $B_{\text{fcc}}$  are the equilibrium amplitudes of the modes on the reciprocal lattice  $\mathcal{R}_{\text{fcc}}^{(1)} = \{\mathbf{q}_{-4}, \dots, \mathbf{q}_{-1}, \mathbf{q}_1, \dots, \mathbf{q}_4\}$  and  $\mathcal{R}_{\text{fcc}}^{(4/3)} = \{\mathbf{p}_{-3}, \dots, \mathbf{p}_{-1}, \mathbf{p}_1, \dots, \mathbf{p}_3\}$ , respectively, where

$$\begin{aligned} \mathbf{q}_1 &= (-1, 1, 1)/\sqrt{3}, & \mathbf{p}_1 &= (2, 0, 0)/\sqrt{3}, \\ \mathbf{q}_2 &= (1, -1, 1)/\sqrt{3}, & \mathbf{p}_2 &= (0, 2, 0)/\sqrt{3}, \\ \mathbf{q}_3 &= (1, 1, -1)/\sqrt{3}, & \mathbf{p}_3 &= (0, 0, 2)/\sqrt{3}, \\ \mathbf{q}_4 &= (1, 1, 1)/\sqrt{3}, \end{aligned} \quad (64)$$

with  $\mathbf{q}_{-n} = -\mathbf{q}_n$  and  $\mathbf{p}_{-n} = -\mathbf{p}_n$  [see Fig. 5(b)].  $A_{\text{fcc}}$  and  $B_{\text{fcc}}$  are found by minimization of the free energy. By deforming the two-mode approximation by a displacement field  $\mathbf{u}$ , we find (Appendix B 4)

$$h_{ij}^{(3D\text{ fcc})} = \frac{4}{9} A_{\text{fcc}}^2 \partial_k u_i \sum_{\mathbf{q}_n \in \mathcal{R}_{\text{fcc}}^{(1)}} q_{nk} q_{nl} q_{ni} q_{nj} \\ + \frac{4}{9} B_{\text{fcc}}^2 \partial_k u_i \sum_{\mathbf{p}_n \in \mathcal{R}_{\text{fcc}}^{(4/3)}} p_{nk} p_{nl} p_{ni} p_{nj}. \quad (65)$$

The tetradic product sums are given by

$$\sum_{\mathbf{q}_n \in \mathcal{R}_{\text{fcc}}^{(1)}} q_{ni} q_{nj} q_{nk} q_{nl} = \frac{8}{9} (\delta_{ij} \delta_{kl} + 2\delta_{k(i} \delta_{j)l} - 2\delta_{ijkl}), \quad (66)$$

$$\sum_{\mathbf{p}_n \in \mathcal{R}_{\text{fcc}}^{(4/3)}} p_{ni} p_{nj} p_{nk} p_{nl} = \frac{32}{9} \delta_{ijkl}, \quad (67)$$

which gives elastic constants  $\lambda = \mu = \frac{32}{81} A_{\text{fcc}}^2$  and  $\gamma = \frac{64}{81} (2B_{\text{fcc}}^2 - A_{\text{fcc}}^2)$ , as found for the fcc PFC in Ref. [38]. The expression for  $\gamma$  shows that the fcc lattice exhibits isotropic elasticity ( $\gamma = 0$ ) if  $B_{\text{fcc}} = A_{\text{fcc}}/\sqrt{2}$ , which solved with the equilibrium condition on the amplitudes gives

$$r = -\frac{255\bar{\psi}^2}{49}, \quad (68)$$

which falls within the region of a stable fcc phase, indicating that a stable configuration of isotropic elasticity for the fcc lattice does exist [38].

We prepare a  $60 \times 60 \times 5$  fcc PFC lattice in the two-mode approximation on periodic boundaries with lattice vectors reciprocal to  $\mathcal{R}_{\text{fcc}}^{(1)}$ , which gives a lattice constant of  $2\pi\sqrt{3}$ . We choose a grid spacing of  $\Delta x = \Delta y = \Delta z = a_0/11$  and parameters  $r = -0.3$  with  $\bar{\psi} = -0.3$ . We perform the same distortion of the fcc PFC by the bulk and shear displacement fields, for which the elastic energy density scales with the square of the strain as in Eqs. (41) and (42). The results are shown in Fig. 2.

### E. 3D sc lattice

Extending the idea of favoring modes of the reciprocal lattice to achieve other symmetries, a natural generalization of the free energy in Eq. (60) can be chosen as follows. The three sets of modes that are closest to the origin on the sc reciprocal lattice are given by  $\mathcal{R}_{\text{sc}}^{(1)} = \{\mathbf{q}_{-3}, \dots, \mathbf{q}_{-1}, \mathbf{q}_1, \dots, \mathbf{q}_3\}$ ,  $\mathcal{R}_{\text{sc}}^{(2)} = \{\mathbf{p}_{-6}, \dots, \mathbf{p}_{-1}, \mathbf{p}_1, \dots, \mathbf{p}_6\}$  and  $\mathcal{R}_{\text{sc}}^{(3)} = \{\mathbf{t}_{-4}, \dots, \mathbf{t}_{-1}, \mathbf{t}_1, \dots, \mathbf{t}_4\}$ , where

$$\begin{aligned} \mathbf{q}_1 &= (1, 0, 0), & \mathbf{p}_1 &= (0, 1, 1), & \mathbf{t}_1 &= (-1, 1, 1), \\ \mathbf{q}_2 &= (0, 1, 0), & \mathbf{p}_2 &= (1, 0, 1), & \mathbf{t}_2 &= (1, -1, 1), \\ \mathbf{q}_3 &= (0, 0, 1), & \mathbf{p}_3 &= (1, 1, 0), & \mathbf{t}_3 &= (1, 1, -1), \\ & & \mathbf{p}_4 &= (0, -1, 1), & \mathbf{t}_4 &= (1, 1, 1), \\ & & \mathbf{p}_5 &= (-1, 0, 1), & & \\ & & \mathbf{p}_6 &= (-1, 1, 0), \end{aligned} \quad (69)$$

with  $\mathbf{q}_{-n} = -\mathbf{q}_n$ ,  $\mathbf{p}_{-n} = -\mathbf{p}_n$ , and  $\mathbf{t}_{-n} = -\mathbf{t}_n$  [see Fig. 5(c)]. Thus, a way to explicitly favor the simple cubic structure is to introduce the free energy  $F = \int d^3r \tilde{f}^{(\text{sc})}$  where

$$\tilde{f}^{(\text{sc})} = \frac{1}{2} (\mathcal{L}_1 \mathcal{L}_2 \mathcal{L}_3 \psi)^2 + \frac{r}{2} \psi^2 + \frac{1}{4} \psi^4, \quad (70)$$

which corresponds to a special case of the multimode PFC expansion of Ref. [40]. In order to ensure a stable sc phase, one needs to consider the competing symmetries, calculate the average free energy density for each symmetry, and find coexistence regions by Maxwell construction. We leave this task for future work, since the interest of the current paper is to find a point in configuration space  $(r, \bar{\psi})$  for which the sc phase is stable. This can be done by searching for parameters  $(r, \bar{\psi})$  for which a random initial condition condenses into the simple cubic phase. We have found  $(r, \bar{\psi}) = (-0.3, -0.325)$  to be such a point. Expanding the ground state in the three-mode expansion,

$$\psi^{\text{eq}} = \bar{\psi} + A_{\text{sc}} \sum_{\mathbf{q}_n \in \mathcal{R}_{\text{sc}}^{(1)}} e^{i\mathbf{q}_n \cdot \mathbf{r}} + B_{\text{sc}} \sum_{\mathbf{p}_n \in \mathcal{R}_{\text{sc}}^{(2)}} e^{i\mathbf{p}_n \cdot \mathbf{r}} \\ + C_{\text{sc}} \sum_{\mathbf{t}_n \in \mathcal{R}_{\text{sc}}^{(3)}} e^{i\mathbf{t}_n \cdot \mathbf{r}}, \quad (71)$$

inserting into the free energy Eq. (70), and averaging over a unit cell of size  $(2\pi)^3$  gives

$$\begin{aligned} \langle \tilde{f}^{(\text{sc})} \rangle &= \frac{1}{2} (6\bar{\psi})^2 + \frac{r}{2} \bar{\psi}^2 + \frac{1}{4} \bar{\psi}^4 \\ &+ \frac{45}{2} A_{\text{sc}}^4 + 288 A_{\text{sc}}^2 B_{\text{sc}}^2 + 135 B_{\text{sc}}^4 + 48 A_{\text{sc}}^3 C_{\text{sc}} \\ &+ 432 A_{\text{sc}} B_{\text{sc}}^2 C_{\text{sc}} + 108 A_{\text{sc}}^2 C_{\text{sc}}^2 + 324 B_{\text{sc}}^2 C_{\text{sc}}^2 \\ &+ 54 C_{\text{sc}}^4 + 72 A_{\text{sc}}^2 B_{\text{sc}} C_{\text{sc}} \bar{\psi} + 48 B_{\text{sc}}^3 \bar{\psi} \\ &+ 144 A_{\text{sc}} B_{\text{sc}} C_{\text{sc}} \bar{\psi} + 9 A_{\text{sc}}^2 \bar{\psi}^2 + 18 B_{\text{sc}}^2 \bar{\psi}^2 \\ &+ 12 C_{\text{sc}}^2 \bar{\psi}^2 + 3 A_{\text{sc}}^2 r + 6 B_{\text{sc}}^2 r + 4 C_{\text{sc}}^2 r, \end{aligned} \quad (72)$$

where the equilibrium values of  $A_{\text{sc}}$ ,  $B_{\text{sc}}$ ,  $C_{\text{sc}}$  are determined by minimization of the free energy. From Eq. (70), we get

$$\begin{aligned} \tilde{f}'_{m_1 m_2} &= 11 \mathcal{L}_1 \mathcal{L}_2 \mathcal{L}_3 \psi \delta_{m_1 m_2}, \\ \tilde{f}'_{m_1 m_2 m_3 m_4} &= 6 \mathcal{L}_1 \mathcal{L}_2 \mathcal{L}_3 \psi \delta_{(m_1 m_2) \delta_{m_3 m_4}}, \\ \tilde{f}'_{m_1 m_2 m_3 m_4 m_5 m_6} &= \mathcal{L}_1 \mathcal{L}_2 \mathcal{L}_3 \psi \delta_{(m_1 m_2) \delta_{m_3 m_4} \delta_{m_5 m_6}}, \end{aligned} \quad (73)$$

which gives

$$\begin{aligned} h_{ij}^{(3D\ sc)} &= \langle M_{ij}^{(2)} \rangle + \langle M_{ij}^{(4)} \rangle + \langle M_{ij}^{(6)} \rangle \\ &= -2\langle (\mathcal{L}_1 \mathcal{L}_2 \mathcal{L}_3 \psi) (\mathcal{L}_2 \mathcal{L}_3 + \mathcal{L}_1 \mathcal{L}_3 + \mathcal{L}_1 \mathcal{L}_2) \delta_{ij} \psi \rangle. \end{aligned} \quad (74)$$

By deforming the three-mode expansion by a displacement field  $\mathbf{u}$ , we find (Appendix B 5)

$$\begin{aligned} h_{ij}^{(3D\ sc)} &= 16A_{sc}^2 \partial_k u_l \sum_{\mathbf{q}_n \in \mathcal{R}_{sc}^{(1)}} q_{ni} q_{nj} q_{nk} q_{nl} \\ &\quad + 4B_{sc}^2 \partial_k u_l \sum_{\mathbf{p}_n \in \mathcal{R}_{sc}^{(2)}} p_{ni} p_{nj} p_{nk} p_{nl} \\ &\quad + 16C_{sc} \partial_k u_l \sum_{\mathbf{t}_n \in \mathcal{R}_{sc}^{(3)}} t_{ni} t_{nj} t_{nk} t_{nl}, \end{aligned} \quad (75)$$

which after using the tetradic product sums

$$\sum_{\mathbf{q}_n \in \mathcal{R}_{sc}^{(1)}} q_{ni} q_{nj} q_{nk} q_{nl} = 2\delta_{ijkl}, \quad (76)$$

$$\sum_{\mathbf{p}_n \in \mathcal{R}_{sc}^{(2)}} p_{ni} p_{nj} p_{nk} p_{nl} = 4(\delta_{ij} \delta_{kl} + 2\delta_{k(i} \delta_{j)l} - \delta_{ijkl}), \quad (77)$$

$$\sum_{\mathbf{t}_n \in \mathcal{R}_{sc}^{(3)}} t_{ni} t_{nj} t_{nk} t_{nl} = 8(\delta_{ij} \delta_{kl} + 2\delta_{k(i} \delta_{j)l} - 2\delta_{ijkl}) \quad (78)$$

gives elastic constants  $\lambda = \mu = 16B_{sc} + 128C_{sc}^2$  and  $\gamma = 32_{sc}A^2 - 16B_{sc}^2 - 256C_{sc}^2$ . The sc PFC would exhibit isotropic elasticity for  $\gamma = 0$ . An exact expression for the domain of isotropic elasticity could in principle be obtained, as for the previous symmetries, by solving the equilibrium condition on the amplitudes with the additional constraint of  $\gamma = 0$ . This is a set of four quartic equations with five unknowns ( $r, \psi, A_{sc}, B_{sc}, C_{sc}$ ) which must be solved simultaneously in order to express the regime of isotropic elasticity. Using computational software [52] suggests that no closed-form solution exists as in the case of the lattices in which only two amplitudes were needed. However, by numerically solving the equations, we have found the following relation for an isotropic domain:

$$r \approx -2.10144\bar{\psi}^2. \quad (79)$$

A PFC model of simple cubic ordering was also considered in Ref. [53] by inclusion of exponential peaks in the correlation function derived from the free energy and in Ref. [54] by adding higher order gradients in the free energy to account for an orientation dependent interaction. However, to our knowledge, the elastic constants for the particular free energy density of Eq. (70) have not previously been derived. The PFC model employed in Ref. [54] has the free energy given in terms of the density field and its derivatives.

We prepare a  $60 \times 60 \times 5$  sc PFC lattice in the three-mode approximation on periodic boundaries with lattice vectors

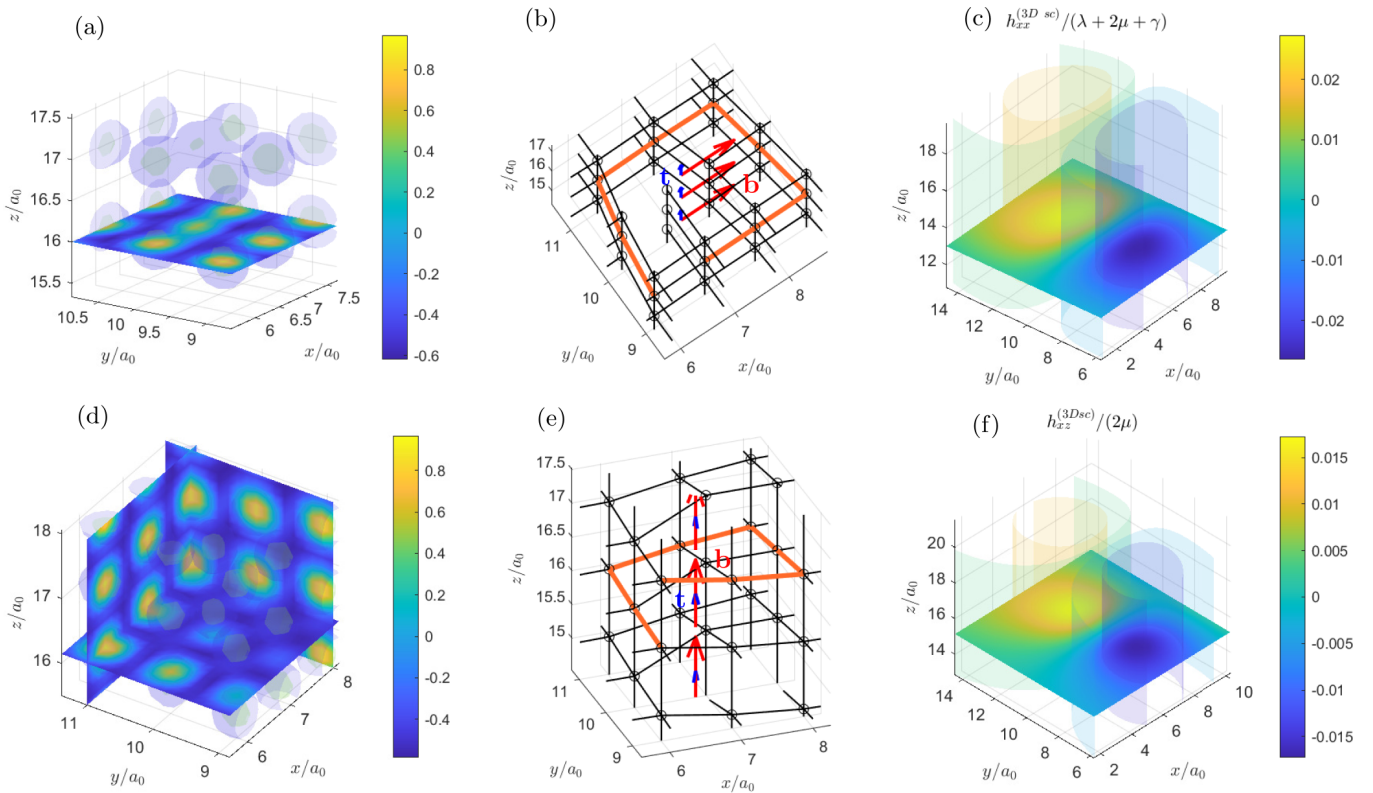


FIG. 6. (a), (d) PFC density field  $\psi$  for (a) an edge dislocation with Burgers vector  $\mathbf{b} = a_0(1, 0, 0)$  and tangent vector  $\mathbf{t} = (0, 0, 1)$  and (d) a screw dislocation with Burgers vector  $\mathbf{b} = a_0(0, 0, 1)$  and tangent vector  $\mathbf{t} = (0, 0, 1)$ . The  $\psi$  field is shown as transparent isosurfaces of the density  $\psi$  with extra inserted 2D density plots for selected planes. (b) and (e) show the peaks of (a) and (d), respectively, connected by lines for illustration. The orange line shows the Burgers circuit with the corresponding closure failure. (c) and (f) show the largest components of the stress fields for each dislocation.

reciprocal to  $R_{sc}^{(1)}$ , which gives a lattice constant of  $2\pi$ . We choose a grid spacing of  $\Delta x = \Delta y = \Delta z = a_0/7$  and parameters  $r = -0.3$  with  $\bar{\psi} = -0.325$ . We perform the same distortion of the sc PFC by the bulk and shear displacement fields, for which the elastic energy density scales with the square of the strain as in Eqs. (41) and (42). The results are shown in Fig. 2.

To exemplify that the formalism extends to defected lattices, we include in Fig. 6 a 3D sc PFC structure in the presence of an edge (screw) dislocation in panel (a) [panel (c)], and its associated stress field in panel (c) [panel (f)]. The PFC configuration was prepared by multiplying the complex amplitudes of the PFC by dislocation charges followed by a brief period of relaxation, as explained in Ref. [25]. Even though dislocations are singular objects (they are phase singularities for the complex amplitudes), the density field  $\psi$  and its corresponding macroscopic stress field remain well defined and smooth, without any core regularization method. It is interesting that the largest value of the stresses  $\approx 0.02$  (in dimensionless units) at the dislocation cores is still nominally on the linear stress-strain curves (see Fig. 2), even though the physics at the core is fundamentally different. This suggests that nonlinear elastic effects may not be necessary to capture the near-core deformations, at least in the PFC models, and that the deviations from linear elasticity are due directly to the lattice incompatibility. However, at present, the stress profiles obtained around dislocations are not constrained to mechanical equilibrium, i.e.,  $\partial_i h_{ij} \neq 0$ , and thus they are not readily comparable with analytical stress profiles from continuum mechanics. The problem of extending the method proposed in Ref. [22] to anisotropic 2D and 3D PFC lattices to constrain the diffusive dynamics of the PFC models to mechanical equilibrium is an open area of research.

## V. CONCLUSION

To summarize, we have presented a versatile method of computing the macroscopic stress tensor for ordered systems starting from a microscopic field description, where there is an intrinsic length scale (hence a finite intrinsic representative volume element) related to lattice periodicity. Within a generic field theory of Ginzburg-Landau type, where the system is described by a free energy that depends on a one-body density field (or order parameter) and an arbitrary number of its gradients, we have derived a general formula for the stress tensor given by Eq. (9). Upon coarse graining to continuum scales, we obtain the macroscopic stress tensor in the linear regime which describes the state of deformation of the ordered phase as a continuum elastic medium.

By adopting the PFC formalism to describe crystals, we have derived the stress tensor for different lattice symmetries in two and three dimensions. In particular, we focused on the

hexagonal and square lattices in two dimensions and bcc, fcc, and sc lattices in three dimensions. For simplicity, we only looked at the equilibrium defect-free crystal configurations to derive the elastic constants at constant macroscopic density. We show how the crystal symmetries constrain the tetradic product sums which determine the number of elastic constants and their values. For instance, the isotropic elasticity of the 2D hexagonal PFC model is due to the sixfold symmetry of its reciprocal lattice. For the other PFC models, we have found regions in parameter space where the elastic behavior is expected to be isotropic, except for the bcc PFC model, which is always anisotropic. Using numerical simulations, we verified the predicted linear elastic response of all models and found that the 3D fcc lattice model quickly enters a nonlinear elastic regime upon compression/extension.

The formalism developed in this paper can be extended to nonequilibrium fields, with the particular example of a hexagonal lattice in two dimensions already discussed in Ref. [22]. In this case, one is concerned with the evolution of defected ordered systems the defects of which move on timescales much longer than the fast relaxation to elastic equilibrium. Our stress tensor formula can be readily applied also in the presence of defects, and can in fact be used to indicate the nucleation and position of defects as discussed in Ref. [24]. While the analysis of ordered systems is limited to linear elasticity, we have shown that due to the emergent regularization of the dislocation core in the PFC model nonlinear strain effects may not be necessary to capture the near-core deformations. The method also is applicable to other Ginzburg-Landau theories with an emergent length scale such as mean-field descriptions of liquid crystals and active matter.

## ACKNOWLEDGMENTS

We thank Jorge Viñals for many stimulating discussions and his valuable comments at various stages during this work. We also thank Marco Salvalaglio for his valuable input on the paper.

## APPENDIX A: PROOF OF THE FORCE BALANCE EQUATION

The microscopic stress tensor is given by

$$\tilde{\sigma}_{ij} = (\tilde{f} - \tilde{\mu}_c \tilde{\rho}) \delta_{ij} + \tilde{h}_{ij}, \quad (\text{A1})$$

where

$$\tilde{\mu}_c = \frac{\delta F}{\delta \tilde{\rho}} = \sum_{\alpha=0}^{\infty} (-1)^\alpha \partial_{m_1 \dots m_\alpha} \tilde{f}'_{m_1 \dots m_\alpha}. \quad (\text{A2})$$

To show that  $\partial_i \tilde{\sigma}_{ij} = -\tilde{\rho} \partial_j \tilde{\mu}_c$ , we need to show that  $\partial_i \tilde{h}_{ij} = \tilde{\mu}_c \partial_j \tilde{\rho} - \partial_j \tilde{f}$ :

$$\begin{aligned} \partial_i \tilde{h}_{ij} &= \partial_i \left( \sum_{\alpha=1}^{\infty} \sum_{\beta=1}^{\alpha} (-1)^\beta (\partial_{m_1 \dots m_{\beta-1}} \tilde{f}'_{m_1 \dots m_{\alpha-1} i}) \partial_{j m_\beta \dots m_{\alpha-1}} \tilde{\rho} \right) \\ &= \sum_{\alpha=1}^{\infty} \sum_{\beta=1}^{\alpha} (-1)^\beta (\partial_{i m_1 \dots m_{\beta-1}} \tilde{f}'_{m_1 \dots m_{\alpha-1} i}) \partial_{j m_\beta \dots m_{\alpha-1}} \tilde{\rho} + \sum_{\alpha=1}^{\infty} \sum_{\beta=1}^{\alpha} (-1)^\beta (\partial_{m_1 \dots m_{\beta-1}} \tilde{f}'_{m_1 \dots m_{\alpha-1} i}) \partial_{i j m_\beta \dots m_{\alpha-1}} \tilde{\rho} \end{aligned}$$



$$\begin{aligned}
&= \sum_{\alpha=1}^{\infty} (-1)^{\alpha} (\partial_{m_1 \dots m_{\alpha-1} i} \tilde{f}'_{m_1 \dots m_{\alpha-1} i}) \partial_j \tilde{\rho} + \underbrace{\sum_{\alpha=1}^{\infty} \sum_{\beta=1}^{\alpha-1} (-1)^{\beta} (\partial_{m_1 \dots m_{\beta-1} i} \tilde{f}'_{m_1 \dots m_{\alpha-1} i}) \partial_{j m_{\beta} \dots m_{\alpha-1}} \tilde{\rho}}_{(1)} \\
&\quad - \sum_{\alpha=1}^{\infty} \tilde{f}'_{m_1 \dots m_{\alpha-1} i} \partial_{m_1 \dots m_{\alpha-1} i j} \tilde{\rho} + \underbrace{\sum_{\alpha=1}^{\infty} \sum_{\beta=2}^{\alpha} (-1)^{\beta} (\partial_{m_1 \dots m_{\beta-1}} \tilde{f}'_{m_1 \dots m_{\alpha-1} i}) \partial_{j i m_{\beta} \dots m_{\alpha-1}} \tilde{\rho}}_{(2)}. \tag{A3}
\end{aligned}$$

In the last equality, the second term on the first line (1) cancels the second term on the second line (2) as is seen by starting with (1), switching dummy indices  $m_{\beta} \leftrightarrow i$ , using that  $\tilde{f}'_{m_1 \dots m_{\alpha}}$  is symmetric under the interchange of indices, and adjusting summation limits as follows:

$$\begin{aligned}
&\sum_{\alpha=1}^{\infty} \sum_{\beta=1}^{\alpha-1} (-1)^{\beta} (\partial_{m_1 \dots m_{\beta-1} i} \tilde{f}'_{m_1 \dots m_{\alpha-1} i}) \partial_{j m_{\beta} \dots m_{\alpha-1}} \tilde{\rho} \\
&= \sum_{\alpha=1}^{\infty} \sum_{\beta=1}^{\alpha-1} (-1)^{\beta} (\partial_{m_1 \dots m_{\beta-1} m_{\beta}} \tilde{f}'_{m_1 \dots m_{\beta-1} i m_{\beta+1} \dots m_{\alpha-1} m_{\beta}}) \partial_{j i m_{\beta+1} \dots m_{\alpha-1}} \tilde{\rho} = - \sum_{\alpha=1}^{\infty} \sum_{\beta=2}^{\alpha} (-1)^{\beta} (\partial_{m_1 \dots m_{\beta-1}} \tilde{f}'_{m_1 \dots m_{\alpha-1} i}) \partial_{j i m_{\beta} \dots m_{\alpha-1}} \tilde{\rho}. \tag{A4}
\end{aligned}$$

Thus, adding and subtracting  $\tilde{f}' \partial_j \tilde{\rho}$  from Eq. (A3), and renaming the dummy index  $i \rightarrow m_{\alpha}$ , we get

$$\begin{aligned}
\partial_i \tilde{h}_{ij} &= \tilde{f}' \partial_j \tilde{\rho} + \sum_{\alpha=1}^{\infty} (-1)^{\alpha} (\partial_{m_1 \dots m_{\alpha}} \tilde{f}'_{m_1 \dots m_{\alpha}}) \partial_j \tilde{\rho} - \tilde{f}' \partial_j \tilde{\rho} - \sum_{\alpha=1}^{\infty} \tilde{f}'_{m_1 \dots m_{\alpha}} \partial_{m_1 \dots m_{\alpha} j} \tilde{\rho} \\
&= \sum_{\alpha=0}^{\infty} (-1)^{\alpha} (\partial_{m_1 \dots m_{\alpha}} \tilde{f}'_{m_1 \dots m_{\alpha}}) \partial_j \tilde{\rho} - \left( \tilde{f}' \partial_j \tilde{\rho} + \sum_{\alpha=1}^{\infty} \tilde{f}'_{m_1 \dots m_{\alpha}} \partial_{m_1 \dots m_{\alpha} j} \tilde{\rho} \right) = \tilde{\mu}_c \partial_j \tilde{\rho} - \partial_j \tilde{f}, \tag{A5}
\end{aligned}$$

where we have used that by the chain rule we have

$$\partial_j \tilde{f} = \tilde{f}' \partial_j \tilde{\rho} + \tilde{f}'_{m_1} \partial_{m_1 j} \tilde{\rho} + \dots = \tilde{f}' \partial_j \tilde{\rho} + \sum_{\alpha=1}^{\infty} \tilde{f}'_{m_1 \dots m_{\alpha}} \partial_{m_1 \dots m_{\alpha} j} \tilde{\rho}. \tag{A6}$$

### The combinatorial factor

When defining  $\tilde{f}'_{m_1, \dots, m_{\alpha}}$ , the combinatorial factor  $N(\{m_1, \dots, m_{\alpha}\})$  appears due to arbitrary gradients of  $\tilde{\rho}$  not being independent, for example,  $\partial_{xy} \tilde{\rho} = \partial_{yx} \tilde{\rho}$ . Therefore, in the Taylor expansion to first order, we should include only one of each term. To illustrate, assume that the free energy  $F[\tilde{\rho}, \{\partial_i \tilde{\rho}\}, \{\partial_{ij} \tilde{\rho}\}]$  is given in terms of  $\tilde{\rho}$ , which is a field in two dimensions, and up to its second order gradients. In this case, the variation of  $F$  is given by

$$\begin{aligned}
\delta F &= \int d^2 r \left( \frac{\partial f}{\partial \tilde{\rho}} \delta \tilde{\rho} + \frac{\partial f}{\partial (\partial_x \tilde{\rho})} \delta (\partial_x \tilde{\rho}) + \frac{\partial f}{\partial (\partial_y \tilde{\rho})} \delta (\partial_y \tilde{\rho}) + \frac{\partial f}{\partial (\partial_{xx} \tilde{\rho})} \delta (\partial_{xx} \tilde{\rho}) + \frac{\partial f}{\partial (\partial_{yy} \tilde{\rho})} \delta (\partial_{yy} \tilde{\rho}) + \frac{\partial f}{\partial (\partial_{xy} \tilde{\rho})} \delta (\partial_{xy} \tilde{\rho}) \right) \\
&= \int d^2 r \left( \frac{\partial f}{\partial \tilde{\rho}} \delta \tilde{\rho} + \frac{\partial f}{\partial (\partial_x \tilde{\rho})} \delta (\partial_x \tilde{\rho}) + \frac{\partial f}{\partial (\partial_y \tilde{\rho})} \delta (\partial_y \tilde{\rho}) + \frac{\partial f}{\partial (\partial_{xx} \tilde{\rho})} \delta (\partial_{xx} \tilde{\rho}) + \frac{\partial f}{\partial (\partial_{yy} \tilde{\rho})} \delta (\partial_{yy} \tilde{\rho}) \right. \\
&\quad \left. + \frac{1}{2} \frac{\partial f}{\partial (\partial_{xy} \tilde{\rho})} \delta (\partial_{xy} \tilde{\rho}) + \frac{1}{2} \frac{\partial f}{\partial (\partial_{yx} \tilde{\rho})} \delta (\partial_{yx} \tilde{\rho}) \right) \\
&= \int d^2 r [\tilde{f}' \delta \tilde{\rho} + \tilde{f}'_{m_1} (\delta \partial_{m_1} \tilde{\rho}) + \tilde{f}'_{m_1 m_2} \delta (\partial_{m_1 m_2} \tilde{\rho})], \tag{A7}
\end{aligned}$$

where the combinatorial factor of  $N(\{x, y\}) = 1/2$  was needed to write the sum over all indices. This gives after integration by parts (ignoring boundary terms)

$$\mu_c = \frac{\delta F}{\delta \tilde{\rho}} = \tilde{f}' - \partial_{m_1} \tilde{f}'_{m_1} + \partial_{m_1 m_2} \tilde{f}'_{m_1 m_2}, \tag{A8}$$

which is Eq. (A2) in two dimensions with a free energy limited to second order gradients of  $\tilde{\rho}$ . The same combinatorial factor appears when writing  $\partial_j \tilde{f}$  in terms of  $\tilde{f}'_{m_1 \dots m_{\alpha}}$  as a sum over all indices.

## APPENDIX B: PFC MODE EXPANSIONS

### 1. 2D hexagonal PFC

We consider the 2D hexagonal PFC in the one-mode expansion for a macroscopic displacement field  $\mathbf{u}$  at constant macroscopic density:

$$\psi = \psi_{\text{eq}}^{\text{hex}}(\mathbf{r} - \mathbf{u}) \equiv \bar{\psi} + \mathcal{A}, \quad (\text{B1})$$

where

$$\mathcal{A} = A_{\text{hex}} \sum_{\mathbf{q}_n \in \mathcal{R}_{\text{hex}}^{(1)}} e^{i\mathbf{q}_n \cdot (\mathbf{r} - \mathbf{u})} \equiv A_{\text{hex}} \sum_{\mathbf{q}_n \in \mathcal{R}_{\text{hex}}^{(1)}} E_{\mathbf{q}_n}^{\mathbf{u}}(\mathbf{r}). \quad (\text{B2})$$

Since  $\mathbf{u}$  varies slowly on the macroscopic scale, the resonance condition dictates

$$\langle E_{\mathbf{q}_n}^{\mathbf{u}}(\mathbf{r}) \rangle = 0, \quad (\text{B3})$$

and

$$\langle E_{\mathbf{q}_n}^{\mathbf{u}}(\mathbf{r}) E_{\mathbf{q}_{n'}}^{\mathbf{u}}(\mathbf{r}) \rangle = \delta_{n, -n'}, \quad (\text{B4})$$

as we only get a nonzero average at resonance, when  $\mathbf{q}_{n'} = -\mathbf{q}_n$  (depending on the method of coarse graining, this may be an approximation, albeit a very good one [43]). Inserting the distorted PFC into the stress tensor, and using these identities, we get

$$\begin{aligned} h_{ij}^{(2\text{D hex})} &= -2\langle (\mathcal{L}_1 \psi) \partial_{ij} \psi \rangle \\ &= -2\langle (\mathcal{L}_1 \bar{\psi}) \partial_{ij} \bar{\psi} \rangle - 2\langle (\mathcal{L}_1 \mathcal{A}) \partial_{ij} \mathcal{A} \rangle \\ &= -2\langle (\mathcal{L}_1 \mathcal{A}) \partial_{ij} \mathcal{A} \rangle. \end{aligned} \quad (\text{B5})$$

First, we calculate, to first order in  $\partial_k u_l$ ,

$$\begin{aligned} \mathcal{L}_1 \mathcal{A} &= A_{\text{hex}} \sum_{\mathbf{q}_n \in \mathcal{R}_{\text{hex}}^{(1)}} (1 - (q_{nk} - q_{nl} \partial_k u_l)^2) E_{\mathbf{q}_n}^{\mathbf{u}}(\mathbf{r}) \\ &= 2A_{\text{hex}} \partial_k u_l \sum_{\mathbf{q}_n \in \mathcal{R}_{\text{hex}}^{(1)}} q_{nk} q_{nl} E_{\mathbf{q}_n}^{\mathbf{u}}(\mathbf{r}), \end{aligned} \quad (\text{B6})$$

from which we get

$$\begin{aligned} &\langle (\mathcal{L}_1 \mathcal{A}) \partial_{ij} \mathcal{A} \rangle \\ &= 2A_{\text{hex}}^2 \sum_{\mathbf{q}_n \in \mathcal{R}_{\text{hex}}^{(1)}} \sum_{\mathbf{q}_{n'} \in \mathcal{R}_{\text{hex}}^{(1)}} q_{nk} q_{nl} (-q_{n'i} q_{n'j}) \\ &\quad \times \langle E_{\mathbf{q}_n}^{\mathbf{u}}(\mathbf{r}) E_{\mathbf{q}_{n'}}^{\mathbf{u}}(\mathbf{r}) \rangle \\ &= -2A_{\text{hex}}^2 \sum_{\mathbf{q}_n \in \mathcal{R}_{\text{hex}}^{(1)}} q_{ni} q_{nj} q_{nk} q_{nl}, \end{aligned} \quad (\text{B7})$$

so

$$h_{ij}^{(2\text{D hex})} = 4A_{\text{hex}}^2 \sum_{\mathbf{q}_n \in \mathcal{R}_{\text{hex}}^{(1)}} q_{ni} q_{nj} q_{nk} q_{nl}. \quad (\text{B8})$$

### 2. 2D square PFC

We consider the 2D square PFC in the two-mode expansion for a macroscopic displacement field  $\mathbf{u}$  at constant macroscopic density:

$$\psi = \bar{\psi} + \mathcal{A} + \mathcal{B}, \quad (\text{B9})$$

where

$$\mathcal{A} = A_{\text{sq}} \sum_{\mathbf{q}_n \in \mathcal{R}_{\text{sq}}^{(1)}} e^{i\mathbf{q}_n \cdot (\mathbf{r} - \mathbf{u})} \equiv A_{\text{sq}} \sum_{\mathbf{q}_n \in \mathcal{R}_{\text{sq}}^{(1)}} E_{\mathbf{q}_n}^{\mathbf{u}}(\mathbf{r}), \quad (\text{B10})$$

$$\mathcal{B} = B_{\text{sq}} \sum_{\mathbf{p}_n \in \mathcal{R}_{\text{sq}}^{(2)}} e^{i\mathbf{p}_n \cdot (\mathbf{r} - \mathbf{u})} \equiv B_{\text{sq}} \sum_{\mathbf{p}_n \in \mathcal{R}_{\text{sq}}^{(2)}} E_{\mathbf{p}_n}^{\mathbf{u}}(\mathbf{r}). \quad (\text{B11})$$

By resonance conditions, we have

$$\langle E_{\mathbf{q}_n}^{\mathbf{u}}(\mathbf{r}) \rangle = \langle E_{\mathbf{p}_n}^{\mathbf{u}}(\mathbf{r}) \rangle = \langle E_{\mathbf{q}_n}^{\mathbf{u}}(\mathbf{r}) E_{\mathbf{p}_{n'}}^{\mathbf{u}}(\mathbf{r}) \rangle = 0, \quad (\text{B12})$$

and

$$\langle E_{\mathbf{q}_n}^{\mathbf{u}}(\mathbf{r}) E_{\mathbf{q}_{n'}}^{\mathbf{u}}(\mathbf{r}) \rangle = \langle E_{\mathbf{p}_n}^{\mathbf{u}}(\mathbf{r}) E_{\mathbf{p}_{n'}}^{\mathbf{u}}(\mathbf{r}) \rangle = \delta_{n', -n}, \quad (\text{B13})$$

from which we find

$$\begin{aligned} h_{ij}^{(2\text{D sq})} &= -2\langle (\mathcal{L}_1 \mathcal{L}_2 \psi) (\mathcal{L}_1 + \mathcal{L}_2) \partial_{ij} \psi \rangle \\ &= -2\langle (\mathcal{L}_1 \mathcal{L}_2 \bar{\psi}) (\mathcal{L}_1 + \mathcal{L}_2) \partial_{ij} \bar{\psi} \rangle \\ &\quad - 2\langle (\mathcal{L}_1 \mathcal{L}_2 \mathcal{A}) (\mathcal{L}_1 + \mathcal{L}_2) \partial_{ij} \mathcal{A} \rangle \\ &\quad - 2\langle (\mathcal{L}_1 \mathcal{L}_2 \mathcal{B}) (\mathcal{L}_1 + \mathcal{L}_2) \partial_{ij} \mathcal{B} \rangle \\ &= -2\langle (\mathcal{L}_1 \mathcal{L}_2 \mathcal{A}) (\mathcal{L}_1 + \mathcal{L}_2) \partial_{ij} \mathcal{A} \rangle \\ &\quad - 2\langle (\mathcal{L}_1 \mathcal{L}_2 \mathcal{B}) (\mathcal{L}_1 + \mathcal{L}_2) \partial_{ij} \mathcal{B} \rangle. \end{aligned} \quad (\text{B14})$$

To first order in  $\partial_k u_l$ , we have

$$\begin{aligned} \mathcal{L}_1 \mathcal{L}_2 \mathcal{A} &= \mathcal{L}_2 \mathcal{L}_1 \mathcal{A} \\ &= \mathcal{L}_2 \left( 2A_{\text{sq}} \partial_k u_l \sum_{\mathbf{q}_n \in \mathcal{R}_{\text{sq}}^{(1)}} q_{nk} q_{nl} E_{\mathbf{q}_n}^{\mathbf{u}}(\mathbf{r}) \right) \\ &= 2A_{\text{sq}} \partial_k u_l \sum_{\mathbf{q}_n \in \mathcal{R}_{\text{sq}}^{(1)}} q_{nk} q_{nl} (2 - \mathbf{q}_{n'}^2) E_{\mathbf{q}_n}^{\mathbf{u}}(\mathbf{r}) \\ &= 2A_{\text{sq}} \partial_k u_l \sum_{\mathbf{q}_n \in \mathcal{R}_{\text{sq}}^{(1)}} q_{nk} q_{nl} E_{\mathbf{q}_n}^{\mathbf{u}}(\mathbf{r}), \end{aligned} \quad (\text{B15})$$

so

$$\begin{aligned} &\langle (\mathcal{L}_1 \mathcal{L}_2 \mathcal{A}) (\mathcal{L}_1 + \mathcal{L}_2) \partial_{ij} \mathcal{A} \rangle \\ &= \langle (\mathcal{L}_1 \mathcal{L}_2 \mathcal{A}) \mathcal{L}_2 \partial_{ij} \mathcal{A} \rangle \\ &= 2A_{\text{sq}}^2 \partial_k u_l \sum_{\mathbf{q}_n \in \mathcal{R}_{\text{sq}}^{(1)}} \sum_{\mathbf{q}_{n'} \in \mathcal{R}_{\text{sq}}^{(1)}} q_{nk} q_{nl} \\ &\quad \times (2 - \mathbf{q}_{n'}^2) (-q_{n'i} q_{n'j}) \langle E_{\mathbf{q}_n}^{\mathbf{u}}(\mathbf{r}) E_{\mathbf{q}_{n'}}^{\mathbf{u}}(\mathbf{r}) \rangle \\ &= -2A_{\text{sq}}^2 \partial_k u_l \sum_{\mathbf{q}_n \in \mathcal{R}_{\text{sq}}^{(1)}} q_{nk} q_{nl} q_{ni} q_{nj}, \end{aligned} \quad (\text{B16})$$

and

$$\begin{aligned} \mathcal{L}_1 \mathcal{L}_2 \mathcal{B} &= \mathcal{L}_1 \left( 2B_{\text{sq}} \partial_k u_l \sum_{\mathbf{p}_n \in \mathcal{R}_{\text{sq}}^{(2)}} p_{nk} p_{nl} E_{\mathbf{p}_n}^{\mathbf{u}}(\mathbf{r}) \right) \\ &= 2B_{\text{sq}} \partial_k u_l \sum_{\mathbf{p}_n \in \mathcal{R}_{\text{sq}}^{(2)}} p_{nk} p_{nl} (1 - \mathbf{p}_{n'}^2) E_{\mathbf{p}_n}^{\mathbf{u}}(\mathbf{r}) \\ &= -2B_{\text{sq}} \partial_k u_l \sum_{\mathbf{p}_n \in \mathcal{R}_{\text{sq}}^{(2)}} p_{nk} p_{nl} E_{\mathbf{p}_n}^{\mathbf{u}}(\mathbf{r}), \end{aligned} \quad (\text{B17})$$

so

$$\begin{aligned}
& \langle (\mathcal{L}_1 \mathcal{L}_2 \mathcal{B})(\mathcal{L}_1 + \mathcal{L}_2) \partial_{ij} \mathcal{B} \rangle \\
&= \langle (\mathcal{L}_1 \mathcal{L}_2 \mathcal{B}) \mathcal{L}_1 \partial_{ij} \mathcal{B} \rangle \\
&= -2B_{\text{sq}}^2 \partial_k u_l \sum_{\mathbf{p}_n \in \mathcal{R}_{\text{sq}}^{(2)}} \sum_{\mathbf{p}_{n'} \in \mathcal{R}_{\text{sq}}^{(2)}} p_{nk} p_{nl} (1 - \mathbf{p}_{n'}^2) (-p_{n'i} p_{n'j}) \\
&\quad \times \langle E_{\mathbf{p}_n}^{\mathbf{u}}(\mathbf{r}) E_{\mathbf{p}_{n'}}^{\mathbf{u}}(\mathbf{r}) \rangle, \\
&= -2B_{\text{sq}}^2 \partial_k u_l \sum_{\mathbf{p}_n \in \mathcal{R}_{\text{sq}}^{(2)}} p_{ni} p_{nj} p_{nk} p_{nl}, \tag{B18}
\end{aligned}$$

which gives

$$\begin{aligned}
h_{ij}^{(2\text{D sq})} &= 4A_{\text{sq}}^2 \partial_k u_l \sum_{\mathbf{q}_n \in \mathcal{R}_{\text{sq}}^{(1)}} q_{nk} q_{nl} q_{ni} q_{nj} \\
&\quad + 4B_{\text{sq}}^2 \partial_k u_l \sum_{\mathbf{p}_n \in \mathcal{R}_{\text{sq}}^{(2)}} p_{ni} p_{nj} p_{nk} p_{nl}. \tag{B19}
\end{aligned}$$

### 3. 3D bcc PFC

We consider the bcc PFC in the one-mode expansion for a macroscopic displacement field  $\mathbf{u}$  at constant macroscopic density:

$$\psi = \psi_{\text{eq}}^{\text{bcc}}(\mathbf{r} - \mathbf{u}) \equiv \bar{\psi} + \mathcal{A}, \tag{B20}$$

where

$$\mathcal{A} = A_{\text{bcc}} \sum_{\mathbf{q}_n \in \mathcal{R}_{\text{bcc}}^{(1)}} e^{i\mathbf{q}_n \cdot (\mathbf{r} - \mathbf{u})} \equiv A_{\text{bcc}} \sum_{\mathbf{q}_n \in \mathcal{R}_{\text{bcc}}^{(1)}} E_{\mathbf{q}_n}^{\mathbf{u}}(\mathbf{r}). \tag{B21}$$

By resonance conditions, we have

$$\langle E_{\mathbf{q}_n}^{\mathbf{u}}(\mathbf{r}) \rangle = 0, \tag{B22}$$

and

$$\langle E_{\mathbf{q}_n}^{\mathbf{u}}(\mathbf{r}) E_{\mathbf{q}_{n'}}^{\mathbf{u}}(\mathbf{r}) \rangle = \delta_{n, -n'} \tag{B23}$$

as we only get a nonzero average at resonance, when  $\mathbf{q}_{n'} = -\mathbf{q}_n$ . Inserting the distorted PFC into the stress tensor, and using these identities, we get

$$\begin{aligned}
h_{ij}^{(3\text{D bcc})} &= -2 \langle (\mathcal{L}_1 \psi) \partial_{ij} \psi \rangle \\
&= -2 \langle (\mathcal{L}_1 \bar{\psi}) \partial_{ij} \bar{\psi} \rangle - 2 \langle (\mathcal{L}_1 \mathcal{A}) \partial_{ij} \mathcal{A} \rangle \\
&= -2 \langle (\mathcal{L}_1 \mathcal{A}) \partial_{ij} \mathcal{A} \rangle. \tag{B24}
\end{aligned}$$

First, we calculate, to first order in  $\partial_k u_l$ ,

$$\begin{aligned}
\mathcal{L}_1 \mathcal{A} &= A_{\text{bcc}} \sum_{\mathbf{q}_n \in \mathcal{R}_{\text{bcc}}^{(1)}} (1 - (q_{nk} - q_{nl} \partial_k u_l)^2) E_{\mathbf{q}_n}^{\mathbf{u}}(\mathbf{r}) \\
&= 2A_{\text{bcc}} \partial_k u_l \sum_{\mathbf{q}_n \in \mathcal{R}_{\text{bcc}}^{(1)}} q_{nk} q_{nl} E_{\mathbf{q}_n}^{\mathbf{u}}(\mathbf{r}), \tag{B25}
\end{aligned}$$

from which we get

$$\begin{aligned}
& \langle (\mathcal{L}_1 \mathcal{A}) \partial_{ij} \mathcal{A} \rangle \\
&= 2A_{\text{bcc}}^2 \sum_{\mathbf{q}_n \in \mathcal{R}_{\text{bcc}}^{(1)}} \sum_{\mathbf{q}_{n'} \in \mathcal{R}_{\text{bcc}}^{(1)}} q_{nk} q_{nl} (-q_{n'i} q_{n'j}) \\
&\quad \times \langle E_{\mathbf{q}_n}^{\mathbf{u}}(\mathbf{r}) E_{\mathbf{q}_{n'}}^{\mathbf{u}}(\mathbf{r}) \rangle \\
&= -2A_{\text{bcc}}^2 \sum_{\mathbf{q}_n \in \mathcal{R}_{\text{bcc}}^{(1)}} q_{ni} q_{nj} q_{nk} q_{nl}, \tag{B26}
\end{aligned}$$

so

$$h_{ij}^{(3\text{D bcc})} = 4A_{\text{bcc}}^2 \sum_{\mathbf{q}_n \in \mathcal{R}_{\text{bcc}}^{(1)}} q_{ni} q_{nj} q_{nk} q_{nl}. \tag{B27}$$

### 4. 3D fcc PFC

We consider the fcc PFC in the two-mode expansion for a macroscopic displacement field  $\mathbf{u}$  at constant macroscopic density:

$$\psi = \bar{\psi} + \mathcal{A} + \mathcal{B}, \tag{B28}$$

where

$$\mathcal{A} = A_{\text{fcc}} \sum_{\mathbf{q}_n \in \mathcal{R}_{\text{fcc}}^{(1)}} e^{i\mathbf{q}_n \cdot (\mathbf{r} - \mathbf{u})} \equiv A_{\text{fcc}} \sum_{\mathbf{q}_n \in \mathcal{R}_{\text{fcc}}^{(1)}} E_{\mathbf{q}_n}^{\mathbf{u}}(\mathbf{r}), \tag{B29}$$

$$\mathcal{B} = B_{\text{fcc}} \sum_{\mathbf{p}_n \in \mathcal{R}_{\text{fcc}}^{(4/3)}} e^{i\mathbf{p}_n \cdot (\mathbf{r} - \mathbf{u})} \equiv B_{\text{fcc}} \sum_{\mathbf{p}_n \in \mathcal{R}_{\text{fcc}}^{(4/3)}} E_{\mathbf{p}_n}^{\mathbf{u}}(\mathbf{r}). \tag{B30}$$

By resonance conditions, we have

$$\langle E_{\mathbf{q}_n}^{\mathbf{u}}(\mathbf{r}) \rangle = \langle E_{\mathbf{p}_n}^{\mathbf{u}}(\mathbf{r}) \rangle = \langle E_{\mathbf{q}_n}^{\mathbf{u}}(\mathbf{r}) E_{\mathbf{p}_{n'}}^{\mathbf{u}}(\mathbf{r}) \rangle = 0, \tag{B31}$$

and

$$\langle E_{\mathbf{q}_n}^{\mathbf{u}}(\mathbf{r}) E_{\mathbf{q}_{n'}}^{\mathbf{u}}(\mathbf{r}) \rangle = \langle E_{\mathbf{p}_n}^{\mathbf{u}}(\mathbf{r}) E_{\mathbf{p}_{n'}}^{\mathbf{u}}(\mathbf{r}) \rangle = \delta_{n', -n}, \tag{B32}$$

from which we find

$$\begin{aligned}
h_{ij}^{(3\text{D fcc})} &= -2 \langle (\mathcal{L}_1 \mathcal{L}_{\frac{4}{3}} \psi) (\mathcal{L}_1 + \mathcal{L}_{\frac{4}{3}}) \partial_{ij} \psi \rangle \\
&= -2 \langle (\mathcal{L}_1 \mathcal{L}_{\frac{4}{3}} \bar{\psi}) (\mathcal{L}_1 + \mathcal{L}_{\frac{4}{3}}) \partial_{ij} \bar{\psi} \rangle \\
&\quad - 2 \langle (\mathcal{L}_1 \mathcal{L}_{\frac{4}{3}} \mathcal{A}) (\mathcal{L}_1 + \mathcal{L}_{\frac{4}{3}}) \partial_{ij} \mathcal{A} \rangle \\
&\quad - 2 \langle (\mathcal{L}_1 \mathcal{L}_{\frac{4}{3}} \mathcal{B}) (\mathcal{L}_1 + \mathcal{L}_{\frac{4}{3}}) \partial_{ij} \mathcal{B} \rangle \\
&= -2 \langle (\mathcal{L}_1 \mathcal{L}_{\frac{4}{3}} \mathcal{A}) (\mathcal{L}_1 + \mathcal{L}_{\frac{4}{3}}) \partial_{ij} \mathcal{A} \rangle \\
&\quad - 2 \langle (\mathcal{L}_1 \mathcal{L}_{\frac{4}{3}} \mathcal{B}) (\mathcal{L}_1 + \mathcal{L}_{\frac{4}{3}}) \partial_{ij} \mathcal{B} \rangle. \tag{B33}
\end{aligned}$$

To first order in  $\partial_k u_l$ , we have

$$\begin{aligned}
\mathcal{L}_1 \mathcal{L}_{\frac{4}{3}} \mathcal{A} &= \mathcal{L}_{\frac{4}{3}} \mathcal{L}_1 \mathcal{A} \\
&= \mathcal{L}_{\frac{4}{3}} \left( 2A_{\text{fcc}} \partial_k u_l \sum_{\mathbf{q}_n \in \mathcal{R}_{\text{fcc}}^{(1)}} q_{nk} q_{nl} E_{\mathbf{q}_n}^{\mathbf{u}}(\mathbf{r}) \right) \\
&= 2A_{\text{fcc}} \partial_k u_l \sum_{\mathbf{q}_n \in \mathcal{R}_{\text{fcc}}^{(1)}} q_{nk} q_{nl} \left( \frac{4}{3} - \mathbf{q}_n^2 \right) E_{\mathbf{q}_n}^{\mathbf{u}}(\mathbf{r}) \\
&= \frac{2}{3} A_{\text{fcc}} \partial_k u_l \sum_{\mathbf{q}_n \in \mathcal{R}_{\text{fcc}}^{(1)}} q_{nk} q_{nl} E_{\mathbf{q}_n}^{\mathbf{u}}(\mathbf{r}), \tag{B34}
\end{aligned}$$

so

$$\begin{aligned}
& \langle (\mathcal{L}_1 \mathcal{L}_{\frac{4}{3}} \mathcal{A}) (\mathcal{L}_1 + \mathcal{L}_{\frac{4}{3}}) \partial_{ij} \mathcal{A} \rangle \\
&= \langle (\mathcal{L}_1 \mathcal{L}_{\frac{4}{3}} \mathcal{A}) \mathcal{L}_{\frac{4}{3}} \partial_{ij} \mathcal{A} \rangle \\
&= \frac{2}{3} A_{\text{fcc}}^2 \partial_k u_l \sum_{\mathbf{q}_n \in \mathcal{R}_{\text{fcc}}^{(1)}} \sum_{\mathbf{q}_{n'} \in \mathcal{R}_{\text{fcc}}^{(1)}} q_{nk} q_{nl} \left( \frac{4}{3} - \mathbf{q}_{n'}^2 \right)
\end{aligned}$$

$$\begin{aligned} & \times (-q_{n'i}q_{n'j}) \langle E_{\mathbf{q}_n}^{\mathbf{u}}(\mathbf{r}) E_{\mathbf{q}_{n'}}^{\mathbf{u}}(\mathbf{r}) \rangle \\ & = -\frac{2}{9} A_{\text{fcc}}^2 \partial_k u_l \sum_{\mathbf{q}_n \in \mathcal{R}_{\text{fcc}}^{(1)}} q_{nk} q_{nl} q_{ni} q_{nj}, \end{aligned} \quad (\text{B35})$$

and

$$\begin{aligned} \mathcal{L}_1 \mathcal{L}_{\frac{4}{3}} \mathcal{B} & = \mathcal{L}_1 \left( 2B_{\text{fcc}} \partial_k u_l \sum_{\mathbf{p}_n \in \mathcal{R}_{\text{fcc}}^{(4/3)}} p_{nk} p_{nl} E_{\mathbf{p}_n}^{\mathbf{u}}(\mathbf{r}) \right) \\ & = 2B_{\text{fcc}} \partial_k u_l \sum_{\mathbf{p}_n \in \mathcal{R}_{\text{fcc}}^{(4/3)}} p_{nk} p_{nl} (1 - \mathbf{p}_n^2) E_{\mathbf{p}_n}^{\mathbf{u}}(\mathbf{r}) \\ & = -\frac{2}{3} B_{\text{fcc}} \partial_k u_l \sum_{\mathbf{p}_n \in \mathcal{R}_{\text{fcc}}^{(4/3)}} p_{nk} p_{nl} E_{\mathbf{p}_n}^{\mathbf{u}}(\mathbf{r}), \end{aligned} \quad (\text{B36})$$

so

$$\begin{aligned} & \langle (\mathcal{L}_1 \mathcal{L}_{\frac{4}{3}} \mathcal{B})(\mathcal{L}_1 + \mathcal{L}_{\frac{4}{3}}) \partial_{ij} \mathcal{B} \rangle \\ & = \langle (\mathcal{L}_1 \mathcal{L}_2 \mathcal{B}) \mathcal{L}_1 \partial_{ij} \mathcal{B} \rangle \\ & = -\frac{2}{3} B_{\text{fcc}}^2 \partial_k u_l \sum_{\mathbf{p}_n \in \mathcal{R}_{\text{fcc}}^{(4/3)}} \sum_{\mathbf{p}_{n'} \in \mathcal{R}_{\text{fcc}}^{(4/3)}} p_{nk} p_{nl} (1 - \mathbf{p}_{n'}^2) \\ & \quad \times (-p_{n'i} p_{n'j}) \langle E_{\mathbf{p}_n}^{\mathbf{u}}(\mathbf{r}) E_{\mathbf{p}_{n'}}^{\mathbf{u}}(\mathbf{r}) \rangle \\ & = -\frac{2}{9} B_{\text{fcc}}^2 \partial_k u_l \sum_{\mathbf{p}_n \in \mathcal{R}_{\text{fcc}}^{(4/3)}} p_{ni} p_{nj} p_{nk} p_{nl}, \end{aligned} \quad (\text{B37})$$

which gives

$$\begin{aligned} h_{ij}^{(3\text{D fcc})} & = \frac{4}{9} A_{\text{fcc}}^2 \partial_k u_l \sum_{\mathbf{q}_n \in \mathcal{R}_{\text{fcc}}^{(1)}} q_{nk} q_{nl} q_{ni} q_{nj} \\ & \quad + \frac{4}{9} B_{\text{fcc}}^2 \partial_k u_l \sum_{\mathbf{p}_n \in \mathcal{R}_{\text{fcc}}^{(4/3)}} p_{ni} p_{nj} p_{nk} p_{nl}. \end{aligned} \quad (\text{B38})$$

### 5. 3D sc PFC

We consider the sc PFC in the three-mode expansion for a macroscopic displacement field  $\mathbf{u}$  at constant macroscopic density:

$$\psi = \bar{\psi} + \mathcal{A} + \mathcal{B} + \mathcal{C}, \quad (\text{B39})$$

where

$$\mathcal{A} = A_{\text{sc}} \sum_{\mathbf{q}_n \in \mathcal{R}_{\text{sc}}^{(1)}} E_{\mathbf{q}_n}^{\mathbf{u}}(\mathbf{r}), \quad (\text{B40})$$

$$\mathcal{B} = B_{\text{sc}} \sum_{\mathbf{q}_n \in \mathcal{R}_{\text{sc}}^{(2)}} E_{\mathbf{q}_n}^{\mathbf{u}}(\mathbf{r}), \quad (\text{B41})$$

$$\mathcal{C} = C_{\text{sc}} \sum_{\mathbf{t}_n \in \mathcal{R}_{\text{sc}}^{(3)}} E_{\mathbf{t}_n}^{\mathbf{u}}(\mathbf{r}). \quad (\text{B42})$$

By resonance conditions, we have

$$\begin{aligned} \langle E_{\mathbf{q}_n}^{\mathbf{u}}(\mathbf{r}) \rangle & = \langle E_{\mathbf{p}_n}^{\mathbf{u}}(\mathbf{r}) \rangle = \langle E_{\mathbf{t}_n}^{\mathbf{u}}(\mathbf{r}) \rangle = \langle E_{\mathbf{p}_n}^{\mathbf{u}}(\mathbf{r}) E_{\mathbf{t}_{n'}}^{\mathbf{u}}(\mathbf{r}) \rangle \\ & = \langle E_{\mathbf{q}_n}^{\mathbf{u}}(\mathbf{r}) E_{\mathbf{t}_{n'}}^{\mathbf{u}}(\mathbf{r}) \rangle = \langle E_{\mathbf{q}_n}^{\mathbf{u}}(\mathbf{r}) E_{\mathbf{p}_{n'}}^{\mathbf{u}}(\mathbf{r}) \rangle = 0, \end{aligned} \quad (\text{B43})$$

and

$$\langle E_{\mathbf{q}_n}^{\mathbf{u}}(\mathbf{r}) E_{\mathbf{q}_{n'}}^{\mathbf{u}}(\mathbf{r}) \rangle = \langle E_{\mathbf{p}_n}^{\mathbf{u}}(\mathbf{r}) E_{\mathbf{p}_{n'}}^{\mathbf{u}}(\mathbf{r}) \rangle = \langle E_{\mathbf{t}_n}^{\mathbf{u}}(\mathbf{r}) E_{\mathbf{t}_{n'}}^{\mathbf{u}}(\mathbf{r}) \rangle = \delta_{n', -n}, \quad (\text{B44})$$

from which we get

$$\begin{aligned} h_{ij}^{(3\text{D sc})} & = -2 \langle (\mathcal{L}_1 \mathcal{L}_2 \mathcal{L}_3 \psi)(\mathcal{L}_2 \mathcal{L}_3 + \mathcal{L}_1 \mathcal{L}_3 + \mathcal{L}_1 \mathcal{L}_2) \partial_{ij} \psi \rangle \\ & = -2 \langle (\mathcal{L}_1 \mathcal{L}_2 \mathcal{L}_3 \bar{\psi})(\mathcal{L}_2 \mathcal{L}_3 + \mathcal{L}_1 \mathcal{L}_3 + \mathcal{L}_1 \mathcal{L}_2) \partial_{ij} \bar{\psi} \rangle - 2 \langle (\mathcal{L}_1 \mathcal{L}_2 \mathcal{L}_3 \mathcal{A})(\mathcal{L}_2 \mathcal{L}_3 + \mathcal{L}_1 \mathcal{L}_3 + \mathcal{L}_1 \mathcal{L}_2) \partial_{ij} \mathcal{A} \rangle \\ & \quad - 2 \langle (\mathcal{L}_1 \mathcal{L}_2 \mathcal{L}_3 \mathcal{B})(\mathcal{L}_2 \mathcal{L}_3 + \mathcal{L}_1 \mathcal{L}_3 + \mathcal{L}_1 \mathcal{L}_2) \partial_{ij} \mathcal{B} \rangle - 2 \langle (\mathcal{L}_1 \mathcal{L}_2 \mathcal{L}_3 \mathcal{C})(\mathcal{L}_2 \mathcal{L}_3 + \mathcal{L}_1 \mathcal{L}_3 + \mathcal{L}_1 \mathcal{L}_2) \partial_{ij} \mathcal{C} \rangle \\ & = -2 \langle (\mathcal{L}_1 \mathcal{L}_2 \mathcal{L}_3 \mathcal{A})(\mathcal{L}_2 \mathcal{L}_3 + \mathcal{L}_1 \mathcal{L}_3 + \mathcal{L}_1 \mathcal{L}_2) \partial_{ij} \mathcal{A} \rangle - 2 \langle (\mathcal{L}_1 \mathcal{L}_2 \mathcal{L}_3 \mathcal{B})(\mathcal{L}_2 \mathcal{L}_3 + \mathcal{L}_1 \mathcal{L}_3 + \mathcal{L}_1 \mathcal{L}_2) \partial_{ij} \mathcal{B} \rangle \\ & \quad - 2 \langle (\mathcal{L}_1 \mathcal{L}_2 \mathcal{L}_3 \mathcal{C})(\mathcal{L}_2 \mathcal{L}_3 + \mathcal{L}_1 \mathcal{L}_3 + \mathcal{L}_1 \mathcal{L}_2) \partial_{ij} \mathcal{C} \rangle. \end{aligned} \quad (\text{B45})$$

To first order in  $\partial_k u_l$ , we have

$$\begin{aligned} \mathcal{L}_1 \mathcal{L}_2 \mathcal{L}_3 \mathcal{A} & = \mathcal{L}_2 \mathcal{L}_3 \mathcal{L}_1 \mathcal{A} = 2A_{\text{sc}} \mathcal{L}_2 \mathcal{L}_3 \partial_k u_l \sum_{\mathbf{q}_n \in \mathcal{R}_{\text{sc}}^{(1)}} q_{nk} q_{nl} E_{\mathbf{q}_n}^{\mathbf{u}}(\mathbf{r}) \\ & = 2A_{\text{sc}} \partial_k u_l \sum_{\mathbf{q}_n \in \mathcal{R}_{\text{sc}}^{(1)}} (2 - \mathbf{q}_n^2)(3 - \mathbf{q}_n^2) q_{nk} q_{nl} E_{\mathbf{q}_n}^{\mathbf{u}}(\mathbf{r}) = 4A_{\text{sc}} \partial_k u_l \sum_{\mathbf{q}_n \in \mathcal{R}_{\text{sc}}^{(1)}} q_{nk} q_{nl} E_{\mathbf{q}_n}^{\mathbf{u}}(\mathbf{r}), \end{aligned} \quad (\text{B46})$$

so

$$\begin{aligned} \langle (\mathcal{L}_1 \mathcal{L}_2 \mathcal{L}_3 \mathcal{A})(\mathcal{L}_2 \mathcal{L}_3 + \mathcal{L}_1 \mathcal{L}_3 + \mathcal{L}_1 \mathcal{L}_2) \partial_{ij} \mathcal{A} \rangle & = \langle (\mathcal{L}_1 \mathcal{L}_2 \mathcal{L}_3 \mathcal{A}) \mathcal{L}_2 \mathcal{L}_3 \partial_{ij} \mathcal{A} \rangle \\ & = 4A_{\text{sc}}^2 \partial_k u_l \sum_{\mathbf{q}_n \in \mathcal{R}_{\text{sc}}^{(1)}} q_{nk} q_{nl} (-q_{n'i} q_{n'j}) (2 - \mathbf{q}_n^2)(3 - \mathbf{q}_{n'}^2) \langle E_{\mathbf{q}_n}^{\mathbf{u}}(\mathbf{r}) E_{\mathbf{q}_{n'}}^{\mathbf{u}}(\mathbf{r}) \rangle = -8A_{\text{sc}}^2 \partial_k u_l \sum_{\mathbf{q}_n \in \mathcal{R}_{\text{sc}}^{(1)}} q_{ni} q_{nj} q_{nk} q_{nl}, \end{aligned} \quad (\text{B47})$$

$$\begin{aligned} \mathcal{L}_1 \mathcal{L}_2 \mathcal{L}_3 \mathcal{B} & = \mathcal{L}_1 \mathcal{L}_3 \mathcal{L}_2 \mathcal{B} = 2B_{\text{sc}} \partial_k u_l \mathcal{L}_1 \mathcal{L}_3 \sum_{\mathbf{p}_n \in \mathcal{R}_{\text{sc}}^{(2)}} p_{nk} p_{nl} E_{\mathbf{p}_n}^{\mathbf{u}}(\mathbf{r}) \\ & = 2B_{\text{sc}} \partial_k u_l \sum_{\mathbf{p}_n \in \mathcal{R}_{\text{sc}}^{(2)}} (1 - \mathbf{p}_n^2)(3 - \mathbf{p}_n^2) p_{nk} p_{nl} E_{\mathbf{p}_n}^{\mathbf{u}}(\mathbf{r}) = -2B_{\text{sc}} \partial_k u_l \sum_{\mathbf{p}_n \in \mathcal{R}_{\text{sc}}^{(2)}} p_{nk} p_{nl} E_{\mathbf{p}_n}^{\mathbf{u}}(\mathbf{r}), \end{aligned} \quad (\text{B48})$$

so

$$\begin{aligned}
& \langle (\mathcal{L}_1 \mathcal{L}_2 \mathcal{L}_3 \mathcal{B})(\mathcal{L}_2 \mathcal{L}_3 + \mathcal{L}_1 \mathcal{L}_3 + \mathcal{L}_1 \mathcal{L}_2) \partial_{ij} \mathcal{B} \rangle \\
&= \langle (\mathcal{L}_1 \mathcal{L}_2 \mathcal{L}_3 \mathcal{B}) \mathcal{L}_1 \mathcal{L}_3 \partial_{ij} \mathcal{B} \rangle = -2B_{\text{sc}}^2 \partial_k u_l \sum_{\mathbf{p}_n \in \mathcal{R}_{\text{sc}}^{(2)}} p_{nk} p_{nl} (-p_{n'i} p_{n'j}) (1 - \mathbf{p}_n^2) (3 - \mathbf{p}_n^2) \langle E_{\mathbf{p}_n}^{\mathbf{u}}(\mathbf{r}) E_{\mathbf{p}_n'}^{\mathbf{u}}(\mathbf{r}) \rangle \\
&= -2B_{\text{sc}}^2 \partial_k u_l \sum_{\mathbf{p}_n \in \mathcal{R}_{\text{sc}}^{(2)}} p_{ni} p_{nj} p_{nk} p_{nl},
\end{aligned} \tag{B49}$$

and

$$\mathcal{L}_1 \mathcal{L}_2 \mathcal{L}_3 \mathcal{C} = 2C_{\text{sc}} \partial_k u_l \mathcal{L}_1 \mathcal{L}_2 \sum_{\mathbf{t}_n \in \mathcal{R}_{\text{sc}}^{(3)}} t_{nk} t_{nl} E_{\mathbf{t}_n}^{\mathbf{u}}(\mathbf{r}) = 2C_{\text{sc}} \partial_k u_l \sum_{\mathbf{t}_n \in \mathcal{R}_{\text{sc}}^{(3)}} (1 - \mathbf{t}_n^2) (2 - \mathbf{t}_n^2) t_{nk} t_{nl} E_{\mathbf{t}_n}^{\mathbf{u}}(\mathbf{r}) = 4C_{\text{sc}} \partial_k u_l \sum_{\mathbf{t}_n \in \mathcal{R}_{\text{sc}}^{(3)}} p_{nk} p_{nl} E_{\mathbf{t}_n}^{\mathbf{u}}(\mathbf{r}), \tag{B50}$$

so

$$\begin{aligned}
& \langle (\mathcal{L}_1 \mathcal{L}_2 \mathcal{L}_3 \mathcal{C})(\mathcal{L}_2 \mathcal{L}_3 + \mathcal{L}_1 \mathcal{L}_3 + \mathcal{L}_1 \mathcal{L}_2) \partial_{ij} \mathcal{C} \rangle \langle (\mathcal{L}_1 \mathcal{L}_2 \mathcal{L}_3 \mathcal{C}) \mathcal{L}_1 \mathcal{L}_2 \partial_{ij} \mathcal{C} \rangle \\
&= 4C_{\text{sc}}^2 \partial_k u_l \sum_{\mathbf{t}_n \in \mathcal{R}_{\text{sc}}^{(3)}} t_{nk} t_{nl} (-t_{n'i} t_{n'j}) (1 - \mathbf{t}_n^2) (2 - \mathbf{t}_n^2) \langle E_{\mathbf{t}_n}^{\mathbf{u}}(\mathbf{r}) E_{\mathbf{t}_n'}^{\mathbf{u}}(\mathbf{r}) \rangle = -8C_{\text{sc}}^2 \partial_k u_l \sum_{\mathbf{t}_n \in \mathcal{R}_{\text{sc}}^{(3)}} t_{ni} t_{nj} t_{nk} t_{nl}.
\end{aligned} \tag{B51}$$

Thus, we find

$$h_{ij}^{(3\text{D sc})} = 16A_{\text{sc}}^2 \partial_k u_l \sum_{\mathbf{q}_n \in \mathcal{R}_{\text{sc}}^{(1)}} q_{ni} q_{nj} q_{nk} q_{nl} + 4B_{\text{sc}}^2 \partial_k u_l \sum_{\mathbf{p}_n \in \mathcal{R}_{\text{sc}}^{(2)}} p_{ni} p_{nj} p_{nk} p_{nl} + 16C_{\text{sc}}^2 \partial_k u_l \sum_{\mathbf{t}_n \in \mathcal{R}_{\text{sc}}^{(3)}} t_{ni} t_{nj} t_{nk} t_{nl}. \tag{B52}$$

- 
- [1] M. Baggioli, V. C. Castillo, and O. Pujolàs, Scale invariant solids, *Phys. Rev. D* **101**, 086005 (2020).
- [2] M. D. Uchic, D. M. Dimiduk, J. N. Florando, and W. D. Nix, Sample dimensions influence strength and crystal plasticity, *Science* **305**, 986 (2004).
- [3] D. M. Dimiduk, M. D. Uchic, and T. A. Parthasarathy, Size-affected single-slip behavior of pure nickel microcrystals, *Acta Mater.* **53**, 4065 (2005).
- [4] J. R. Greer and J. T. D. Hosson, Plasticity in small-sized metallic systems: Intrinsic versus extrinsic size effect, *Prog. Mater. Sci.* **56**, 654 (2011).
- [5] P. J. Guruprasad and A. A. Benzerga, Size effects under homogeneous deformation of single crystals: A discrete dislocation analysis, *J. Mech. Phys. Solids* **56**, 132 (2008).
- [6] S. Papanikolaou, Y. Cui, and N. Ghoniem, Avalanches and plastic flow in crystal plasticity: An overview, *Modell. Simul. Mater. Sci. Eng.* **26**, 013001 (2017).
- [7] M. Ovaska, A. Lehtinen, M. J. Alava, L. Laurson, and S. Zapperi, Excitation Spectra in Crystal Plasticity, *Phys. Rev. Lett.* **119**, 265501 (2017).
- [8] J. Weiss, W. B. Rhouma, T. Richeton, S. Dechanel, F. Louchet, and L. Truskinovsky, From Mild to Wild Fluctuations in Crystal Plasticity, *Phys. Rev. Lett.* **114**, 105504 (2015).
- [9] C. Zhou, S. B. Biner, and R. LeSar, Discrete dislocation dynamics simulations of plasticity at small scales, *Acta Mater.* **58**, 1565 (2010).
- [10] J. Hu, H. Song, Z. Liu, Z. Zhuang, X. Liu, and S. Sandfeld, Predicting the flow stress and dominant yielding mechanisms: Analytical models based on discrete dislocation plasticity, *Sci. Rep.* **9**, 20422 (2019).
- [11] S. Limkumnerd and J. P. Sethna, Mesoscale Theory of Grains and Cells: Crystal Plasticity and Coarsening, *Phys. Rev. Lett.* **96**, 095503 (2006).
- [12] O. U. Salman and L. Truskinovsky, Minimal Integer Automaton behind Crystal Plasticity, *Phys. Rev. Lett.* **106**, 175503 (2011).
- [13] R. Baggio, E. Arbib, P. Biscari, S. Conti, L. Truskinovsky, G. Zanzotto, and O. U. Salman, Landau-Type Theory of Planar Crystal Plasticity, *Phys. Rev. Lett.* **123**, 205501 (2019).
- [14] N. A. Fleck, G. M. Muller, M. F. Ashby, and J. W. Hutchinson, Strain gradient plasticity: Theory and experiment, *Acta Metall. Mater.* **42**, 475 (1994).
- [15] D. Liu and D. J. Dunstan, Material length scale of strain gradient plasticity: A physical interpretation, *Int. J. Plast.* **98**, 156 (2017).
- [16] M. Lazar and G. A. Maugin, Nonsingular stress and strain fields of dislocations and disclinations in first strain gradient elasticity, *Int. J. Eng. Sci.* **43**, 1157 (2005).
- [17] K. R. Elder and M. Grant, Modeling elastic and plastic deformations in nonequilibrium processing using phase field crystals, *Phys. Rev. E* **70**, 051605 (2004).
- [18] K. R. Elder, N. Provatas, J. Berry, P. Stefanovic, and M. Grant, Phase-field crystal modeling and classical density functional theory of freezing, *Phys. Rev. B* **75**, 064107 (2007).
- [19] H. Emmerich, H. Löwen, R. Wittkowski, T. Gruhn, G. I. Tóth, G. Tegze, and László Gránásy, Phase-field-crystal models for condensed matter dynamics on atomic length and diffusive time scales: An overview, *Adv. Phys.* **61**, 665 (2012).
- [20] P. Stefanovic, M. Haataja, and N. Provatas, Phase-Field Crystals with Elastic Interactions, *Phys. Rev. Lett.* **96**, 225504 (2006).
- [21] V. Heinonen, C. V. Achim, J. M. Kosterlitz, S.-C. Ying, J. Lowengrub, and T. Ala-Nissila, Consistent Hydrodynamics for Phase Field Crystals, *Phys. Rev. Lett.* **116**, 024303 (2016).
- [22] A. Skaugen, L. Angheluta, and J. Viñals, Separation of Elastic and Plastic Timescales in a Phase Field Crystal Model, *Phys. Rev. Lett.* **121**, 255501 (2018).

- [23] M. Salvalaglio, L. Angheluta, Z.-F. Huang, A. Voigt, K. R. Elder, and J. Viñals, A coarse-grained phase-field crystal model of plastic motion, *J. Mech. Phys. Solids* **137**, 103856 (2020).
- [24] V. Skogvoll, A. Skaugen, L. Angheluta, and J. Viñals, Dislocation nucleation in the phase-field crystal model, *Phys. Rev. B* **103**, 014107 (2021).
- [25] A. Skaugen, L. Angheluta, and J. Viñals, Dislocation dynamics and crystal plasticity in the phase-field crystal model, *Phys. Rev. B* **97**, 054113 (2018).
- [26] J. Irving and J. G. Kirkwood, The statistical mechanical theory of transport processes. IV. The equations of hydrodynamics, *J. Chem. Phys.* **18**, 817 (1950).
- [27] L. J. Bartolotti and R. G. Parr, The concept of pressure in density functional theory, *J. Chem. Phys.* **72**, 1593 (1980).
- [28] A. Dal Corso and R. Resta, Density-functional theory of macroscopic stress: Gradient-corrected calculations for crystalline Se, *Phys. Rev. B* **50**, 4327 (1994).
- [29] A. Filippetti and V. Fiorentini, Theory and applications of the stress density, *Phys. Rev. B* **61**, 8433 (2000).
- [30] M. Krüger, A. Solon, V. Démery, C. M. Rohwer, and D. S. Dean, Stresses in non-equilibrium fluids: Exact formulation and coarse-grained theory, *J. Chem. Phys.* **148**, 084503 (2018).
- [31] D. H. Tsai, The virial theorem and stress calculation in molecular dynamics, *J. Chem. Phys.* **70**, 1375 (1979).
- [32] J. F. Lutsko, Stress and elastic constants in anisotropic solids: Molecular dynamics techniques, *J. Appl. Phys.* **64**, 1152 (1988).
- [33] H. Chen and S. Orszag, Moment isotropy and discrete rotational symmetry of two-dimensional lattice vectors, *Philos. Trans. R. Soc. A* **369**, 2176 (2011).
- [34] M. te Vrugt, H. Löwen, and R. Wittkowski, Classical dynamical density functional theory: From fundamentals to applications, *Adv. Phys.* **69**, 121 (2020).
- [35] O. H. Nielsen and R. M. Martin, Stresses in semiconductors: Ab initio calculations on Si, Ge, and GaAs, *Phys. Rev. B* **32**, 3792 (1985).
- [36] N. Chetty and R. M. Martin, First-principles energy density and its applications to selected polar surfaces, *Phys. Rev. B* **45**, 6074 (1992).
- [37] R. Lifshitz and D. M. Petrich, Theoretical Model for Faraday Waves with Multiple-Frequency Forcing, *Phys. Rev. Lett.* **79**, 1261 (1997).
- [38] K.-A. Wu, A. Adland, and A. Karma, Phase-field-crystal model for fcc ordering, *Phys. Rev. E* **81**, 061601 (2010).
- [39] K.-A. Wu, M. Plapp, and P. W. Voorhees, Controlling crystal symmetries in phase-field crystal models, *J. Phys.: Condens. Matter* **22**, 364102 (2010).
- [40] S. K. Mkhonta, K. R. Elder, and Z.-F. Huang, Exploring the Complex World of Two-Dimensional Ordering with Three Modes, *Phys. Rev. Lett.* **111**, 035501 (2013).
- [41] P. M. Chaikin and T. C. Lubensky, *Principles of Condensed Matter Physics* (Cambridge University Press, Cambridge, England, 1995).
- [42] V. Heinonen, C. V. Achim, K. R. Elder, S. Buyukdagli, and T. Ala-Nissila, Phase-field-crystal models and mechanical equilibrium, *Phys. Rev. E* **89**, 032411 (2014).
- [43] Here, we have implicitly imposed a convention of the numbering  $n \in \mathbb{Z}$  of reciprocal lattice vectors. Since reciprocal lattice vectors come in oppositely signed pairs, we are free to define an indexing in which  $\mathbf{K}_{-n} = -\mathbf{K}_n$  for all  $n$ . This convention sets  $\mathbf{K}_0 = \mathbf{0}$ . Additionally, we would only obtain an exact delta function if coarse graining was performed over an exact number of unit cells. With the coarse graining definition of Eq. (16), the value of  $\langle e^{i(\mathbf{K}_n + \mathbf{K}_{n'}) \cdot \mathbf{r}} \rangle$  will be  $e^{-\frac{1}{2}a_0^2(\mathbf{K}_n + \mathbf{K}_{n'})^2}$ , which is 1 for  $n = -n'$ , and for a vector sum  $(\mathbf{K}_n + \mathbf{K}_{n'})$  giving one of the closest reciprocal modes, where  $a_0|\mathbf{K}_n + \mathbf{K}_{n'}| \sim 2\pi$ , we get  $e^{-\frac{1}{2}a_0^2(\mathbf{K}_n + \mathbf{K}_{n'})^2} \sim e^{-2\pi^2} = 2.67 \times 10^{-9}$ .
- [44] J. Rigelesaiyin, A. Diaz, W. Li, L. Xiong, and Y. Chen, Asymmetry of the atomic-level stress tensor in homogeneous and inhomogeneous materials, *Proc. Math. Phys. Eng. Sci.* **474**, 20180155 (2018).
- [45] C. Hüter, M. Friák, M. Weikamp, J. Neugebauer, N. Goldenfeld, B. Svendsen, and R. Spatschek, Nonlinear elastic effects in phase field crystal and amplitude equations: Comparison to ab initio simulations of bcc metals and graphene, *Phys. Rev. B* **93**, 214105 (2016).
- [46] Z.-L. Wang, Z.-F. Huang, and Z. Liu, Elastic constants of stressed and unstressed materials in the phase-field crystal model, *Phys. Rev. B* **97**, 144112 (2018).
- [47] M. Ainsworth and Z. Mao, Phase field crystal based prediction of temperature and density dependence of elastic constants through a structural phase transition, *Phys. Rev. B* **100**, 104101 (2019).
- [48] K.-A. Wu and A. Karma, Phase-field crystal modeling of equilibrium bcc-liquid interfaces, *Phys. Rev. B* **76**, 184107 (2007).
- [49] A. Jaatinen and T. Ala-Nissila, Extended phase diagram of the three-dimensional phase field crystal model, *J. Phys.: Condens. Matter* **22**, 205402 (2010).
- [50] A. Emdadi, M. Asle Zaeem, and E. Asadi, Revisiting phase diagrams of two-mode phase-field crystal models, *Comput. Mater. Sci.* **123**, 139 (2016).
- [51] K. L. M. Elder, M. Seymour, M. Lee, M. Hilke, and N. Provatas, Two-component structural phase-field crystal models for graphene symmetries, *Philos. Trans. R. Soc. A* **376**, 20170211 (2018).
- [52] Mathematica, version 12.2, Wolfram, Inc., Champaign, IL, 2020.
- [53] M. Greenwood, N. Provatas, and J. Rottler, Free Energy Functionals for Efficient Phase Field Crystal Modeling of Structural Phase Transformations, *Phys. Rev. Lett.* **105**, 045702 (2010).
- [54] Z.-L. Wang, Z. Liu, and Z.-F. Huang, Angle-adjustable density field formulation for the modeling of crystalline microstructure, *Phys. Rev. B* **97**, 180102(R) (2018).

## PAPER III







# A phase field crystal theory of the kinematics of dislocation lines

Vidar Skogvoll <sup>a,\*</sup>, Luiza Angheluta <sup>a</sup>, Audun Skaugen <sup>a</sup>, Marco Salvalaglio <sup>b,c</sup>,  
Jorge Viñals <sup>d</sup>

<sup>a</sup> PoreLab, Njord Centre, Department of Physics, University of Oslo, P.O. Box 1048, 0316 Oslo, Norway

<sup>b</sup> Institute of Scientific Computing, TU Dresden, 01062 Dresden, Germany

<sup>c</sup> Dresden Center for Computational Materials Science (DCMS), TU Dresden, 01062 Dresden, Germany

<sup>d</sup> School of Physics and Astronomy, University of Minnesota, Minneapolis, MN 55455, United States of America

## ARTICLE INFO

### Keywords:

Structure of solids and liquids  
Atomistic models  
Computational methods  
Phase-field crystal modeling  
Dislocation dynamics  
Crystal plasticity

## ABSTRACT

We introduce a dislocation density tensor and derive its kinematic evolution law from a phase field description of crystal deformations in three dimensions. The phase field crystal (PFC) model is used to define the lattice distortion, including topological singularities, and the associated configurational stresses. We derive an exact expression for the velocity of dislocation line determined by the phase field evolution, and show that dislocation motion in the PFC is driven by a Peach–Koehler force. As is well known from earlier PFC model studies, the configurational stress is not divergence free for a general field configuration. Therefore, we also present a method (PFCMEq) to constrain the diffusive dynamics to mechanical equilibrium by adding an independent and integrable distortion so that the total resulting stress is divergence free. In the PFCMEq model, the far-field stress agrees very well with the predictions from continuum elasticity, while the near-field stress around the dislocation core is regularized by the smooth nature of the phase-field. We apply this framework to study the rate of shrinkage of an dislocation loop seeded in its glide plane.

## 1. Introduction

Plasticity in crystalline solids primarily refers to permanent deformations resulting from the nucleation, motion, and interaction of extended dislocations. Classical plasticity theories deal with the yielding of materials within continuum solid mechanics (Hill, 1998; Wu, 2004). Deviations from elastic response are described with additional variables (e.g., the plastic strain), which effectively describe the onset of plasticity (yielding criteria), as well as the mechanical properties of plastically deformed media (e.g., work hardening). A macroscopic description of the collective behavior of dislocation ensembles is thus achieved, usually assuming homogeneous media for large systems. In crystal plasticity, inhomogeneities and anisotropies are accounted for, with the theory having been implemented as a computationally efficient finite element model (Roters et al., 2010; Pokharel et al., 2014). These theories are largely phenomenological in nature, and rely on constitutive laws and material parameters to be determined by other methods, or extracted from experiments. They can be finely tuned, but sometimes fail in describing mesoscale effects (Rollett et al., 2015). On the other hand, remarkable mesoscale descriptions have been developed by tracking single dislocations (Kubin et al., 1992; Bulatov et al., 1998; Sills et al., 2016; Koslowski et al., 2002; Rodney et al., 2003). These approaches typically evolve dislocation lines through Peach–Koehler type forces while incorporating their slip system, mobilities, and dislocation reactions phenomenologically. Stress fields are described within classical elasticity theory (Anderson et al., 2017). Since linear elasticity

\* Corresponding author.

E-mail address: [vidarsko@uio.no](mailto:vidarsko@uio.no) (V. Skogvoll).

<https://doi.org/10.1016/j.jmps.2022.104932>

Received 4 November 2021; Received in revised form 4 May 2022; Accepted 11 May 2022

Available online 31 May 2022

0022-5096/© 2022 The Author(s). Published by Elsevier Ltd. This is an open access article under the CC BY license (<http://creativecommons.org/licenses/by/4.0/>).

predicts a singular elastic field at the dislocation core, theories featuring its regularization are usually exploited. Prominent examples are the non-singular theory obtained by spreading the Burgers vector isotropically about dislocation lines (Cai et al., 2006), and the stress field regularization obtained within a strain gradient elasticity framework (Lazar and Maugin, 2005). Plastic behavior then emerges when considering systems with many dislocations and proper statistical sampling (Devincere et al., 2008). Still, the accuracy and predictive power of these approaches depend on how well dislocations are modeled as isolated objects. In this context, mesoscale theories that require a limited set of phenomenological inputs are instrumental in connecting macroscopic plastic behavior to microscopic features of crystalline materials.

The Phase Field Crystal (PFC) model is an alternative framework to describe the nonequilibrium evolution of defected materials at the mesoscale (Elder et al., 2002; Emmerich et al., 2012; Momeni et al., 2018). Within the phase field description, complex processes such as dislocation nucleation (Skogvoll et al., 2021b), dislocation dissociation and stacking fault formation (Mianroodi and Svendsen, 2015), creep (Berry et al., 2015), fracture (Liu et al., 2020), and boundary driven grain motion (Provatas et al., 2007; Wu and Voorhees, 2012; Yamanaka et al., 2017; Salvalaglio et al., 2018) have been studied. The phase field allows a short scale regularization of defect core divergences inherent in classical elasticity, while allowing for the treatment of defect topology, grain boundary structures, and associated mobilities. For static studies, the only constitutive input required is the (defect free) equilibrium free energy, functional of the phase field, which has a minimizer that corresponds to a spatially periodic configuration. For time dependent problems, the phase field is generally assumed to obey a gradient flow that minimizes the free energy functional. When topological defects are present in the phase field configuration, their motion directly follows from the gradient flow, without any additional specification of slip systems, stacking fault energies, and line or boundary mobilities. The PFC model thus begins with the definition of a scalar order parameter (or phase field)  $\psi(\mathbf{r}, t)$ , function of space and time, so that its equilibrium configuration corresponds to a perfectly periodic, undistorted, configuration. A non-convex free energy functional  $F[\psi]$  of the field and its gradients is chosen so that its minimizer has the same spatial symmetry as the lattice of interest (Elder et al., 2010). The requisite free energies have been derived by using the methods of density functional theory (Elder et al., 2007; Huang et al., 2010; Archer et al., 2019), although our calculations below will rely on modified forms of the classical Brazovskii functional description of modulated phases (Brazovskii, 1975), also known as the Swift–Hohenberg model in the convection literature (Swift and Hohenberg, 1977).

Despite the model’s successes to date, a clear connection with classical theory of dislocation motion in crystalline solids is lacking. At its most basic level, the phase field does not carry mass, and hence momentum. Therefore the only stresses (momentum current) that appear in the theory are the reversible contributions that arise from variations of the free energy with respect to distortions of the phase field (Skaugen et al., 2018a). Neither momentum currents that arise in a material due to Galilean invariance, nor dissipative currents that would couple directly to the material distortion are present (Forster, 1975). Unlike classical theories of dislocation motion, the primary object of the model is the phase field, from which other quantities are derived. For an appropriate choice of the free energy functional, the phase field minimizer is a “crystalline” phase in that translational symmetry is broken. As is conventionally the case, the minimizer admits an expansion in a reciprocal space basis set. This expansion is further restricted to include only those wave vector modes in reciprocal space that are critical at onset of the broken symmetry phase. Configurational distortions of the phase field appear as slow (in space and time) modulations of the complex amplitudes of the expansion. A displacement vector is defined from the phase of the modulation. Configurational topological defects are possible and appear as (combinations of) zeros of the complex amplitudes, points at which the phases of the modulation are singular. The corresponding defect current, however, is solely related to the phase field, and to the equation governing its temporal evolution. This is in contrast with more general dislocation density currents in solid mechanics which also include dissipative contributions. An attempt to bridge the PFC description and a field theory of dislocation *mechanics* has been given in Ref. Acharya and Viñals (2020), where an extended free energy is introduced, which includes a material elastic contribution and the coupling between the two.

Since the theory lacks a proper description of momentum conservation, it also cannot describe the relaxation of elastic excitations. The first attempt at extending the PFC model to include elastic interactions considered a phenomenological second order temporal derivative in the equation of motion for the phase field (Stefanovic et al., 2006), which allowed for fast relaxation of short-wavelength elastic disturbances. Later efforts have included coupling the PFC phase field to a velocity field (Ramos et al., 2010), or various methods of coarse graining it to develop a consistent hydrodynamical description (Tóth et al., 2013; Heinonen et al., 2016). Such approaches are necessary for a proper description of processes where elastic interactions are important, such as crack propagation and defect dynamics. Other efforts have been made to develop efficient modeling approaches in which the time scale of elastic interactions is *a priori* set to zero  $\tau_E = 0$ , i.e. when mechanical equilibrium is obeyed at all times. The latter approach is justified when deformations are slow, including many of the applications mentioned such as creep and boundary driven grain motion. This approach was first introduced in Ref. Heinonen et al. (2014) which involved relaxing elastic excitations separately and instantaneously within the amplitude equation formulation of the PFC model (Goldenfeld et al., 2005). The same strategy was later developed for the PFC model in two dimensional isotropic 2D lattices by adding to the phase-field a correction at each time step that ensured instantaneous mechanical equilibrium (Skaugen et al., 2018b; Salvalaglio et al., 2020). In this paper, we present a generalization of this approach to anisotropic crystals in three dimensions (PFC-MEq). Since a distorted phase field configuration determines the corresponding configurational stresses (Skaugen et al., 2018a; Skogvoll et al., 2021a), the method yields regularized stress profiles for dislocation lines in three dimensions down to the defect core. In the case of a point defect, it was shown in Ref. Salvalaglio et al. (2020) that the stress field at the core agrees with the predictions of the non-singular theory of Ref. Cai et al. (2006), and with gradient elasticity models (Lazar and Maugin, 2005; Lazar, 2017), indicating that the results obtained here can serve as benchmarks for similar theories in three dimensions. The specific example of a dislocation loop in a bcc lattice is considered, and the far-field stresses given by the  $\psi$  field are shown to coincide with predictions by continuum elasticity.

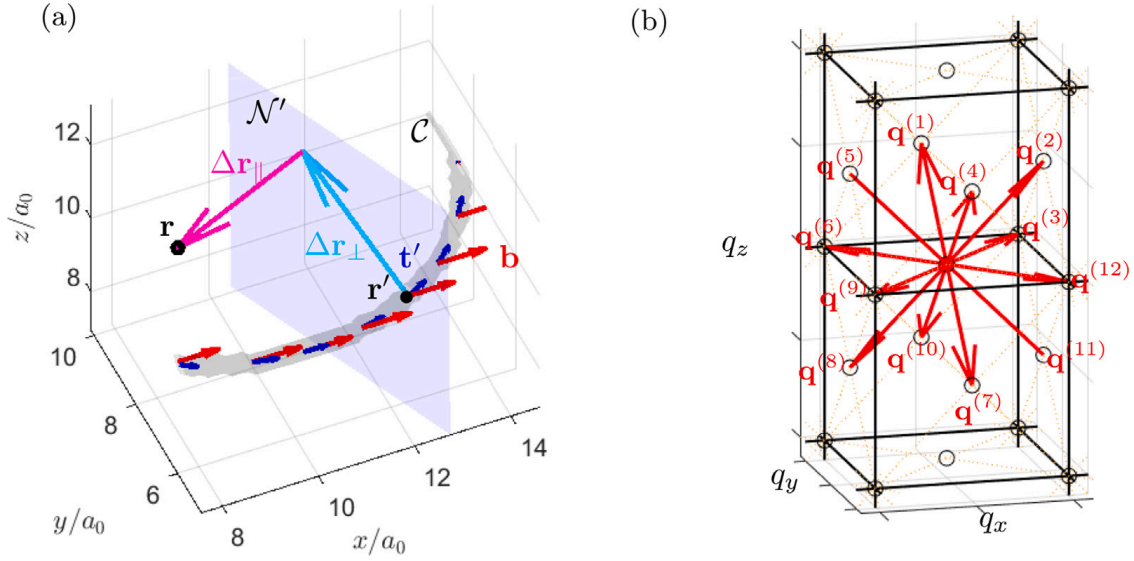


Fig. 1. (a) A dislocation line  $C$  consisting of points  $\mathbf{r}'$  characterized by the tangent vector  $\mathbf{t}'$  and the Burgers vector  $\mathbf{b}$  at that point. The difference  $\mathbf{r} - \mathbf{r}'$  from a point  $\mathbf{r}$  to a point  $\mathbf{r}'$  on the line can be decomposed into a 2D in-plane vector  $\Delta\mathbf{r}_\perp$ , which is the projection of  $\mathbf{r} - \mathbf{r}'$  onto the plane  $\mathcal{N}'$  normal to  $\mathbf{t}'$  and a distance  $|\Delta\mathbf{r}_\parallel|$  from this plane. In this figure,  $\Delta\mathbf{r}_\parallel \cdot \mathbf{t}' = -3.47a_0$  and  $|\Delta\mathbf{r}_\perp| = 3.42a_0$ . (b) The  $N = 12$  primary reciprocal lattice vectors  $\{\mathbf{q}^{(n)}\}_{n=1}^{12}$  of length  $q_0$  of a bcc lattice (Eq. (20)). Higher modes (dots) correspond to higher harmonics  $\{\mathbf{p}_n\}_{n>N}$  in the expansion of the equilibrium phase-field configuration  $\psi^{eq}$ , Eq. (3).

The rest of the paper is structured as follows. In Section 2, we introduce the theoretical method used to define topological defects from a periodic  $\psi$ -field. This allows us to define a dislocation density tensor in terms of the phase field (Eq. (12)), and obtain the dislocation line velocity (Eq. (16)). These are key results, which are applied in several examples in Section 3. First, we use the PFC model to numerically study the shrinkage of a dislocation loop in a bcc lattice. Then, we show analytically that Eq. (16) captures the motion of dislocations driven by a Peach–Koehler type force, and hence by a local stress. Finally, we introduce the PFC-MEq model, and compare the shrinkage of the dislocation loop under PFC and PFC-MEq dynamics. While the results are qualitatively similar for the case of a shear dislocation loop, the constraint of mechanical equilibrium causes the shrinkage to happen much faster. We finally confirm that the stress field derived from the  $\psi$  field in the PFC-MEq model agrees with that which would follow from continuum elasticity theory, with the same singular dislocation density as source, and with no adjustable parameters.

## 2. Kinematics of a dislocation line in three dimensions

Dislocations in 3D crystals are line defects, where each point  $\mathbf{r}'$  on the line  $C$  is characterized by the tangent vector  $\mathbf{t}'$  at that point and a Burgers vector  $\mathbf{b}$ , see Fig. 1(a). By introducing a local Cartesian plane  $\mathcal{N}'$  normal to  $\mathbf{t}'$ , the distance of an arbitrary point  $\mathbf{r}$  to a point  $\mathbf{r}'$  on  $C$  can be decomposed into an in-plane vector  $\Delta\mathbf{r}_\perp \perp \mathbf{t}'$  and a vector  $\Delta\mathbf{r}_\parallel \parallel \mathbf{t}'$ , i.e.  $\mathbf{r} - \mathbf{r}' = \Delta\mathbf{r}_\perp + \Delta\mathbf{r}_\parallel$ . A deformed state can be described by a displacement field  $\mathbf{u}$  and, in the presence of a dislocation,  $\mathbf{u}$  is discontinuous across a surface (branch cut) spanned by the dislocation, given by

$$\oint_{\Gamma'} d\mathbf{u} = \mathbf{u}^+ - \mathbf{u}^- = -\mathbf{b}, \quad (1)$$

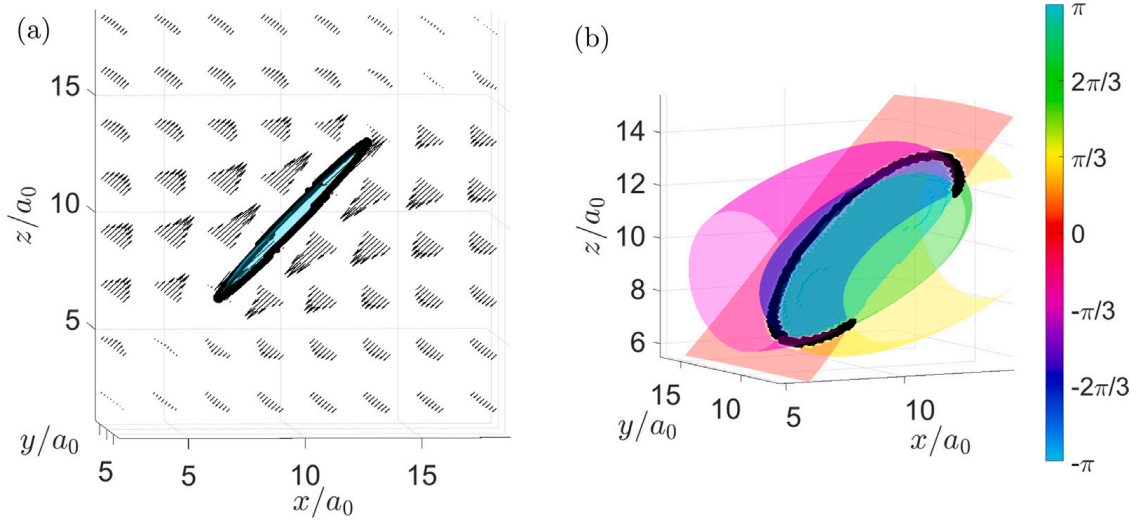
where  $\mathbf{u}^+$  and  $\mathbf{u}^-$  are the values of the displacement field at each side of the branch cut, respectively. We use the negative sign convention relating the contour integral with the Burgers vector. Here,  $\Gamma'$  is a small circuit enclosing the dislocation line in the  $\mathcal{N}'$ -plane, directed according to the right-hand rule with respect to  $\mathbf{t}'$ . The dislocation density tensor associated with the line is (Lazar, 2014)

$$\alpha = \delta^{(2)}(C) \otimes \mathbf{b} = \left( \int_C d\mathbf{l}' \delta^{(3)}(\mathbf{r} - \mathbf{r}') \right) \otimes \mathbf{b} \quad \left( \alpha_{ij}(\mathbf{r}) = b_j \delta_i^{(2)}(C) = b_j \int_C d\mathbf{l}'_i \delta^{(3)}(\mathbf{r} - \mathbf{r}') \right), \quad (2)$$

where  $b_j$  is the  $j$  component of the Burgers vector of the line, and  $d\mathbf{l}'_i = \mathbf{t}'_i d\mathbf{l}'$  is the line element in the direction of the line.  $\delta_i^{(2)}(C)$  is a short-hand notation for the delta function, with dimension of inverse area, locating the position of the dislocation line for each component  $i$  of the dislocation density tensor. It is defined by the line integral over the dislocation line of the full delta function (which scales as inverse volume). The dislocation density tensor is defined so that  $\int_{\mathcal{N}'} d^2r_\perp \alpha_{ij} \mathbf{t}'_i = b_j$ , where we are using the Einstein summation convention over repeated indices.

In the PFC models, a crystal state is represented by a periodic phase field  $\psi(\mathbf{r})$  of a given crystal symmetry. A reference crystalline lattice,

$$\psi^{eq}(\mathbf{r}) = \bar{\psi} + \sum_{n=1}^N \eta_n e^{i\mathbf{q}^{(n)} \cdot \mathbf{r}} + \sum_{n>N} \eta_n e^{i\mathbf{p}^{(n)} \cdot \mathbf{r}}, \quad (3)$$



**Fig. 2.** (a) Example of a discontinuous displacement field  $\mathbf{u}$  in the presence of a dislocation loop (black line) with Burgers vector  $\mathbf{b}$  (Eq. (1)). (b) Isosurfaces of one of the phases  $\theta_n$  possessing the same discontinuity as the displacement field (Eq. (5)).

is defined by a set of  $N$  primary (smallest) reciprocal lattice vectors  $\{\mathbf{q}^{(n)}\}_{n=1}^N$  of length  $q_0$ , and higher harmonics  $\{\mathbf{p}_n\}_{n>N}$ , also on the reciprocal lattice but with  $|\mathbf{p}_n| > q_0$  (see, e.g.,  $\{\mathbf{q}^{(n)}\}$  with  $|\mathbf{q}^{(n)}| = q_0$  for a bcc lattice in Fig. 1(b)). The lattice constant of the crystal is then given by  $a_0 \sim 2\pi/q_0$ . This represents a perfect crystal configuration in the absence of defects and distortion, where the average value  $\bar{\psi}$  and the amplitudes  $\eta_n$  are constants. In the phase-field crystal theory presented in Refs. Elder et al. (2002) and Elder and Grant (2004), near the solid–liquid transition point, only the terms from the primary reciprocal lattice vectors contribute to  $\psi^{eq}$ , while in general for more sharply peaked density profiles, there are also contributions from the higher order harmonics  $\{\mathbf{p}_n\}_{n>N}$ . For a distorted crystal lattice, the mode amplitudes  $\eta_n$  become complex scalar fields, henceforth named *complex amplitudes*  $\eta_n(\mathbf{r})$ , such that

$$\psi(\mathbf{r}) \approx \bar{\psi}(\mathbf{r}) + \sum_{n=1}^N \eta_n(\mathbf{r}) e^{i\mathbf{q}^{(n)} \cdot \mathbf{r}} + \sum_{n>N} \eta_n(\mathbf{r}) e^{i\mathbf{p}^{(n)} \cdot \mathbf{r}}. \quad (4)$$

In this section, we provide an accurate description of dislocation lines as topological defects in the phase of the complex amplitudes  $\eta_n(\mathbf{r})$ . We generalize the method of tracking topological defects as zeros of a complex order parameter as introduced in Refs. Halperin (1981) and Mazenko (1997), and apply it to accurately derive the kinematics of dislocation lines.

Given a phase field configuration  $\psi(\mathbf{r})$ , the complex amplitudes can be found by a demodulation as described in Appendix A.1. Decomposing each amplitude  $\eta_n(\mathbf{r}) = \rho_n(\mathbf{r}) e^{i\theta_n(\mathbf{r})}$ , into its modulus  $\rho_n(\mathbf{r})$  and phase  $\theta_n(\mathbf{r})$ , we have that for a perfect lattice,  $\theta_n^{(0)} = 0$  and  $\rho_n$  is constant. Displacing a lattice plane by a slowly varying  $\mathbf{u}$  transforms the phase as  $\theta_n \rightarrow \theta_n^{(0)} - \mathbf{q}^{(n)} \cdot \mathbf{u}$ . Thus, the phase provides a direct measure of the displacement field  $\mathbf{u}(\mathbf{r})$  relative to the reference lattice, i.e.,

$$\theta_n(\mathbf{r}) = -\mathbf{q}^{(n)} \cdot \mathbf{u}(\mathbf{r}) \quad \left( \theta_n(\mathbf{r}) = -q_i^{(n)} u_i(\mathbf{r}) \right), \quad (5)$$

where  $q_i^{(n)}$  denotes the  $i$ th Cartesian coordinate of  $\mathbf{q}^{(n)}$ . It is possible to invert Eq. (5), and solve for the displacement field  $\mathbf{u}$  as function of the phases  $\theta_n$  and reciprocal vectors. We use the following identity which is valid for lattices with cubic symmetry, where all primary reciprocal lattice vectors have the same length  $q_0$  (see Appendix B)

$$\sum_{n=1}^N \mathbf{q}^{(n)} \otimes \mathbf{q}^{(n)} = \frac{Nq_0^2}{3} \mathbb{1} \quad \left( \sum_{n=1}^N q_i^{(n)} q_j^{(n)} = \frac{Nq_0^2}{3} \delta_{ij} \right), \quad (6)$$

so that the displacement  $\mathbf{u}$  is given by

$$\mathbf{u}(\mathbf{r}) = -\frac{3}{Nq_0^2} \sum_{n=1}^N \mathbf{q}^{(n)} \theta_n(\mathbf{r}). \quad (7)$$

Eq. (7) shows that a dislocation line, which introduces a discontinuity in the displacement field, leads to a discontinuity in the phases  $\theta_n(\mathbf{r})$ . This is the first key insight, which we illustrate in Fig. 2. By using Eq. (5) and the fact that the Burgers vector  $\mathbf{b}$  is constant along the dislocation line, we relate the Burgers vector to the phase  $\theta_n$  as

$$\oint_{\Gamma'} d\theta_n = - \oint_{\Gamma'} \mathbf{q}^{(n)} \cdot d\mathbf{u} = \mathbf{q}^{(n)} \cdot \mathbf{b} \equiv 2\pi s_n, \quad (8)$$

where  $s_n$  is the (integer) winding number of the phase  $\theta_n$  around the dislocation line. That  $s_n$  is an integer follows from the fact that while  $\theta_n(\mathbf{r})$  may have a discontinuity across the branch cut, the complex amplitude  $\eta_n(\mathbf{r})$  is well-defined and continuous everywhere.



Therefore the circulation of the phase must be an integer multiple of  $2\pi$ . By the same reasoning, for an amplitude for which  $\mathbf{q}^{(n)} \cdot \mathbf{b} \neq 0$ , at the dislocation line, the phase  $\theta_n(\mathbf{r})$  is undefined (singular), so the modulus  $\rho_n(\mathbf{r})$  must go to zero for  $\eta_n(\mathbf{r})$  to remain continuous. This is the second key insight, which allows us to identify the location of the dislocation line with the zeros of the complex amplitudes  $\eta_n(\mathbf{r})$ .

The complex amplitude  $\eta_n(\mathbf{r})$  is isomorphic to a 2-component vector field  $\Psi(\mathbf{r}) \equiv (\Psi_1(\mathbf{r}), \Psi_2(\mathbf{r})) = (\Re(\eta_n(\mathbf{r})), \Im(\eta_n(\mathbf{r})))$ . The study of how to track zeros of any dimensional vector field in any dimensions was introduced in Ref. Halperin (1981). The orientation field  $\Psi(\mathbf{r})/|\Psi(\mathbf{r})|$  is continuous wherever  $|\Psi(\mathbf{r})| \neq 0$  and supports 1D topological defects in 3 dimensions which are located precisely where  $|\Psi(\mathbf{r})| = 0$ . The topological line density  $\rho_i$  of the line  $C$ , which satisfies  $\int d^2r_\perp \rho_i = s_n t'_i$ , is given by

$$\rho = s_n \delta^{(2)}(C) \quad \left( \rho_i = s_n \delta_i^{(2)}(C) \right). \quad (9)$$

Like  $\delta_i^{(2)}(C)$ , the dimension of  $\rho_i$  is that of a two-dimensional vector density. This topological charge density is expressed explicitly in terms of the real-valued positions  $C = \{\mathbf{r}'\}$  of the topological defect line. Since these positions coincide with the zero-line of the vector field  $\Psi(\mathbf{r})$ , it is possible to relate the expression to the delta-function locating the zeros of  $\Psi(\mathbf{r})$ , through the transformation law  $s_n \delta^{(2)}(C) = D_i(\mathbf{r}) \delta^{(2)}(\Psi(\mathbf{r}))$ , with the determinant vector field  $D_i(\mathbf{r}) = \epsilon_{ijk} (\partial_j \Psi_1(\mathbf{r})) (\partial_k \Psi_2(\mathbf{r}))$ . Comparing this to Eq. (2), using Eq. (8) and re-expressing  $D_i^{(n)}(\mathbf{r})$  (with the added superscript  $n$ ) in terms of the complex amplitude  $\eta_n(\mathbf{r})$ , we end up with the central equation for tracking the evolution of the dislocation density

$$\frac{1}{2\pi} \mathbf{q}^{(n)} \cdot \alpha(\mathbf{r}) = \delta^{(2)}(\eta_n(\mathbf{r})) \mathbf{D}^{(n)}(\mathbf{r}) \quad \left( \frac{1}{2\pi} q_k^{(n)} \alpha_{ik}(\mathbf{r}) = \delta^{(2)}(\eta_n(\mathbf{r})) D_i^{(n)}(\mathbf{r}) \right), \quad (10)$$

where  $\delta^{(2)}(\eta_n) = \delta(\Re(\eta_n)) \delta(\Im(\eta_n))$  and

$$\mathbf{D}^{(n)}(\mathbf{r}) = \nabla \Re(\eta_n(\mathbf{r})) \times \nabla \Im(\eta_n(\mathbf{r})) \quad \left( D_i^{(n)}(\mathbf{r}) = \epsilon_{ijk} (\partial_j \Re(\eta_n(\mathbf{r}))) (\partial_k \Im(\eta_n(\mathbf{r}))) \right). \quad (11)$$

In the following, for ease of notation, we suppress the explicit positional dependence of  $\alpha_{ij}$ ,  $D_i^{(n)}$  and  $\eta_n$ . The dislocation line is located at  $\eta_n = 0$ , which is the intersection of the surfaces  $\Re(\eta_n) = 0$  and  $\Im(\eta_n) = 0$ . As we see from its definition,  $\mathbf{D}^{(n)}$  is perpendicular to both these surfaces and is thus directed along the tangent to the line. We can reconstruct the dislocation density tensor from an appropriate summation over the modes with singular phases, namely by multiplying Eq. (10) by  $q_j^{(n)}$ , summing over the reciprocal modes and using Eq. (6) to arrive at

$$\alpha = \frac{6\pi}{N q_0^2} \sum_{n=1}^N \delta^{(2)}(\eta_n) \mathbf{D}^{(n)} \otimes \mathbf{q}^{(n)} \quad \left( \alpha_{ij} = \frac{6\pi}{N q_0^2} \sum_{n=1}^N \delta^{(2)}(\eta_n) D_i^{(n)} q_j^{(n)} \right). \quad (12)$$

Having a closed form of the dislocation density in terms of the complex amplitudes  $\eta_n$ , we now turn to deriving a closed form expression for its kinematic in terms of the time evolution of  $\eta_n$ . Taking the time derivative of Eq. (2), we show in Appendix C.1 that for a dislocation density tensor described by a single loop or string, we have  $\partial_t \alpha_{ij} = -\epsilon_{ikl} \partial_k J_{lj}^{(\alpha)}$ , where

$$\mathcal{J}^{(\alpha)} = \alpha \times \mathbf{V} \quad \left( J_{ij}^{(\alpha)} = \epsilon_{lmn} \alpha_{mj} V_n \right), \quad (13)$$

and  $\mathbf{V}$  is a vector field defined on the string by the velocity of the line segment perpendicular to the tangent vector. Taking the time derivative of Eq. (12), we show in Appendix C.2 that we get  $\partial_t \alpha_{ij} = -\epsilon_{ikl} \partial_k J_{lj}$ , where

$$\mathcal{J} = \frac{6\pi}{N q_0^2} \sum_{n=1}^N \delta^{(2)}(\eta_n) \mathbf{J}^{(n)} \otimes \mathbf{q}^{(n)} \quad \left( J_{ij} = \frac{6\pi}{N q_0^2} \sum_{n=1}^N \delta^{(2)}(\eta_n) J_i^{(n)} q_j^{(n)} \right), \quad (14)$$

and  $J_i^{(n)} = (\partial_t \Re(\eta_n)) \partial_t \Im(\eta_n) - (\partial_t \Im(\eta_n)) \partial_t \Re(\eta_n) = \Im(\partial_t \eta_n \partial_t \eta_n^*)$ . Note that  $J_{ij}$  depends on  $\partial_t \eta_n$ , and hence on the law governing the temporal evolution of the phase field.  $J_{ij}^{(\alpha)}$  is the well-known expression in terms of the dislocation velocity and  $J_{ij}$  is what we predict from the evolution of the phase field crystal density  $\psi$ . Under the assumption that both currents are equal, we show in the following that we are able to determine the dislocation velocity directly from the evolution of the phase field  $\psi$  at the dislocation core. We have checked numerically that the dislocation velocity predicted with this assumption is in excellent agreement with the one computed by tracking the position of the dislocation line at successive time steps.

By contracting Eq. (10) with  $D_i^{(n)}$ , we can express the delta-function in terms of the dislocation density tensor  $\delta^{(2)}(\eta_n) = \alpha_{ik} D_i^{(n)} q_k^{(n)} / (2\pi |\mathbf{D}^{(n)}|^2)$ , which we can insert into Eq. (14). Then, by equating  $J_{ij}$  and  $J_{ij}^{(\alpha)}$  at a point  $\mathbf{r}'$  on the dislocation line, where  $\alpha_{ik} = t'_i b_k \delta^{(2)}(\Delta \mathbf{r}_\perp)$ , we get after contracting with  $\mathbf{b}$  and integrating the delta-functions in  $\mathcal{N}'$  (details in Appendix D)

$$\frac{12\pi^2}{N q_0^2 |\mathbf{b}|^2} \sum_{n=1}^N s_n^2 \left( \frac{\mathbf{t}' \cdot \mathbf{D}^{(n)}}{|\mathbf{D}^{(n)}|^2} \right) \mathbf{J}^{(n)} = \mathbf{t}' \times \mathbf{v}' \quad \left( \frac{12\pi^2}{N q_0^2 |\mathbf{b}|^2} \sum_{n=1}^N s_n^2 \frac{t'_i D_i^{(n)}}{|\mathbf{D}^{(n)}|^2} J_l^{(n)} = \epsilon_{lmn} t'_m v'_n \right), \quad (15)$$

where  $\mathbf{v}'$  is the velocity of the dislocation node at  $\mathbf{r}'$ . Since  $\mathbf{t}' \perp \mathbf{v}'$ , we can easily invert this relation to find  $\mathbf{v}'$ , and using that  $\mathbf{D}^{(n)} \parallel \mathbf{t}'$  gives

$$\mathbf{v}' = \frac{12\pi^2}{N q_0^2 |\mathbf{b}|^2} \sum_{n=1}^N s_n^2 \frac{\mathbf{J}^{(n)} \times \mathbf{D}^{(n)}}{|\mathbf{D}^{(n)}|^2} \quad \left( v'_s = \frac{12\pi^2}{N q_0^2 |\mathbf{b}|^2} \sum_{n=1}^N s_n^2 \frac{\epsilon_{slr} J_l^{(n)} D_r^{(n)}}{|\mathbf{D}^{(n)}|^2} \right). \quad (16)$$

Eqs. (12) and (16) are the key results of this paper. Eq. (12) defines the dislocation density tensor from the demodulated amplitudes  $\eta_n$  of the phase field, while Eq. (16) gives an explicit expression for the dislocation line velocity. Both equations bridge the continuum description of the dislocation density and velocity with the microscopic scale of the phase field.

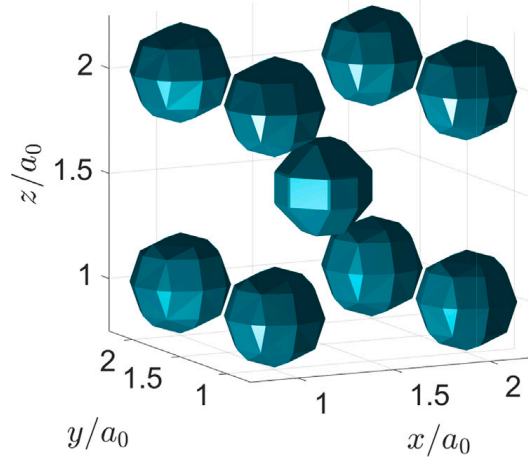


Fig. 3. A bcc unit cell in the PFC model shown by isosurfaces of constant  $\psi$ . Using the model parameters given in Appendix A,  $\psi(\mathbf{r})$  varies between peaks of  $\psi = 0.7447$  and troughs of  $\psi = -0.6148$  with the isosurfaces drawn at  $\psi = 0.0694$ .

### 3. Dislocation motion in a bcc lattice

We apply here the framework developed in Section 2 to a phase field crystal model of dislocation motion in a bcc lattice (Elder et al., 2002; Elder and Grant, 2004; Emmerich et al., 2012). The free energy  $F_\psi$  is a functional of the phase field  $\psi$  over the domain  $\Omega$ , given by

$$F_\psi = \int_{\Omega} \left[ \frac{\Delta B_0}{2} \psi^2 + \frac{B_0^x}{2} \psi \mathcal{L}^2 \psi - \frac{T}{3} \psi^3 + \frac{V}{4} \psi^4 \right] d\mathbf{r}, \quad (17)$$

where  $\mathcal{L} = q_0^2 + \nabla^2$ , and  $\Delta B_0$ ,  $B_0^x$ ,  $V$ , and  $T$  are constant parameters (Elder et al., 2007). The dissipative relaxation of  $\psi$  reads as

$$\frac{\partial \psi}{\partial t} = \Gamma \nabla^2 \frac{\delta F_\psi}{\delta \psi}. \quad (18)$$

with constant mobility  $\Gamma$ . We will refer to Eq. (18) as the ‘‘classical’’ PFC dynamics. As a characteristic unit of time given these model parameters, we use  $\tau = (\Gamma B_0^x q_0^6)^{-1}$ . For appropriate parameter values, the ground state of this energy is a bcc lattice which is well described in the one mode approximation

$$\psi(\mathbf{r}) = \psi_0 + \sum_{n=1}^{12} \eta_0 e^{i\mathbf{q}^{(n)} \cdot \mathbf{r}}, \quad (19)$$

where  $\psi_0$  is the average density,  $\eta_0$  is the equilibrium amplitude found by minimizing the free energy (Eq. (17)) with this ansatz for  $\psi(\mathbf{r})$ , and  $\{\mathbf{q}_n\}$  are the  $N = 12$  smallest reciprocal lattice vectors

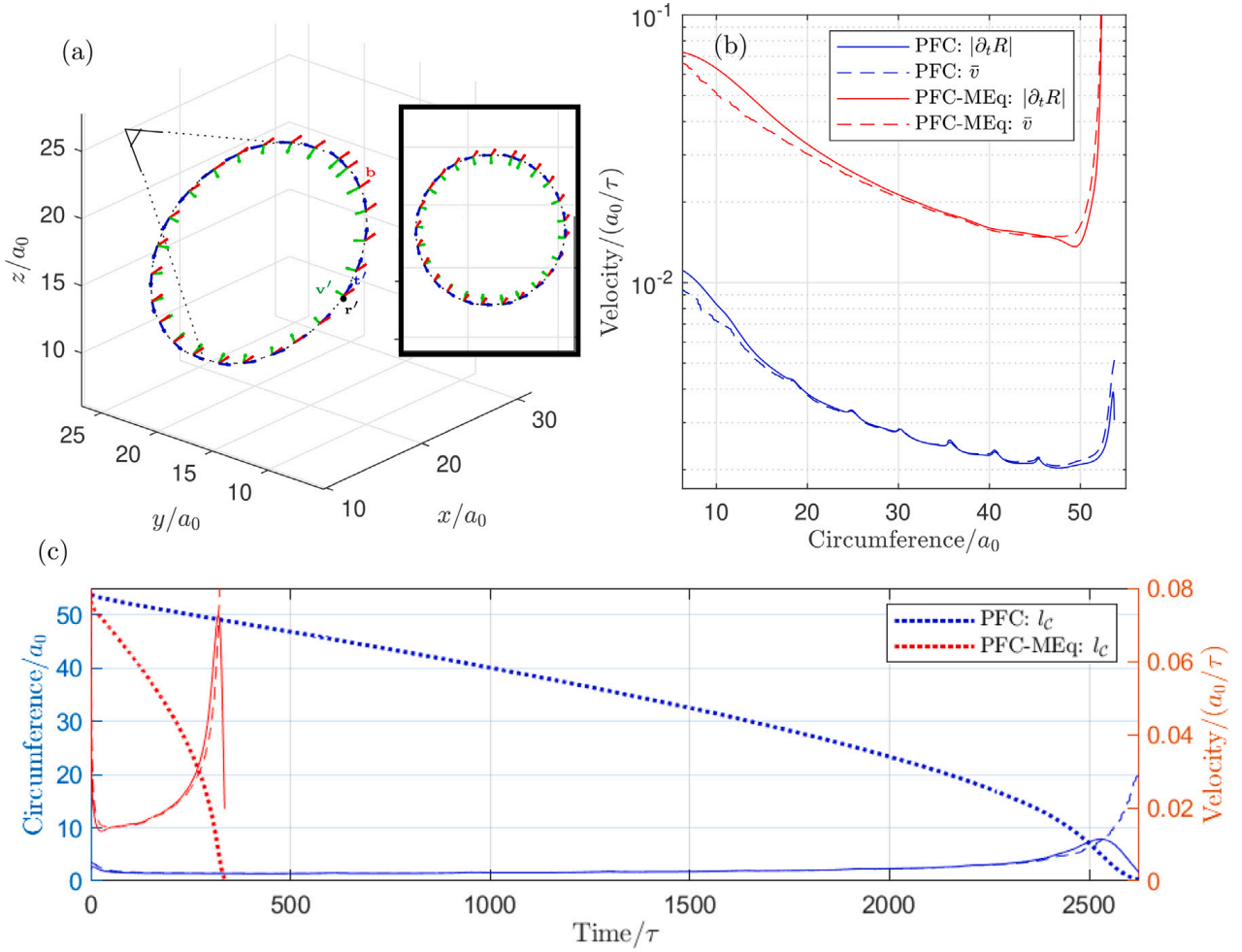
$$\begin{aligned} \mathbf{q}^{(1)} &= q_0(0, 1, 1)/\sqrt{2}, & \mathbf{q}^{(4)} &= q_0(0, -1, 1)/\sqrt{2}, \\ \mathbf{q}^{(2)} &= q_0(1, 0, 1)/\sqrt{2}, & \mathbf{q}^{(5)} &= q_0(-1, 0, 1)/\sqrt{2}, \\ \mathbf{q}^{(3)} &= q_0(1, 1, 0)/\sqrt{2}, & \mathbf{q}^{(6)} &= q_0(-1, 1, 0)/\sqrt{2}, \end{aligned} \quad (20)$$

with  $\mathbf{q}^{(n)} = -\mathbf{q}^{(n-6)}$  for  $n = 7, \dots, 12$ , see Fig. 1(b). Fig. 3 shows one bcc unit cell of a phase-field initialized in the one-mode approximation. Given the equilibrium configuration, the lattice constant  $a_0$  will be used as the characteristic unit of length and the shear modulus  $\mu$  calculated from the phase-field will serve as the characteristic unit of stress (Skogvoll et al., 2021a). As we see, the functional form of the free energy determines the base vectors  $\mathbf{q}^{(n)}$ , and no further assumptions about slip systems or constitutive laws for dislocation velocity (or plastic strain rates) need to be introduced.

The model parameters ( $\Delta B_0$ ,  $B_0^x$ ,  $T$ ,  $V$ , and  $\Gamma$ ) and variables ( $F_\psi$ ,  $\psi$ ,  $\mathbf{r}$ , and  $t$ ) can be rescaled to a dimensionless form in which  $B_0^x = V = q_0 = \Gamma = 1$ , thus leaving only three tunable model parameters: the quenching depth  $\Delta B_0$ ,  $T$  and the average density  $\psi_0$  (due to the conserved nature of Eq. (18)). All simulations are performed in these dimensionless units as described in Appendix A.3.

#### 3.1. Numerical analysis: shrinkage of a dislocation loop

In order to have a lattice containing one dislocation loop as the initial condition, we consider first the demodulation of the  $\psi$  field in the one mode approximation. A dislocation loop is introduced into the perfect lattice by multiplying the equilibrium amplitudes by complex phases  $\eta_0 \rightarrow \eta_n(\mathbf{r})$  with the appropriate charges  $s_n$  (see Appendix A.4) and then reconstructing the phase field  $\psi$  through Eq. (19). We then integrate Eq. (18) forward in time as detailed in Appendix A.3. A fast relaxation follows from the initial configuration with the loop. This relaxation leads to the regularization of the singularity at the dislocation line ( $\eta_n \rightarrow 0$



**Fig. 4.** (a) The initial dislocation loop in a  $35 \times 35 \times 35$  bcc PFC lattice with periodic boundary conditions. The dislocation loop is on the slip system given by plane normal  $[-1, 0, 1]$  and slip direction (Burgers vector)  $\frac{a_0}{2}[1, -1, 1]$ . Inset: the dislocation viewed from the indicated angle. (b) Comparison of average point velocity  $\bar{v}$  (Eq. (22)) to the average loop radius shrinkage velocity  $|\partial_t R|$  (Eq. (21)) as functions of the loop circumference. PFC and PFC-MEq refer, respectively, to the classical PFC model, and the PFC model constrained to mechanical equilibrium as introduced in Section 3.3. (c) The circumference  $l_C$  of the dislocation loop. Superimposed on the right  $y$ -axis are the velocities of panel (b) as functions of time.

$s_n \neq 0$ ) as achieved in PFC approaches (Skaugen et al., 2018a; Salvalaglio et al., 2019, 2020). From then onward,  $\psi$  evolves in time leading to the motion of the dislocation line which may be analyzed by the methods outlined in Section 2, using the amplitudes  $\{\eta_n\}$  extracted from  $\psi$  extracted as detailed in Appendix A.1.

Numerically, we approximate the delta function in Eq. (12) as a sharply peaked 2D Gaussian distribution, i.e.,  $\delta^{(2)}(\eta_n) \simeq \exp(-\frac{|\eta_n|^2}{2\omega^2})/(2\pi\omega^2)$  with a standard deviation of  $\omega = \eta_0/10$ . Near the dislocation line, the dislocation density  $\alpha_{ij}$  thus takes the form of a sharply peaked function, which can be treated numerically. The decomposition of  $\alpha_{ij}$  into its outer product factors  $t_i^j$  and a Burgers vector density  $B_j = b_j \delta^{(2)}(\Delta \mathbf{r}_\perp)$  is done by singular value decomposition (see Appendix A.2), and the Burgers vector of the point is extracted by performing a local surface integral in  $\mathcal{N}'$ . We prepare a  $35 \times 35 \times 35$  unit cell 3D PFC lattice on periodic boundary conditions with a resolution of  $\Delta x = \Delta y = \Delta z = a_0/7$ . A dislocation loop is introduced as the initial condition in the slip system given by a plane normal  $[-1, 0, 1]$  with slip direction (Burgers vector)  $\frac{a_0}{2}[1, -1, 1]$ . Fig. 4(a) shows the initial dislocation density decomposed as described, where we also have calculated the velocity  $\mathbf{v}'$  at each point given by Eq (16).

In order to obtain the velocity of the dislocation loop segments, we identify  $M$  nodes on the loop and evaluate Eq. (16) by using numerical differentiation of the  $\psi$  field to calculate the amplitude currents  $J_l^{(m)}$ . To serve as a benchmark, we also calculate the circumference  $l_C$  of the dislocation loop  $C$  at each time (further details in Appendix A.5), so that we compare the rate of shrinkage  $|\partial_t R|$

$$|\partial_t R| = \frac{1}{2\pi} |\partial_t l_C|, \quad (21)$$

(solid blue line in Fig. 4(b)) to the average velocity of the  $M$  dislocation nodes

$$\bar{v} = \frac{1}{M} \sum_{m=1}^M |\mathbf{v}^{(m)}|, \quad (22)$$

(dashed blue line in Fig. 4(b)) where  $\mathbf{v}^{(m)}$  is the velocity of the dislocation line at node  $m$ , calculated by the velocity formula Eq. (16).  $|\partial_t R|$  and  $\bar{v}$  should agree in the case of the shrinking of a perfectly circular loop and the figure shows excellent agreement between the two. Interestingly, we observe that both are sensitive to the Peierls like barriers during their motion, as shown by the oscillations in Fig. 4(b). The maxima are separated by  $2\pi a_0$ , confirming that the oscillation is related to the motion of a loop segment over one lattice spacing  $a_0$  (Boyer and Viñals, 2002). This observation confirms that even though Eqs. (12) and (16) are continuum level descriptions of the system, they still exhibit behavior related to the underlying lattice configuration. The initial fast drop in velocity is due to the fast relaxation of the initial condition. The evolution of the variables under the dynamics of Eq. (18) are shown together with the evolution given by the PFC-MEQ model which will be introduced in Section 3.3.

### 3.2. Theoretical analysis: Peach Koehler law

In this section, we show that the general expression Eq. (16) of the defect velocity agrees with the dissipative motion of a dislocation as given by the classical Peach–Koehler force (Pismen, 1999; Kosevich, 1979). To calculate an analytical expression for the amplitude currents  $J_l$ , we employ the amplitude formulation of the PFC model, which directly expresses the free energy and dynamical equations in terms of the complex amplitudes  $\eta_n$  (Goldenfeld et al., 2005; Athreya et al., 2006; Salvalaglio and Elder, 2022). For our lattice symmetry, real valuedness of  $\psi$  requires that  $\eta_{n+6} = \eta_n^*$ , and the dynamical equations need only consider the amplitudes  $\{\eta_n\}_{n=1}^6$ . By substituting Eq. (19) in  $F_\psi$  and integrating over the unit cell, under the assumption of slowly-varying amplitudes, one obtains the following free energy as a function of the complex amplitudes,

$$F_\eta = \int_\Omega \left[ \frac{\Delta B_0}{2} \Phi + \frac{3V}{4} \Phi^2 + \sum_{n=1}^6 \left( B_0^x |\mathcal{G}_n \eta_n|^2 - \frac{3V}{2} |\eta_n|^4 \right) + f^s(\{\eta_n\}, \{\eta_n^*\}) \right] d\mathbf{r}, \quad (23)$$

where  $\mathcal{G}_n = \nabla^2 + 2i\mathbf{q}_n \cdot \nabla$  and  $\Phi = 2 \sum_{n=1}^6 |\eta_n|^2$ .  $f^s(\{\eta_n\}, \{\eta_n^*\})$  is a polynomial in  $\eta_n$  and  $\eta_n^*$  that depends in general on the specific crystalline symmetry under consideration (Goldenfeld et al., 2005; Elder et al., 2010; Salvalaglio and Elder, 2022) (here bcc, see Appendix E for its expression). Eq. (23) is obtained when considering a set of vectors  $\mathbf{q}$  of length  $q_0$ , while similar forms may be achieved when considering different length scales (Elder et al., 2010; Salvalaglio et al., 2021). The evolution of  $\eta_n$ , which follows from Eq. (18) is (Goldenfeld et al., 2005; Salvalaglio and Elder, 2022),

$$\frac{\partial \eta_n}{\partial t} = -\Gamma q_0^2 \frac{\delta F}{\delta \eta_n^*}, \quad (24)$$

with

$$\frac{\delta F}{\delta \eta_n^*} = [\Delta B_0 + B_0^x \mathcal{G}_n^2 + 3V (\Phi - |\eta_n|^2)] \eta_n + \frac{\partial f^s}{\partial \eta_n^*}, \quad (25)$$

where the last term comes from the nonlinear contributions  $\psi^3$  and  $\psi^4$  in the local free energy density, and depend on the other amplitudes  $\{\eta_m\}_{m \neq n}$ . However, for the amplitudes that go to zero at the defect, it can be shown that  $\frac{\partial f^s}{\partial \eta_n^*} = 0$  at the defect (for more details, see Appendix E). Thus, the evolution of  $\eta_n$  near the defect core is dictated solely by the non-local gradient term, namely

$$\partial_t \eta_n \approx -\Gamma B_0^x q_0^2 \mathcal{G}_n^2 \eta_n. \quad (26)$$

Furthermore, this implies that the complex amplitude  $\eta_n$  of a stationary defect satisfy  $\mathcal{G}_n^2 \eta_n^{(0)} = 0$  at the core. We now add an imposed, smooth displacement  $\tilde{\mathbf{u}}$  to the amplitudes as  $\eta_n = \eta_n^{(0)} e^{-i\mathbf{q}_n \cdot \tilde{\mathbf{u}}}$  to represent the far-field displacement induced by a different line segment, defect, or externally applied loads (Skaugen et al., 2018a). This displacement is in addition to the discontinuous displacement field  $\mathbf{u}$ , described in Section 2, which is captured by stationary solution  $\eta_n^{(0)}$  and defines the Burgers vector of the dislocation line (Fig. 2). Inserting this ansatz of the complex amplitudes into Eq. (11), and in the approximation of small distortions,  $|\nabla \tilde{\mathbf{u}}| \ll 1$ , we find

$$\mathbf{D}^{(n)} = \mathbf{D}^{(n),0} + \frac{1}{2} \nabla(\mathbf{q}^{(n)} \cdot \tilde{\mathbf{u}}) \times \nabla(|\eta_n^{(0)}|^2), \quad \left( D_i^{(n)}(\mathbf{r}) = D_i^{(n),0} + \frac{1}{2} \epsilon_{irs} q_m^{(n)} (\partial_r \tilde{u}_m) \partial_s (|\eta_n^{(0)}|^2) \right), \quad (27)$$

where  $D_i^{(n),0}$  is the determinant vector field calculated from  $\eta_n^{(0)}$ . The corresponding defect density current is

$$\mathbf{J}^{(n)} = 4\Gamma B_0^x q_0^2 \Im \left( i(\nabla \eta_n^{(0)*}) \otimes (\nabla + i\mathbf{q}^{(n)}) \mathcal{G}_n \eta_n^{(0)} \right) \cdot \nabla(\mathbf{q}^{(n)} \cdot \tilde{\mathbf{u}}) \quad \left( J_l^{(n)} = 4\Gamma B_0^x q_0^2 q_i^{(n)} (\partial_k \tilde{u}_i) \Im \left( i(\partial_l \eta_n^{(0)*}) (\partial_k + i q_k^{(n)}) \mathcal{G}_n \eta_n^{(0)} \right) \right). \quad (28)$$

Arguably, the simplest solution of Eq. (26) is the isotropic, simple vortex  $\eta_n^{(0')}$  which is linear with the distance from the core and  $s_n = \pm 1$ . At a node  $\mathbf{r}'$  on the dislocation line,  $\eta_n^{(0')}$  can be written in terms of the Cartesian coordinates  $x_\perp, y_\perp$  in the plane  $\mathcal{N}'$  (Section 2), where it takes the form  $\eta_n^{(0')} = \kappa(x_\perp + i s_n y_\perp)$ , with  $\kappa$  a proportionality constant. The gradients of  $\eta_n^{(0')}$  can be evaluated in these coordinates and gives at  $\mathbf{r}'$ ,  $\Im \left( i(\partial_l \eta_n^{(0')*}) (\partial_m \eta_n^{(0')}) \right) = \kappa^2 (\delta_{lm} - t'_l t'_m)$ , from which we get the current

$$\mathbf{J}^{(n)} = -8\kappa^2 \Gamma B_0^x q_0^2 (\mathbf{q}^{(n)} \cdot \nabla(\mathbf{q} \cdot \tilde{\mathbf{u}})) (\mathbb{1} - \mathbf{t}' \otimes \mathbf{t}') \cdot \mathbf{q}^{(n)} \quad \left( J_l^{(n)} = -8\kappa^2 \Gamma B_0^x q_0^2 q_i^{(n)} q_k^{(n)} q_m^{(n)} (\partial_k \tilde{u}_i) (\delta_{lm} - t'_l t'_m) \right) \quad (29)$$

in terms of the local tangent vector  $\mathbf{t}'$ . At  $\mathbf{r}'$ , we also get  $D_i^{(n)} = \kappa^2 s_n t'_i$ , which leads to an expression of the dislocation velocity (where the proportionality constant  $\kappa$  cancels out), given by

$$v'_s = -\epsilon_{srl} \frac{\Gamma \pi}{|\mathbf{b}|^2} b_j t'_r 4B_0^x \sum_{n=1}^{12} q_i^{(n)} q_j^{(n)} q_k^{(n)} q_l^{(n)} (\partial_k \tilde{u}_i) = \frac{\Gamma \pi}{\eta_0^2 |\mathbf{b}|^2} \epsilon_{srl} t'_r \tilde{\sigma}_{lj} b_j, \quad (30)$$



where  $\tilde{\sigma}_{ij}$  is the stress tensor for a bcc PFC that has been deformed by  $\tilde{\mathbf{u}}$  (Skogvoll et al., 2021a),

$$\tilde{\sigma}_{ij} = 4B_0^x \eta_0^2 \sum_{n=1}^{12} q_i^{(n)} q_j^{(n)} q_k^{(n)} q_l^{(n)} \partial_k \tilde{u}_l. \quad (31)$$

Thus, the velocity of the dislocation line is proportional to the stress on the line. In vectorial form, this equation reads

$$\mathbf{v} = M \mathbf{t} \times (\tilde{\boldsymbol{\sigma}} \cdot \mathbf{b}). \quad (32)$$

with isotropic mobility  $M = \Gamma \pi / (|\mathbf{b}|^2 \eta_0^2)$ .

A stationary dislocation induces a stress field  $\sigma_{ij}^{(0)}$ , but only the imposed stress  $\tilde{\sigma}_{ij}$  appears in the equation above. This is analogous to how the stress field of the dislocation itself is not included when the Peach–Koeher force as calculated (Kosevich, 1979). Thus, if  $\sigma_{ij}^\psi$  is the configurational stress of the phase field at any given time, the part responsible for dislocation motion is the imposed stress

$$\tilde{\sigma}_{ij} = \sigma_{ij}^\psi - \sigma_{ij}^{(0)}. \quad (33)$$

Note that the stationary solution necessarily satisfies mechanical equilibrium,  $\partial_j \sigma_{ij}^{(0)}$ , so that if the configurational PFC stress  $\sigma_{ij}^\psi$  is in mechanical equilibrium, so is the imposed stress  $\tilde{\sigma}_{ij}$  on the dislocation segment. The imposed stress used can be attributed to external load, other dislocations, or other parts of the dislocation loop. The framework predicts a defect mobility which is isotropic and does not discriminate between dislocation climb and glide motion. Numerically however, we have seen that at deeper quenches  $\Delta B_0$ , climb motion is prohibited in the PFC model. The result in this section should therefore be interpreted as a first-order approximation, valid at shallow quenches. This apparent equal mobility for glide and climb may result from the employment of the amplitude phase-field model (which is only exact for  $|\Delta B_0| \rightarrow 0$ ) or the assumption of an isotropic defect core in the calculation.

### 3.3. PFC dynamics constrained to mechanical equilibrium (PFC-MEq)

In the previous section, we found that the motion of a dislocation is governed by a configurational stress  $\sigma_{ij}^\psi$  which derives from the PFC free energy. Since this stress is a functional only of the phase field configuration, it does not satisfy, in general, the condition of mechanical equilibrium. Refs. Skaugen et al. (2018a) and Skogvoll et al. (2021a) give an explicit expression for this stress defined as the variation of the free energy with respect to distortion,

$$\sigma_{ij}^\psi = -2B_0^x \langle \mathcal{L} \psi \partial_{ij} \psi \rangle, \quad (34)$$

where  $\langle \cdot \rangle$  is a spatial average over  $1/q_0$  in order to eliminate the base periodicity of the phase field (see Appendix A.1).

In this section, we discuss a modification of the PFC in three dimensions and in an anisotropic lattice so as to maintain elastic equilibrium in the medium while  $\psi$  evolves according to Eq. (18). Let  $\psi^{(U)}$  be the field that results from the evolution defined by Eq. (18) alone. At each time, we define

$$\psi(\mathbf{r}) = \psi^{(U)}(\mathbf{r} - \mathbf{u}^\delta), \quad (35)$$

where  $\mathbf{u}^\delta$  is a small continuous displacement computed so that the configurational stress associated with  $\psi(\mathbf{r})$  is divergence free. We now show a method to determine  $\mathbf{u}^\delta$ . Suppose that at some time  $t$  the PFC configuration  $\psi$  has an associated configurational stress  $\sigma_{ij}^{\psi,U}$  (from Eq. (34), where  $\partial_j \sigma_{ij}^{\psi,U} \neq 0$ ). Within linear elasticity, the stress  $\sigma_{ij}^\psi$  after displacement of the current configuration by  $\mathbf{u}^\delta$  is given by

$$\sigma_{ij}^\psi = \sigma_{ij}^{\psi,U} + C_{ijkl} e_{kl}^\delta, \quad (36)$$

where  $C_{ijkl}$  is the elastic constant tensor, and  $e_{ij}^\delta = \frac{1}{2}(\partial_i u_j^\delta + \partial_j u_i^\delta)$ .  $\mathbf{u}^\delta$  is determined by requiring that

$$\partial_j \sigma_{ij}^\psi = \partial_j (\sigma_{ij}^{\psi,U} + C_{ijkl} e_{kl}^\delta) = 0. \quad (37)$$

By using the symmetry  $i \leftrightarrow j$  of the elastic constant tensor, we can rewrite this equation explicitly in terms of  $\mathbf{u}^\delta$ ,

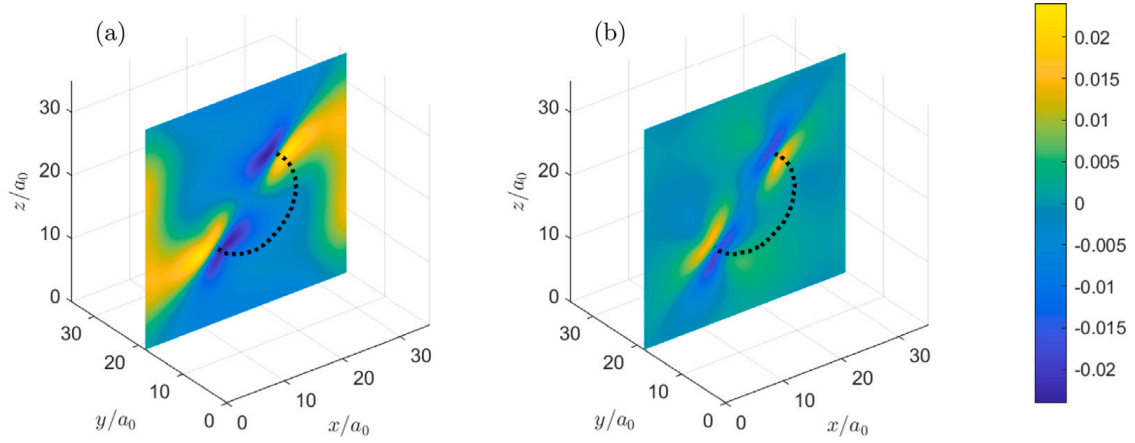
$$g_i^{\psi,U} + C_{ijkl} \partial_{jk} u_l^\delta = 0, \quad (38)$$

where

$$g_i^{\psi,U} = \partial_j \sigma_{ij}^{\psi,U} = \left\langle \frac{\delta F_\psi}{\delta \psi} \partial_i \psi - \partial_i f \right\rangle \quad (39)$$

is the body force from the stress (Skogvoll et al., 2021a). The quantity  $f$  is the free energy density from Eq. (17).

Given the periodic boundary conditions used, the system of Eqs. (38) is solved by using a Fourier decomposition with the Green's function for elastic displacement in cubic anisotropic materials (Dederichs and Leibfried, 1969). Once  $\mathbf{u}^\delta$  is obtained,  $\psi$  is updated according to Eq. (35), and evolved according to Eq. (18) from its current state  $\psi(t)$  to  $\psi^{(U)}(t + \Delta t)$ . Note that Eqs. (38) can, in general, be solved for any elastic constant tensor, so that the method introduced is not limited to cubic anisotropy. Since the state  $\psi^{(U)}$  can only be updated according to Eq. (35) every  $\Delta t$ , this effectively sets a time scale of elastic relaxation in the model. We found that



**Fig. 5.** In-plane sections ( $y = 17.5a_0$ ) of the configurational stress  $\sigma_{xz}^w/\mu$  for the dislocation loop after shrinking to 90% of its initial circumference under (a) PFC dynamics and (b) PFC-MEq dynamics. Because the latter evolves faster, the snapshots are taken at different times, namely  $t = 389.0\tau$  and  $t = 34.4\tau$ , respectively. A lot of residual (unrelaxed) stress is visible in the configurational stress for the classical PFC model.

the numerical discretization scheme for imposing mechanical equilibrium at every  $\Delta t$  has a slow convergence with decreasing time resolution. Thus, the rate of loop shrinkage also depends slightly on  $\Delta t$ . This is further discussed in Appendix A.

Fig. 4 contrasts numerical results for the evolution of an initial dislocation loop with and without using the method just described. The computed line velocities are very different as they are highly sensitive to the local stress experienced by the dislocation loop segments. This stems from the fact that under classical PFC dynamics, the stress is always given by  $\sigma_{ij}^{w,U}$ , and a consequence of the results from Section 3.2 is that the velocity of an element of the defect line will be quite different depending on whether the stress acting on it is  $\sigma_{ij}^{w,U}$  or  $\sigma_{ij}^w$ . Fig. 5 shows the dislocation loop after its circumference has shrunk to 90% of its initial value, and the resulting  $xz$  component of the stress for both models. As expected, the correction provided by the PFC-MEq model is necessary to relax the stress originating from the initial loop. The figure shows a large residual stress far from the dislocation loop that can only decay diffusively in the standard phase field model. Indeed, we have verified numerically that the configurational stress is only divergence-less for the PFC-MEq model. We note that in our set the loop is seeded in a glide plane, thus its shape remains approximately circular for both models, while the shrinkage rate is different. Note that with the addition of this advection step, the model is no longer guaranteed to be fully dissipative.

The problem addressed in this section involves finding the elastic distortion  $u_{kl}$  (which away from defects it can be written as  $u_{kl} = \partial_k u_l$  for a displacement field  $\mathbf{u}$ ) given the dislocation density tensor  $\alpha_{ij}$  as a state variable (Acharya et al., 2019). The first part is the incompatibility of the elastic distortion

$$\epsilon_{ilm} \partial_l u_{mk} = -\alpha_{ik}, \tag{40}$$

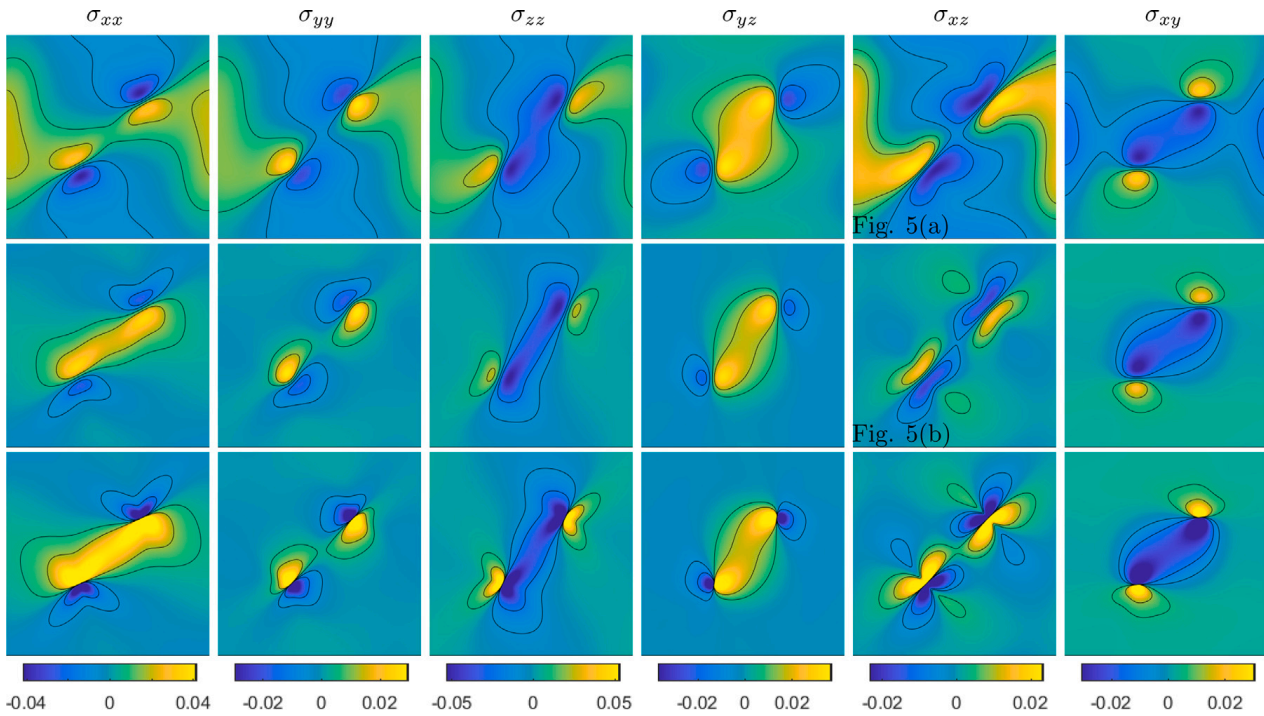
and the second is the mechanical equilibrium condition on  $u_{kl}$

$$\partial_j C_{ijkl}(u_{kl})_S = 0, \tag{41}$$

where  $C_{ijkl}$  is the tensor of elastic constants, and  $(S)$  denotes the symmetric part of the tensor. Eq. (40) has a non trivial kernel consisting of gradients of vector fields  $\nabla \mathbf{u}^\delta$ . This vector field is determined by Eq. (41) given appropriate boundary conditions that guarantee uniqueness. A computational method for solving for  $u_{kl}$  and  $\mathbf{u}^\delta$ , using the dislocation density as a state variable, was first given in Ref. Roy and Acharya (2005). The main difference between this reference and the method outlined in this section is that, since the incompatibility of the distortion is captured by the state of the phase field, we only need to solve for the compatible part of the distortion using the force density  $\mathbf{g}^w$  from the phase field as a source.

While the stress profile shown in Fig. 5(b), can be shown numerically to have vanishing divergence, we would like to see a direct comparison of the stress with the prediction from continuum elasticity. As the model purports to evolve the phase-field at mechanical equilibrium, and we are able to extract the dislocation density from the phase-field at any time through Eq. (12), this amounts to the problem of finding the stress tensor for a given dislocation density, under the constraint of mechanical equilibrium and with periodic boundary conditions (zero surface traction). This problem was addressed in Ref. Brenner et al. (2014), and in Appendix A.6, we show how we solve Eqs. (40)–(41) to derive the equilibrium stress field from  $\alpha_{ij}$  using spectral methods. Fig. 6 shows all the stress components after the dislocation loop has shrunk to 90% of its initial diameter for both dynamical models, as well as the stress  $\sigma^{(\alpha)}$  computed directly from the dislocation density tensor.<sup>1</sup> Note that the mean value of the components of  $\sigma_{ij}^{(\alpha)}$ , is not determined by Eqs. (40)–(41), and is set to zero. In this comparison, we have also subtracted from  $\sigma_{ij}^w$  its mean value. As

<sup>1</sup> Due to the geometric similarity in how the loop annihilates in the different models, there is no observable difference in the continuum elastic stress field predictions between using  $\alpha$  from either model as a source.



**Fig. 6.** In-plane sections ( $y = 17.5a_0$ ) of the stresses for the dislocation loop after it has shrunk to 90% of its initial circumference in (top row) the PFC model  $\sigma_{ij}^{\psi,U}$ , (middle row) the PFC-MEq model  $\sigma_{ij}^{\psi}$  and (bottom row) the prediction from continuum elasticity  $\sigma_{ij}^{(\alpha)}$  using the dislocation density extracted from the PFC as a source. The stresses predicted from continuum elasticity are singular, so the colorbar for each column is saturated at  $\pm \max(|\sigma_{ij}^{\psi,U}|)$  and contour lines are drawn at  $\pm 15\%, \pm 40\%$  of this value. For the comparison, we have subtracted from  $\sigma_{ij}^{\psi,U}$  and  $\sigma_{ij}^{\psi}$  their mean values (see text). The stresses are given in units of the shear modulus  $\mu$ .

expected, the stresses obtained from the PFC-MEq model agree well with  $\sigma_{ij}^{(\alpha)}$ . The small differences observed are due to the fact that the configurational stress determined by  $\psi$  is naturally regularized by the lattice spacing and the finite defect core, whereas the stress  $\sigma_{ij}^{(\alpha)}$  is for a continuum elastic medium with a singular dislocation source (numerically, the  $\delta$ -functions in Eq. (12) is regularized by an arbitrary width of the Gaussian approximation). Investigating exactly which length scale of core regularization derives from the PFC model is an open and interesting question that we will address in the future.

#### 4. Conclusions

We have introduced a theoretical method, and the associated numerical implementation, to study topological defect motion in a three dimensional, anisotropic, crystalline PFC lattice. The dislocation density tensor and velocity are directly defined by the spatially periodic phase field, where dislocations are identified with the zeros of its complex amplitudes.

To illustrate the method, we have studied the motion of a shear dislocation loop, and found that it accurately tracks the loop position, circumference, and velocity. As an application, we have shown that under certain simplifying assumptions, the overdamped dislocation velocity follows from the Peach–Koehler force, with the defect mobility determined by equilibrium lattice properties. We have introduced the PFC-MEq model for three dimensional anisotropic media which constrains the classical PFC model evolution to remain in mechanical equilibrium, and shown that loop motion is much faster with this modification. The PFC-MEq model produces stress profiles that are in agreement, especially far from the defect core, to stress fields directly computed from the instantaneous dislocation density tensor.

In summary, we have presented a comprehensive framework, based on the phase field crystal model for the analysis of dislocation motion in crystalline phases in three spatial dimensions. Starting from a free energy that has a ground state of the proper symmetry, the model naturally incorporates defects, the associated topological densities, and the resulting defect line kinematic laws that are compatible with topological density conservation. Configurational stresses induced by defects are defined and analyzed, and shown to lead to a Peach–Koehler type force on defects, with an explicit expression for the line segment mobility given.

#### CRediT authorship contribution statement

**Vidar Skogvoll:** Developed the theory, Performed the numerical simulations of Sec. 3, Derived the theoretical analysis of Sec. 3.2, Developed the theoretical framework of 3.3, Discussed the result, Contributed to the final manuscript. **Luiza Angheluta:** Conceived of the presented idea in Sec. 2, Derived the theoretical analysis of Sec. 3.2, Discussed the result, Contributed to the final manuscript. **Audun Skaugen:** Discussed the result, Contributed to the final manuscript. **Marco Salvalaglio:** Derived the theoretical analysis of Sec. 3.2, Discussed the result, Contributed to the final manuscript. **Jorge Viñals:** Conceived of the presented idea in Sec. 2, Discussed the result, Contributed to the final manuscript.

## Declaration of competing interest

The authors declare that they have no known competing financial interests or personal relationships that could have appeared to influence the work reported in this paper.

## Acknowledgments

V.S. and L.A. acknowledge support from the Research Council of Norway through the Center of Excellence funding scheme, Project No. 262644 (PoreLab). M.S. acknowledges support from the Emmy Noether Programme of the German Research Foundation (DFG) under Grant No. SA4032/2-1. The research of J.V. is supported by the National Science Foundation, USA, contract No. DMR-1838977.

## Appendix A. Numerical methods

### A.1. Amplitude demodulation

Given a phase-field configuration described by slowly varying amplitudes  $\eta_n(\mathbf{r})$

$$\psi(\mathbf{r}) = \bar{\psi}(\mathbf{r}) + \sum_{n'} \eta_{n'}(\mathbf{r}) e^{i\mathbf{q}^{(n')} \cdot \mathbf{r}}, \quad (\text{A.1})$$

we can find the amplitudes using the principle of resonance under coarse graining. Coarse graining  $\tilde{X}$  with respect to a length scale  $a_0$  is introduced as a convolution with a Gaussian filter function

$$\langle \tilde{X} \rangle(\mathbf{r}) = \int d\mathbf{r}' \frac{\tilde{X}(\mathbf{r}')}{(2\pi a_0^2)^{d/2}} \exp\left(-\frac{(\mathbf{r} - \mathbf{r}')^2}{2a_0^2}\right). \quad (\text{A.2})$$

Given the PFC configuration of Eq. (A.1), to find  $\eta_n(\mathbf{r})$ , we multiply by  $e^{-\mathbf{q}^{(n)} \cdot \mathbf{r}}$  and coarse grain to get

$$\langle \psi(\mathbf{r}) e^{-\mathbf{q}^{(n)} \cdot \mathbf{r}} \rangle = \bar{\psi}(\mathbf{r}) \langle e^{-\mathbf{q}^{(n)} \cdot \mathbf{r}} \rangle + \sum_{n'} \eta_{n'}(\mathbf{r}) \langle e^{i(\mathbf{q}^{(n')} - \mathbf{q}^{(n)}) \cdot \mathbf{r}} \rangle = \eta_n(\mathbf{r}), \quad (\text{A.3})$$

where we have used the slowly varying nature of the complex amplitudes to pull them out of the coarse graining operation and used the resonance condition  $\langle e^{i(\mathbf{q}^{(n')} - \mathbf{q}^{(n)}) \cdot \mathbf{r}} \rangle = \delta_{nn'}$  (Skogvoll et al., 2021a).

### A.2. Dislocation density tensor decomposition

A singular value decomposition of  $\alpha$  is introduced as  $\alpha = U \Sigma V^T$ , where  $\Sigma$  is a diagonal matrix containing the singular values of  $\alpha$ , and  $U$  and  $V$  are unitary matrices containing the normalized eigenvectors of  $(\alpha \alpha^T)$  and  $(\alpha^T \alpha)$ , respectively. We assume that the dislocation density tensor can be written as the outer product of the unitary tangent vector  $\mathbf{t}$  and a local spatial Burgers vector density  $\mathbf{B}(\mathbf{r})$ , i.e.,  $\alpha_{ij} = t_i B_j$ . Under this assumption, one finds  $\Sigma$  with only one non zero singular value,  $|\mathbf{B}|$ , and the columns of  $U$  and  $V$  that correspond to this singular value will be  $\mathbf{t}$  and  $\mathbf{B}/|\mathbf{B}|$ , respectively.

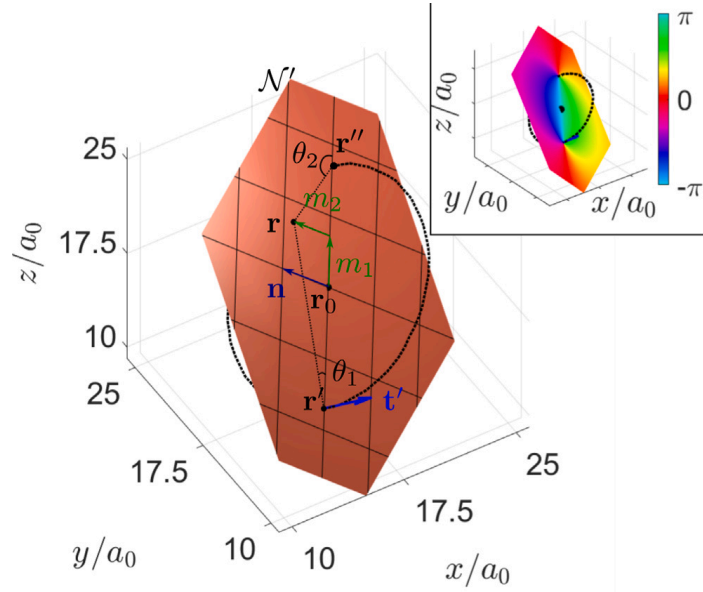
### A.3. Evolution of the phase field

The dimensionless parameters for the bcc ground state are set to:  $\Delta B_0 = -0.3$ ,  $T = 0$  and  $\psi_0 = -0.325$ . Lengths have been made dimensionless by choosing  $|\mathbf{q}^{(n)}| = q_0 = 1$ , yielding a bcc lattice constant  $a_0 = 2\pi\sqrt{2}$ . In all simulations, the computational domain is given by  $35 \times 35 \times 35$  base periods of the undistorted bcc lattice, with grid spacing  $\Delta x = \Delta y = \Delta z = a_0/7$ . Periodic boundary conditions are used throughout. Eq. (18) is integrated forward in time with an explicit method (Cox and Matthews, 2002), and  $\Delta t = 0.1$ . A Fourier decomposition of the spatial fields is introduced to compute the spatial derivatives of the fields, while nonlinear terms are computed in real space.

#### A.3.1. Mechanical equilibrium

We implement the correction scheme of Eq. (35) between every time step  $\Delta t$ . If  $u_{\max} = \max_{\mathbf{r} \in \text{Domain}}(\mathbf{u}^\delta(\mathbf{r})) > 0.1a_0$ , we rescale  $\mathbf{u}^\delta$  so that  $u_{\max} = 0.1a_0$ , and repeat the process again until elastic equilibrium is achieved. Typically, when initializing the PFC field with a dislocation, around 5 such iterations are needed, after which,  $u_{\max}$  is on the order of  $0.01a_0$  at each correction step.

The dislocation loop shrink velocity is sensitive to the time interval  $\Delta t$  between each equilibration correction. As shown in Fig. 4, the effect of imposing this correction at every time interval  $\Delta t = 0.1$  accelerates the annihilation process by approximately a factor of  $|\mathbf{v}_{\text{PFCMEq}, \Delta t=0.1}|/|\mathbf{v}_{\text{PFC}}| \approx 7.5$ . A slow convergence in the limit  $\Delta t \rightarrow 0$  is observed, where we have estimated that the shrink velocity increases up to  $|\mathbf{v}_{\text{PFCMEq}, \Delta t \rightarrow 0}|/|\mathbf{v}_{\text{PFC}}| \approx 9.8$ . However, to reach this numerical convergence is computationally demanding. Indeed, this slow convergence suggests that the time scale of the elastic field relaxation is important for the process of shear dislocation loop shrinkage. For static problems however, such as obtaining regularized stress profiles for dislocation loops, or defect nucleation under quasi-static loading, this slow convergence is not an issue.



**Fig. A.7.** Geometry of the circular dislocation loop in a slip plane given by the normal vector  $\mathbf{n}$ .  $\mathcal{N}'$  is the plane normal to the tangent vector  $\mathbf{t}'$  upon which we impose a Cartesian coordinate system to determine the angles  $\theta_1, \theta_2$  that are used to construct the (inset) initial amplitude phase configuration. For more details, see [Appendix A.4](#).

**Table A.1**

Dislocation charges  $s_n = \frac{1}{2\pi} \mathbf{b} \cdot \mathbf{q}^{(n)}$  for different Burgers vectors  $\mathbf{b}$  in the bcc lattice.  $\mathbf{q}^{(n)}$  is defined in Eq. (20).

$\mathbf{b}$	$s_1$	$s_2$	$s_3$	$s_4$	$s_5$	$s_6$
$\frac{a_0}{2}(-1, 1, 1)$	1	0	0	0	1	1
$\frac{a_0}{2}(1, -1, 1)$	0	1	0	1	0	-1
$\frac{a_0}{2}(1, 1, -1)$	0	0	1	-1	-1	0
$\frac{a_0}{2}(1, 1, 1)$	1	1	1	0	0	0
$a_0(1, 0, 0)$	0	1	1	0	-1	-1
$a_0(0, 1, 0)$	1	0	1	-1	0	1
$a_0(0, 0, 1)$	1	1	0	1	1	0

#### A.4. Initializing a dislocation loop in the PFC model

In this section, we show how to multiply the initial amplitudes  $\eta_0$  with complex phases, to produce a dislocation loop with Burgers vector  $\mathbf{b}$  in a slip plane given by normal vector  $\mathbf{n}$  (see Section 3.1). Given a point  $\mathbf{r}$ , it belongs to a plane  $\mathcal{N}'$  perpendicular to  $\mathbf{t}'$  for some point  $\mathbf{r}'$  on the dislocation loop (see Fig. A.7). This plane also intersects the diametrically opposed point  $\mathbf{r}''$  of the dislocation loop. If  $\mathbf{r}_0$  is the center of the loop, the distance vector  $\mathbf{r} - \mathbf{r}_0$  lies in  $\mathcal{N}'$ . Let  $(m_1, m_2)$  be the first and second coordinate in the Cartesian coordinate system defined by the right-handed orthonormal system  $\{(\mathbf{n} \times \mathbf{t}'), \mathbf{n}, \mathbf{t}'\}$  centered at  $\mathbf{r}_0$ . If  $m_1 > 0$ , we get from geometrical considerations

$$m_2 = (\mathbf{r} - \mathbf{r}_0) \cdot \mathbf{n}, \tag{A.4}$$

$$m_1 = |(\mathbf{r} - \mathbf{r}_0) - m_2 \mathbf{n}|. \tag{A.5}$$

Both  $m_1$  and  $m_2$  are thus determined by  $\mathbf{r}$ ,  $\mathbf{r}_0$  and the normal vector to the loop plane  $\mathbf{n}$ .  $\theta_1$  ( $\theta_2$ ) is the angle between  $\mathbf{r} - \mathbf{r}'$  ( $\mathbf{r} - \mathbf{r}''$ ) and  $\mathbf{n} \times \mathbf{t}'$  in the plane  $\mathcal{N}'$  and are found numerically by using the four-quadrant inverse tangent  $\text{atan2}(y, x)$ , so that

$$\theta_1 = \text{atan2}(m_2, m_1 + R) \tag{A.6}$$

$$\theta_2 = \text{atan2}(m_2, m_1 - R), \tag{A.7}$$

where  $R$  is the radius of the loop. For each point  $\mathbf{r}$ , we determine  $\theta_1(\mathbf{r})$  and  $\theta_2(\mathbf{r})$  according to the equations above and initiate the PFC with the phases

$$\eta_n = \eta_0 e^{i s_n (\theta_1(\mathbf{r}) - \theta_2(\mathbf{r}))}, \tag{A.8}$$

where  $s_n = \frac{1}{2\pi} \mathbf{q}^{(n)} \cdot \mathbf{b}$  is given in Table A.1. This ensures that the complex phases have the right topological charge (Eq. (8)). The inset in Fig. A.7 shows the phase of  $e^{i(\theta_1 - \theta_2)}$  in  $\mathcal{N}'$  for  $\mathbf{n} = \frac{1}{\sqrt{2}}[-1, 0, 1]$ , which is the slip plane chosen in the simulation in



Section 3.1. Note that points  $\mathbf{r}$  for which  $m_l < 0$  are computed by the same equation for the tangent vector at  $\mathbf{r}'$ , with the same formula, thus validating the Eqs. (A.6)–(A.7) for all values in  $\mathcal{N}'$ . Since the expressions are independent of the particular plane  $\mathcal{N}'$  and each point  $\mathbf{r}$  belongs to one such plane, they are also valid for all points in the simulation domain.

#### A.5. Calculating the perimeter of a dislocation loop

To calculate numerically the perimeter of a dislocation loop, recall that

$$\alpha_{ij} = b_j \int_C dl'_i \delta^{(3)}(\mathbf{r} - \mathbf{r}'_{(l)}), \tag{A.9}$$

where we have added a subscript  $(l)$  onto  $\mathbf{r}'$  to emphasize that it is the point on the loop as indexed by the line element  $d\mathbf{l}$ . Taking the double dot product with itself, we find

$$\alpha_{ij}\alpha_{ij} = |\mathbf{b}|^2 \int_C \int_C dl'_i dm'_i \delta^{(3)}(\mathbf{r} - \mathbf{r}'_{(l)}) \delta^{(3)}(\mathbf{r} - \mathbf{r}'_{(m)}). \tag{A.10}$$

The contributions to this integral will only come from points on the loop  $C$  and only when  $\mathbf{r}'_{(l)} = \mathbf{r}'_{(m)}$ , where  $dl'_i = dm'_i$ , so  $dl_i dm_i = (d\mathbf{l})^2 = |dl_i|^2 = |dl_i| |dm_i|$ . Thus

$$\alpha_{ij}\alpha_{ij} = |\mathbf{b}|^2 \int_C |dl'_i| \delta^{(3)}(\mathbf{r} - \mathbf{r}'_{(l)}) \int_C |dm'_i| \delta^{(3)}(\mathbf{r} - \mathbf{r}'_{(m)}) = |\mathbf{b}|^2 \left( \int_C |dl'_i| \delta^{(3)}(\mathbf{r} - \mathbf{r}'_{(l)}) \right)^2. \tag{A.11}$$

Taking the square root and integrating over all space, we find

$$\int d^3r \sqrt{\alpha_{ij}\alpha_{ij}} = |\mathbf{b}| \int_C |dl_i| \int d^3r \delta^{(3)}(\mathbf{r} - \mathbf{r}'_{(l)}) = |\mathbf{b}|L, \tag{A.12}$$

where  $L$  is the perimeter of the dislocation loop. Thus,

$$L = \frac{1}{|\mathbf{b}|} \int d^3r \sqrt{\alpha_{ij}\alpha_{ij}}. \tag{A.13}$$

#### A.6. Direct computation of stress fields

The dislocation density tensor is calculated directly from the phase field  $\psi$  through Eq. (12). The general method of solving Eqs. (40)–(41) on a periodic medium is given in Ref. Brenner et al. (2014) given  $\alpha_{ij}$ , where also the uniqueness of the elastic fields is proven given appropriate conditions on the dislocation density  $\alpha_{ij}$ . In the present case, the conditions on  $\alpha_{ij}$  are automatically satisfied as it is calculated from the phase-field. In this section, we thus show for our computational setup, how we compute the Green's function in the relating the distortion  $u_{ij}$  to the dislocation density tensor  $\alpha_{ij}$  as a source. Since (40)–(41) given the periodic boundary conditions can be solved uniquely, we Fourier transform both sets of equations and add the condition of mechanical equilibrium (Eq. (41)) to the diagonal equations ( $i = k$ ) in Eq. (40), which gives in Fourier space

$$\delta_{(i)k} \frac{\mathbb{i}C_{(i)jml}}{\mu} q_j \tilde{u}_{ml} - \mathbb{i}\epsilon_{ilm} q_l \tilde{u}_{mk} = \tilde{\alpha}_{ik}, \tag{A.14}$$

where there is no summation over  $(i)$ , and we have multiplied the elastic constant tensor by  $\mathbb{i}/\mu$  where  $\mu$  is the shear modulus of the cubic lattice, and  $C_{ijkl} = \lambda\delta_{ij}\delta_{kl} + \mu(\delta_{ik}\delta_{jl} + \delta_{il}\delta_{jk}) + \gamma\delta_{ijkl}$ . By defining the 1D vectors  $\tilde{\mathbf{U}}$  and  $\tilde{\alpha}$  as

$$\begin{aligned} \tilde{\mathbf{U}}^T &= (u_{11}, u_{12}, u_{13}, u_{21}, u_{22}, u_{23}, u_{31}, u_{32}, u_{33}), \\ \tilde{\alpha}^T &= (\alpha_{11}, \alpha_{12}, \alpha_{13}, \alpha_{21}, \alpha_{22}, \alpha_{23}, \alpha_{31}, \alpha_{32}, \alpha_{33}), \end{aligned}$$

we rewrite Eq. (A.14) more compactly as

$$M(\mathbf{q})\tilde{\mathbf{U}} = \tilde{\alpha}, \tag{A.15}$$

where the explicit form of  $M(\mathbf{q})$  in the case of cubic anisotropy is given by

$$M(\mathbf{q}) = \mathbb{i} \begin{pmatrix} \frac{\lambda+2\mu+\gamma}{\mu}q_1 & q_2 & q_3 & q_2+q_3 & \frac{\lambda}{\mu}q_1 & 0 & -q_2+q_3 & 0 & \frac{\lambda}{\mu}q_1 \\ 0 & 0 & 0 & 0 & q_3 & 0 & 0 & -q_2 & 0 \\ 0 & 0 & 0 & 0 & 0 & q_3 & 0 & 0 & -q_2 \\ -q_3 & 0 & 0 & 0 & 0 & 0 & q_1 & 0 & 0 \\ \frac{\lambda}{\mu}q_2 & q_1-q_3 & 0 & q_1 & \frac{\lambda+2\mu+\gamma}{\mu}q_2 & q_3 & 0 & q_1+q_3 & \frac{\lambda}{\mu}q_2 \\ 0 & 0 & -q_3 & 0 & 0 & 0 & 0 & 0 & q_1 \\ q_2 & 0 & 0 & -q_1 & 0 & 0 & 0 & 0 & 0 \\ 0 & q_2 & 0 & 0 & -q_1 & 0 & 0 & 0 & 0 \\ \frac{\lambda}{\mu}q_3 & 0 & q_1+q_2 & 0 & \frac{\lambda}{\mu}q_3 & -q_1+q_2 & q_1 & q_2 & \frac{\lambda+2\mu+\gamma}{\mu}q_3 \end{pmatrix}. \tag{A.16}$$

$M(\mathbf{q})$  can be inverted to yield the Fourier transform of the distortion  $\mathbf{U}$ ,

$$\tilde{\mathbf{U}} = M^{-1}(\mathbf{q})\tilde{\alpha}. \quad (\text{A.17})$$

Once  $\tilde{\mathbf{U}}$  (denoted by  $\tilde{u}_{kl}$  in components) is known, we compute the stress field in mechanical equilibrium

$$\tilde{\sigma}_{ij} = C_{ijkl}\tilde{u}_{kl}. \quad (\text{A.18})$$

The dislocation density  $\alpha_{ik}$  as obtained from the phase field as in Eq. (12) has a very small divergence due to numerical round-off errors. We impose  $\partial_i\alpha_{ik} = 0$  explicitly before evaluating  $\tilde{\sigma}$ , which improves numerical stability.

## Appendix B. Inversion formula for highly symmetric lattice vector sets

In inverting Eq. (5) to obtain the displacement field  $\mathbf{u}$  in terms of the phases  $\theta_n$ , we used the result of Eq. (6). This follows from the properties of moment tensors constructed from lattice vector sets  $\mathcal{Q} = \{\mathbf{q}^{(n)}\}_{n=1}^N$ . The  $p$ th order moment tensor constructed from  $\mathcal{Q}$  is given by

$$Q_{i_1 \dots i_p} = \sum_{n=1}^N q_{i_1}^{(n)} \dots q_{i_p}^{(n)}. \quad (\text{B.1})$$

In two dimensions, for a parity-invariant lattice vector set that has a  $B$ -fold symmetry, Ref. Chen and Orszag (2011) showed that all  $p$ th order moments vanish for odd  $p$  and are isotropic for  $p < B$ . Every isotropic rank 2 tensor is proportional to the identity tensor  $\delta_{ij}$ , so for a 2D lattice vector set having four-fold symmetry, such as the set of shortest reciprocal lattice vectors  $\{\mathbf{q}^{(n)}\}_{n=1}^4$  of the square lattice, we have  $\sum_{n=1}^4 q_i^{(n)} q_j^{(n)} \propto \delta_{ij}$  (Figs. 3 and 5 in Ref. Skogvoll et al. (2021a) show the reciprocal lattice vector sets discussed in this appendix). Taking the trace and using that the vectors have the same length  $|\mathbf{q}^{(n)}| = q_0$ , we get  $\sum_{n=1}^4 q_i^{(n)} q_i^{(n)} = 4q_0^2 \delta_{ij}$ . In general, for any 2D parity invariant lattice vector set  $\{\mathbf{q}^{(n)}\}_{n=1}^N$  with a  $B$ -fold symmetry where  $B > 2$ , we have

$$2\text{D: } \sum_{n=1}^N q_i^{(n)} q_j^{(n)} = \frac{Nq_0^2}{2} \delta_{ij}. \quad (\text{B.2})$$

As mentioned, this holds for the 2D square lattice, but it also holds for the 2D hexagonal lattice. In fact, the six-fold symmetry of the hexagonal lattice ensures that also every fourth-order moment tensor is isotropic, which results in elastic properties of the 2D hexagonal PFC model being isotropic (Skogvoll et al., 2021a).

To show this identity for a 3D parity invariant vector set with cubic symmetry, we generalize the proof in Ref. Chen and Orszag (2011) to a particular case of a 3D vector set that is symmetric with respect to  $90^\circ$  rotations around each coordinate axis, such as the set of shortest reciprocal lattice vectors  $\{\mathbf{q}^{(n)}\}_{n=1}^N$  of bcc, fcc or simple cubic structures. Let  $\mathbf{v}$  be an eigenvector of  $Q_{ij}$  with eigenvalue  $\lambda$ , i.e.,  $Q_{ij}v_j = \lambda v_i$ . Since  $Q_{ij}$  is invariant under a  $90^\circ$  rotation  $R_{ij}^{(x)}$  around the  $x$ -axis (i.e.,  $R_{ik}^{(x)} Q_{kl} (R^{(x)T})_{kj} = Q_{ij}$ ), we get  $Q_{ij} R_{jl}^{(x)} v_l = \lambda R_{il}^{(x)} v_l$ , showing that  $R^{(x)}\mathbf{v}$  is also an eigenvector of  $Q_{ij}$  with the same eigenvalue  $\lambda$ . Repeating for a rotation around the  $y$ -axis demonstrates that  $Q_{ij}$  has only one eigenvalue  $\lambda$ , so that it must be proportional to the rank 2 identity tensor  $Q_{ij} \propto \delta_{ij}$ . Taking the trace and using that the vectors have the same length  $|\mathbf{q}^{(n)}| = q_0$ , we find

$$3\text{D: } \sum_{n=1}^N q_i^{(n)} q_j^{(n)} = \frac{Nq_0^2}{3} \delta_{ij}. \quad (\text{B.3})$$

## Appendix C. Time derivatives of the dislocation density tensor

### C.1. Delta-function form

Consider a moving dislocation line  $C = \{\mathbf{r}'(\lambda, t)\}$  of points  $\mathbf{r}(\lambda, t)$  parametrized by the time  $t$  and a dimensionless  $\lambda$  which can be taken to go from 0 to 1 without loss of generality. Keeping the labeling fixed through its time evolution, we get

$$\alpha_{ij}(\mathbf{r}, t) = b_j \int_{\lambda=0}^1 \delta^{(3)}(\mathbf{r} - \mathbf{r}'(\lambda, t)) (\partial_\lambda r'_i(\lambda, t)) d\lambda. \quad (\text{C.1})$$

Suppressing the dependence of  $\mathbf{r}'$  on  $\lambda$  and  $t$ , we get taking the time derivative of Eq. (2),

$$\partial_t \alpha_{ij} = b_j \underbrace{\int_{\lambda=0}^1 (\partial_t \delta^{(3)}(\mathbf{r} - \mathbf{r}')) (\partial_\lambda r'_i) d\lambda}_{(1)} + b_j \underbrace{\int_{\lambda=0}^1 \delta^{(3)}(\mathbf{r} - \mathbf{r}') (\partial_t \partial_\lambda r'_i) d\lambda}_{(2)}. \quad (\text{C.2})$$

Starting with the first term using the chain rule, we have

$$(1) = b_j \int_{\lambda=0}^1 (\partial_{k'} \delta^{(3)}(\mathbf{r} - \mathbf{r}')) V_k(\mathbf{r}') (\partial_\lambda r'_i) d\lambda, \quad (\text{C.3})$$

where  $\partial_{k'} = \partial/\partial r'_k$  and  $V_k$  is a field at time  $t$  which is defined on  $\mathbf{r}' \in C$  as  $\mathbf{V}(\mathbf{r}') = \partial_t \mathbf{r}'$ , the velocity of the line segment perpendicular to the tangent vector. We can rewrite  $\partial_{k'} \delta^{(3)}(\mathbf{r} - \mathbf{r}') = -\partial_k \delta^{(3)}(\mathbf{r} - \mathbf{r}')$  and pull it outside the integral. Additionally, since  $V_k(\mathbf{r}')$  is multiplied by a delta function, we can replace it by  $V_k(\mathbf{r})$ , so we get

$$(1) = -\partial_k \left( b_j \int_{\lambda=0}^1 \delta^{(3)}(\mathbf{r} - \mathbf{r}') (\partial_{\lambda} r'_i) d\lambda (V_k(\mathbf{r})) \right) = -\partial_k (\alpha_{ij} V_k). \tag{C.4}$$

Turning to the second term, we get

$$(2) = b_j \int_{\lambda=0}^1 \delta^{(3)}(\mathbf{r} - \mathbf{r}') (\partial_{\lambda} V_i(\mathbf{r}')) d\lambda = b_j \int_{\lambda=0}^1 \delta^{(3)}(\mathbf{r} - \mathbf{r}') (\partial_{k'} V_i(\mathbf{r}')) (\partial_{\lambda} r'_k) d\lambda. \tag{C.5}$$

Since  $\partial_{k'} V_i(\mathbf{r}')$  is multiplied with a delta-function inside the integral, we can replace it by  $\partial_k V_i(\mathbf{r})$ . We thus get

$$(2) = \left( b_j \int_{\lambda=0}^1 \delta^{(3)}(\mathbf{r} - \mathbf{r}') (\partial_{\lambda} r'_k) d\lambda \right) (\partial_k V_i) = \alpha_{kj} \partial_k V_i = \partial_k (\alpha_{kj} V_i), \tag{C.6}$$

since  $\partial_k \alpha_{kj} = \partial_k (b_j \int_C \delta^{(3)}(\mathbf{r} - \mathbf{r}') dr'_k) = -b_j \int_C (\partial_{k'} \delta^{(3)}(\mathbf{r} - \mathbf{r}')) dr'_k = -b_j [\delta(\mathbf{r} - \mathbf{r}')]_{\mathbf{r}'(\lambda=0)}^{\mathbf{r}'(\lambda=1)} = 0$ , either because  $C$  is a loop such that  $\mathbf{r}'(\lambda = 0) = \mathbf{r}'(\lambda = 1)$  or else  $\mathbf{r}'(\lambda = 0) \neq \mathbf{r} \neq \mathbf{r}'(\lambda = 1)$  since the dislocation cannot end inside the crystal. This gives

$$\partial_t \alpha_{ij} = -\partial_k (\alpha_{ij} V_k) + \partial_k (\alpha_{kj} V_i) = -\epsilon_{ikl} \partial_k (\epsilon_{lmn} \alpha_{mj} V_n). \tag{C.7}$$

### C.2. Amplitude form

Taking the time derivative of Eq. (12), we have

$$\partial_t \alpha_{ij} = \underbrace{\frac{6\pi}{Nq_0^2} \sum_{n=1}^N q_j^{(n)} (\partial_t D_i^{(n)}) \delta^{(2)}(\eta_n)}_{(1)} + \underbrace{\frac{6\pi}{Nq_0^2} \sum_{n=1}^N q_j^{(n)} D_i^{(n)} \partial_t \delta^{(2)}(\eta_n)}_{(2)}. \tag{C.8}$$

The vector field  $D_i^{(n)}$  satisfies a conservation law which can be obtained by differentiating Eq. (11) with respect to time (Angheluta et al., 2012; Mazenko, 1999). This gives  $\partial_t D_i^{(n)} = -\epsilon_{ikl} \partial_k J_l^{(n)}$ , with the associated current given by  $J_l^{(n)} = \mathfrak{S}(\partial_t \eta_n \partial_l \eta_n^*)$ . Thus

$$(1) = -\epsilon_{ikl} \frac{6\pi}{Nq_0^2} \sum_{n=1}^N q_j^{(n)} (\partial_k J_l^{(n)}) \delta^{(2)}(\eta_n). \tag{C.9}$$

Differentiating through the delta-function in the second term (2), we get

$$D_i^{(n)} \partial_t \delta^{(2)}(\eta_n) = \epsilon_{ikl} (\partial_k \eta_{n,1}) (\partial_l \eta_{n,2}) \sum_{r=1}^2 \left( \frac{\partial}{\partial \eta_{n,r}} \delta^{(2)}(\eta_n) \right) \partial_t \eta_{n,r}, \tag{C.10}$$

where  $\eta_{n,1}$  and  $\eta_{n,2}$  denotes the real and imaginary part of  $\eta_n$ , respectively. Straight forward, but tedious algebra, shows that this is equal to

$$-\epsilon_{ikl} J_l^{(n)} \partial_k \delta^{(2)}(\eta_n) = -\epsilon_{ikl} \mathfrak{S}(\partial_t \eta_n \partial_l \eta_n^*) \sum_{r=1}^2 \left( \frac{\partial}{\partial \eta_{n,r}} \delta^{(2)}(\eta_n) \right) \partial_k \eta_{n,r}, \tag{C.11}$$

after inserting  $\eta_n = \eta_{n,1} + i\eta_{n,2}$ . Thus

$$(2) = -\epsilon_{ikl} \frac{6\pi}{Nq_0^2} \sum_{n=1}^N q_j^{(n)} J_l^{(n)} \partial_k \delta^{(2)}(\eta_n). \tag{C.12}$$

Taken together, this gives

$$\partial_t \alpha_{ij} = -\epsilon_{ikl} \partial_k \left( \frac{6\pi}{Nq_0^2} \sum_{n=1}^N q_j^{(n)} J_l^{(n)} \delta^{(2)}(\eta_n) \right), \tag{C.13}$$

as desired.

### Appendix D. Calculation details of dislocation velocity

Inserting the expression for the delta-function in terms of the dislocation density tensor  $\delta^{(2)}(\eta_n) = \alpha_{ik} D_i^{(n)} q_k^{(n)} / (2\pi |\mathbf{D}^{(n)}|^2)$  into Eq. (14), we get

$$J_{lj} = \frac{6\pi}{Nq_0^2} \sum_{n=1}^N \alpha_{ik} J_l^{(n)} q_j^{(n)} \frac{D_i^{(n)} q_k^{(n)}}{2\pi |\mathbf{D}^{(n)}|^2}. \tag{D.1}$$



Equating  $\mathcal{J}_{ij}^{(\alpha)}$  and  $\mathcal{J}_{ij}$  at a point  $\mathbf{r}'$  on the dislocation line, where  $\alpha_{ij} = t'_i b_j \delta^{(2)}(\Delta \mathbf{r}_\perp)$  using  $\mathbf{b} \cdot \mathbf{q}^{(n)} = 2\pi s_n$ ,

$$\epsilon_{lmn} t'_m b_j v'_n \delta^{(2)}(\Delta \mathbf{r}_\perp) = \frac{6\pi}{N q_0^2} \sum_{n=1}^N s_n t'_i \delta^{(2)}(\Delta \mathbf{r}_\perp) J_l^{(n)} q_j^{(n)} \frac{D_i^{(n)}}{|\mathbf{D}^{(n)}|^2}. \tag{D.2}$$

We now integrate out the delta-function in the  $\mathcal{N}'$ -plane and contract both sides of the equation with  $b_j$  to get

$$\epsilon_{lmn} t'_m v'_n = \frac{12\pi^2}{N q_0^2 |\mathbf{b}|^2} \sum_{n=1}^N s_n^2 \frac{t'_i D_i^{(n)}}{|\mathbf{D}^{(n)}|^2} J_l^{(n)}, \tag{D.3}$$

as desired.

### Appendix E. Amplitude decoupling

The (complex) polynomial  $f^s$  (see Eq. (23)) results from the amplitude expansion of the  $\psi^3$  and  $\psi^4$  terms in Eq. (17). It may be computed by substituting Eq. (19) into Eq. (17) and integrating over the unit cell, under the assumption of constant amplitudes (Goldenfeld et al., 2005; Athreya et al., 2006; Salvalaglio and Elder, 2022). It features terms reading  $\prod_{\ell=1}^L \eta_{n_\ell}$ , with  $L = 3, 4$  and  $n_\ell$  for which the condition  $\sum_{\ell=1}^L \mathbf{q}^{(n_\ell)} = 0$  is satisfied. By multiplying this condition by  $\mathbf{b}$  and using Eq. (8) it then follows that

$$\sum_{\ell=1}^L s_{n_\ell} = 0. \tag{E.1}$$

In the equation for the dislocation velocity, Eq. (16), the only contributing amplitudes are those for which  $s_n \neq 0$ . The condition (E.1) implies that at least one of the other amplitudes,  $\{\eta_m\}_{m \neq n}$ , appearing in terms of  $f^s$  containing  $\eta_n$ , also has  $s_m \neq 0$  and then vanishes at the corresponding defect. Thus, for a given amplitude  $\eta_n$  with  $s_n \neq 0$ , the terms in  $\frac{\partial f^s}{\partial \eta_n^*}$  always contain at least one vanishing amplitude. Eq. (25) then reduces to Eq. (26) at the defect as  $\eta_n = 0$  and  $\frac{\partial f^s}{\partial \eta_n^*} = 0$  there. Importantly, a full decoupling of the evolution equation for amplitudes which vanish at the defect is obtained.

This can be straightforwardly verified for specific lattice symmetries and dislocations. When accounting for the bcc lattice symmetry through  $\mathbf{q}^{(n)}$  as in Eq. (20), the (complex) polynomial  $f^s$  entering the coarse-grained energy  $F_\eta$  defined in Eq. (23) is

$$f^s = -2T(\eta_1^* \eta_2 \eta_6 + \eta_1^* \eta_3 \eta_5 + \eta_2^* \eta_3 \eta_4 + \eta_4 \eta_5^* \eta_6) + 6V(\eta_1^* \eta_2 \eta_4^* \eta_5 + \eta_1^* \eta_3 \eta_4 \eta_6 + \eta_2^* \eta_3 \eta_5 \eta_6^*) + \text{c.c.} \tag{E.2}$$

which gives

$$\begin{aligned} \frac{\partial f^s}{\partial \eta_1^*} &= -2T(\eta_2 \eta_6 + \eta_3 \eta_5) + 6V(\eta_2 \eta_4^* \eta_5 + \eta_3 \eta_4 \eta_6), \\ \frac{\partial f^s}{\partial \eta_2^*} &= -2T(\eta_1 \eta_6^* + \eta_3 \eta_4) + 6V(\eta_1 \eta_4 \eta_5^* + \eta_3 \eta_5 \eta_6^*), \\ \frac{\partial f^s}{\partial \eta_3^*} &= -2T(\eta_1 \eta_5^* + \eta_2 \eta_4^*) + 6V(\eta_1 \eta_4^* \eta_6^* + \eta_2 \eta_5^* \eta_6), \\ \frac{\partial f^s}{\partial \eta_4^*} &= -2T(\eta_2 \eta_3^* + \eta_5 \eta_6^*) + 6V(\eta_1^* \eta_2 \eta_5 + \eta_1 \eta_3^* \eta_6^*), \\ \frac{\partial f^s}{\partial \eta_5^*} &= -2T(\eta_1 \eta_3^* + \eta_4 \eta_6) + 6V(\eta_1 \eta_2^* \eta_4 + \eta_2 \eta_3^* \eta_6), \\ \frac{\partial f^s}{\partial \eta_6^*} &= -2T(\eta_1 \eta_2^* + \eta_4^* \eta_5) + 6V(\eta_1 \eta_3^* \eta_4^* + \eta_2^* \eta_3 \eta_5). \end{aligned} \tag{E.3}$$

By comparing Eqs. (E.3) with the dislocation charges for the possible Burgers vector in the bcc lattice, Table A.1, and noting that, at the dislocation core,  $\eta_n = 0$  for  $s_n \neq 0$ , we find

$$s_n \neq 0 : \quad \frac{\partial f^s}{\partial \eta_n} = 0, \tag{E.4}$$

allowing for a decoupled system of evolution relations for  $\eta_1, \dots, \eta_6$ , as described by Eq. (26).

### References

Acharya, A., Knops, R.J., Sivaloganathan, J., 2019. On the structure of linear dislocation field theory. *J. Mech. Phys. Solids* (ISSN: 0022-5096) 130, 216–244. <http://dx.doi.org/10.1016/j.jmps.2019.06.002>.

Acharya, Amit, Viñals, Jorge, 2020. Field dislocation mechanics and phase field crystal models. *Phys. Rev. B* 102 (6), 064109. <http://dx.doi.org/10.1103/PhysRevB.102.064109>.

Anderson, Peter M., Hirth, John P., Lothe, Jens, 2017. *Theory of Dislocations*. Cambridge University Press, ISBN: 978-0-521-86436-7.

Angheluta, Luiza, Jeraldo, Patricio, Goldenfeld, Nigel, 2012. Anisotropic velocity statistics of topological defects under shear flow. *Phys. Rev. E* 85 (1), 011153. <http://dx.doi.org/10.1103/PhysRevE.85.011153>.

Archer, Andrew J., Ratliff, Daniel J., Rucklidge, Alastair M., Subramanian, Priya, 2019. Deriving phase field crystal theory from dynamical density functional theory: Consequences of the approximations. *Phys. Rev. E* 100 (2), 022140. <http://dx.doi.org/10.1103/PhysRevE.100.022140>.

- Athreya, Badrinarayan P., Goldenfeld, Nigel, Dantzig, Jonathan A., 2006. Renormalization-group theory for the phase-field crystal equation. *Phys. Rev. E* 74 (1), 011601. <http://dx.doi.org/10.1103/PhysRevE.74.011601>.
- Berry, Joel, Rottler, Jörg, Sinclair, Chad W., Provatas, Nikolas, 2015. Atomistic study of diffusion-mediated plasticity and creep using phase field crystal methods. *Phys. Rev. B* 92 (13), 134103. <http://dx.doi.org/10.1103/PhysRevB.92.134103>.
- Boyer, Denis, Viñals, Jorge, 2002. Weakly nonlinear theory of grain boundary motion in patterns with crystalline symmetry. *Phys. Rev. Lett.* 89 (5), 055501.
- Brazovskii, S., 1975. Phase transition of an isotropic system to a nonuniform state. *Sov. J. Exp. Theor. Phys.* 41, 85.
- Brenner, R., Beaudoin, A.J., Suquet, P., Acharya, A., 2014. Numerical implementation of static field dislocation mechanics theory for periodic media. *Phil. Mag.* (ISSN: 1478-6435) 94 (16), 1764–1787. <http://dx.doi.org/10.1080/14786435.2014.896081>.
- Bulatov, Vasily, Abraham, Farid F., Kubin, Ladislav, Devincere, Benoit, Yip, Sidney, 1998. Connecting atomistic and mesoscale simulations of crystal plasticity. *Nature* (ISSN: 1476-4687) 391 (6668), 669–672. <http://dx.doi.org/10.1038/35577>.
- Cai, Wei, Arsenlis, Athanasios, Weinberger, Christopher R., Bulatov, Vasily V., 2006. A non-singular continuum theory of dislocations. *J. Mech. Phys. Solids* (ISSN: 0022-5096) 54 (3), 561–587. <http://dx.doi.org/10.1016/j.jmps.2005.09.005>.
- Chen, Hudong, Orszag, Steven, 2011. Moment isotropy and discrete rotational symmetry of two-dimensional lattice vectors. *Phil. Trans. R. Soc. A* 369 (1944), 2176–2183. <http://dx.doi.org/10.1098/rsta.2010.0376>.
- Cox, S.M., Matthews, P.C., 2002. Exponential time differencing for stiff systems. *J. Comput. Phys.* (ISSN: 0021-9991) 176 (2), 430–455. <http://dx.doi.org/10.1006/jcph.2002.6995>.
- Dederichs, P.H., Leibfried, G., 1969. Elastic Green's function for anisotropic cubic crystals. *Phys. Rev.* 188 (3), 1175–1183. <http://dx.doi.org/10.1103/PhysRev.188.1175>.
- Devincere, B., Hoc, T., Kubin, L., 2008. Dislocation mean free paths and strain hardening of crystals. *Science* 320 (5884), 1745–1748. <http://dx.doi.org/10.1126/science.1156101>.
- Elder, K.R., Grant, Martin, 2004. Modeling elastic and plastic deformations in nonequilibrium processing using phase field crystals. *Phys. Rev. E* 70 (5), 051605. <http://dx.doi.org/10.1103/PhysRevE.70.051605>.
- Elder, K.R., Huang, Zhi-Feng, Provatas, Nikolas, 2010. Amplitude expansion of the binary phase-field-crystal model. *Phys. Rev. E* 81 (1), 011602. <http://dx.doi.org/10.1103/PhysRevE.81.011602>.
- Elder, K.R., Katakowski, Mark, Haataja, Mikko, Grant, Martin, 2002. Modeling elasticity in crystal growth. *Phys. Rev. Lett.* 88 (24), 245701. <http://dx.doi.org/10.1103/PhysRevLett.88.245701>.
- Elder, K.R., Provatas, Nikolas, Berry, Joel, Stefanovic, Peter, Grant, Martin, 2007. Phase-field crystal modeling and classical density functional theory of freezing. *Phys. Rev. B* 75 (6), 064107. <http://dx.doi.org/10.1103/PhysRevB.75.064107>.
- Emmerich, Heike, Löwen, Hartmut, Wittkowski, Raphael, Gruhn, Thomas, Tóth, Gyula I., Tegze, György, László Gránágy, 2012. Phase-field-crystal models for condensed matter dynamics on atomic length and diffusive time scales: An overview. *Adv. Phys.* 61 (6), 665–743. <http://dx.doi.org/10.1080/00018732.2012.737555>.
- Forster, D., 1975. *Hydrodynamic Fluctuations, Broken Symmetry, and Correlation Functions*. Benjamin/Cummings, Reading, MA.
- Goldenfeld, Nigel, Athreya, Badrinarayan P., Dantzig, Jonathan A., 2005. Renormalization group approach to multiscale simulation of polycrystalline materials using the phase field crystal model. *Phys. Rev. E* 72 (2), 020601. <http://dx.doi.org/10.1103/PhysRevE.72.020601>.
- Halperin, Bertrand I., 1981. Statistical mechanics of topological defects. In: Balian, Roger, Kléman, Maurice, Poirier, Jean-Paul (Eds.), *Physique des Défauts/Physics of Defects*. North-Holland, Amsterdam, pp. 812–857, ISBN: 0-444-86225-0.
- Heinonen, V., Achim, C.V., Elder, K.R., Buyukdagli, S., Ala-Nissila, T., 2014. Phase-field-crystal models and mechanical equilibrium. *Phys. Rev. E* 89 (3), 032411. <http://dx.doi.org/10.1103/PhysRevE.89.032411>.
- Heinonen, V., Achim, C.V., Kosterlitz, J.M., Ying, See-Chen, Lowengrub, J., Ala-Nissila, T., 2016. Consistent hydrodynamics for phase field crystals. *Phys. Rev. Lett.* 116 (2), 024303. <http://dx.doi.org/10.1103/PhysRevLett.116.024303>.
- Hill, Rodney, 1998. *The Mathematical Theory of Plasticity*. Clarendon Press, ISBN: 978-0-19-850367-5.
- Huang, Zhi-Feng, Elder, K.R., Provatas, Nikolas, 2010. Phase-field-crystal dynamics for binary systems: Derivation from dynamical density functional theory, amplitude equation formalism, and applications to alloy heterostructures. *Phys. Rev. E* 82 (2), 021605. <http://dx.doi.org/10.1103/PhysRevE.82.021605>.
- Kosevich, A.M., 1979. Crystal dislocations and the theory of elasticity. In: Nabarro, F.R.N. (Ed.), *Dislocations in Solids, Vol. 1*. North-Holland, Amsterdam, pp. 33–141.
- Koslowski, M., Cuitiño, A.M., Ortiz, M., 2002. A phase-field theory of dislocation dynamics, strain hardening and hysteresis in ductile single crystals. *J. Mech. Phys. Solids* (ISSN: 0022-5096) 50 (12), 2597–2635. [http://dx.doi.org/10.1016/S0022-5096\(02\)00037-6](http://dx.doi.org/10.1016/S0022-5096(02)00037-6).
- Kubin, Ladislav P., Canova, G., Condat, M., Devincere, Benoit, Pontikis, V., Bréchet, Yves, 1992. Dislocation microstructures and plastic flow: A 3D simulation. In: *Non Linear Phenomena in Materials Science II*. In: *Solid State Phenomena*, vol. 23, Trans Tech Publications Ltd, pp. 455–472. <http://dx.doi.org/10.4028/www.scientific.net/SSP.23-24.455>.
- Lazar, Markus, 2014. On gradient field theories: Gradient magnetostatics and gradient elasticity. *Phil. Mag.* (ISSN: 1478-6435) 94 (25), 2840–2874. <http://dx.doi.org/10.1080/14786435.2014.935512>.
- Lazar, Markus, 2017. Non-singular dislocation continuum theories: Strain gradient elasticity vs. peierls-nabarro model. *Phil. Mag.* (ISSN: 1478-6435) 97 (34), 3246–3275. <http://dx.doi.org/10.1080/14786435.2017.1375608>.
- Lazar, Markus, Maugin, Gérard A., 2005. Nonsingular stress and strain fields of dislocations and disclinations in first strain gradient elasticity. *Internat. J. Engrg. Sci.* (ISSN: 0020-7225) 43 (13), 1157–1184. <http://dx.doi.org/10.1016/j.ijengsci.2005.01.006>.
- Liu, Zhe-Yuan, Gao, Ying-Jun, Deng, Qian-Qian, Li, Yi-Xuan, Huang, Zong-Ji, Liao, Kun, Luo, Zhi-Rong, 2020. A nanoscale study of nucleation and propagation of zener types cracks at dislocations: Phase field crystal model. *Comput. Mater. Sci.* (ISSN: 0927-0256) 179, 109640. <http://dx.doi.org/10.1016/j.commatsci.2020.109640>.
- Mazenko, Gene F., 1997. Vortex velocities in the O(n) symmetric time-dependent Ginzburg-Landau model. *Phys. Rev. Lett.* 78 (3), 401–404. <http://dx.doi.org/10.1103/PhysRevLett.78.401>.
- Mazenko, Gene F., 1999. Velocity distribution for strings in phase-ordering kinetics. *Phys. Rev. E* 59 (2), 1574–1584. <http://dx.doi.org/10.1103/PhysRevE.59.1574>.
- Mianroodi, Jaber Rezaei, Svendsen, Bob, 2015. Atomistically determined phase-field modeling of dislocation dissociation, stacking fault formation, dislocation slip, and reactions in fcc systems. *J. Mech. Phys. Solids* (ISSN: 0022-5096) 77, 109–122. <http://dx.doi.org/10.1016/j.jmps.2015.01.007>.
- Momeni, Kasra, Ji, Yanzhou, Zhang, Kehao, Robinson, Joshua A., Chen, Long-Qing, 2018. Multiscale framework for simulation-guided growth of 2D materials. *Npj 2D Mater. Appl.* (ISSN: 2397-7132) 2 (1), 1–7. <http://dx.doi.org/10.1038/s41699-018-0072-4>.
- Pismen, Len, 1999. *Vortices in Nonlinear Fields: From Liquid Crystals to Superfluids, from Non-Equilibrium Patterns to Cosmic Strings*, Vol. 100. Oxford University Press.
- Pokharel, Reeru, Lind, Jonathan, Kanjarla, Anand K., Lebensohn, Ricardo A., Li, Shiu Fai, Kenesei, Peter, Suter, Robert M., Rollett, Anthony D., 2014. Polycrystal plasticity: comparison between grain - scale observations of deformation and simulations. *Annu. Rev. Condens. Matter Phys.* 5 (1), 317–346. <http://dx.doi.org/10.1146/annurev-conmatphys-031113-133846>.
- Provatas, N., Dantzig, J.A., Athreya, B., Chan, P., Stefanovic, P., Goldenfeld, N., Elder, K.R., 2007. Using the phase-field crystal method in the multi-scale modeling of microstructure evolution. *JOM* (ISSN: 1543-1851) 59 (7), 83–90. <http://dx.doi.org/10.1007/s11837-007-0095-3>.

- Ramos, J.A.P., Granato, E., Ying, S.C., Achim, C.V., Elder, K.R., Ala-Nissila, T., 2010. Dynamical transitions and sliding friction of the phase-field-crystal model with pinning. *Phys. Rev. E* 81 (1), 011121. <http://dx.doi.org/10.1103/PhysRevE.81.011121>.
- Rodney, D., Le Bouar, Y., Finel, A., 2003. Phase field methods and dislocations. *Acta Mater.* (ISSN: 1359-6454) 51 (1), 17–30. [http://dx.doi.org/10.1016/S1359-6454\(01\)00379-2](http://dx.doi.org/10.1016/S1359-6454(01)00379-2).
- Rollett, A.D., Rohrer, G.S., Suter, R.M., 2015. Understanding materials microstructure and behavior at the mesoscale. *MRS Bull.* 40 (11), 951–960. <http://dx.doi.org/10.1557/mrs.2015.262>, (ISSN: 0883-7694, 1938-1425).
- Roters, F., Eisenlohr, P., Hantcherli, L., Tjahjanto, D.D., Bieler, T.R., Raabe, D., 2010. Overview of constitutive laws, kinematics, homogenization and multiscale methods in crystal plasticity finite-element modeling: Theory, experiments, applications. *Acta Mater.* (ISSN: 1359-6454) 58 (4), 1152–1211. <http://dx.doi.org/10.1016/j.actamat.2009.10.058>.
- Roy, Anish, Acharya, Amit, 2005. Finite element approximation of field dislocation mechanics. *J. Mech. Phys. Solids* (ISSN: 0022-5096) 53 (1), 143–170. <http://dx.doi.org/10.1016/j.jmps.2004.05.007>.
- Salvalaglio, Marco, Angheluta, Luiza, Huang, Zhi-Feng, Voigt, Axel, Elder, Ken R., Viñals, Jorge, 2020. A coarse-grained phase-field crystal model of plastic motion. *J. Mech. Phys. Solids* (ISSN: 0022-5096) 137, 103856. <http://dx.doi.org/10.1016/j.jmps.2019.103856>.
- Salvalaglio, Marco, Backofen, Rainer, Elder, K.R., Voigt, Axel, 2018. Defects at grain boundaries: A coarse-grained, three-dimensional description by the amplitude expansion of the phase-field crystal model. *Phys. Rev. Mater.* 2 (5), 053804. <http://dx.doi.org/10.1103/PhysRevMaterials.2.053804>.
- Salvalaglio, Marco, Elder, Ken R., 2022. Coarse-grained modeling of crystals by the amplitude expansion of the phase-field crystal model: an overview. *Modelling Simulation Mater. Sci. Eng.* <http://dx.doi.org/10.1088/1361-651X/ac681e>.
- Salvalaglio, Marco, Voigt, Axel, Elder, Ken R., 2019. Closing the gap between atomic-scale lattice deformations and continuum elasticity. *Npj Comput. Mater.* (ISSN: 2057-3960) 5 (1), 48. <http://dx.doi.org/10.1038/s41524-019-0185-0>.
- Salvalaglio, Marco, Voigt, Axel, Huang, Zhi-Feng, Elder, Ken R., 2021. Mesoscale defect motion in binary systems: Effects of compositional strain and cottrell atmospheres. *Phys. Rev. Lett.* 126 (18), 185502. <http://dx.doi.org/10.1103/PhysRevLett.126.185502>.
- Sills, Ryan B., Kuykendall, William P., Aghaei, Amin, Cai, Wei, 2016. Fundamentals of dislocation dynamics simulations. In: Weinberger, Christopher R., Tucker, Garritt J. (Eds.), *Multiscale Materials Modeling for Nanomechanics*. In: Springer Series in Materials Science, Springer International Publishing, Cham, ISBN: 978-3-319-33480-6, pp. 53–87. [http://dx.doi.org/10.1007/978-3-319-33480-6\\_2](http://dx.doi.org/10.1007/978-3-319-33480-6_2).
- Skaugen, Audun, Angheluta, Luiza, Viñals, Jorge, 2018a. Dislocation dynamics and crystal plasticity in the phase-field crystal model. *Phys. Rev. B* 97 (5), 054113. <http://dx.doi.org/10.1103/PhysRevB.97.054113>.
- Skaugen, Audun, Angheluta, Luiza, Viñals, Jorge, 2018b. Separation of elastic and plastic timescales in a phase field crystal model. *Phys. Rev. Lett.* 121 (25), 255501. <http://dx.doi.org/10.1103/PhysRevLett.121.255501>.
- Skogvoll, Vidar, Skaugen, Audun, Angheluta, Luiza, 2021a. Stress in ordered systems: Ginzburg-Landau-type density field theory. *Phys. Rev. B* 103 (22), 224107. <http://dx.doi.org/10.1103/PhysRevB.103.224107>.
- Skogvoll, Vidar, Skaugen, Audun, Angheluta, Luiza, Viñals, Jorge, 2021b. Dislocation nucleation in the phase-field crystal model. *Phys. Rev. B* 103 (1), 014107. <http://dx.doi.org/10.1103/PhysRevB.103.014107>.
- Stefanovic, Peter, Haataja, Mikko, Provatas, Nikolas, 2006. Phase-field crystals with elastic interactions. *Phys. Rev. Lett.* 96 (22), 225504. <http://dx.doi.org/10.1103/PhysRevLett.96.225504>.
- Swift, J., Hohenberg, P.C., 1977. Hydrodynamic fluctuations at the convective instability. *Phys. Rev. A* 15 (1), 319–328. <http://dx.doi.org/10.1103/PhysRevA.15.319>.
- Tóth, Gyula I., Gránásy, László, Tegze, György, 2013. Nonlinear hydrodynamic theory of crystallization. *J. Phys.: Condens. Matter* (ISSN: 0953-8984) 26 (5), 055001. <http://dx.doi.org/10.1088/0953-8984/26/5/055001>.
- Wu, Han-Chin, 2004. *Continuum Mechanics and Plasticity*. Chapman and Hall/CRC, New York, ISBN: 978-0-429-20880-5, <http://dx.doi.org/10.1201/9780203491997>.
- Wu, Kuo-An, Voorhees, Peter W., 2012. Phase field crystal simulations of nanocrystalline grain growth in two dimensions. *Acta Mater.* (ISSN: 1359-6454) 60 (1), 407–419. <http://dx.doi.org/10.1016/j.actamat.2011.09.035>.
- Yamanaka, Akinori, McReynolds, Kevin, Voorhees, Peter W., 2017. Phase field crystal simulation of grain boundary motion, grain rotation and dislocation reactions in a BCC bicrystal. *Acta Mater.* (ISSN: 1359-6454) 133, 160–171. <http://dx.doi.org/10.1016/j.actamat.2017.05.022>.



## PAPER IV



PAPER

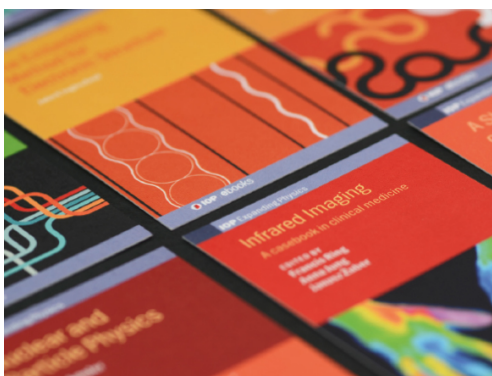
## Hydrodynamic phase field crystal approach to interfaces, dislocations, and multi-grain networks

To cite this article: Vidar Skogvoll *et al* 2022 *Modelling Simul. Mater. Sci. Eng.* **30** 084002

View the [article online](#) for updates and enhancements.

### You may also like

- [Derivation and analysis of a phase field crystal model for a mixture of active and passive particles](#)  
Michael te Vrugt, Max Philipp Holl, Aron Koch *et al.*
- [The phase field technique for modeling multiphase materials](#)  
I Singer-Loginova and H M Singer
- [Elasticity versus phase field driven motion in the phase field crystal model](#)  
Amit Acharya, Luiza Angheluta and Jorge Viñals



**IOP | ebooks™**

Bringing together innovative digital publishing with leading authors from the global scientific community.

Start exploring the collection—download the first chapter of every title for free.

## PAPER V





# A unified field theory of topological defects and non-linear local excitations

Vidar Skogvoll, Jonas Rønning, Marco Salvalaglio, and Luiza Angheluta

(Dated: March 29, 2023)

Topological defects and excitations of ground states determine the properties of systems exhibiting collective order. We introduce a general framework that comprehensively describes these excitations, including metastable configurations and transient dynamics, and show that it delivers general information for understanding and tailoring collective behaviors. We focus on systems with  $O(n)$  broken rotational symmetry described by order parameters which are uniform in the ordered phase and vanish in the disordered phase. From these smooth order parameters, we derive a non-singular defect density, a conserved quantity that tracks both topological defects and non-linear localized excitations. Its associated conserved density current is determined by the evolution of the order parameter and describes defect dynamics. Within this formalism, we explore fast events, such as defect nucleation/annihilation and dynamical phase transitions where the interaction between excitations becomes particularly important. In particular, we use this framework to highlight the similar topological structures and precursory patterns for the nucleation of topological defects in superfluid Bose-Einstein condensates, active nematics, and crystal lattices. For the last two examples, where translational symmetry is essential, our formalism also sheds light on a hierarchy of topological defects associated with coexisting broken symmetries and their role in dynamical transitions.

## I. INTRODUCTION

Topological defects are hallmarks of systems exhibiting collective order. They are widely encountered from condensed matter, including biological systems, to elementary particles, and the very early Universe [1–8]. The small-scale dynamics of interacting topological defects are crucial for the emergence of large-scale non-equilibrium phenomena, such as quantum turbulence in superfluids [9], spontaneous flows in active matter [10], or dislocation plasticity in crystals [11]. In fact, classical discrete modeling approaches such as point vortex models [12] and discrete dislocation dynamics [13] describe turbulence and plasticity in terms of the collective dynamics of topological defects as interacting charged points (in 2D) or line defects (in 3D). In most of these theories, the interactions of topological defects are modeled through the linear excitations that they induce in the far fields. The physics of events on short time- and length scales, such as core energies, nucleation conditions, defect interaction, etc., are often introduced by ad-hoc rules, such as cut-off parameters, Schmidt stress nucleation criteria, and defect line recombination rules. However, the dynamics of these events play a vital role in the transitions between different dynamical regimes. This is the case, for example, in stirred Bose-Einstein condensates where different superfluid flow regimes are observed depending on the size and speed of the moving obstacle [14–19], and where there is a subtle interplay between vortices and shock waves. Active nematic fluids are characterized by a dynamic transition to active turbulence at a sufficiently large activity where the spontaneous flows are sustained by the creation and annihilation of orientational defects [20, 21]. During plastic deformation of polycrystals, grains are progressively fragmented, a process governed by the nucleation and patterning of dislocations [22]. A number of macroscopic criteria exist for the nucleation of topological defects in crystals [23–

25]. Due to the highly non-linear nature of this process, however, it still remains poorly understood.

In this paper, we present a formalism to describe the evolution of ordered systems from the dynamics of their topological defects and their interactions with smooth but localized excitations. The versatility of the approach allows us to gain new insight into defect annihilation, the onset of collective behavior, and new perspectives on defect structures. In particular, we apply the method to systems of increasing topological and dynamical complexity. First, we study the motion of isolated vortices in Bose-Einstein condensates, which, in addition to confirming that the method correctly identifies topological defects and their velocities, sheds new light on changes in quantum pressure arising from the interplay between phase slips and shock waves. For active nematics, we observe that the onset of active turbulence as a melting of periodic arches is signaled by the formation of bound dipoles of nematic defects at the core of dislocations in the nematic arches. Similarly, bound dipoles of phase slips are also associated with the nucleation of dislocations in a crystal lattice.

The proposed approach builds upon the classical method introduced by Halperin and Mazenko (hereafter called the HM-method) [26, 27] to track and derive analytical results for topological defects. Therefore, in Section II, we begin with preliminary details of homotopy theory for topological defects and how the HM-method can be used for  $O(n)$ -symmetric theories to track their location and kinematics. In Sec. III, we then develop a non-singular field theory as a generalization of the HM-method which constitutes our primary reduced defect field. The method is then applied to the aforementioned physical systems in Secs. IV–VI. For the sake of readability, a rigorous derivation of the theoretical framework for arbitrary dimensions and details of the numerical simulations are reported in the Appendix. Conclusions and perspectives for further study are outlined in the final

section VII.

## II. CLASSICAL DESCRIPTION OF TOPOLOGICAL DEFECTS

Collective order is typically described by an order parameter field representative of symmetries and carrying information about topological defects and smooth, localized excitations. Although the order parameters are well-established for conventional systems, one often needs to define them for more novel/exotic systems [28, 29]. In this paper, we focus on well-known order parameters for systems with broken  $O(n)$  rotational symmetries, where  $n$  is the intrinsic dimension of the order parameter.

Homotopy theory provides a valuable identification and classification of topological defects [1]. The fundamental idea of homotopy theory is that the order parameter can be mapped onto a particular topological space  $R$  and that the elements of the *homotopy* group of  $R$  classify topological defects. For example, in the  $XY$ -model of ferromagnetism, and more generally for any system with  $O(2)$  broken symmetry, the order parameter is mapped by a 2D unit vector  $\mathbf{u}$  onto  $R = \mathcal{S}^1$ , the unit circle. The homotopy group of  $R = \mathcal{S}^1$  consists of closed circuits (loops) in  $R$  that are homotopically different, i.e., that cannot be continuously deformed into another. This group is isomorphic to  $\mathbb{Z}$  since the difference between two loops that are not homotopic is how many times they have looped around the circle  $\mathcal{S}^1$ . Therefore, in regions of space where  $\mathbf{u}$  is continuous and well-defined, a closed circuit  $\partial\mathcal{M}$  in real space corresponds to a closed circuit in  $\mathcal{S}^1$ , and the topological charge  $s_{\text{top}}$  contained in  $\partial\mathcal{M}$  is given as an integer by the isomorphism between homotopy group of  $\mathcal{S}^1$  and  $\mathbb{Z}$ . This topological charge is obtained from  $\mathbf{u} = (\cos \theta, \sin \theta)$ , by the contour integral

$$s_{\text{top}} = \frac{1}{2\pi} \oint_{\partial\mathcal{M}} d\theta, \quad (1)$$

which is invariant under any smooth deformations of  $\partial\mathcal{M}$ . This also implies that by shrinking  $\partial\mathcal{M}$  down to a point and given that  $s_{\text{top}}$  is a constant, there must be regions inside  $\partial\mathcal{M}$  where  $\mathbf{u}$  is undefined. These are the topological defects that have a  $s_{\text{top}}$  charge. Therefore, topological defects for  $R = \mathcal{S}^1$  in 2D are points with their charge determined by corresponding loop integration. On the other hand, such topological defects (with  $R = \mathcal{S}^1$ ) in three dimensions are *lines*.

In field theories of symmetry-breaking transitions, the ground state of the order parameter minimizes a free energy constructed from symmetry considerations. For broken rotational symmetries, the order parameter is a vector field  $\Psi$ , which in the ordered (ground) state has a constant magnitude  $|\Psi| = \Psi_0$ , meaning that the ground state manifold is  $\mathcal{S}^{n-1}$ , where  $n$  is the number of components of  $\Psi$ . The link between the order parameter  $\Psi$ , and 2D unit vector (director) field  $\mathbf{u} \in \text{mathcal{S}}^1$  is given by  $\mathbf{u} = \Psi/|\Psi|$  and topological defects are located

at positions where  $\mathbf{u}$  is undefined, which corresponds to  $|\Psi| = 0$  as shown in Fig. 1 (a-b).

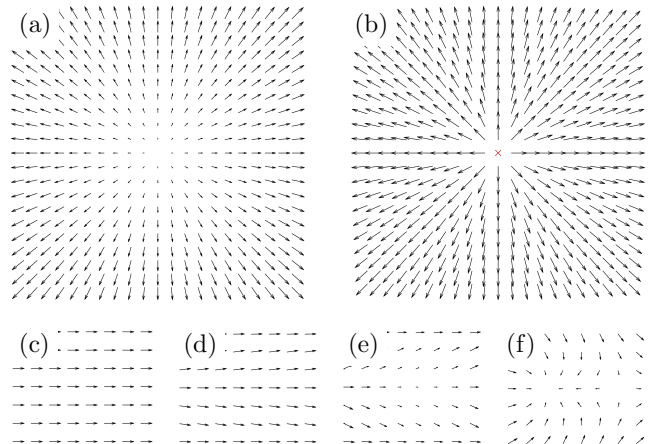


Figure 1. A +1 defect shown in (a) the order parameter field  $\Psi$  and (b) in the director field  $\mathbf{u} = \Psi/|\Psi|$ . Excitations of (c) the ground state can be categorized into (d) linear excitations with variations in the orientation of  $\Psi$ , (e) local non-linear excitations for which also the magnitude  $|\Psi|$  varies and (f) topological defects.

A description of topological defects as zeros of order parameters in  $O(n)$  models and their kinematics was proposed originally by Halperin and Mazenko in the context of phase-ordering kinetics [26, 27] and extended to systems driven out of equilibrium, such as in stirred Bose-Einstein condensation [18, 30, 31], active nematics [32, 33], and deformed crystals [34–36]. Sticking to  $O(2)$ -symmetry in two dimensions and using the definition of a topological charge given in Eq. (1), it is possible to express the topological defect density in terms of the zeros of the order parameter  $\Psi$  [26] tracked by Dirac-delta functions as

$$\rho_{\text{top}}(\mathbf{r}) \equiv \sum_{\alpha} q_{\alpha} \delta^{(2)}(\mathbf{r} - \mathbf{r}_{\alpha}) = D(\mathbf{r}) \delta^{(2)}(\Psi), \quad (2)$$

where  $q_{\alpha}$  and  $\mathbf{r}_{\alpha}$  are, respectively, the charge and position of the topological defect  $\alpha$ ,  $\delta^{(2)}(\Psi) = \delta(\Psi_1)\delta(\Psi_2)$ , and  $D(\mathbf{r})$  is the (signed) Jacobian determinant of the map  $\Psi$ ,

$$D = \frac{\partial(\Psi_1, \Psi_2)}{\partial(x, y)} = \partial_x \Psi_1 \partial_y \Psi_2 - \partial_x \Psi_2 \partial_y \Psi_1 \\ = \frac{1}{2} \epsilon^{ij} \bar{\epsilon}^{mn} (\partial_i \Psi_m) (\partial_j \Psi_n), \quad (3)$$

where  $\epsilon^{ij}$  ( $\bar{\epsilon}^{mn}$ ) are the components of the Levi-Civita tensor in real space (order parameter space). Nominally, the  $D$  field in Eq. (3) is evaluated at the location of the defect only, because of the  $\delta$ -function in Eq. (2).

## III. NON-SINGULAR DEFECT FIELDS

The  $\delta$ -function in the topological charge density of Eq. (2) locates the topological defects at singular points

where  $\mathbf{u}$  is undefined. In  $O(2)$  models, however, even though the ground state manifold is  $\mathcal{S}^1$ , the topological excitations have a finite core over which the magnitude of the order parameter goes smoothly to zero. This feature is also seen in physical systems, for instance, in liquid crystals, where optical retardance is an order parameter that goes to zero at the core. This has been used to quantify the size and structure of the defect cores in liquid crystals [37]. Motivated by this, we seek to generalize Eq. (2) in a way that will avoid singularities in the resulting charge density.

Since the equilibrium value  $\Psi_0$  of  $|\Psi|$  is constant, the order parameter effectively resides in  $\mathcal{D}^2$ , the unit disk. We propose in this paper that the simplest generalization of  $s_{\text{top}}$  is to consider the relative area of  $\mathcal{D}^2$  swept by  $\Psi$  on the circuit  $\partial\mathcal{M}$ . During an infinitesimal displacement along  $\partial\mathcal{M}$ ,  $\Psi$  sweeps the infinitesimal area given by half of the parallelogram spanned by  $\Psi$  and  $d\Psi$ . This (signed) area is given by  $\frac{1}{2}\tilde{\epsilon}^{mn}\Psi_m d\Psi_n$ , see Fig. 2. The complete area of  $\mathcal{D}^2$  is  $\pi\Psi_0^2$ , and we define the charge  $s$  as the area swept by  $\Psi$  relative to the area of  $\mathcal{D}^2$ ,

$$s = \frac{1}{\pi\Psi_0^2} \oint_{\partial\mathcal{M}} \frac{1}{2}\tilde{\epsilon}^{mn}\Psi_m d\Psi_n, \quad (4)$$

where  $\partial\mathcal{M}$  is defined as in Eq. (1). Naming  $s$  a ‘‘charge’’ suggests that it satisfies a global conservation law, which we shall prove shortly. The connection between  $s$  and  $s_{\text{top}}$  is made by recognizing that in the far field of a topological defect, where  $|\Psi| = \Psi_0$ , the infinitesimal area swept by  $\Psi$  is simply  $\frac{1}{2}\Psi_0^2 d\theta$ , so that the line integral along  $\partial\mathcal{M}$  gives the topological charge in the usual way. Closer to the core, however, the magnitude  $|\Psi|$  decreases and  $s$  is no longer an integer, which is why the associated defect density will give information about the core extent. Using Green’s theorem, we get

$$s = \frac{1}{2\pi\Psi_0^2} \oint_{\partial\mathcal{M}} \tilde{\epsilon}^{mn}\Psi_m \partial_k \Psi_n dl^k = \int_{\mathcal{M}} d^2r \rho(\mathbf{r}), \quad (5)$$

where  $\rho(\mathbf{r})$  is the charge density of  $s$ , given by

$$\rho(\mathbf{r}) = \frac{D(\mathbf{r})}{\pi\Psi_0^2}. \quad (6)$$

Whereas  $\rho_{\text{top}}$  describes topological defects as point singularities in the physical space,  $\rho$  describes topological defects with a finite core size.

The time derivative of Eq. (6) gives a continuity equation

$$\partial_t \rho + \nabla \cdot \mathbf{J} = 0, \quad (7)$$

with the current density determined by the evolution of the order parameter

$$J^i = -\frac{1}{\pi\Psi_0^2} \epsilon^{ij} \tilde{\epsilon}^{mn} (\partial_t \Psi_m) (\partial_j \Psi_n). \quad (8)$$

Thus,  $\rho$  is a globally conserved quantity, and the change in  $s$  contained in a circuit  $\partial\mathcal{M}$  is given by

$$\partial_t s = \partial_t \int_{\mathcal{M}} d^2r \rho(\mathbf{r}) = \int_{\partial\mathcal{M}} \mathbf{J} \cdot d\mathbf{n}, \quad (9)$$

where  $d\mathbf{n}$  is an infinitesimal surface area normal to the circuit  $\partial\mathcal{M}$ . Far away from defects,  $|\Psi| = \Psi_0$  and the time evolution of  $\Psi$  is carried by its phase  $\theta(\mathbf{r}, t)$  through  $\Psi = \Psi_0(\cos \theta, \sin \theta)$  which can be inserted in Eq. (8) to show that  $\mathbf{J} = \mathbf{0}$ . This means that linear perturbations of the ground state, which affect the orientation of  $\Psi$  only, are not described by the charge density  $\rho$ . However, it describes a certain type of local non-linear perturbations, where the magnitude is affected; see Fig. 1(c-f). We will exemplify this distinction in the applications. Due to the standard continuity form of Eq. (7), we can connect it to a velocity field  $\mathbf{v}$  through the charge flux  $\rho\mathbf{v}$ . Eq. (7) only determines the current  $\rho\mathbf{v}$  up to an unknown divergence free contribution  $\mathbf{K}$ , i.e.,  $\mathbf{v} = \frac{1}{\rho}(\mathbf{J} + \mathbf{K})$ , where  $\nabla \cdot \mathbf{K} = 0$ . However, when  $\rho \neq 0$ , there exists a unique velocity field  $\mathbf{v}^{(\Psi)}$  such that the evolution of  $\Psi$  can be written in a generic advection form  $\partial_t \Psi + (\mathbf{v}^{(\Psi)} \cdot \nabla) \Psi = 0$ , equivalently expressed as

$$\begin{pmatrix} \partial_t \Psi_1 \\ \partial_t \Psi_2 \end{pmatrix} + \begin{pmatrix} \partial_1 \Psi_1 & \partial_2 \Psi_1 \\ \partial_1 \Psi_2 & \partial_2 \Psi_2 \end{pmatrix} \begin{pmatrix} v_1^{(\Psi)} \\ v_2^{(\Psi)} \end{pmatrix} = 0. \quad (10)$$

This equation can be inverted to uniquely determine  $\mathbf{v}^{(\Psi)}$  if  $\det(\partial_i \Psi_n) = D(\mathbf{r}) \neq 0$ . To find  $\mathbf{v}^{(\Psi)}$  where this condition holds true, i.e. the regions of interest where also  $\rho(\mathbf{r}) \neq 0$  from Eq. (6), it is then possible to invert Eq. (10). However, it is easier to insert  $\partial_t \Psi = -(\mathbf{v}^{(\Psi)} \cdot \nabla) \Psi$  into the expression  $\mathbf{J}/\rho$  and see that it is  $\mathbf{a}$  (and therefore the *unique*) solution of Eq. (10). Thus, to fix the gauge on  $\mathbf{v}$ , we set  $\mathbf{K} = 0$  to get  $\mathbf{v} = \mathbf{v}^{(\Psi)}$  and find

$$v^i = \frac{J^i}{\rho} = -2 \frac{\epsilon^{ij} \tilde{\epsilon}^{mn} (\partial_t \Psi_m) (\partial_j \Psi_n)}{\epsilon^{ij} \tilde{\epsilon}^{mn} (\partial_i \Psi_m) (\partial_j \Psi_n)}, \quad (11)$$

where it is implied that repeated indices are summed over independently in the numerator and denominator. It follows that if a localized topological defect moves without changing its core structure, Eq. (11) will give this velocity in the region of the core independently of the values of  $\rho$ , which we shall shortly demonstrate. While the expression for the current of  $D$  and the velocity equation (11) have previously been used in the HM-method, several important distinctions can be highlighted. Firstly, the derivation of the  $\rho$  field from the redefined charge, Eq. (6), shows that the field carries topological information and does not only serve as auxiliary transformation determinants of  $\delta$ -functions. Secondly, the velocity field has previously only been rigorously shown to apply to topological defects. In contrast, this derivation also describes the velocity of  $\rho$  for other non-linear excitations. Thirdly, the fixing of the gauge  $\mathbf{K}$  has not been adequately addressed in previous works to the authors’ knowledge. While the derivation above was done for a  $n = 2$  order parameter in  $d = 2$  spatial dimensions for simplicity, topological defects exist whenever  $d \geq n$ . Eq. (4) can be generalized to arbitrary dimensions by replacing the integrand with the spanned volume of the  $n$ -sphere spanned by  $\Psi = (\Psi_1, \dots, \Psi_n)$  and normalizing

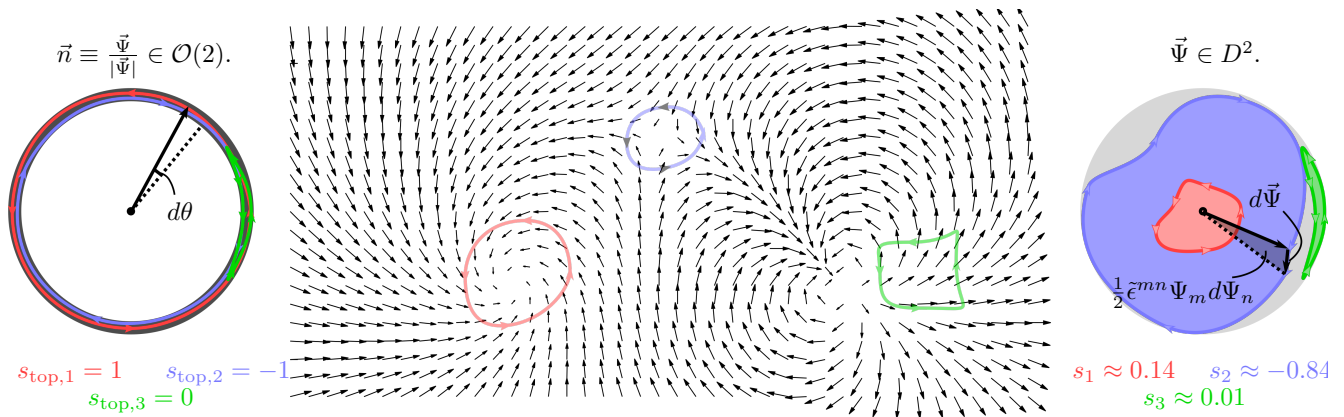


Figure 2. A continuous field  $\Psi(\mathbf{r})$  containing defects with integer charges  $+1$ , a  $-1$  and  $+2$  defect in the director field  $\mathbf{u}$ . The net integer topological charge contained in the circuits is given by the winding number of the director field  $\mathbf{u}$  in  $O(2)$ . The (signed) relative area gives the value of  $s$  for the circuits spanned by the order parameter  $\Psi$  in  $D^2$ .

by the volume  $V_n \Psi_0^n$  of the  $n$ -sphere. We show in Appendix A the formal derivation, and here we state the result that the charge density becomes

$$\begin{aligned} n = 1 : \quad \rho_i &= \frac{\partial_i \Psi}{2\Psi_0} \\ n \geq 2 : \quad \rho_{i_1 \dots i_{d-n}} &= \frac{D_{i_1 \dots i_{d-n}}}{V_n \Psi_0^n} \end{aligned} \quad (12)$$

with

$$D_{i_1 \dots i_{d-n}} = \frac{1}{n!} \epsilon^{\mu_1 \dots \mu_n} \tilde{\epsilon}^{\nu_1 \dots \nu_n} (\partial_{\mu_1} \Psi_{\nu_1}) \dots (\partial_{\mu_n} \Psi_{\nu_n}). \quad (13)$$

Generalizing the derivation of the defect kinematics, we find general expressions for the reduced defect velocity field

$$v^{\mu_1} = -n \frac{\delta_{\nu'_1}^{[\nu_1} \delta_{\nu'_2}^{\nu_2} \dots \delta_{\nu'_n}^{\nu_n]} (\partial_t \Psi_{\nu_1}) (\partial^{\mu_1} \Psi^{\nu_1}) \prod_{l=2}^n (\partial_{\mu_l} \Psi_{\nu_l}) (\partial^{\mu_l} \Psi^{\nu_l})}{\delta_{\nu'_1}^{[\nu_1} \delta_{\nu'_2}^{\nu_2} \dots \delta_{\nu'_n}^{\nu_n]} \prod_{l=1}^n (\partial_{\mu_l} \Psi_{\nu_l}) (\partial^{\mu_l} \Psi^{\nu_l})}, \quad (14)$$

$$\text{Special case } n = d : \quad v^{\mu_1} = -n \frac{\epsilon^{\mu_1 \mu_2 \dots \mu_n} \tilde{\epsilon}^{\nu_1 \dots \nu_n} (\partial_t \Psi_{\nu_1}) \prod_{l=2}^n (\partial_{\mu_l} \Psi_{\nu_l})}{\epsilon^{\mu_1 \dots \mu_n} \tilde{\epsilon}^{\nu_1 \dots \nu_n} \prod_{l=1}^n \partial_{\mu_l} \Psi_{\nu_l}}, \quad (15)$$

where  $[\nu_1 \nu_2 \dots \nu_n]$  is the antisymmetrization over the indices  $\nu_1 \nu_2 \dots \nu_n$ . Eq. (15) is the special case of  $n = d$ , where the velocity can be written in a simpler way. Still, Eq. (14) looks complicated due to the arbitrary number of dimensions and so we have summarized the most important cases of  $n \leq d \leq 3$  in Fig. 9 of Appendix A. Thus, Eqs. (12) and (14) are the primary general expressions of the reduced defect field. The equations generalize the description of topological defects in the HM-method to include both topological defects and non-linear excitations.

There are two important notes to be made on the generalization beyond the case  $d = n = 2$ . Firstly, for  $n \geq 2$ , the charge density is a rank  $(d - n)$  tensor that represents the defect density per  $n$ -dimensional volume-oriented *normal* to the manifold, e.g., how the charge density on a 2D surface is expressed in terms of the *normal* vector to the surface. The case of  $n = 1$  is special because densities on one-dimensional manifolds are usu-

ally expressed in terms of the density *along* the manifold, i.e., the charge density per length *along* the curve. Secondly, in the case of  $n < d$ , the gauge  $\mathbf{K}$  cannot be uniquely determined by looking at the evolution of  $\Psi$  alone. Therefore, another condition is required to obtain Eq. (14). The most natural choice is to restrict the velocity to be parallel to the charge density for  $n = 1$  and perpendicular to it for  $n \geq 2$ . This velocity will be normal to topological structures in the case of topological lines or walls. For further discussions, see Appendix A.

With the method at hand, we study phenomena involving both topological charges and non-linear local excitations through the reduced defect field and the information it conveys, such as the velocity of topological defects. This is done by considering progressively such phenomena in three representative systems with broken  $O(2)$  symmetry and featuring increasing complexity in terms of order parameters and collective behaviors. Both system-specific information and general behaviors will be

outlined. As a starting point, we consider a Bose-Einstein condensate where the order parameter is isomorphic to  $\Psi \in \mathcal{D}^2$  so that the method can be directly applied.

#### IV. DEFECT ANNIHILATION: VORTICES IN BOSE-EINSTEIN CONDENSATES

Within the Gross Pitaevskii theory of a superfluid Bose-Einstein condensate (BEC), the condensed bosons are described by a macroscopic wave function  $\psi$ , and its evolution can be described by damped Gross Pitaevskii equation [18, 38]

$$i\hbar\partial_t\psi = (1 - i\gamma) \left( -\frac{\hbar^2}{2m}\nabla^2 + g|\psi|^2 - \mu \right) \psi, \quad (16)$$

where  $g$  is an effective scattering parameter between condensate atoms,  $\gamma > 0$  is an effective thermal damping coefficient and  $\mu$  is the chemical potential. The complex condensate wavefunction  $\psi$  is isomorphic to a real 2D vector order parameter  $\Psi = (\Psi_1, \Psi_2)$  through  $\psi = \Psi_1 + i\Psi_2$ , the norm of which is given by the absolute value  $|\psi|$ . In the equilibrium ground state, the phase of  $\psi$  (and therefore the direction of  $\Psi$ ) is constant, and the magnitude is given by  $|\psi| = \Psi_0 = \sqrt{\mu/g}$ . Topological defects in the director field correspond to quantized vortices captured by the charge density field

$$\rho^{(\psi)}(\mathbf{r}) = \frac{gD(\mathbf{r})}{\pi\mu}. \quad (17)$$

In this context, the  $D$  field (calculated from  $\Psi$ ) has the physical interpretation of the generalized superfluid vorticity [31]. Linear perturbations of the ground state are phonons, which are characterized by traveling waves in the phase of the order parameter  $\psi$ , and will not be signaled in the defect density field  $\rho$ . Non-linear local perturbations, e.g., brought on by external stirring potentials or obstacles, will lead to a decrease in the magnitude of the order parameter near the obstacle [14, 16, 17, 39], leading to an increase in the quantum pressure, defined as

$$P = -\frac{\hbar^2}{2m} \frac{\nabla^2|\psi|}{|\psi|}. \quad (18)$$

Such excitations are detected by  $\rho^{(\psi)}$ , and mediate the nucleation or annihilation of topological defects. To showcase this, we simulate a BEC seeded with two vortices at  $(x, y) = (\pm 5, -10)$  as dictated by Eq. (16). Numerical details are reported in Appendix B 1. Dimensionless units are defined so that  $\hbar = m = g = \mu = 1$  and the damping coefficient is set to  $\gamma = 0.1$ . Figure 3 illustrates the defect density from Eq. (17) during the fast event of annihilating a vortex with an anti-vortex due to a small thermal drag.

The velocity field from Eq. (14) is plotted close to vortices and shows two exciting features. At the beginning

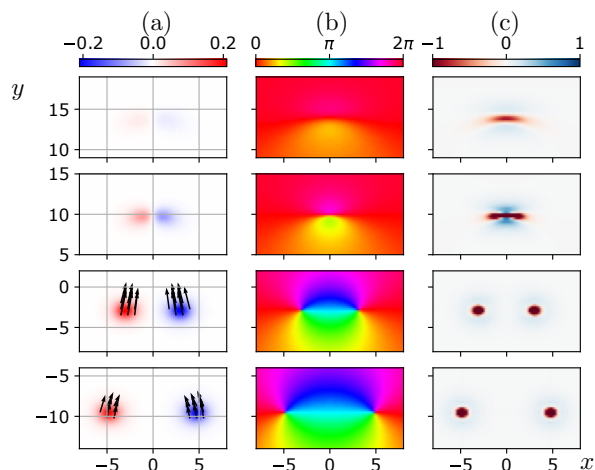


Figure 3. Annihilation of a vortex dipole in a Bose-Einstein condensate. Snapshots of (a) defect density, (b) condensate phase  $\arg(\psi)$  and (c) quantum pressure at different times from bottom to top: at  $t = 5$ ,  $t = 60$  (before annihilation),  $t = 105$  (after) and  $t = 110$ . (a) Defect velocity is included prior before annihilation. Notice in (b) the large phase gradients after the annihilation due to the induced shock-waves which can also be seen in the (c) quantum pressure profiles. The plots in column (c) have saturated colorbars because of the singular pressure at the defect core.

of the simulations ( $t = 5$ ), the non-uniform velocity over the vortex core indicates the early core deformation induced by the initial conditions. After this relaxation, however, vortices retain stationary or rigid cores, which feature a uniform velocity. After the annihilation event, we can see traces of their diffusive cores in the excitations produced by the vortex annihilation, as seen by the quantum pressure in the system, which is shown in Fig. 3(c). We will see in the following that similar traces appear as precursory patterns for defect nucleation. Moreover, after having dealt with a system with only one broken symmetry, we now consider systems that have multiple rotational or translational symmetries.

#### V. ONSET OF COLLECTIVE BEHAVIOR: ACTIVE NEMATICS

In this section, we consider the case of an active nematic system. This system is peculiar as we can construct the defect density from different order parameters. By applying the proposed formalism we can investigate the transition among different regimes and the interplay among defects. Interestingly, we will show that defects in one broken symmetry are the nucleation sites of defects for a separate order.

Within the hydrodynamic approach [40], the nematic orientational order of active matter in two dimensions is described by a rank-2 symmetric and traceless tensor  $Q$

determined by the nematic director  $\mathbf{n} = (\cos(\theta), \sin(\theta))$

$$Q = S \begin{pmatrix} n_1 n_1 - \frac{1}{2} & n_1 n_2 \\ n_2 n_1 & n_2 n_2 - \frac{1}{2} \end{pmatrix} \equiv \begin{pmatrix} \Psi_1 & \Psi_2 \\ \Psi_2 & -\Psi_1 \end{pmatrix}, \quad (19)$$

where  $S$  is an order parameter which is 0 in the disordered phase.  $Q$  is thus related to the  $\mathcal{D}^2$  order parameter  $\Psi$  field by  $\Psi = \frac{S}{2}(\cos(2\theta), \sin(2\theta))$ . The evolution of the  $Q$ -tensor follows dissipative dynamics coupled with an incompressible Stokes fluid flow [41]. Details on the evolution equation and its numerical method are reported in Appendix B. The system is here initialized in a homogeneous nematic phase with small perturbations in the angle of the director field. These perturbations are enhanced by the active stress creating a striped phase that is further destabilized and eventually melts due to the creation of topological defects leading into active turbulence. The ground state corresponds to constant a constant magnitude  $|\Psi| \equiv \Psi_0 = \sqrt{B}/2$  dependent on the parameter  $B$ , which is defined in Appendix B 2. Within the framework introduced in Sec. III, this gives the following expression for the defect density

$$\rho^{(Q)} = \frac{4D(\mathbf{r})}{\pi B}, \quad (20)$$

which supports orientational defects with half-integer charge  $s_{\text{top}} = \pm 1/2$ . In Fig. 4(a), we show the nematic orientation  $\theta$  in the colorbar to emphasize the breaking of translational symmetry and the formation of a (transient) striped order. The striped order arises from modulations in the nematic orientation which, to first order, do not change the magnitude of the order parameter  $\Psi$ . Thus, these are linear perturbations not signaled by  $\rho^{(Q)}$ .

The inset of Fig. 4(a) shows a dislocation in the periodic arches in the nematic director. To describe these defects, we represent the parameter  $\Psi$  as a complex field  $\psi = |\Psi|e^{i\theta}$  and decompose it into a slowly-varying amplitude field of the periodic arch mode as

$$\psi(\mathbf{r}) = \psi_0(\mathbf{r}) + \eta_{\mathbf{q}}(\mathbf{r})e^{i\mathbf{q}\cdot\mathbf{r}} + \eta_{-\mathbf{q}}(\mathbf{r})e^{-i\mathbf{q}\cdot\mathbf{r}}, \quad (21)$$

where  $\psi_0(\mathbf{r})$ ,  $\eta_{\mathbf{q}}$ ,  $\eta_{-\mathbf{q}}$ , are slowly-varying complex fields on the length scale  $a_0$  of the director field modulations.  $\mathbf{q}$  is the wave vector of the modulations which is  $\mathbf{q} = \frac{2\pi}{a_0}\mathbf{e}_x$  due to the initial condition. We can extract the complex amplitude of a  $\mathbf{q}$  mode by a demodulation of  $\psi$ ,

$$\eta_{\mathbf{q}} = \langle \psi e^{-i\mathbf{q}\cdot\mathbf{r}} \rangle, \quad (22)$$

through the convolution with a Gaussian kernel denoted by  $\langle \cdot \rangle$ , which filters out the small-scale variations (Eq. (B6) with  $w = a_0$ ). The modulation length scale  $a_0$  and the equilibrium value  $\eta_0$  of  $|\eta_{\mathbf{q}}|$  are found numerically to be  $a_0 = 10.6$  and  $\eta_0 = 0.20$  for the given parameters. From the order parameter  $\eta_{\mathbf{q}}$ , we can construct the defect density  $\rho^{(\eta_{\mathbf{q}})}$  as for the complex wavefunction in the BEC. This field locates the dislocations from the nematic arches as shown in panel (b) at  $t = 240$ , just prior to the nucleation of nematic defects.

By also showing the reduced defect field  $\rho^{(Q)}$  associated with the rotational symmetry (Fig. 4(c)), we clearly notice that each dislocation detected by  $\rho^{(\eta_{\mathbf{q}})}$  is a source for the nucleation of a dipole of half-integer defects. The precursory pattern of the two bound defects prior to nucleation is similar to the pattern retained by the dipole annihilation in the BEC. However, for active nematics, the bound state is associated with a dislocation in the periodic arches, while for BECs it is a source of quantum pressure. Notice also that the core size of the defects in the state with broken translational symmetry is much bigger than that of the nematic order. The spontaneous nucleation of  $\pm 1/2$  defects from the dissociation of dislocations occurs very fast and simultaneously at various locations, such that the system quickly transitions to active turbulence, where the translational symmetry is fully restored. In this state,  $\rho^{(\eta_{\mathbf{q}})}$  decreases by an order of magnitude and no longer shows well-defined topological defects, which is natural because a description in terms of dislocations in translational order is no longer meaningful. From  $\rho^{(Q)}$  and the velocity formula in Eq. (14), we can track the velocity  $v = \langle |\mathbf{v}| \rangle$  of  $\pm 1/2$  defects at the onset of the nucleation event (insets in Fig. 4). Figure 4(e) shows that prior to nucleation, the two defects have the same speed in their bound state as positive and negative charge coalesce. Once they unbound through nucleation, the  $+1/2$  defect self-propels due to activity.

To summarise this part, our analysis offers an alternative perspective on the onset of active turbulence using the presence of competing symmetries. The transition to a turbulent state from a periodic arch state seems to be mediated by the dissociation of one type of topological defect into a different kind associated with changes in the global symmetries. In the following section, we study a system where the order parameters with  $O(n)$ -symmetry are found by decomposing a more complicated topological space.

## VI. DEFECT STRUCTURES: SOLID CRYSTALS

We focus here on the study of defects and collective order in crystals. The ground state manifold for three-dimensional crystal lattices is the 3-torus  $\mathcal{T}^3$ . However, a factorization into product topology of fundamental  $\mathcal{S}^1$  spaces can be considered and has a straightforward physical interpretation related to the crystals having a well-defined (Bravais) reference lattice reflecting the broken translational symmetry. As discussed below, this implies that the dislocation can be represented as bound vortices in the amplitudes of the fundamental periodic modes, similar to vortices as discussed in previous sections. Indeed, by applying the formalism introduced in Sec. III, analogies with previously discussed systems emerge, as well as peculiar features which will be discussed in detail.

Local distortions from the ground state are character-



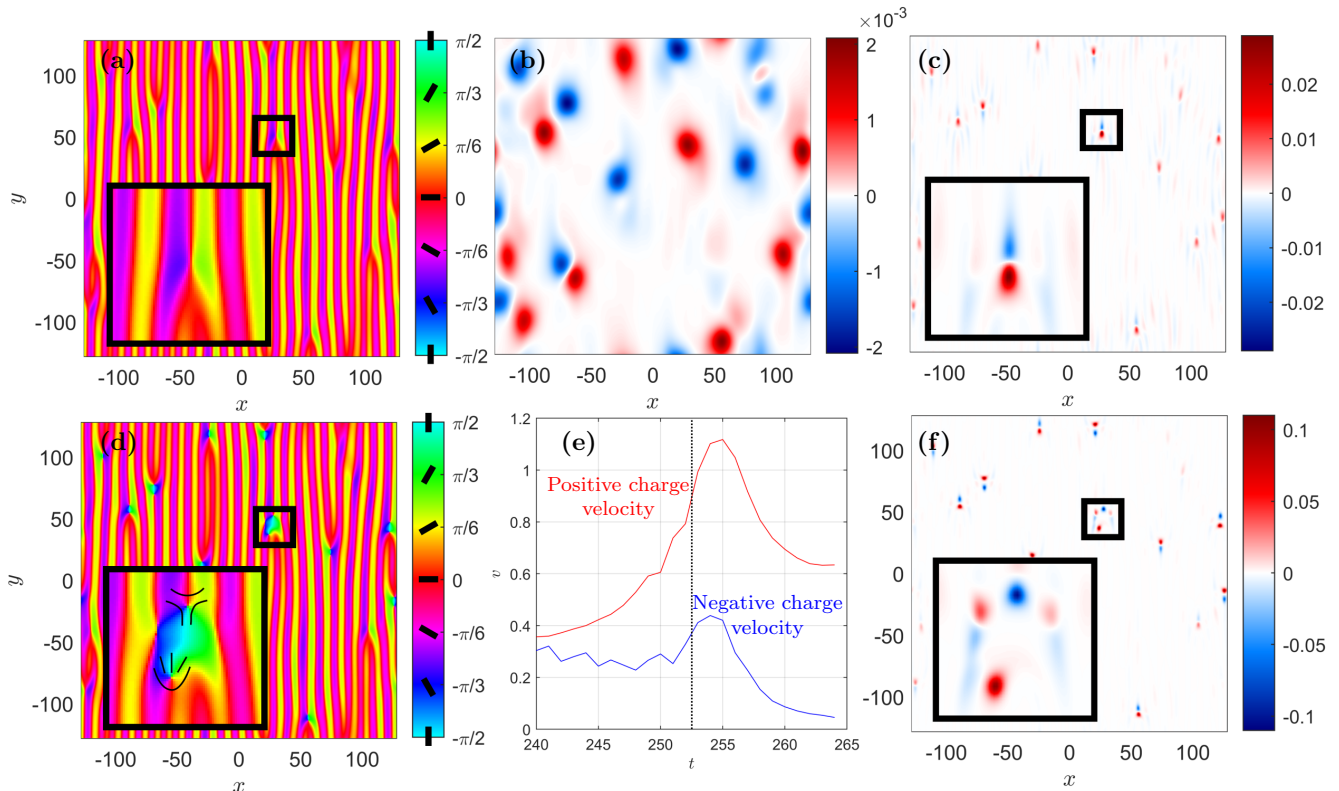


Figure 4. (a) The angle of the nematic director at  $t = 240$ , prior to nucleation of half-integer defects from the unstable periodic arches, and (d) at  $t = 260$ , after nucleation. (b) The defect density  $\rho^{(nq)}$  at  $t = 240$ , corresponding to the broken translational symmetry, shows the charge signature of dislocations with large core structures. The dislocation core harbors a bound dipole (inset) shown in (c) the defect density  $\rho^{(Q)}$  of the charge density associated to nematic order, which splits into fully formed  $\pm \frac{1}{2}$  defects after nucleation as shown in (f)  $\rho^{(Q)}$  at  $t = 260$ . Panel (e) shows the average velocity  $v = \langle |\mathbf{v}| \rangle$  of the positive and negative defect charge at the nucleation site as a function of time  $t$ , where the dashed line indicates the time of nucleation (see text).

ized by a displacement field  $\mathbf{u} \in \mathcal{T}^3$  as a function of space, which supports topological line defects, i.e., dislocations. For a path  $\partial\mathcal{M}$  in real space circling one such defect, the charge is given by the vector difference between the end and starting point, namely the Burgers' vector  $\mathbf{b}$ ,

$$\oint_{\partial\mathcal{M}} d\mathbf{u} = -\mathbf{b}, \quad (23)$$

(minus sign by convention). The corresponding dislocation density tensor  $\alpha_{ij}$  is defined through the integral of some 2D surface  $\mathcal{M}$  bounded by  $\partial\mathcal{M}$

$$\int_{\mathcal{M}} \alpha_{ij} n^i dS = b_j, \quad (24)$$

where  $\mathbf{n}$  is the normal vector to the surface element  $dS$ .

In the conserved Swift-Hohenberg modeling of crystal lattices, commonly named phase-field crystal (PFC) [42, 43], the order parameter is a weakly distorted periodic scalar field  $\psi(\mathbf{r})$ , which preserves the crystalline symme-

tries and can be approximated as

$$\psi(\mathbf{r}) = \bar{\psi} + \sum_{n=1}^N \eta_n e^{i\mathbf{q}^{(n)} \cdot \mathbf{r}}, \quad (25)$$

where  $\bar{\psi}$  and  $\{\eta_n\}_{n=1}^N$  are slowly varying (on the lattice unit length scale) amplitude fields, and  $N$  is the number of reciprocal lattice vectors  $\{\mathbf{q}^{(n)}\}_{n=1}^N$  taken into consideration. For a perfect lattice,  $\bar{\psi}(\mathbf{r}) = \psi_0$  and  $\eta_n(\mathbf{r}) = \eta_0$  are constant, and an affine displacement  $\mathbf{r} \rightarrow \mathbf{r} - \mathbf{u}$  amounts to a phase change  $\eta_n = \eta_0 e^{-\mathbf{q}^{(n)} \cdot \mathbf{u}}$ . As mentioned, the 3-torus is the product space  $\mathcal{T}^3 = \mathcal{S}^1 \times \mathcal{S}^1 \times \mathcal{S}^1$ , which can be seen explicitly by multiplying Eq. (23) with a reciprocal lattice vector  $\mathbf{q}^{(n)}$  of the structure, which gives

$$\oint_{\partial\mathcal{M}} d(\mathbf{q}^{(n)} \cdot \mathbf{u}) = -2\pi s_n, \quad (26)$$

where  $s_n$  is an integer by definition of the reciprocal lattice vector. This shows that the phase of an amplitude  $\theta_n \equiv (-\mathbf{q}^{(n)} \cdot \mathbf{u})$  is a topological order parameter that has integer winding numbers, i.e.,  $\theta_n \in \mathcal{S}^1$ .



The amplitude  $\eta_n$  acts as an order parameter in  $\mathcal{D}^2$ , i.e.,  $\Psi_1 = \Re(\eta_n)$  and  $\Psi_2 = \Im(\eta_n)$ . A topological description of dislocations using the HM-framework has been provided in two and three dimensions in Refs. [34, 36]. Here, we adopt an alternative and convenient description using the charge density from Eq. (12), which is a vector field for 3D lattices

$$\rho_i^{(\eta_n)} = \frac{D_i^{(n)}}{\pi\Psi_0^2}, \quad (27)$$

where

$$\mathbf{D}^{(n)} = \begin{pmatrix} (\partial_y \Psi_1)(\partial_z \Psi_2) - (\partial_y \Psi_2)(\partial_z \Psi_1) \\ (\partial_x \Psi_2)(\partial_y \Psi_1) - (\partial_x \Psi_1)(\partial_y \Psi_2) \\ (\partial_x \Psi_1)(\partial_y \Psi_2) - (\partial_x \Psi_2)(\partial_y \Psi_1) \end{pmatrix}. \quad (28)$$

By contracting Eq. (24) with  $q^j$ , we can relate the dislocation density tensor with the defect charge density in a given amplitude [36]

$$\alpha_{ij} = \frac{2d}{N\eta_0^2} \sum_{n=1}^N D_i^{(n)} q_j^{(n)}, \quad (29)$$

where  $d$  is the spatial dimension. The amplitudes  $\eta_n$  used to calculate  $D^{(n)}$  are extracted from the phase-field  $\psi$  as in Eq. 22, and only the modes corresponding to the shortest reciprocal lattice vectors are used to calculate  $\alpha_{ij}$ .

Next, we focus on two examples to highlight new insights obtained from using this approach. We consider the nucleation of dislocations in a square lattice from the point of view of its precursory pattern formations and quantify the dislocation core size. Then, we consider the classical inclusion problem of a rotated spherical crystal embedded in another crystal with the same lattice symmetry, to show how the surface of the inclusion changes its topology as a function of the lattice misorientation.

### 1. Dislocations in 2D square lattices

A minimal PFC free energy minimized by a square lattice reads [44, 45]

$$F_\psi^{\text{sq}} = \int d^2r \left( \frac{1}{2} (\mathcal{L}_1 \mathcal{L}_2 \psi)^2 + \frac{r}{2} \psi^2 + \frac{1}{4} \psi^4 \right), \quad (30)$$

where  $\mathcal{L}_X = X + \nabla^2$  and  $r$  is a parameter. The minimizer field  $\psi$ , for certain model parameters, has a perfect square lattice symmetry with an accurate two-mode amplitude expansion

$$\psi = \bar{\psi} + \sum_{n=1}^2 \eta_n e^{i\mathbf{q}^{(n)} \cdot \mathbf{r}} + \sum_{n=3}^4 \eta_n e^{i\mathbf{q}^{(n)} \cdot \mathbf{r}} + \text{c.c.}, \quad (31)$$

where  $\{\mathbf{q}^{(n)}\} = \{(1, 0), (0, 1), (1, 1), (1, -1)\}$  are the reciprocal lattice vectors of the square lattice with lengths

1 and  $\sqrt{2}$ . This sets the characteristic length  $a_0 = 2\pi$  of the system, which is the width of the square unit cell. At equilibrium, the amplitude field  $\eta_n$  goes to the equilibrium values  $\eta_{1,2} \rightarrow A_{\text{sq}}$ ,  $\eta_{3,4} \rightarrow B_{\text{sq}}$ . The characteristic unit of stress is given by the elastic shear modulus  $\mu = 16B_{\text{sq}}^2$  [45]. The dislocation density tensor can be factorized as  $\alpha_{ij} = t_i \mathcal{B}_j$ , where  $\mathcal{B}$  is a 2D Burgers vector density and  $\mathbf{t}$  the tangent vector to the dislocation line. In two dimensions, we define  $\mathbf{t}$  to point out-of-plane so that the Burgers vector density is given by

$$\mathcal{B} = (\alpha_{31}, \alpha_{32}). \quad (32)$$

We initiate a perfect square lattice of  $101 \times 101$  unit cells and use the sHPFC model of Ref. [46] to apply a local stress in the central region which causes the nucleation of a dislocation dipole. The PFC deforms gradually, trying to account for the externally imposed stress, increasing from linear to non-linear strains until nucleation of a pure  $\pm a_0 \mathbf{e}_x$  dislocation dipole. Once formed, these dislocations move under the action of the Peach-Koehler force [47], namely they separate at large speeds due to the external stress and slow down as they reach the far-field regions of the crystal. Simulation details are given in Appendix B 3. Figure 5 shows the region of applied stress during the nucleation event. Like for the nucleation of nematic defects, the nucleation is singled by a precursory localised pattern formation in the Burgers vector density, which corresponds to a bound dipole of phase slips. While variations only in the phase of the complex amplitudes are associated with linear elastic perturbations, non-linear elastic strains cause a decrease in the equilibrium value of the amplitudes [48] and so produce a signal in the reduced defect density given by the expression of the dislocation density. Thus, the excitations visible in the dislocation density  $\mathcal{B}$  prior to nucleation are due to non-linear elastic strains. From the signal profile, Fig. 5(c), we observe that these large non-linear elastic strains can be connected to a bound dislocation dipole.

From the defect density corresponding to  $\eta_1$  for  $\mathbf{q} = (1, 0)$ , we can also determine the average velocity  $v = \langle |\mathbf{v}| \rangle$  of dislocations with positive and negative charge before and after nucleation. The defect speed as a function of time is shown in Fig. 5(e). Like for the nucleation of defects in the active nematic, we observe a speed build up prior to nucleation succeeded by a relaxation to a constant speed. Unlike the  $\pm 1/2$  defects in active nematics, however, both dislocations are equally mobile in this case.

The Burgers vector density, in addition to describing the process of nucleation itself, provides us with useful information about the defect core. To extract the core size directly from the Burger vector density without free-tuning parameters, we consider a coarse-grained version of the PFC model, namely its amplitude expansion (APFC) [49, 50]. This approach gives access to phases and lattice deformation directly rather than through the demodulation of Eq. (22). It builds on the definition of a free energy functional  $F_\eta$  derived from the PFC free energy  $F_\psi^{\text{sq}}$  under the approximation of slowly-varying

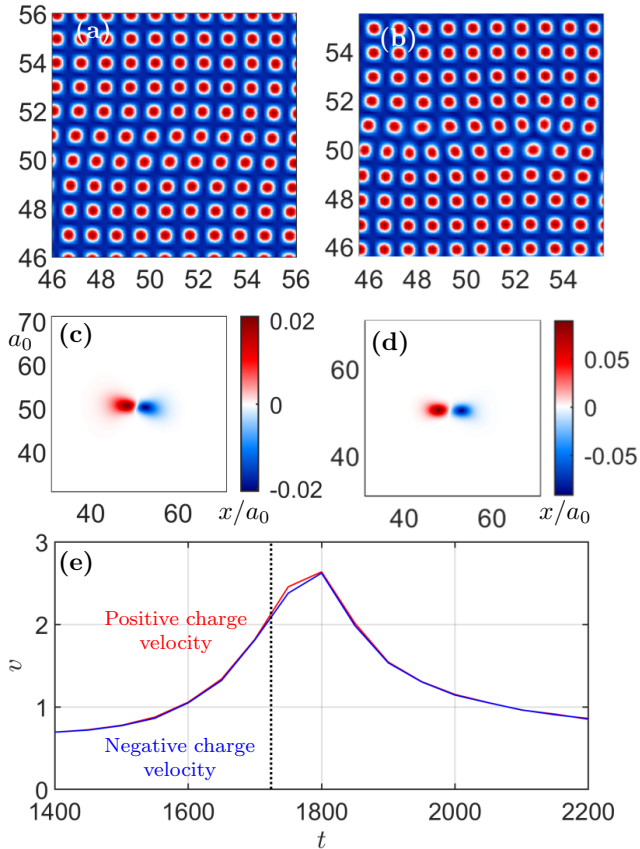


Figure 5. (a) The PFC at  $t = 1600$  prior to the nucleation of (b) a dislocation dipole at  $t = 1800$ . Panels (c) and (d) show the  $x$ -component  $\mathcal{B}_x$  of the dislocation density  $\mathcal{B}$  at  $t = 1600$  and  $t = 1800$ , respectively. The magnitude of  $\mathcal{B}_y$  is, in both cases, two orders of magnitude smaller and not shown. (e) The average velocity  $v = \langle |\mathbf{v}| \rangle$  at the nucleation site of positive charge ( $\mathcal{B}_x > 0$ ) and negative charge ( $\mathcal{B}_x < 0$ ) where the dashed line indicates the time of nucleation (see text).

amplitudes. We simulate a square lattice hosting dislocations in a static, periodic configuration, and focus on a single defect therein. The expression for  $F_\eta$ , the choice of  $\mathbf{q}^{(n)}$ , and details of the simulation setup are given in Appendix B 4. For the given lattice structure, the extension of its core depends on the parameters  $r'$  and  $s$  in the free energy  $F_\eta$ . The parameter  $r'$  corresponds to a phenomenological temperature controlling a first-order order-disorder phase transition at  $r' = r_0$  with  $r_0$  the critical point and ordered (disordered) phase for  $r' < r_0$  ( $r' > r_0$ ), and  $s$  is a constant scaling the elastic moduli [51, 52].  $\Delta r = r_0 - r'$  is referred to as the quenching depth. These parameters affect the competition among gradient terms and the bulk energy terms in  $F_\eta$ . Fig. 6(a)–(b) illustrate two different core sizes for the same dislocation obtained with different values for  $r'$  and  $s$ . They show the reconstructed densities obtained by computing Eq. (25) with the numerical solution for the amplitudes (first column), the Burgers vector den-

sity component  $\mathcal{B}_x$  (second column), a plot of  $\mathcal{B}_x(x, 0)$  and  $\mathcal{B}_x(0, y)$  (third column, empty symbols) with Gaussian fits (solid lines). The data fitting is obtained via  $G \exp(-x^2/2\sigma_x^2 - y^2/2\sigma_y^2)$  with  $G$ ,  $\sigma_x$  and  $\sigma_y$  fitting parameters (dashed lines), well reproducing its shape and allowing for an estimation of the core size. The definition here introduced for the Burgers vector density fully characterizes the loss of coherency at the dislocation core. Importantly, it realizes a spreading of the topological charge at the core similar to non-singular continuum theories based either on regularization of singularities [53] or within strain-gradient elasticity theories [54, 55].

The amplitude expansion defined in Eq. (25), and thus the density field  $\psi$ , correspond to the sum of plane waves (Fourier modes) which are periodic stripe phases similar to the one shown in Fig. 4. The dislocation in the crystal then corresponds to the superposition of defects in such stripe phases. Interestingly, dislocations do not necessarily correspond to a defect for all the coupled stripe phases. Indeed, by applying Eq. (1) to the phase of the amplitudes one gets  $-\oint \mathbf{q}^{(n)} \cdot \mathbf{u} = 2\pi \mathbf{q}^{(n)} \cdot \mathbf{b}$ . At least for perfect dislocations, those having a translation vector of the lattice as Burgers vector, we have that  $\mathbf{q}^{(n)} \cdot \mathbf{b} = 0$ , for some  $n$ . Thus, while for stripe phases, the (single) order parameter vanishes at the core, de-facto corresponding to a disordered phase, a different ordered phase forms at the core of dislocations in periodic density fields. This is further shown in Fig. 6(c), reporting the fields  $\eta_n e^{i\mathbf{q}^{(n)} \cdot \mathbf{r}}$  entering the sum in Eq. (25). Three out of four stripe phases ( $n = 1, 3, 4$ ) vanish at the core, while one ( $n = 2$ ) features a small variation of its amplitudes with no topological content.

The defect core can then be interpreted as a transition region between two different ordered phases, one of which is present at the dislocation core only. By comparing its extension with the width of a solid-liquid interface,  $w$ , which corresponds to the order-disorder correlation length, we find some analogies and differences in the dependence on the parameters entering the free energy. For the latter, traveling-wave solutions exist with amplitudes having hyperbolic tangent profiles and width  $\xi \propto \sqrt{s}/(1 + \sqrt{1 - 8r'/9r_0})$  [52, 56, 57]. Measuring the size of the core through  $\sigma_x$  and  $\sigma_y$  from a Gaussian fit as in Fig. 6(a)–(b), we find that it scales linearly with  $w$  when varying  $s$ , while a different scaling is observed when varying  $r'$ , c.f. Fig. 6(d). The width  $w$  is computed here for an interface with normal along the  $x$ -axis ( $\langle 10 \rangle$  crystallographic direction, further details are reported in Appendix B 4). Here  $s$  is an energy scale that is associated with gradients in the amplitudes, similar to theories based on Ginzburg-Landau energy functionals [57].  $r'$ , instead, affects the equilibrium values of the amplitudes, which are qualitatively different for an interface, where they all vanish in the disordered phase, and a defect, where some amplitudes are non-zero owing to a non-singular phase (see Fig. 6(c)). Also, for  $r' \neq r_0$ , interfaces move, which affects the width  $w$  [58]. A more detailed analysis would require finding a solution

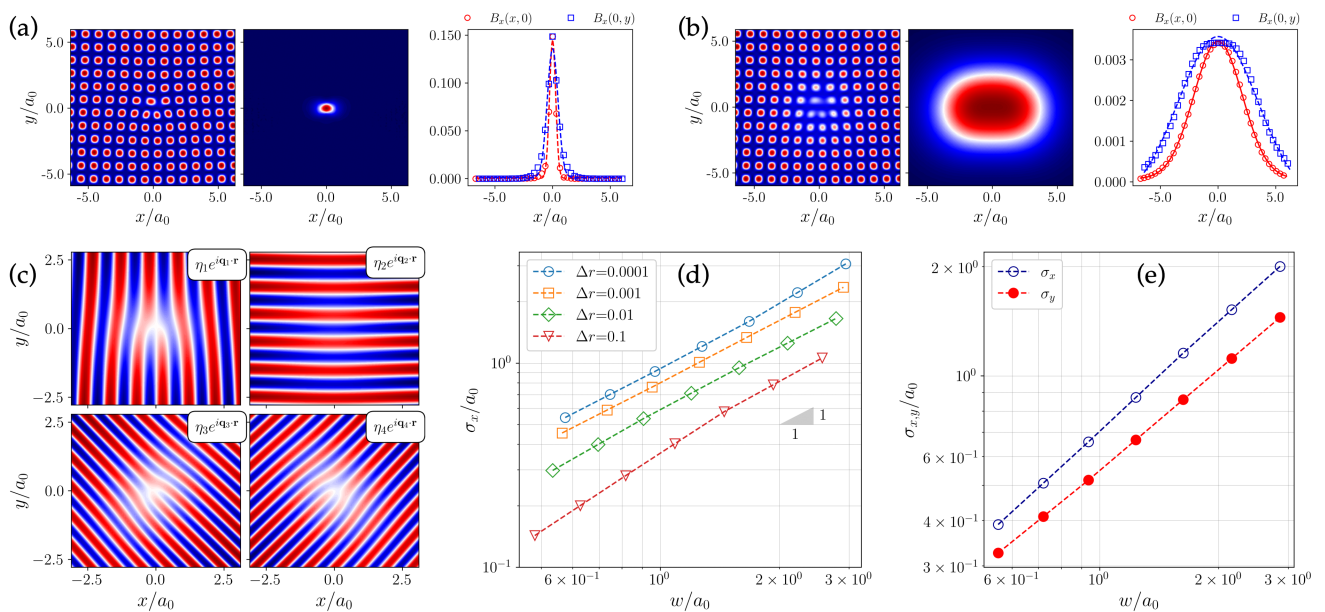


Figure 6. Dislocation core size near melting by APFC modeling. (a)–(b) Reconstructed density (left),  $\mathcal{B}_x$  (center), and  $\mathcal{B}_x$  along  $x$  and  $y$  direction for a relatively small and large core size, respectively obtained with (a)  $\Delta r = 10^{-4}$ ,  $s = 3.16$  and (b)  $\Delta r = 10^{-1}$ ,  $s = 1$ , with  $r_0 = 7.455 \cdot 10^{-2}$  the critical point. Symbols show values from APFC simulations; dashed lines correspond to Gaussian fits. The latter are exploited to quantify the size of the core in terms of the variance along  $x$  and  $y$ , namely  $\sigma_x$  and  $\sigma_y$ . (c) Periodic modes  $\eta_n e^{i \mathbf{q}_n \cdot \mathbf{r}} + \text{c.c.}$  for the density in panel (b). (d) Core size in terms of  $\sigma_x$  as a function of the order-disorder correlation length  $w$ , for various values of  $s$  and  $r'$  (the latter shown by different colors and symbols). (e) Comparison of  $\sigma_x$  and  $\sigma_y$  as function of  $w$  for  $\Delta r = 0.00464$  and  $s \in [10^{-1}, 3.16]$ .

for the amplitudes' profile at defects, which goes beyond the goals of this investigation and will be addressed in future work.

The evaluation of the Burgers vector density also allows for the characterization of anisotropies in the behavior of phases at the core as illustrated in Fig. 6(d).  $\sigma_y/\sigma_x \approx 0.75$  throughout the whole range of parameters investigated here as also illustrated in Fig. 6(e). This may be ascribed to the asymmetry introduced by the specific orientation of the Burgers vector. We conclude that, for systems described by order parameters as in the phase-field crystal model, as well as in descriptions exploited in previous sections, the defect density may be exploited to characterize the loss of coherency at defects.

## 2. Order transition for 3D crystal inclusions

Like the melting of translational order in the nematic liquid crystal through the nucleation of defects in the nematic field, the global translational order in a single crystal is also destroyed under large deformations and rotations. To highlight this, we use a full 3D PFC model corresponding to a cubic lattice for which the PFC density in the one-mode approximation reads as

$$\psi(\mathbf{r}) = \psi_0 + \sum_{\mathbf{q} \in \mathcal{R}_{\text{bcc}}^{(1)}} \eta_0 e^{i \mathbf{q}^{(n)} \cdot \mathbf{r}}, \quad (33)$$

where  $\mathcal{R}_{\text{bcc}}^{(1)}$  are the reciprocal lattice vectors of the bcc Bravais lattice with unit length [45]. This sets the length of the bcc unit cell as  $a_0 = 2\pi\sqrt{2}$ . We consider spherical inclusions with radius  $17a_0$ , rotated at an angle  $\theta_{\text{rot}}$  about the  $[1, 1, 1]$ -axis. The initial condition is relaxed by dissipative dynamics with an appropriate symmetry-conserving free energy; see further details in Appendix B 5. We choose three representative angles  $\theta_{\text{rot}}$  and calculate the Frobenius norm  $|\alpha| = \sqrt{\alpha^{ij} \alpha_{ij}}$  of  $\alpha$  at each angle. Since  $|\alpha| > 0$ , we plot its isosurface at half its maximum value  $|\alpha|_M = \max_{\mathbf{r}} (|\alpha|(\mathbf{r}))$  in Fig. 7 for three representative misorientation angles  $\theta_{\text{rot}}$ . For small lattice misorientations,  $|\alpha| \ll 1$ , indicating only slight non-linear elastic excitations (and no fully formed dislocations) at the interface between the inclusion and the matrix. As expected, these non-linear strains are largest in the plane perpendicular to the rotation axis, since the rotation deformation field scales with distance from the rotation axis. Notably, we observe a three-fold symmetry in the profile of  $|\alpha|$ , which can be ascribed to the underlying crystallographic orientation. For larger values of  $\theta_{\text{rot}}$ , the non-linear distortions increase and localize into a network of dislocations. Notice that such a defect network is determined directly by the Burgers vector density rather than through arbitrary reconstructions [59, 60]. The description breaks down at large misorientations, as witnessed by the decrease in the magnitude of the defect density field since there is no longer a global transla-

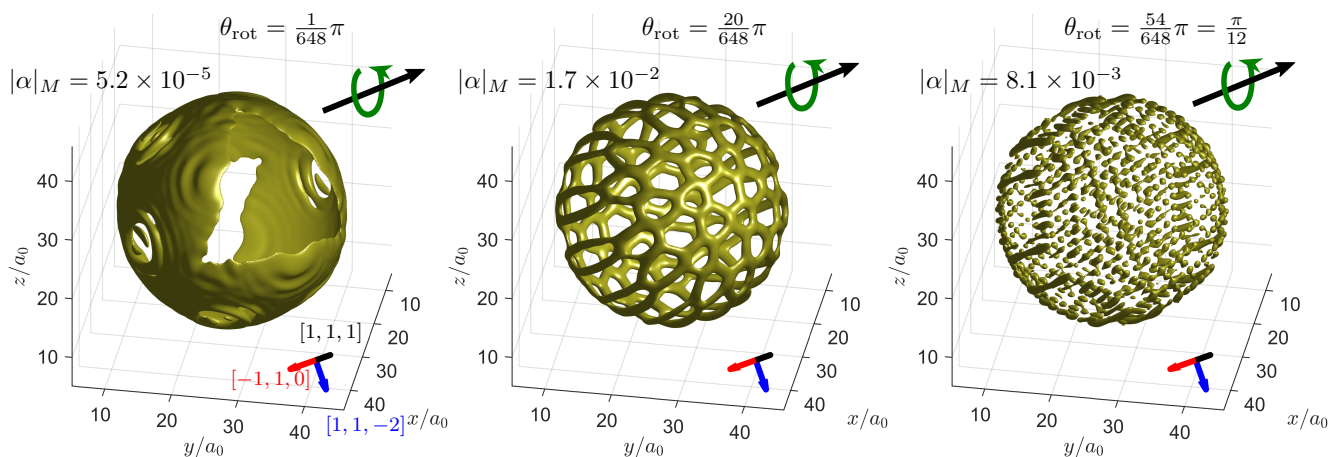


Figure 7. Rotated inclusions in the bcc PFC model. The panels show, for three representative rotation angles  $\theta_{\text{rot}}$  the isosurface of the Frobenius norm of the coarse dislocation density tensor  $|\alpha| = \sqrt{\alpha^{ij}\alpha_{ij}}$  at 50% of its maximal value  $|\alpha|_M = \max_{\mathbf{r}}(|\alpha|(\mathbf{r}))$ , which is given in the panels.

tional order. Indeed, large misorientations lead to the nucleation of grain boundaries which are fully described by accounting for the bicrystallography of the two crystals meeting at the interface rather than the deformation with respect to a reference lattice [61]. Such a regime shift echoes the onset of active turbulence in the nematic liquid, where the description in terms of the order parameter  $\rho^{(\eta_a)}$  also breaks down due to the destruction of global translational order.

## VII. CONCLUSIONS

In-depth understanding and tailoring of collective behaviors require a unified description of defects associated with symmetry breaking and the non-topological excitations of ground states. Here, we proposed a systematic way of deriving reduced defect fields from order parameters associated with  $O(n)$  broken symmetries which captures topological defects, localized non-linear excitations, and their dynamics. This enables the non-singular description of defects and their interaction, accounting for precursory and resulting patterns involving non-topological excitations. Moreover, the proposed framework can be used to study concurrent symmetry breakings and order transitions. Applications to systems of general interest, such as superfluids, active nematics, and solid crystals, are shown to showcase the considered framework, while we envisage applications in many other contexts.

We have shown that the method accurately tracks topological defects since these appear as localized blobs in the defect density field. The associated current density and velocity field determine the kinematics of the defects, and its utility has been shown to extend beyond tracking the velocity of topological defects. For example, in the case of the motion of vortices in a BEC, the velocity field

accounts for both the overall velocity of the defect and local variations associated with the early-stage rearrangements of the defect core evolving towards its stationary shape. Thus, the uniformity of the velocity field over the core extent tests whether the frozen-core approximation [1] is valid. For active nematics and solid crystals, the velocity formula is shown to track the dynamics of defect dipoles, during, and after the nucleation of topological defects, pointing at interesting analogies and differences between processes in different physical systems. The rigorous derivation of these fields given in the appendix for any dimensions makes the equations readily applicable to tracking topological defects and localized excitations in general.

We have found interesting features and new insights about the evolution of these systems with broken symmetries. After the annihilation of the vortex dipole in the BEC, the remaining shock wave produces a signal in the defect density field that echoes the charge density pattern of the dipole. In the active nematics, the large cores of the dislocation in the translational order harbor a bound dipole of orientational defects associated with the rotational order. This picture presents the idea of a hierarchy of topological defects, where the defects associated with one symmetry can spontaneously dissociate into stable defects for a different symmetry and melt the former ordered state. This is a non-equilibrium transition that echos the equilibrium Kosterlitz-Thouless transition for melting of 2D crystals via the hexatic phase [62].

In the case of a 3D crystal, a rotated inclusion was shown to be described as a network of topological defects (dislocations) up to a point before these dissociated into other types of defects (grain boundaries) and the global orientational order was destroyed. The best topological description of polycrystalline materials is an open challenge, even though candidates, such as interacting disconnections [61], exist. Applying this formalism to

such topologies is a fascinating avenue of research. Employing the APFC framework, where the periodic nature of crystal densities is inherently coarse-grained, we have shown that dislocation cores in Swift-Hohenberg theories emerge as transition regions from crystalline to pointwise stripe-like phases. When approaching the solid-liquid coexistence limit, analogies between the dislocation core size and the extensions of order-disordered interfaces have been found.

Finally, while the whole framework is presented for systems with one broken rotational symmetry, it is a powerful tool that can be generalized to systems with multiple broken symmetries and reveal hidden hierarchies of topological defects associated with each symmetry, laying the foundation for unified theories in systems characterized by collective behaviors.

#### **ACKNOWLEDGEMENT**

We are grateful to Jorge Viñals for many interesting discussions. M.S. acknowledges support from the German Research Foundation (DFG) under Grant No. SA4032/2-1. Computing resources have been provided by the Center for Information Services and High-Performance Computing (ZIH) at TU-Dresden.

#### **AUTHOR CONTRIBUTIONS**

V.S: concept and theory development, simulations, data analysis, manuscript writings. J.R: concept and theory development, simulations, data analysis, manuscript writings. M.S: concept and theory development, supervision, simulations, manuscript writings. L.A: concept and theory development, supervision, manuscript writings.

#### **CONFLICTS OF INTEREST**

The authors declare that there are no competing interests.

#### **DATA AVAILABILITY**

The data will be provided by the corresponding author upon reasonable request.

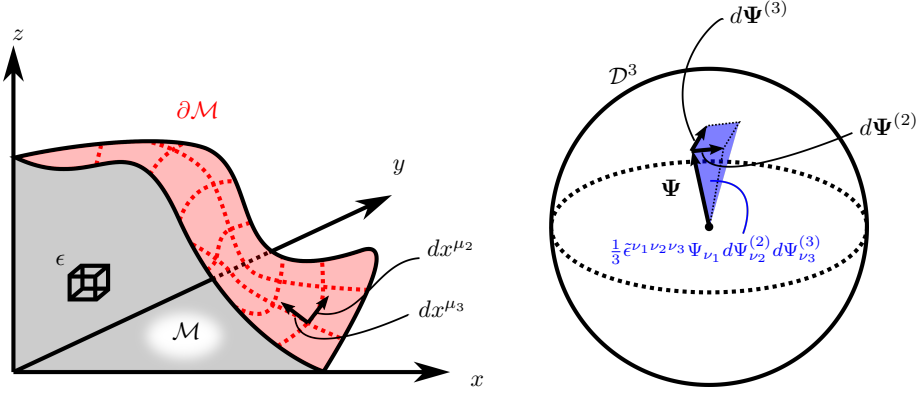


Figure 8. Real 3D space and order parameter space for a  $\mathcal{D}^3$  order parameter.  $\partial\mathcal{M}$  is the boundary of a 3D subvolume  $\mathcal{M}$ , on which variations along the surface ( $dx^{\mu_2}, dx^{\mu_3}$ ) lead to variations of the order parameter ( $d\Psi^{(2)}, d\Psi^{(3)}$ ).

### Appendix A: Generalization to arbitrary dimensions

For the proofs in this section, we follow the notation conventions of Ref. [63]. We consider topological defects for  $\mathcal{S}^k$  order parameters, which is the space consisting of  $(k+1)$ -dimensional unit vectors. It is known that the  $i$ -th homotopy group of  $\mathcal{S}^k$  is trivial for  $i < k$ . In particular, every loop ( $i = 1$ ) on the two-sphere ( $k = 2$ ) can be reduced to a point by a continuous deformation. Thus, to get a description of the topological defects for  $\mathcal{S}^k$  order parameters, we need to consider the  $k$ -th homotopy groups  $\pi_k(\mathcal{S}^k) \simeq \mathbb{Z}$  corresponding to topological defects with integer charges. The dimension of the defect is given by  $d_{\text{top}} = d - (k+1)$ , where  $d$  is the physical space dimension. The homotopy classification of loops in  $\mathcal{S}^k$  is useful beyond the direct application to models from this group because, in many systems, their order parameter space can be mapped or decomposed into products of  $\mathcal{S}^k$  spaces. We define an order parameter  $\Psi = (\Psi_1, \dots, \Psi_n)$  which resides in the order parameter space  $\mathcal{D}^n$ . The subvolume of  $\mathcal{D}^n$  swept by  $\Psi$  and  $n-1$  independent variations  $\{d\Psi^{(k)}\}_{k=2}^n$  is given by the (signed) volume of the  $n$ -dimensional cone

$$\frac{1}{n} \tilde{\epsilon}^{\nu_1 \dots \nu_n} \Psi_{\nu_1} d\Psi_{\nu_2}^{(2)} \dots d\Psi_{\nu_n}^{(n)}, \quad (\text{A1})$$

where  $\tilde{\epsilon}^{\nu_1 \dots \nu_n}$  are the components of the Levi-Civita tensor in order parameter space. See Fig. 8 for an example of  $n = d = 3$ . The charge  $s$  is then given as the natural generalization of Eq. (4), i.e.,

$$s = \frac{1}{V_n \Psi_0^n} \oint_{\partial\mathcal{M}} \frac{1}{n} \tilde{\epsilon}^{\nu_1 \dots \nu_n} \Psi_{\nu_1} d\Psi_{\nu_2}^{(2)} \dots d\Psi_{\nu_n}^{(n)}. \quad (\text{A2})$$

Here,  $\partial\mathcal{M}$  is a  $(n-1)$ -dimensional submanifold of  $\mathbb{R}^d$ , the boundary of some  $n$ -dimensional submanifold  $\mathcal{M}$ , and  $\{d\Psi^{(k)}\}_{k=2}^n$  are changes in  $\Psi$  due to displacements  $dx^\mu$  on  $\partial\mathcal{M}$ . Formally, we write the integrand in terms of the coordinates  $\{x^\mu\}_{\mu=1}^d$  of  $\mathbb{R}^d$  as follows

$$\omega = \frac{1}{n} \tilde{\epsilon}^{\nu_1 \dots \nu_n} \Psi_{\nu_1} (\partial_{\mu_2} \Psi_{\nu_2}) \dots (\partial_{\mu_n} \Psi_{\nu_n}) dx^{\mu_2} \otimes \dots \otimes dx^{\mu_n}, \quad (\text{A3})$$

Since  $\omega_{\mu_2 \dots \mu_n}$  is completely anti-symmetric under interchange of indices,  $\omega$  is a  $(n-1)$ -form and we can apply Stokes' generalized theorem

$$\oint_{\partial\mathcal{M}} \omega = \int_{\mathcal{M}} d\omega \quad (\text{A4})$$

where  $d\omega$  is the exterior derivative of  $\omega$ , whose components are given by

$$(d\omega)_{\mu_1 \dots \mu_n} = n \partial_{[\mu_1} \omega_{\mu_2 \dots \mu_n]} = \partial_{[\mu_1} (\tilde{\epsilon}^{\nu_1 \dots \nu_n} \Psi_{\nu_1} (\partial_{\mu_2} \Psi_{\nu_2}) \dots (\partial_{\mu_n} \Psi_{\nu_n})) = \tilde{\epsilon}^{\nu_1 \dots \nu_n} (\partial_{\mu_1} \Psi_{\nu_1}) \dots (\partial_{\mu_n} \Psi_{\nu_n}), \quad (\text{A5})$$

where the notation  $[\dots]$  is the antisymmetrization over free indices  $(\mu_1 \dots \mu_n)$ . Thus, we get

$$s = \frac{1}{V_n \Psi_0^n} \int_{\mathcal{M}} \tilde{\epsilon}^{\nu_1 \dots \nu_n} (\partial_{\mu_1} \Psi_{\nu_1}) \dots (\partial_{\mu_n} \Psi_{\nu_n}) dx^{\mu_1} \otimes \dots \otimes dx^{\mu_n}. \quad (\text{A6})$$



In the case of  $n = 1$ , for which  $V_1 = 2$ , integrals over  $\mathcal{M}$  are typically evaluated in this way, i.e., as line integrals over the one-dimensional manifold  $\mathcal{M}$ . We then immediately recover the defect density for  $n = 1$ , given by

$$\boxed{\rho_\mu = \frac{\partial_\mu \Psi}{2\Psi_0} \quad (n = 1).} \quad (\text{A7})$$

For higher values of  $n$ , however, one evaluates the integral in coordinates on the manifold  $\mathcal{M}$ . Thus, at each point, we choose  $d - n$  orthogonal unit vectors  $\{\mathbf{n}_{(k)}\}_{k=1}^{d-n}$  normal to the manifold  $\mathcal{M}$  and introduce local coordinates  $\{y^i\}_{i=1}^n$  on  $\mathcal{M}$ . Expressed in these coordinates, we have

$$\begin{aligned} s &= \frac{1}{V_n \Psi_0^n} \int_{\mathcal{M}} \tilde{\epsilon}^{\nu_1 \dots \nu_n} (\partial_{\tau_1} \Psi_{\nu_1}) \dots (\partial_{\tau_n} \Psi_{\nu_n}) dy^{\tau_1} \otimes \dots \otimes dy^{\tau_n} \\ &= \frac{1}{V_n \Psi_0^n} \int_{\mathcal{M}} \tilde{\epsilon}^{\nu_1 \dots \nu_n} (\partial_{\tau_1} \Psi_{\nu_1}) \dots (\partial_{\tau_n} \Psi_{\nu_n}) \delta_{\kappa_1}^{\tau_1} \dots \delta_{\kappa_n}^{\tau_n} dy^{\kappa_1} \otimes \dots \otimes dy^{\kappa_n}, \end{aligned} \quad (\text{A8})$$

where  $\tau$ -indices iterate from 1 to  $n$ . Now, we invoke the identity

$$n! \delta_{\kappa_1}^{[\tau_1} \dots \delta_{\kappa_n}^{\tau_n]} = \tilde{\epsilon}^{\tau_1 \dots \tau_n} \hat{\epsilon}_{\kappa_1 \dots \kappa_n} \quad (\text{A9})$$

where  $\hat{\epsilon}$  is the Levi-Civita tensor on  $\mathcal{M}$ , i.e., the induced volume element from  $\mathbb{R}^d$ . Using the fact that the integrand is already anti-symmetric in  $\tau$ -indices, we can replace  $\delta_{\kappa_1}^{\tau_1} \dots \delta_{\kappa_n}^{\tau_n} \rightarrow \delta_{\kappa_1}^{[\tau_1} \dots \delta_{\kappa_n}^{\tau_n]}$  and get

$$\begin{aligned} s &= \frac{1}{V_n \Psi_0^n} \int_{\mathcal{M}} \tilde{\epsilon}^{\nu_1 \dots \nu_n} (\partial_{\tau_1} \Psi_{\nu_1}) \dots (\partial_{\tau_n} \Psi_{\nu_n}) \frac{1}{n!} \tilde{\epsilon}^{\tau_1 \dots \tau_n} \hat{\epsilon}_{\kappa_1 \dots \kappa_n} dy^{\kappa_1} \otimes \dots \otimes dy^{\kappa_n} \\ &= \frac{1}{V_n \Psi_0^n} \int_{\mathcal{M}} \frac{1}{n!} \hat{\epsilon}^{\tau_1 \dots \tau_n} \tilde{\epsilon}^{\nu_1 \dots \nu_n} (\partial_{\tau_1} \Psi_{\nu_1}) \dots (\partial_{\tau_n} \Psi_{\nu_n}) \hat{\epsilon} \end{aligned} \quad (\text{A10})$$

Finally, we want to express the integrand in terms of coordinates of  $\mathbb{R}^d$ . Using that  $\hat{\epsilon}$  expressed in these coordinates is

$$\hat{\epsilon}^{\mu_1 \dots \mu_n} = N^{i_1 \dots i_{d-n}} \epsilon_{i_1 \dots i_{d-n}}^{\mu_1 \dots \mu_n} \quad (\text{A11})$$

where  $N^{i_1 \dots i_{d-n}} \equiv n_{(1)}^{i_1} \dots n_{(d-n)}^{i_{d-n}}$ , we get

$$s = \frac{1}{V_n \Psi_0^n} \int_{\mathcal{M}} \frac{1}{n!} \epsilon^{\mu_1 \dots \mu_n}_{i_1 \dots i_{d-n}} \tilde{\epsilon}^{\nu_1 \dots \nu_n} (\partial_{\mu_1} \Psi_{\nu_1}) \dots (\partial_{\mu_n} \Psi_{\nu_n}) N^{i_1 \dots i_{d-n}} \hat{\epsilon} \quad (\text{A12})$$

Identifying  $N^{i_1 \dots i_{d-n}} \hat{\epsilon}$  as the oriented volume element of  $\mathcal{M}$ , we identify the defect density as

$$\boxed{\rho_{i_1 \dots i_{d-n}} = \frac{D_{i_1 \dots i_{d-n}}}{V_n \Psi_0^n} \quad (n \geq 2)} \quad (\text{A13})$$

where

$$D_{i_1 \dots i_{d-n}} = \frac{1}{n!} \epsilon^{\mu_1 \dots \mu_n}_{i_1 \dots i_{d-n}} \tilde{\epsilon}^{\nu_1 \dots \nu_n} (\partial_{\mu_1} \Psi_{\nu_1}) \dots (\partial_{\mu_n} \Psi_{\nu_n}). \quad (\text{A14})$$

We now turn to finding the general equation for the velocity of the defect density. To differentiate Eq. (A13) with respect to time, consider

$$\begin{aligned} \partial_t D_{i_1 \dots i_{d-n}} &= \partial_t \left( \frac{1}{n!} \epsilon^{\mu_1 \dots \mu_n}_{i_1 \dots i_{d-n}} \tilde{\epsilon}^{\nu_1 \dots \nu_n} (\partial_{\mu_1} \Psi_{\nu_1}) \dots (\partial_{\mu_n} \Psi_{\nu_n}) \right) \\ &= \frac{1}{n!} \epsilon^{\mu_1 \dots \mu_n}_{i_1 \dots i_{d-n}} \tilde{\epsilon}^{\nu_1 \dots \nu_n} \left( (\partial_{\mu_1} \partial_t \Psi_{\nu_1}) \dots (\partial_{\mu_n} \Psi_{\nu_n}) + \dots + (\partial_{\mu_1} \Psi_{\nu_1}) \dots (\partial_{\mu_n} \partial_t \Psi_{\nu_n}) \right) \\ &= \frac{1}{n!} \epsilon^{\mu_1 \dots \mu_n}_{i_1 \dots i_{d-n}} \tilde{\epsilon}^{\nu_1 \dots \nu_n} \left( (\partial_{\mu_1} \partial_t \Psi_{\nu_1}) \dots (\partial_{\mu_n} \Psi_{\nu_n}) + \dots + (\partial_{\mu_n} \Psi_{\nu_n}) + \dots + (\partial_{\mu_n} \Psi_{\nu_n}) \dots (\partial_{\mu_1} \partial_t \Psi_{\nu_1}) \right) \\ &= \frac{1}{(n-1)!} \epsilon^{\mu_1 \dots \mu_n}_{i_1 \dots i_{d-n}} \tilde{\epsilon}^{\nu_1 \dots \nu_n} (\partial_{\mu_1} \partial_t \Psi_{\nu_1}) \dots (\partial_{\mu_n} \Psi_{\nu_n}) \\ &= \partial_{\mu_1} \left( \frac{1}{(n-1)!} \epsilon^{\mu_1 \dots \mu_n}_{i_1 \dots i_{d-n}} \tilde{\epsilon}^{\nu_1 \dots \nu_n} (\partial_t \Psi_{\nu_1}) \dots (\partial_{\mu_n} \Psi_{\nu_n}) \right), \end{aligned} \quad (\text{A15})$$

where, in going from line 2 to 3, we have used that due to the contraction with both the anti-symmetric Levi-Civitas, the terms are invariant under simultaneously interchanging  $\mu_k \leftrightarrow \mu_{k'}$  and  $\nu_k \leftrightarrow \nu_{k'}$ , so that we can write every term in the parenthesis like the first. In going from line 4 to 5, we have used that the contraction with  $\epsilon^{\mu_1 \dots \mu_n}_{i_1 \dots i_{d-n}}$  ensures that only the first term survives when applying the product rule. Thus, we find  $\partial_t \rho_{i_1 \dots i_{d-n}} + \partial_{\mu_1} J^{\mu_1}_{i_1 \dots i_{d-n}} = 0$ , where

$$J^{\mu_1}_{i_1 \dots i_{d-n}} = \frac{-1}{V_n \Psi_0^n (n-1)!} \epsilon^{\mu_1 \mu_2 \dots \mu_n}_{i_1 \dots i_{d-n}} \tilde{\epsilon}^{\nu_1 \dots \nu_n} (\partial_t \Psi_{\nu_1}) (\partial_{\mu_2} \Psi_{\nu_2}) \dots (\partial_{\mu_n} \Psi_{\nu_n}). \quad (\text{A16})$$

Like for the  $d = n = 2$  case, we want to identify this expression with the density current  $v^{\mu_1} \rho_{i_1 \dots i_{d-n}}$ . They are related up to a divergence free contribution  $\partial_{\mu_1} K^{\mu_1}_{i_1 \dots i_{d-n}} = 0$ , so

$$v^m \rho_{i_1 \dots i_{d-n}} = J^{\mu_1}_{i_1 \dots i_{d-n}} + K^{\mu_1}_{i_1 \dots i_{d-n}}. \quad (\text{A17})$$

In the  $d = n = 2$  case, the charge density on the left-hand side had no free indices and so we could simply divide by the charge density to solve for  $\mathbf{v}$ . In the general case, however, we project the equation by contracting with  $\frac{\rho^{i_1 \dots i_{d-n}}}{|\rho|^2}$ , where  $|\rho| = \sqrt{\rho^{i_1 \dots i_{d-n}} \rho_{i_1 \dots i_{d-n}}}$  is the Frobenius norm, and get

$$v_1^\mu = \frac{\rho^{i_1 \dots i_{d-n}} J^{\mu_1}_{i_1 \dots i_{d-n}}}{|\rho|^2} + \frac{\rho_{i_1 \dots i_{d-n}} K^{\mu_1}_{i_1 \dots i_{d-n}}}{|\rho|^2}. \quad (\text{A18})$$

In order to fix the gauge  $K^{\mu_1}_{i_1 \dots i_{d-n}}$ , we look at the evolution of the order parameter  $\Psi$  as advected by a velocity field  $\mathbf{v}(\Psi)$

$$\partial_t \Psi_n + v^{\mu_1}_{(\Psi)} \partial_{\mu_1} \Psi_n = 0. \quad (\text{A19})$$

These are  $n$  linearly independent linear equations to determine  $d$  components of the velocity  $\mathbf{v}(\Psi)$ . If  $n < d$ , it is under-determined and therefore  $d - n$  additional equations are needed to determine  $v^{\mu_1}$  uniquely. We define

$$\begin{aligned} v_{\text{candidate}}^{\mu_1} &\equiv \frac{\rho^{i_1 \dots i_{d-n}} J^{\mu_1}_{i_1 \dots i_{d-n}}}{|\rho|^2} \\ &= \frac{\frac{1}{n!} \epsilon_{\mu'_1 \dots \mu'_n}^{i_1 \dots i_{d-n}} \tilde{\epsilon}_{\nu'_1 \dots \nu'_n} (\partial_{\mu'_1} \Psi^{\nu'_1}) \dots (\partial_{\mu'_n} \Psi^{\nu'_n}) \frac{-1}{(n-1)!} \epsilon^{\mu_1 \mu_2 \dots \mu_n}_{i_1 \dots i_{d-n}} \tilde{\epsilon}^{\nu_1 \dots \nu_n} (\partial_t \Psi_{\nu_1}) (\partial_{\mu_2} \Psi_{\nu_2}) \dots (\partial_{\mu_n} \Psi_{\nu_n})}{|D|^2} \\ &= - \frac{(d-n)! \delta_{[\mu'_1}^{\mu_2} \delta_{\mu'_2}^{\mu_3} \dots \delta_{\mu'_n}^{\mu_n]} \tilde{\epsilon}_{\nu'_1 \dots \nu'_n} (\partial_{\mu'_1} \Psi^{\nu'_1}) \dots (\partial_{\mu'_n} \Psi^{\nu'_n}) \tilde{\epsilon}^{\nu_1 \dots \nu_n} (\partial_t \Psi_{\nu_1}) (\partial_{\mu_2} \Psi_{\nu_2}) \dots (\partial_{\mu_n} \Psi_{\nu_n})}{(n-1)! |D|^2} \\ &= - \frac{(d-n)! n! \delta_{\nu'_1}^{[\nu_1} \dots \delta_{\nu'_n}^{\nu_n]} (\partial^{\mu_1} \Psi^{\nu'_1}) \dots (\partial^{\mu_n} \Psi^{\nu'_n}) (\partial_t \Psi_{\nu_1}) (\partial_{\mu_2} \Psi_{\nu_2}) \dots (\partial_{\mu_n} \Psi_{\nu_n})}{(n-1)! |D|^2} \\ &= - \frac{(d-n)! n}{|D|^2} \delta_{\nu'_1}^{[\nu_1} \dots \delta_{\nu'_n}^{\nu_n]} (\partial_t \Psi_{\nu_1}) (\partial^{\mu_1} \Psi^{\nu'_1}) \prod_{l=2}^n (\partial_{\mu_l} \Psi_{\nu_l}) (\partial^{\mu_l} \Psi^{\nu'_l}) \quad (\text{A20}) \end{aligned}$$

Calculating  $|D|^2$  gives

$$\begin{aligned} |D|^2 &= \frac{1}{n!} \epsilon^{\mu_1 \dots \mu_n}_{i_1 \dots i_{d-n}} \tilde{\epsilon}^{\nu_1 \dots \nu_n} (\partial_{\mu_1} \Psi_{\nu_1}) \dots (\partial_{\mu_n} \Psi_{\nu_n}) \frac{1}{n!} \epsilon_{\mu'_1 \dots \mu'_n}^{i_1 \dots i_{d-n}} \tilde{\epsilon}_{\nu'_1 \dots \nu'_n} (\partial^{\mu_1} \Psi^{\nu'_1}) \dots (\partial^{\mu_n} \Psi^{\nu'_n}) \\ &= \frac{1}{(n!)^2} n! (d-n)! \delta_{\mu'_1}^{[\mu_1} \dots \delta_{\mu'_n}^{\mu_n]} \tilde{\epsilon}^{\nu_1 \dots \nu_n} (\partial_{\mu_1} \Psi_{\nu_1}) \dots (\partial_{\mu_n} \Psi_{\nu_n}) \tilde{\epsilon}_{\nu'_1 \dots \nu'_n} (\partial^{\mu_1} \Psi^{\nu'_1}) \dots (\partial^{\mu_n} \Psi^{\nu'_n}) \\ &= (d-n)! \delta_{\nu'_1}^{[\nu_1} \dots \delta_{\nu'_n}^{\nu_n]} \prod_{l=1}^n (\partial_{\mu_l} \Psi_{\nu_l}) (\partial^{\mu_l} \Psi^{\nu'_l}). \quad (\text{A21}) \end{aligned}$$

which gives

$$v_{\text{candidate}}^{\mu_1} = -n \frac{\delta_{\nu'_1}^{[\nu_1} \dots \delta_{\nu'_n}^{\nu_n]} (\partial_t \Psi_{\nu_1}) (\partial^{\mu_1} \Psi^{\nu'_1}) \prod_{l=2}^n (\partial_{\mu_l} \Psi_{\nu_l}) (\partial^{\mu_l} \Psi^{\nu'_l})}{\delta_{\nu'_1}^{[\nu_1} \dots \delta_{\nu'_n}^{\nu_n]} \prod_{l=1}^n (\partial_{\mu_l} \Psi_{\nu_l}) (\partial^{\mu_l} \Psi^{\nu'_l})} \quad (\text{A22})$$



where it is understood that the repeated indices are summed over independently in the numerator and denominator. By inserting this expression in the LHS of Eq. (A19) after multiplying by the denominator, we get

$$\underbrace{\delta_{\nu'_1}^{[\nu_1 \dots \nu_n]} \left( \prod_{l=1}^n (\partial_{\mu_l} \Psi_{\nu_l}) (\partial^{\mu_l} \Psi^{\nu'_l}) \right)}_{\text{(Mercury)}} \partial_t \Psi_k - \underbrace{n \delta_{\nu'_1}^{[\nu_1 \dots \nu_n]} (\partial_t \Psi_{\nu_1}) (\partial^{\mu_1} \Psi^{\nu'_1}) \left( \prod_{l=2}^n (\partial_{\mu_l} \Psi_{\nu_l}) (\partial^{\mu_l} \Psi^{\nu'_l}) \right)}_{\text{(Venus)}} \partial_{\mu_1} \Psi_k. \quad (\text{A23})$$

We split the term (Venus) into  $\nu_1 = k$  and  $\nu_1 \neq k$  as follows

$$\begin{aligned} \text{(Venus)} = & \underbrace{n \delta_{\nu'_1}^{[k \delta_{\nu'_2}^{\nu_2} \dots \delta_{\nu'_n}^{\nu_n}]} (\partial_t \Psi_k) (\partial^{\mu_1} \Psi^{\nu'_1}) \left( \prod_{l=2}^n (\partial_{\mu_l} \Psi_{\nu_l}) (\partial^{\mu_l} \Psi^{\nu'_l}) \right)}_{\text{(Tellus)}} \partial_{\mu_1} \Psi_k \\ & + n \underbrace{\sum_{\nu_1 \neq k} \delta_{\nu'_1}^{[\nu_1 \dots \nu_n]} (\partial_t \Psi_{\nu_1}) (\partial^{\mu_1} \Psi^{\nu'_1}) \left( \prod_{l=2}^n (\partial_{\mu_l} \Psi_{\nu_l}) (\partial^{\mu_l} \Psi^{\nu'_l}) \right)}_{\text{(Mars)}} \partial_{\mu_1} \Psi_k. \end{aligned} \quad (\text{A24})$$

(Mars) is identically zero, which the following argument shows: Because of the antisymmetrization over  $\nu_1 \dots \nu_n$ , in every term in (Mars)  $\nu_1, \dots, \nu_n$  will take every value  $1, \dots, n$ . Since  $\nu_1 \neq k$ , it means that there is some  $m > 1$  such that  $\nu_m = k$ . Isolating the corresponding factor from the product, we get

$$\text{(Mars)} = n \sum_{\nu_1 \neq k} \delta_{\nu'_1}^{[\nu_1 \dots \nu_n]} (\partial_t \Psi_{\nu_1}) (\partial^{\mu_1} \Psi^{\nu'_1}) (\partial_{\mu_1} \Psi_k) (\partial_{\mu_m} \Psi_k) (\partial^{\mu_m} \Psi^{\nu'_m}) \left( \prod_{l=2, l \neq m}^n (\partial_{\mu_l} \Psi_{\nu_l}) (\partial^{\mu_l} \Psi^{\nu'_l}) \right) = 0 \quad (\text{A25})$$

because the factor  $(\partial^{\mu_1} \Psi^{\nu'_1}) (\partial_{\mu_1} \Psi_k) (\partial_{\mu_m} \Psi_k) (\partial^{\mu_m} \Psi^{\nu'_m})$ , this is symmetric under the interchange  $\nu'_1 \leftrightarrow \nu'_m$ , but the Kronecker-delta product is antisymmetric. Now consider (Mercury). As before, in every term,  $\nu_1, \dots, \nu_n$  will take every value  $1, \dots, n$ . Thus, in each term of (Mercury), there will be an  $m$  such that  $\nu_m = k$ , so we write

$$\begin{aligned} \text{(Mercury)} &= \sum_{m=1}^n \delta_{\nu'_1}^{[\nu_1 \dots \delta_{\nu'_m}^k \dots \delta_{\nu'_n}^{\nu_n}]} (\partial_{\mu_m} \Psi_k) (\partial^{\mu_m} \Psi^{\nu'_m}) \left( \prod_{l=1, l \neq m}^n (\partial_{\mu_l} \Psi_{\nu_l}) (\partial^{\mu_l} \Psi^{\nu'_l}) \right) (\partial_t \Psi_k) \\ &= \sum_{m=1}^n \delta_{\nu'_m}^{[k \delta_{\nu'_1}^{\nu_1} \dots \delta_{\nu'_{m-1}}^{\nu_{m-1}} \delta_{\nu'_{m+1}}^{\nu_{m+1}} \dots \delta_{\nu'_n}^{\nu_n}]} (\partial_{\mu_m} \Psi_k) (\partial^{\mu_m} \Psi^{\nu'_m}) \left( \prod_{l=1, l \neq m}^n (\partial_{\mu_l} \Psi_{\nu_l}) (\partial^{\mu_l} \Psi^{\nu'_l}) \right) (\partial_t \Psi_k). \end{aligned} \quad (\text{A26})$$

Now, renaming  $\nu'_m \rightarrow \nu'_1$ ,  $\nu_1 \rightarrow \nu_2$ ,  $\nu'_1 \rightarrow \nu'_2$ , and so on up to  $\nu'_{m-1} \rightarrow \nu'_m$ , and  $\mu_m \rightarrow \mu_1$ ,  $\mu_1 \rightarrow \mu_2$ , and so on up to  $\mu_{m-1} \rightarrow \mu_m$ , we get

$$\begin{aligned} \text{(Mercury)} &= \sum_{m=1}^n \delta_{\nu'_1}^{[k \delta_{\nu'_2}^{\nu_2} \dots \delta_{\nu'_n}^{\nu_n}]} (\partial_{\mu_1} \Psi_k) (\partial^{\mu_1} \Psi^{\nu'_1}) \left( \prod_{l=2}^n (\partial_{\mu_l} \Psi_{\nu_l}) (\partial^{\mu_l} \Psi^{\nu'_l}) \right) (\partial_t \Psi_k) \\ &= n \delta_{\nu'_1}^{[k \delta_{\nu'_2}^{\nu_2} \dots \delta_{\nu'_n}^{\nu_n}]} (\partial_{\mu_1} \Psi_k) (\partial^{\mu_1} \Psi^{\nu'_1}) \left( \prod_{l=2}^n (\partial_{\mu_l} \Psi_{\nu_l}) (\partial^{\mu_l} \Psi^{\nu'_l}) \right) (\partial_t \Psi_k) = \text{(Tellus)}. \end{aligned} \quad (\text{A27})$$

This, in turn, means (Mercury) = (Venus), which shows that  $v_{\text{candidate}}^{\mu_1}$  is a solution to Eq. (A19). We have verified this calculation explicitly up to  $n = d = 5$ , using symbolic mathematical software. In addition, it is straight-forward to show that  $v_{\text{candidate}}^{\mu_1}$  is orthogonal to  $\rho_{i_1 \dots i_{d-n}}$  in the sense that  $v_{\text{candidate}}^{\mu_1} \rho_{i_1 \dots i_k \dots i_{d-n}} = 0$  for all  $k$ . Identifying these as the  $(d-n)$  necessary conditions to determine  $\mathbf{v}^{(\Psi)}$ , we get  $\mathbf{v}_{(\Psi)} = \mathbf{v}_{\text{candidate}}$ , and fix the gauge on  $\mathbf{v}$  by  $\mathbf{v} = \mathbf{v}_{(\Psi)}$ , which gives, finally, the closed expression for the velocity

$$v^\mu = -n \frac{\delta_{\nu'_1}^{[\nu_1 \dots \delta_{\nu'_n}^{\nu_n}]} (\partial_t \Psi_{\nu_1}) (\partial^{\mu_1} \Psi^{\nu'_1}) \prod_{l=2}^n (\partial_{\mu_l} \Psi_{\nu_l}) (\partial^{\mu_l} \Psi^{\nu'_l})}{\delta_{\nu'_1}^{[\nu_1 \dots \delta_{\nu'_n}^{\nu_n}]} \prod_{l=1}^n (\partial_{\mu_l} \Psi_{\nu_l}) (\partial^{\mu_l} \Psi^{\nu'_l})} \quad (\text{A28})$$

While this derivation holds in general, we note that in the case of  $n = d$ , there is no contraction in getting to Eq. (A18), so the velocity can be equivalently written as

$$\text{Special case } n = d: \quad v^\mu = \frac{J^\mu}{\rho} = -n \frac{\epsilon^{\mu_1 \dots \mu_n} \tilde{\epsilon}^{\nu_1 \dots \nu_n} (\partial_t \Psi_{\nu_1}) \prod_{l=2}^n (\partial_{\mu_l} \Psi_{\nu_l})}{\epsilon^{\mu_1 \dots \mu_n} \tilde{\epsilon}^{\nu_1 \dots \nu_n} \prod_{l=1}^n \partial_{\mu_l} \Psi_{\nu_l}}, \quad (\text{A29})$$

which together gives the expressions of the velocities in Eq. (14). For the physically most interesting cases of  $n \leq d \leq 3$ , see Fig. 9.

## Appendix B: Numerical methods

### 1. Bose-Einstein condensates

The damped Gross Pitaevskii equation, Eq. (16), is solved by using a Fourier pseudo-spectral integration scheme on a periodic grid of size  $[-32, 32] \times [-32, 32]$  with spatial discretization  $\Delta x = \Delta y = 0.25$ .

### 2. Active nematic liquid crystals

The evolution of the  $Q$ -tensor follows dissipative dynamics coupled with an incompressible Stokes fluid flow [41]

$$\partial_t Q_{ij} + \mathbf{v} \cdot \nabla Q_{ij} - Q_{ik} \Omega_{kj} + \Omega_{ik} Q_{kj} = \lambda \mathcal{W}_{ij} + \gamma^{-1} H_{ij}, \quad (\text{B1})$$

$$(\Gamma - \eta \nabla^2) v_i = \partial_j (\alpha Q_{ji}) - \nabla p, \quad \nabla \cdot \mathbf{v} = 0, \quad (\text{B2})$$

where  $\mathbf{v}$  is the flow velocity that advects the nematic structure,  $p$  is the fluid pressure,  $\Gamma$  is the friction with a substrate,  $\eta$  is the viscosity and  $\alpha Q$  is the active stress. The vorticity tensor  $2\Omega_{ij} = (\partial_i v_j - \partial_j v_i)$  rotates the nematic structure,  $\lambda$  is the flow alignment parameter which aligns the nematic orientation in the direction of shear

$$\mathcal{W}_{ij} = E_{ij} + (E_{ik} Q_{kj} + Q_{ik} E_{kj}) - Q_{lk} E_{kl} (\delta_{ij} + Q_{ij}),$$

with the trace less strain rate  $2E_{ij} = (\partial_i v_j + \partial_j v_i - \delta_{ij} \partial_k v_k)$ . The molecular field

$$H_{ij} = K \nabla^2 Q_{ij} + A(B - 2Q_{kk}^2) Q_{ij}. \quad (\text{B3})$$

controls the relaxation to equilibrium with  $\gamma$  as the rotational diffusivity. We have here assumed a single Frank elastic constant  $K$ , treating splay and bend distortions similarly. The second term in the molecular field is a relaxation to a homogeneous nematic state. The parameter  $A$  is the quench depth, and  $B$  sets the value of the order parameter  $S_0 = \sqrt{B}$  in the homogeneous state. We discretize the above equations on a  $[-64, 64] \times [-64, 64]$  grid with spatial discretization  $\Delta x = \Delta y = 0.5$ , and solve the system using pseudo-spectral methods. The parameters are set to  $K = \Gamma = \gamma = 1$ ,  $A = \lambda = \eta = 0.5$ ,  $B = 2$  and  $\alpha = -1.4$ . The initial state is  $S = \sqrt{2}$  with the angle of the director  $\theta$  being uniformly distributed in the interval  $(-0.05, 0.05)$ .

### 3. 2D square lattice PFC

To simulate the PFC dynamics, we use the sHPFC model proposed in Ref. [46], namely

$$\partial_t \psi = \Gamma \nabla^2 \frac{\delta F_\psi^{\text{sq}}}{\delta \psi} - \mathbf{v} \cdot \nabla \psi, \quad (\text{B4})$$

coupled to a momentum equation for  $\partial_t \mathbf{v}$

$$\rho_0 \partial_t \mathbf{v} = \langle \tilde{\mu}_c \nabla \psi - \nabla \tilde{f} \rangle + \Gamma_S \nabla^2 \mathbf{v} + \mathbf{f}^{(\text{ext})}. \quad (\text{B5})$$

$\langle \cdot \rangle$  is a convolution with a Gaussian kernel given by

$$\langle \tilde{X} \rangle = \int d\mathbf{r}' \frac{\tilde{X}(\mathbf{r}')}{2\pi w^2} \exp\left(-\frac{(\mathbf{r} - \mathbf{r}')^2}{2w^2}\right), \quad (\text{B6})$$

which filters out variations on length scales smaller than  $w$ . The quench depth in Eq (30) is set to  $r = -0.3$  and the average density to  $\bar{\psi} = -0.3$ . Parameters are set to  $\Gamma = 1$ ,  $\rho_0 = \Gamma_S = 2^{-6}$ , and an initial velocity field  $\mathbf{v} = 0$ . As detailed in Ref. [46], we solve the system of coupled equations with a Fourier pseudo-spectral method. The spatial grid of the simulation is set to  $\Delta x = \Delta y = a_0/7$ .

In the simulation reported in Fig. 5, the perfect lattice is indented by an applied external force density given by a Gaussian profile  $\mathbf{f}^{(\text{ext})} = f_0 \frac{(y-y_0)}{a_0} \exp\left(-\frac{(\mathbf{r}-\mathbf{r}_0)^2}{2w^2}\right) \mathbf{e}_x$ . Above a critical strength  $f_0 = 3.5\mu/a_0$  and width  $w = a_0$ , this force causes the nucleation of a dislocation dipole.

### 4. 2D square lattice APFC

The evolution of the amplitudes as delivered by the APFC model can then be directly expressed as

$$\frac{\partial \eta_n}{\partial t} = - \left| \mathbf{q}^{(n)} \right|^2 \frac{\delta F_\eta}{\delta \eta_n^*}, \quad (\text{B7})$$

with  $F_\eta$  the free energy depending on  $\{\eta_n\}$  that can be derived by substituting Eq. (25) in  $F_\psi^{\text{sq}}$  and integrating over the unit cell [57]. By assuming constant  $\bar{\psi}$  it reads

$$F_\eta = \int d^2 r \left( s \sum_{n=1}^N |\mathcal{G}_n \eta_n|^2 + W(\{\eta_n\}) + C(\bar{\psi}) \right), \quad (\text{B8})$$

with  $\mathcal{G}_n = (\nabla^2 + 2i\mathbf{q}^{(n)} \cdot \nabla)$ ,  $s$  a coefficient that controls elastic constants,  $W(\{\eta_n\}) = r' \Phi/2 + (3/4) \Phi^2 -$

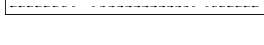

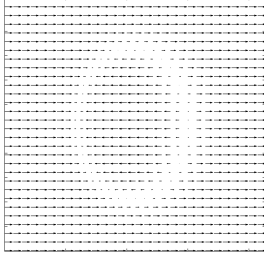
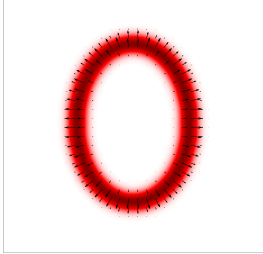
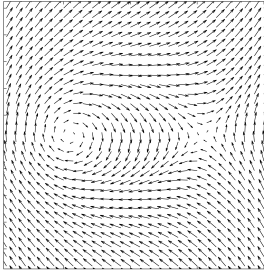
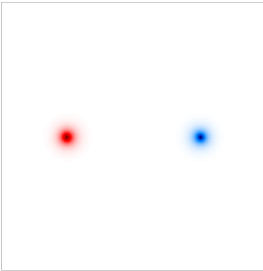
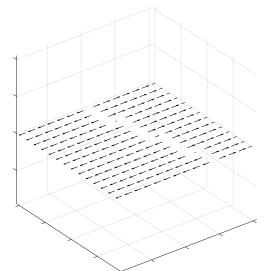
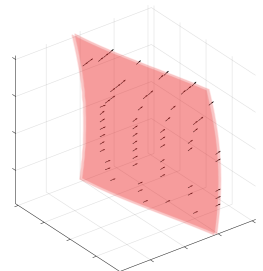
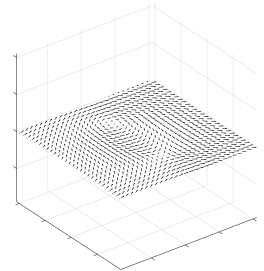
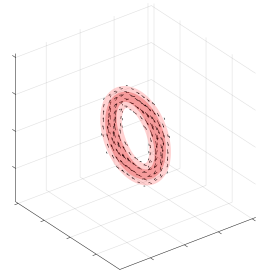
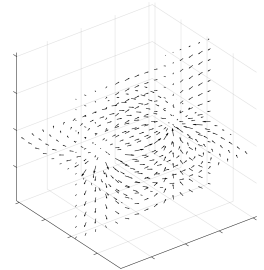
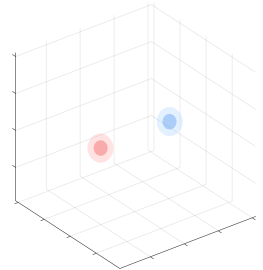
Case	Order parameter	Charge density	Formulae
$d = 1, n = 1$ Point defects			$\rho = \frac{\partial_x \Psi}{2\Psi_0}$ $v_x = -\frac{\partial_x \Psi}{\partial_x \Psi}$
$d = 2, n = 1$ Line defects			$\rho_i = \frac{\partial_i \Psi}{2\Psi_0}$ $v_i = -\frac{\partial_i \Psi \partial_t \Psi}{ \nabla \Psi ^2}$
$d = 2, n = 2$ Point defects			$\rho = \frac{\epsilon^{ij} \bar{\epsilon}^{mn} (\partial_i \Psi_m) (\partial_j \Psi_n)}{2\pi \Psi_0^2}$ $v_i = -2 \frac{\epsilon^{ij} \bar{\epsilon}^{mn} (\partial_t \Psi_m) (\partial_j \Psi_n)}{\epsilon^{ij} \bar{\epsilon}^{mn} (\partial_i \Psi_m) (\partial_j \Psi_n)}$
$d = 3, n = 1$ Wall defects			$\rho_i = \frac{\partial_i \Psi}{2\Psi_0}$ $v_i = -\frac{\partial_i \Psi \partial_t \Psi}{ \nabla \Psi ^2}$
$d = 3, n = 2$ Line defects			$\rho_i = \frac{\epsilon^{ijk} \bar{\epsilon}^{mn} (\partial_j \Psi_m) (\partial_k \Psi_n)}{2\pi \Psi_0^2}$ $v_i = -2 \frac{\delta_m^{[m} \delta_n^{n]} (\partial_t \Psi_m) (\partial^i \Psi^{m'}) (\partial_j \Psi_n) (\partial^j \Psi^{n'})}{\delta_m^{[m} \delta_n^{n]} (\partial_i \Psi_m) (\partial^i \Psi^{m'}) (\partial_j \Psi_n) (\partial^j \Psi^{n'})}$
$d = 3, n = 3$ Point defects			$\rho = \frac{\epsilon^{ijk} \bar{\epsilon}^{mno} (\partial_i \Psi_m) (\partial_j \Psi_n) (\partial_k \Psi_o)}{8\pi \Psi_0^3}$ $v^i = -3 \frac{\epsilon^{ijk} \bar{\epsilon}^{mno} \partial_t \Psi_m \partial_j \Psi_n \partial_k \Psi_o}{\epsilon^{ijk} \bar{\epsilon}^{mno} \partial_i \Psi_m \partial_j \Psi_n \partial_k \Psi_o}$

Figure 9. Examples of reduced defect field corresponding to stable topological defects in  $O(n)$  models for  $n = 1, 2, 3$  in  $d = 1, 2, 3$ .

$(3/4) \sum_{n=1}^N |\eta_n|^4 + f^s(\{\eta_n\})$ ,  $r' = r + 3\bar{\psi}^2$ ,  $\Phi = \sum_{n=1}^N |\eta_n|^2$ , and  $f^s(\{\eta_n\})$  a symmetry-dependent polynomial in the amplitudes. For the square symmetry as encoded in Eq. (30) and the choice  $\mathbf{q}^{(1)} = (1, 0)$ ,  $\mathbf{q}^{(2)} = (0, 1)$ ,  $\mathbf{q}^{(3)} = (1, 1)$ ,  $\mathbf{q}^{(4)} = (-1, 1)$  and  $\{\mathbf{q}^{(n)}\} = \{-\mathbf{q}^{(n-4)}\}$  for  $n = 5, \dots, 8$ , we have  $f^s(\{\eta_n\}) = 2\psi(\eta_1\eta_2\eta_3^* + \eta_1\eta_2^*\eta_4) + 3(\eta_1^2\eta_3^*\eta_4 + \eta_2^2\eta_3^*\eta_4^*) + \text{c.c.}$ , with  $\{\eta_n^*\} = \{\eta_{n-4}\}$  for  $n = 5, \dots, 8$  as  $\psi$  is a real function. Therefore, one may consider just  $\eta_n$  with  $n = 1, \dots, 4$  as variables.  $C(\bar{\psi})$  is a constant depending on  $\bar{\psi}$  [57], set here to  $\bar{\psi} = -0.3$  as set in the corresponding PFC modeling of the 2D square lattice.  $r'$  corresponds to a phenomenological temperature. With  $r_0$  the solid-liquid critical point, the solid crystalline phase is favored for  $r' < r_0$ .

We simulate a stationary system hosting dislocations with the APFC model exploiting the (FEM) numerical approach with adaptive grid refinement outlined in Refs. [64, 65]. We consider dislocations with spacing  $L = 50a_0$  arranged in a periodic, 2D matrix with alternating Burgers vectors  $\pm a_0 \hat{x}$ . The system is initialized by setting the displacement field of dislocation known from classical continuum mechanics [47] in the phase of amplitudes,  $-\mathbf{q}^{(n)} \cdot \mathbf{u}$ , and let relaxed according to the amplitudes evolution law (B7). We can consider a system  $2L \times 2L$  by exploiting periodic boundary conditions.

In section VI, we characterize the extension of the core of dislocations through the field  $\mathbf{D}^{(n)}$  as entering the definition of the dislocation density tensor  $\alpha$ , Eq. (29). We compare the size of the defects extracted with the aid of Gaussian fits (see Fig. 6(a)-(b)) with the extension of a solid-liquid interface,  $w$ , computed numerically as the average of interface width for single amplitudes. This is obtained by initializing the solid phase with a straight interface having normal along the x-axis and letting the system evolve by Eq. (B7) until reaching a steady state. Then, a fit of each amplitude with a function  $\phi_i = \bar{A}_i [1 - \tanh(x - \bar{x}_i) / \bar{w}_i]$ , representing a travelling wave solution for a solid-liquid interface [52, 56, 58], is performed with  $\bar{A}_i$ ,  $\bar{x}_i$  and  $\bar{w}_i$  parameters and the solid-liquid interface thickness extracted as  $w = \sum_{i=1}^4 \bar{w}_i / 4$ .

## 5. 3D bcc lattice PFC

Numerical simulations reported in Sec. VI 2 are obtained by solving the classical PFC equation encoding dissipative dynamics,

$$\partial_t \psi = \nabla^2 \frac{\delta F_\psi^{\text{bcc}}}{\delta \psi}, \quad (\text{B9})$$

where  $F_\psi^{\text{bcc}}$  is a free energy functional that produces a stable bcc lattice, given by

$$F_\psi^{\text{bcc}} = \int d^3r \frac{1}{2} (\mathcal{L}_1 \psi)^2 + \frac{r}{2} \psi^2 + \frac{1}{4} \psi^4. \quad (\text{B10})$$

As parameters, we use  $r = -0.3$  and  $\psi_0 = -0.325$  with spatial discretization  $\Delta x = \Delta y = \Delta z = a_0/7$  and

exploiting a Fourier pseudo-spectral integration scheme. We consider a  $51 \times 51 \times 51$  cubic crystal as matrix in which we embed a spherical inclusion with radius  $17a_0$  rotated at an angle  $\theta_{\text{rot}}$  about the  $[1, 1, 1]$ -axis. This initial condition is obtained just by a rotation of grid points inside the inclusion. This leaves a sharp (and unphysical) interface which is regularized by letting this initial condition relax as dictated by Eq. (B9) for 300 time steps with  $\Delta t = 0.1$ .

- 
- [1] N. D. Mermin, The topological theory of defects in ordered media, *Rev. Mod. Phys.* **51**, 591 (1979).
- [2] T. W. B. Kibble, Topology of cosmic domains and strings, *J. Phys. A* **9**, 1387 (1976).
- [3] L. Michel, Symmetry defects and broken symmetry. configurations hidden symmetry, *Rev. Mod. Phys.* **52**, 617 (1980).
- [4] A. Vilenkin and E. P. S. Shellard, *Cosmic strings and other topological defects* (Cambridge University Press, 1994).
- [5] P. M. Chaikin and T. C. Lubensky, Topological defects, in *Principles of Condensed Matter Physics* (Cambridge University Press, 1995) p. 495–589.
- [6] D. R. Nelson, *Defects and geometry in condensed matter physics* (Cambridge University Press, 2002).
- [7] T. Ozawa, H. M. Price, A. Amo, N. Goldman, M. Hafezi, L. Lu, M. C. Rechtsman, D. Schuster, J. Simon, O. Zeitler, *et al.*, Topological photonics, *Rev. Mod. Phys.* **91**, 015006 (2019).
- [8] A. Ardaševa and A. Doostmohammadi, Topological defects in biological matter, *Nat. Rev. Phys.* **4**, 354 (2022).
- [9] L. Madeira, M. A. Caracanhas, F. dos Santos, and V. S. Bagnato, Quantum turbulence in quantum gases, *Annu. Rev. Condens. Matter Phys.* **11**, 37 (2020).
- [10] R. Alert, J. Casademunt, and J.-F. Joanny, Active turbulence, *Annu. Rev. Condens. Matter Phys.* **13**, 10.1146/annurev-conmatphys-082321-035957 (2022).
- [11] S. Papanikolaou, Y. Cui, and N. Ghoniem, Avalanches and plastic flow in crystal plasticity: an overview, *Model. Simul. Mat. Sci. Eng.* **26**, 013001 (2017).
- [12] G. L. Eyink and K. R. Sreenivasan, Onsager and the theory of hydrodynamic turbulence, *Rev. Mod. Phys.* **78**, 87 (2006).
- [13] C. Zhou, S. B. Biner, and R. LeSar, Discrete dislocation dynamics simulations of plasticity at small scales, *Acta Mater.* **58**, 1565 (2010).
- [14] T. W. Neely, E. C. Samson, A. S. Bradley, M. J. Davis, and B. P. Anderson, Observation of vortex dipoles in an oblate bose-einstein condensate, *Phys. Rev. Lett.* **104**, 160401 (2010).
- [15] W. J. Kwon, G. Moon, S. W. Seo, and Y.-i. Shin, Critical velocity for vortex shedding in a bose-einstein condensate, *Phys. Rev. A* **91**, 053615 (2015).
- [16] T. Aioi, T. Kadokura, T. Kishimoto, and H. Saito, Controlled generation and manipulation of vortex dipoles in a Bose-Einstein condensate, *Phys. Rev. X* **1**, 021003 (2011).
- [17] M. Kunimi and Y. Kato, Metastability, excitations, fluctuations, and multiple-swallowtail structures of a superfluid in a Bose-Einstein condensate in the presence of a uniformly moving defect, *Phys. Rev. A* **91**, 053608 (2015).
- [18] A. Skaugen and L. Angheluta, Vortex clustering and universal scaling laws in two-dimensional quantum turbulence, *Phys. Rev. E* **93**, 032106 (2016).
- [19] T. Neely, A. Bradley, E. Samson, S. Rooney, E. M. Wright, K. Law, R. Carretero-González, P. Kevrekidis, M. Davis, and B. P. Anderson, Characteristics of two-dimensional quantum turbulence in a compressible superfluid, *Phys. Rev. Lett.* **111**, 235301 (2013).
- [20] S. P. Thampi, R. Golestanian, and J. M. Yeomans, Vorticity, defects and correlations in active turbulence, *Philos. Trans. Royal Soc. A* **372**, 20130366 (2014).
- [21] A. Doostmohammadi, T. N. Shendruk, K. Thijssen, and J. M. Yeomans, Onset of meso-scale turbulence in active nematics, *Nat. Commun.* **8**, 1 (2017).
- [22] N. Zolotarevsky, V. Rybin, E. Ushanova, N. Ermakova, and V. Perevezentsev, Large-scale fragmentation of grains in plastically deformed polycrystalline iron, *Mater. Today Commun.* **31**, 103816 (2022).
- [23] J. Li, T. Zhu, S. Yip, K. J. V. Vliet, and S. Suresh, Elastic criterion for dislocation nucleation, *Mater. Sci. Eng. A* **365**, 25 (2004).
- [24] R. E. Miller and A. Acharya, A stress-gradient based criterion for dislocation nucleation in crystals, *J. Mech. Phys. Solids* **52**, 1507 (2004).
- [25] A. Garg, A. Acharya, and C. E. Maloney, A study of conditions for dislocation nucleation in coarser-than-atomistic scale models, *J. Mech. Phys. Solids* **75**, 76 (2015).
- [26] B. I. Halperin, Statistical Mechanics of Topological Defects, in *Physique Des Défauts/ Physics of Defects*, edited by R. Balian, M. Kléman, and J.-P. Poirier (North-Holland, Amsterdam, 1981) pp. 812–857.
- [27] G. F. Mazenko, Vortex velocities in the O(n) symmetric time-dependent ginzburg-landau model, *Phys. Rev. Lett.* **78**, 401 (1997).
- [28] A. Mietke and J. Dunkel, Anyonic defect braiding and spontaneous chiral symmetry breaking in dihedral liquid crystals, *Phys. Rev. X* **12**, 011027 (2022).
- [29] P. A. Monderkamp, R. Wittmann, M. Te Vrugt, A. Voigt, R. Wittkowski, and H. Löwen, Topological fine structure of smectic grain boundaries and tetratic disclination lines within three-dimensional smectic liquid crystals, *Phys. Chem. Chem. Phys.* **24**, 15691 (2022).
- [30] J. Rønning, A. Skaugen, E. Hernández-García, C. Lopez, and L. Angheluta, Classical analogies for the force acting on an impurity in a Bose-Einstein condensate, *New J. Phys.* **22**, 073018 (2020).
- [31] J. Rønning and L. Angheluta, Nucleation and kinematics of vortices in stirred Bose Einstein condensates (2022), arXiv:2210.14620 [cond-mat].
- [32] L. Angheluta, Z. Chen, M. C. Marchetti, and M. J. Bowick, The role of fluid flow in the dynamics of active nematic defects, *New J. Phys.* **23**, 033009 (2021).
- [33] J. Rønning, M. C. Marchetti, M. J. Bowick, and L. Angheluta, Flow around topological defects in active nematic films, arXiv:2111.08537 [cond-mat] (2021), arXiv:2111.08537 [cond-mat].
- [34] A. Skaugen, L. Angheluta, and J. Viñals, Dislocation dynamics and crystal plasticity in the phase-field crystal model, *Phys. Rev. B* **97**, 054113 (2018).
- [35] V. Skogvoll, A. Skaugen, L. Angheluta, and J. Viñals, Dislocation nucleation in the phase-field crystal model, *Phys. Rev. B* **103**, 014107 (2021).
- [36] V. Skogvoll, L. Angheluta, A. Skaugen, M. Salvalaglio, and J. Viñals, A phase field crystal theory of the kinematics of dislocation lines, *J. Mech. Phys. Solids* **166**, 104932 (2022).
- [37] S. Zhou, S. V. Shiyankovskii, H.-S. Park, and O. D. Lavrentovich, Fine structure of the topological defect cores studied for disclinations in lyotropic chromonic liq-

- uid crystals, *Nat. Commun.* **8**, 14974 (2017).
- [38] M. T. Reeves, T. P. Billam, B. P. Anderson, and A. S. Bradley, Inverse energy cascade in forced two-dimensional quantum turbulence, *Phys. Rev. Lett.* **110**, 104501 (2013).
- [39] G. Astrakharchik and L. Pitaevskii, Motion of a heavy impurity through a bose-einstein condensate, *Physical Review A* **70**, 013608 (2004).
- [40] M. C. Marchetti, J.-F. Joanny, S. Ramaswamy, T. B. Liverpool, J. Prost, M. Rao, and R. A. Simha, Hydrodynamics of soft active matter, *Rev. Mod. Phys.* **85**, 1143 (2013).
- [41] M. R. Nejad, A. Doostmohammadi, and J. M. Yeomans, Memory effects, arches and polar defect ordering at the cross-over from wet to dry active nematics, *Soft Matter* **17**, 2500 (2021).
- [42] K. R. Elder, M. Katakowski, M. Haataja, and M. Grant, Modeling Elasticity in Crystal Growth, *Phys. Rev. Lett.* **88**, 245701 (2002).
- [43] K. R. Elder and M. Grant, Modeling elastic and plastic deformations in nonequilibrium processing using phase field crystals, *Phys. Rev. E* **70**, 051605 (2004).
- [44] A. Emdadi, M. Asle Zaeem, and E. Asadi, Revisiting phase diagrams of two-mode phase-field crystal models, *Comput. Mater. Sci.* **123**, 139 (2016).
- [45] V. Skogvoll, A. Skaugen, and L. Angheluta, Stress in ordered systems: Ginzburg-Landau-type density field theory, *Phys. Rev. B* **103**, 224107 (2021).
- [46] V. Skogvoll, M. Salvalaglio, and L. Angheluta, Hydrodynamic phase field crystal approach to interfaces, dislocations and multi-grain networks, *Model. Simul. Mater. Sci. Eng.* **30**, 084002 (2022).
- [47] P. Anderson, J. Hirth, and J. Lothe, *Theory of Dislocations* (Cambridge University Press, 2017).
- [48] C. Hüter, M. Friák, M. Weikamp, J. Neugebauer, N. Goldenfeld, B. Svendsen, and R. Spatschek, Nonlinear elastic effects in phase field crystal and amplitude equations: Comparison to ab initio simulations of bcc metals and graphene, *Phys. Rev. B* **93**, 214105 (2016).
- [49] N. Goldenfeld, B. P. Athreya, and J. A. Dantzig, Renormalization group approach to multiscale simulation of polycrystalline materials using the phase field crystal model, *Phys. Rev. E* **72**, 020601 (2005).
- [50] B. P. Athreya, G. Nigel, and J. A. Dantzig, Renormalization-group theory for the phase field crystal model, *Phys. Rev. E* **74**, 011601 (2006).
- [51] K. R. Elder, N. Provatas, J. Berry, P. Stefanovic, and M. Grant, *Phys. Rev. B* **75**, 064107 (2007).
- [52] P. Galenko, F. I. Sanches, and K. Elder, Traveling wave profiles for a crystalline front invading liquid states: Analytical and numerical solutions, *Phys. D: Nonlinear Phenom.* **308**, 1 (2015).
- [53] W. Cai, A. Arsenlis, C. Weinberger, and V. Bulatov, A non-singular continuum theory of dislocations, *J. Mech. Phys. Solids* **54**, 561 (2006).
- [54] M. Lazar and G. A. Maugin, Nonsingular stress and strain fields of dislocations and disclinations in first strain gradient elasticity, *Int. J. Eng. Sci.* **43**, 1157 (2005).
- [55] M. Lazar, G. A. Maugin, and E. C. Aifantis, Dislocations in second strain gradient elasticity, *Int. J. Solids Struct.* **43**, 1787 (2006).
- [56] V. Ankudinov, K. R. Elder, and P. K. Galenko, Traveling waves of the solidification and melting of cubic crystal lattices, *Phys. Rev. E* **102**, 062802 (2020).
- [57] M. Salvalaglio and K. R. Elder, Coarse-grained modeling of crystals by the amplitude expansion of the phase-field crystal model: an overview, *Model. Simul. Mater. Sci. Eng.* **30**, 053001 (2022).
- [58] I. G. Nizovtseva and P. K. Galenko, Travelling-wave amplitudes as solutions of the phase-field crystal equation, *Philos. Trans. R. Soc. A* **376**, 20170202 (2018).
- [59] A. Yamanaka, K. McReynolds, and P. W. Voorhees, Phase field crystal simulation of grain boundary motion, grain rotation and dislocation reactions in a BCC bicrystal, *Acta Mater.* **133**, 160 (2017).
- [60] M. Salvalaglio, R. Backofen, K. R. Elder, and A. Voigt, Defects at grain boundaries: A coarse-grained, three-dimensional description by the amplitude expansion of the phase-field crystal model, *Phys. Rev. Materials* **2**, 053804 (2018).
- [61] J. Han, S. L. Thomas, and D. J. Srolovitz, Grain-boundary kinetics: A unified approach, *Prog. Mater. Sci.* **98**, 386 (2018).
- [62] D. R. Nelson and B. Halperin, Dislocation-mediated melting in two dimensions, *Physical Review B* **19**, 2457 (1979).
- [63] S. Carroll, *Spacetime and Geometry: Pearson New International Edition* (Pearson Education Limited, 2014).
- [64] M. Salvalaglio, R. Backofen, A. Voigt, and K. R. Elder, Controlling the energy of defects and interfaces in the amplitude expansion of the phase-field crystal model, *Phys. Rev E* **96**, 023301 (2017).
- [65] S. Praetorius, M. Salvalaglio, and A. Voigt, An efficient numerical framework for the amplitude expansion of the phase-field crystal model, *Model. Simul. Mater. Sci. Eng.* **27**, 044004 (2019).